Investigating the ability to use the CT scan projection radiograph to monitor adolescent idiopathic scoliosis

Faisal Abdulrazaq W Alrehily

School of Health and Society

University of Salford

Submitted in Partial Fulfilment of the Requirements of the

Degree of Doctor of Philosophy (PhD)

2019

Research Supervisors

1. **Dr. Andrew K. Tootell** (main supervisor)

   Directorate of Radiography
   L617, Allerton Building, Frederick Road Campus,
   University of Salford, Manchester M6 6PU
   Email: A.K.Tootell@salford.ac.uk

2. **Prof. Peter Hogg** (co-supervisor)

   AD114, Allerton building, Frederick Road Campus,
   University of Salford, Manchester M6 6PU
   Email: P.Hogg@Salford.ac.uk

3. **Dr. Martin Twiste** (co-supervisor)

   PO53, Brain Blatchford Building, Frederick Road Campus,
   University of Salford, Manchester M6 6PU
   Emil: M.Twiste@salford.ac.uk

Table of Contents

List of Tables

List of Figures

List of Publications and Presentations

Date	Title	Type	Status
October 2018	Commenting on the paper entitled "Does collimation affect patient dose in antero-posterior thoraco-lumbar spine?"	Letter to the editor	Published
May 2018	Adolescent scoliosis imaging: radiation dose and image quality	Showcase Poster	Presented
June 2018	Quantifying radiation dose from using CT scout mode to assess scoliosis	Seminar presentation	Presented
February 2019	Scoliosis imaging: An analysis of radiation risk in the CT scan projection radiograph and a comparison with projection radiography and EOS	Journal paper	Published
June 2019	Scoliosis imaging – an analysis of organ dose in the CT Scan Projection Radiograph	Conference poster (United Kingdom Imaging and Oncology [UKIO])	Presented
July 2019	A comparative study of radiation risk in scoliosis imaging	Conference poster (SPARK)	Presented
July 2019	A comparative study of radiation risk in scoliosis imaging	Conference presentation (SPARK)	Presented
November 2019	Development and validation of a bespoke phantom to test accuracy of Cobb angle measurements	Journal paper	Published
November 2019	The accuracy of Cobb angle measurement on CT scan projection radiograph images	Journal paper	Published

Date	Title	Type	Status
February 2020	Investigating the ability to use scan projection radiograph in CT scan to assess AIS	Seminar presentation	Presented
March 2020	Development and validation of a bespoke phantom to test accuracy of Cobb angle measurements	Conference poster (European Congress of Radiology (ECR)	Accepted*
March 2020	The accuracy of Cobb angle measurement on CT scan projection radiograph images	Conference poster (ECR)	Accepted*
March 2020	The effect of fat mass on the accuracy of Cobb angle measurements in patients with adolescent idiopathic scoliosis: a phantom study	Conference poster (ECR)	Accepted*
2020	The effect of fat mass on the accuracy of Cobb angle measurements in patients with adolescent idiopathic scoliosis: a phantom study	Journal paper	Under review
* The posters will be presented in July 2020.			

Training Sessions Attended During the Study

Data	Training sessions
12.10.2016	Completing a Learning Agreement.
19.10.2016	Doctoral training Seminar.
24.10.2016	Building a healthy working relationship with your supervision.
25.10.2016	Intro to Endnote X7.
26.10.2016	Lab Skills training session 1
27.10.2016	Lab skills training session 2
27.10.2016	Introduction to SPSS.
01.11.2016	Confidence Building for public speaking.
02.11.2016	A survival guide to doing a Ph.D.
03.11.2016	Excel: the basics
15.11.2016	Doing a literature review.
17.11.2016	Handling MOSFET
21.11.2016	Calibrating MOSFET
30.11.2016	Word: Formatting dissertation or thesis.
01.12.2016	Introduction to Critical and Analytical Skills
19.01.2017	Quantitative research analysis with SPSS
08.02.2017	Research ethics for PGRs
08.02.2017	Health & safety session to use prosthetics and orthotics facility.
03.03.2017	Presentation skills
18.10.2017	Technology for learning workshop - PGR seminar
02.11.2017	Get more out of your reading
02.11.2017	The literature review and your critical ‘voice’
02.11.2017	Introduction to EndNote and reference management
15.11.2017	Talk about your research - PGR seminar
06.12.2017	Using social media to develop professional and academic profile - PGR seminar

Data	Training sessions
10.01.2018	Writing for publication - PGR seminar
11.01.2018	Planning a cohesive story - PGR writing workshop
17.01.2018	Writing argument - PGR writing workshop
22.01.2018	Peer review and feedback - PGR writing workshop
05.02.2018	Peer review and feedback - PGR writing workshop
07.02.2018	Ontological Foundations-Philosophical Stance 1
08.02.2018	Writing for your IA and IE
08.02.2018	Proof reading, editing and letting go
08.02 2018	How to write an abstract Researcher
14.02.2018	Epistemological Foundations -Philosophical Stance 1
21.02.2018	Axiological Foundations- Philosophical Stance 1
26.02.2018	Abstract writing - PGR writing workshop
28.02.2018	Methodological Choices - Philosophical Stance 1
07.03.2018	Multi versus Mixed Methods -Philosophical Stance 1
14.03.2018	Defending the Position - Philosophical Stance 1
14.03.2018	Peer review and feedback - PGR writing workshop
10.05.2018	The Thesis Explored
10.05.2018	Thesis writing retreat
10.05.2018	Defending your thesis
16.05.2018	What happens in IA and IE? - PGR seminar
20.06.2018	Student presentation - PGR seminar
03.10.2018	Writing argument - PGR writing workshop
10.10.2018	Peer review and feedback - PGR writing workshop
17.10.2018	Theories of learning and teaching.
23.10.2018	Peer review and feedback - PGR writing workshop
25.10.2018	Welcoming PGR students - PGR seminar
31.10.2018	Larger group and small group teaching.

Data	Training sessions
07.11.2018	Peer review and feedback - PGR writing workshop
13.11.2018	Abstract writing- PGR writing workshop
14.11.2018	Technology enhanced learning
21.11.2018	Peer review and feedback - PGR writing workshop
22.11.2018	How to use social media for academic networking and research- PGR seminar
28.11.2018	Inclusive teaching and classroom management.
06.12.2018	Student presentation - PGR seminar
28.11.2019	Getting ready for the viva

Acknowledgement

I would like to express my gratitude and appreciation for Dr. Andrew Tootell, Prof. Peter Hogg and Dr. Martin Twiste, for their consistent support and guidance during the running of this research project. Furthermore, I would like to thank Chris Beaumont for his huge help in constructing the [PoP] phantom. My gratitude also extends to the staff at the radiography departments in Manchester Children's Hospital and Alder Hey Hospital for facilitating performing dose experiments at their hospitals

I would like to thank my parents, relatives and friends for their continuous support and endless prayers. I also would like to express my thanks to my patient and supportive wife and son, who have supported me throughout this research project. Finally, I would like to thank my employer, Taibah University, and the Saudi Cultural Bureau in London for giving me the opportunity to do this study.

List of Abbreviations

Acronym	Definition
AAPM	American Association for Physicist in Medicine
ABM	Active Bone Marrow
AD	Absorbed Dose
AEC	Automatic Exposure Control
AIS	Adolescent Idiopathic Scoliosis
AP	Anteroposterior
ATOM	Anthropomorphic
ATR	Angle of Trunk Rotation
BEIR	Biologic Effects of Ionizing Radiation
$CDTI_{vol}$	Computed Tomography Dose Index volume
CEC	Commission of the European Communities
CF	Calibration Factor
CNR	Contrast to Noise Ratio
COV	Coefficient of Variation
CR	Computed Radiography
CT	Computed Tomography
CTDI	Computed Tomography Dose Index
DAP	Dose Area Product
DR	Digital Radiography
DRL	Diagnostic Reference Level
EAR	Excess Absolute Risk
ED	Effective Dose
ER	Effective Risk
ERR	Excess Relative Risk
ESAK	Entrance Surface Air Kerma
ESD	Entrance Surface Dose
FBT	Adam's Forward Bend Test
H_T	Equivalent Dose
HU	Hounsfield Units
IAEA	International Atomic Energy Agency
IC	Image Criteria
ICC	Interclass Correlation
ICRP	International Commission on Radiological Protection
ICRU	International Commission on Radiation Units
IEC	International Electrotechnical Commission
IPEM	Institute of Physics and Engineering in Medicine
IQ	Image Quality
kV	Tube Kilovoltage
LAR	Lifetime Attributable Risk

Acronym	Definition
LDRL	Local Diagnostic Reference Level
LNT	Linear No-Threshold Model
LQ	Linear-Quadratic Model
LSS	Lifespan Study
mA	X-Ray Tube Milliampere (Tube Current)
MC	Monte Carlo Simulation Software
MOSFET	Metal–Oxide–Semiconductor Field-Effect Transistors
MR	Magmatic Resonance
MRI	Magnetic Resonance Imaging
mSv	Millisieverts
NAS	National Academy of Sciences
NICE	National Institute for Health and Care Excellence
OD	Organ Dose
OID	Object-To-Image Receptor Distance
OSLD	Optically Stimulated Luminescence Dosimeters
PA	Posteroanterior
P_{KA}	Air Kerma–Area Product
$P_{KL,CT}$	Air Kerma–Length Product
PMMA	Poly (Methyl Methacrylate
PoP	Plaster of Paris
RCR	Royal College of Radiologists
ROC	Receiver Operating Characteristics
ROI	Region of Interest
r_T	Lifetime Radiation-Attributable Tissue-Specific Cancer Risk
SCoR	Society and College of Radiographers
SD	Standard Deviation
SF	Screen-Film
SID	Source to Image Receptor Distance
SNR	Signal to Noise Ration
SPR	Scan Projection Radiograph
SRS	Scoliosis Research Society
ST	Surface Topography
TLD	Thermoluminescent Dosimeter
U/S	Ultrasound
VGA	Visual Grading Analysis
W_R	Radiation Weighting Factors
W_T	Tissue Weighting Factor

Abstract

Introduction: Adolescent idiopathic scoliosis (AIS) is a spinal deformity that causes the spine to bend laterally. Patients with AIS undergo frequent X-ray examinations to monitor the progression of the deformity through the measurement of the Cobb angle, increasing the risk of developing radiation-induced cancer. The aim of this study was to investigate the use of scan projection radiograph (SPR) in computed tomography (CT) to assess AIS by quantifying radiation dose from the SPR acquisitions and comparing it to those of digital radiography (DR) and a dedicated scoliosis imaging system (EOS) and by evaluating the accuracy of Cobb angle measurements on SPR images using a bespoke validated phantom.

Methods: A dosimetry phantom representing a 10-year-old child and thermoluminescent dosimeters were used for measuring organ dose to calculate effective dose (ED) and effective risk (ER). Twenty-seven CT SPR protocols were used. A comparison was made to doses from imaging protocols using DR and the EOS system. The effectiveness of a scoliosis shawl for selected projections was also tested. To test the accuracy of Cobb angle measurements on SPR images, a scoliotic phantom was constructed and validated. Poly-methyl methacrylate (PMMA) and plaster of Paris (PoP) were used to represent human soft tissue and bone tissue, respectively, to construct a phantom exhibiting a 15° lateral curve of the spine. The phantom was validated by comparing the Hounsfield unit (HU) of its vertebrae with those of a human and an animal. Additionally, comparisons of signal-to-noise ratio (SNR) to those from a commercially available phantom were made. The angle of the curve in the phantom was measured directly to confirm that it was 15°. The constructed phantom was scanned in CT SPR mode, and the resulting images were visually evaluated against set criteria to determine

their suitability for Cobb angle measurements. Those deemed of insufficient quality were excluded. Cobb angle measurements were then performed on the remaining images (n = 10) by 13 observers.

Results: EOS had the lowest ED and ER when it was used to irradiate the phantom in AP positions. Five SPR AP imaging protocols and seven PA imaging protocols delivered significantly lower radiation dose and risk than their corresponding imaging positions in DR ($p < 0.05$). The scoliosis shawl significantly lowered the ED and ER of SPR and DR AP imaging protocols ($p < 0.05$). The validation of the PoP phantom revealed that the HU of the PoP vertebrae was 628 (SD= 56), human vertebrae was 598 (SD= 79) and sheep vertebra was 605 (SD= 83). The SNR values of the two phantoms correlated strongly ($r = 0.93$ [($p < 0.05$]). The measured scoliosis angle was 14 degrees. When the phantom was imaged using SPR, the difference between the measured Cobb angle and the known angle was, on average, –2.75° (SD = 1.46°). The agreement among the observers was good ($p = 0.861$, 95% CI [0.70–0.95]) and comparable to similar studies on other imaging modalities which are used for Cobb angle estimation.

Conclusion: EOS had the lowest dose. Where this technology is not available, there is a potential for organ dose (OD) reduction in AIS imaging using CT SPR compared with DR. The PoP phantom has physical characteristics (in terms of spinal deformity) and radiological characteristics (in terms of HU and SNR values) of the spine of a 10-year-old child with AIS. CT SPR images can be used for AIS assessment with the 5° margin of error that is clinically acceptable. A few SPR imaging protocols (CT4, 8 and 11) had the lower radiation risk compared with the DR and provided the most accurate Cobb angle measurements.

Implications for practice: The bespoke phantom can be used to investigate new X-ray imaging techniques and technology in the assessment of scoliosis and has utility for the optimisation of X-ray imaging techniques in 10-year-old children. Overall, the outcome is promising for patients and health providers because it provides an opportunity to reduce patient dose and achieve clinically acceptable Cobb angle measurements whilst using existing CT technology.

Chapter 1: Introduction and thesis structure

1.1 Introduction

Scoliosis is defined as a deformity of the spine in the form of lateral curvature in the coronal plane. Despite it being defined as a lateral curvature, scoliosis is a deformity in three dimensions: side to side, front to back and rotation around the spine's longitudinal axis. It affects not only the spine, but also the entire skeletal system. Moreover, its impact on patients may even affect the digestive, hormonal and nervous systems. On rare occasions, patients with severe scoliosis may have breathing difficulties and heart problems.

Scoliosis can be categorised based on the causes of the deformity as follows: neuromuscular, congenital and idiopathic. The latter is the most common type of scoliosis, but its causes are unknown (Heary and Albert, 2014). Idiopathic scoliosis can be categorised into four subgroups based on age of onset: infantile (birth to 3 years), juvenile (4–9 years), adolescent (10–18 years) and adult (after skeletal maturity). This thesis will focus on adolescent idiopathic scoliosis (AIS) which represents 75–90% of scoliosis cases (Konieczny et al., 2013; Blevins et al., 2018). The United Kingdom (UK) Scoliosis Association estimates that approximately three to four children per 1,000 are diagnosed with AIS. In most cases, AIS does not require treatment; instead, the deformity is observed until patients mature completely.

Prior to exploring how AIS is observed, it is necessary to understand the anatomy of the spine. The spine consists of 26 vertebrae spread over five regions: cervical, thoracic, lumbar,

sacral and coccygeal. Each region has a specific number of vertebrae: 7 cervical, 12 thoracic, 5 lumbar, 1 sacral (5 fused vertebrae) and 1 coccygeal (4 usually fused vertebrae). The spinal regions have normal curves that give the spine flexibility, help absorb shock and support the human body. These curves can be either concave posteriorly, i.e. in the cervical and lumbar regions, or convex posteriorly, i.e. in the thoracic and sacral regions, as illustrated in **Figure 1.1**. At birth, only the convex curvature is well-developed, whereas the other curvature is developed by the age of two years (Marieb et al., 2012). In a normal spine, no axial rotation should be present. During development, the size of the vertebrae increases to accommodate body growth, and this change is gender-dependent (Cunningham et al., 2016). The vertebrae of a female spine are longer and narrower than that of a male.

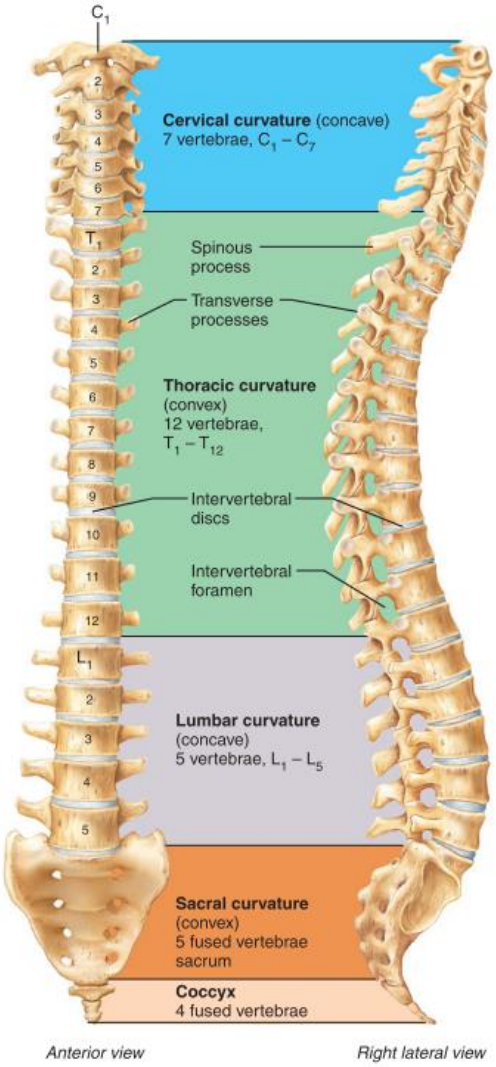

Figure 1.1: Anterior and lateral view of the spine shows the five areas of the spine and the normal curves (Marieb et al., 2012).

In scoliosis, the spine deviates in the coronal plane, creating a curvature in which the degree of the curve is 10° or more. In some cases, patients with scoliosis may have visible symptoms of the deformity that can be recognised. The signs can be shoulder asymmetry, where one shoulder appears higher than the other; waistline asymmetry, a shift of the body to one side; or rib hump, where the back ribs are pushed posteriorly due to vertebral rotation (**Figure 1.2**). Depending on shape and magnitude of the curve, these signs can appear individually or together.

Figure 1.2: Images of patients with scoliosis; some scoliosis symptoms such as body shifting and shoulder asymmetry are obvious in the images (Weinstein et al., 2008).

Screening for scoliosis is usually carried out by visually inspecting the shoulder, spine and pelvis. The screening may involve physical examination using the Adam's forward bend test (FBT) and measuring the angle of trunk rotation (ATR) using a scoliometer. If a child is suspected to have scoliosis, then a referral for X-ray examination is made to confirm the diagnosis. The screening aim is to identify children with scoliosis as soon as possible to prevent the condition from worsening. However, screening for scoliosis is not common in most countries, as can be seen in the following section. In the United States (US), the most recent publication by the US Preventive Task Force recommends against establishing a screening programme because its benefits would be uncertain (Grossman et al., 2018). The UK Screening Committee concluded this as well based on similar reasoning. In its latest review, the committee determined not to have screening programmes in the UK for the following reasons: (1) it is not clear when children can be screened; (2) the ability of a screening programme to identify the severity of a certain case is very low; (3) treatment plans

cannot be based on the outcomes of the screening; and (4) lastly, the added benefit of a screening programme is questionable (UK National Screening Committee, 2015).

Due to the lack of scoliosis screening programmes, the prevalence of AIS is not well investigated in the literature. There are few reports of the outcomes of scoliosis screening programmes from several countries (**Table 1.1**). Moreover, the main weaknesses of the existing studies are related to the lack of a standard screening protocol. First, the number and age of participants vary among the studies. Second, the participants are from different nations, which can greatly affect the prevalence rate. Geographic location and ethnicity affect AIS prevalence (Machida et al., 2018). For example, AIS is more common in higher-latitude countries than in the lower-latitude countries (Grivas et al., 2006). Finally, some studies include curves of less than 10°, which is not scoliosis according to the Scoliosis Research Society (SRS) definition (SRS, 2000). Nevertheless, conclusions can still be drawn from these studies, as illustrated in the following paragraphs.

Table 1.1: Summary of the most recent scoliosis screening programmes in different countries.						
Study	Year	Country	Number of participants (total number) (females – males)	Age (years)	Percentage of participants diagnosed with scoliosis (% of females – % of males)	Percentage of participants with Cobb angle from 10˚ to 19˚
Soucacos *et al.*	1997	Greece	82,901 (40,962–41,939)	9–14	1.73 (74.86–25.14)	87.40
Wong *et al.*	2005	Singapore	72,966 (37,141–35,558)	6–14	0.59 (86.48–13.52)	65.03
Kamtsiuris *et al.*	2007	Germany	17,641 (8,656–8,995)	0–17	5.2 (56.76–43.23)	Not stated
Cilli *et al*	2009	Turkey	3,175 (1,538–1,637)	10–15	0.47 (66.66–33.33)	Not stated
Nery *et al.*	2010	Brazil	1,340 (684–656)	10–14	1.4 (73.68–26.32)	Not stated
Suh *et al.*	2011	South Korea	1,134,890 (550,336–584,554)	10–14	3.29 (70.30–29.70)	89.09
Ueno *et al.*	2011	Japan	255,857 (127,903–127,972)	11–14	1.18 (93.08–6.92)	73.63
Adobor *et al.*	2011	Norway	4,000 (not stated)	12	0.55 (72.73–27.27)	Not stated

The main findings of the screening programmes can be summarised as follows: children who are diagnosed with scoliosis represent 0.55–5.2% of the participants, and the prevalence rate increases as the children's ages increase. This is supported by the earlier statement that AIS, which affects children aged 10–18 years, accounts for up to 90% of scoliosis cases. The reason behind this can be correlated to the rapid growth that takes place at this age and that the skeletal system has not reached maturity (Sanders et al., 2007; Adobor et al., 2012; Heary and Albert, 2014).

Another finding that can be inferred from the published studies is that scoliosis is more prevalent in females than males. A greater number of females were diagnosed with scoliosis than males; their spinal curvature was also more severe than that in male participants. No obvious causative factors for this gender difference in prevalence have been discovered. Possible causes include high levels of growth hormone (Latalski et al., 2017) and a weaker spine due to the shape of the vertebrae in females compared to males (Cunningham et al., 2016). As indicated earlier, female vertebrae are narrower and longer than those of males, which renders them more susceptible to bending. Nevertheless, the causes of this gender difference in the prevalence rate remains ambiguous.

1.2 Diagnosis of AIS

Confirmation of AIS diagnosis requires radiological examination. Patients are referred to undergo imaging for full-length frontal (anteroposterior [AP] or posteroanterior [PA]), lateral and lateral-bending images of the spine. These images are used to determine the severity and flexibility of the curve and skeletal maturity (W. Kim et al., 2018; Blevins et al., 2018). AP/PA and lateral/lateral-bending images are the usual projections undertaken for assessing the spine at the initial visit, but sometimes other images are requested, such as assessment of

bone age (imaging of the non-dominant hand and wrist). Only before treatment AP/PA and lateral images are required. In the follow-up sessions, the progression of the curve is monitored, but for surgical planning, it is important to assess the prognosis of the AIS by evaluating vertebral rotation (Yazici et al., 2001; Kim et al., 2010). Imaging might take place at intervals of 3–12 months, depending on the curve severity, patient's age and the management plan: it is estimated that patients with milder cases can have three X-ray images per year, and patients with more severe cases can have up to 12 X-ray images per year (Presciutti et al., 2014). The number and frequency of X-ray imaging sessions are not well-investigated in the literature; most of the recent studies are built on a cohort study carried out in the early years of the twentieth century. These studies have estimated that patients with scoliosis might undergo X-ray imaging up to 22 times over a 3-year period (Nash et al., 1979; Doody et al., 2000). A more recent study that used the same cohort study found that patients with AIS had undergone 27 X-ray examinations during the period of disorder management (Simony et al., 2016).

1.3 Diagnostic measurements

X-ray images provide details that aid in the evaluation of scoliosis. During the initial visit, PA and lateral images are captured (PA is preferable to AP because it lowers the risk from radiation compared with AP [Chaparian, Kanani and Baghbanian, 2014; Ng and Bettany-Saltikov, 2017]). The Cobb angle, vertebral rotation, skeletal maturity and curve type are determined from the PA image. Lateral images aid in the determination of pelvic obliquity, pelvic incidence, sacral angle and abnormal lordosis and kyphosis. In the follow-up session, only AP or PA images are acquired to measure the Cobb angle to monitor the progression of

the disorder. The following sections illustrate how the most common radiographic measures are quantified from an X-ray image.

1.3.1 Cobb angle

The Cobb angle was introduced to determine the severity of spinal deformity by quantifying the degree of the curvature (Cobb, 1948). It is the gold standard for evaluating scoliosis. Lines are drawn on the uppermost and lowermost tilted vertebrae: the intersection of these lines forms the Cobb angle, or it is formed by the intersection of two lines drawn perpendicular to the initial lines, as shown in **Figure 1.3**. The measurement can be performed manually on an X-ray image, or digitally using specialised image viewing software. The difference between the accuracy of these measurements is discussed in **Section 2.5.1.3** on **page 50**.

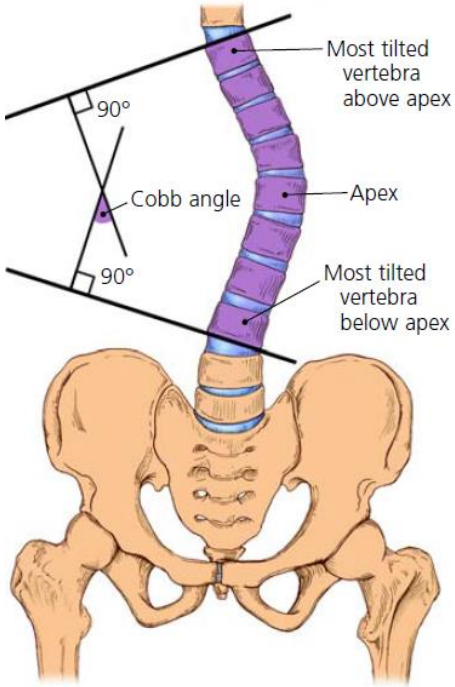

Figure 1.3: Illustration of how the Cobb angle is measured (Greiner, 2002).

The Cobb method for assessing scoliosis has a few limitations. First, it is dependent on the patient's posture during the scanning, which can be affected by the gravitational loading on

the spine (Wessberg et al., 2006; Keenan et al., 2014). The gravitational loading is at maximum when in the standing position, resulting in a larger Cobb angle. The other weakness is that it does not account for vertebral rotation (Yazici et al., 2001; Lam et al., 2008; Brink, Colo, et al., 2017). For this reason, obtaining two X-ray images (i.e. AP/PA and lateral views) at the initial assessment are preferred for better visualisation of the deformity. In addition, the Cobb method of assessing spinal curvature is linked with large variations. Intra-observer and inter-observer variabilities of 3–5° and 6–9°, respectively, have been reported in the literature (Morrissy et al., 1990; Carman et al., 1990; Pruijs et al., 1994). However, the use of digital radiographic images and digital tools to measure the Cobb angle has helped in lowering the variation in the measurements (further explanation of this improvement is discussed in **Section 2.5.1.3**). Intra-observer and inter-observer variabilities of 2–3.4° and 3.6–5.4°, respectively, have been reported in more recent studies (Tanure et al., 2010; Zhang, Lou, Shi, et al., 2010; Langensiepen et al., 2013; Tauchi et al., 2016; Schmid et al., 2016). Because of the existence of the variation in Cobb angle measurements, it is widely accepted that a change in the measurement is considered significant only if the difference between the measurements of two consecutive radiographs is 5° or more (Gstoettner et al., 2007; Keenan et al., 2014; Allam et al., 2016; Tauchi et al., 2016).

1.3.2 Vertebral rotation

Vertebral rotation is associated with the lateral deviation of the spinal deformity. It is defined as the angulation of the vertebra in the transverse plane. This plane cannot be shown from conventional two-dimension (2D) X-ray images; therefore, several methods have been developed to quantify the vertebral rotation from the X-ray images. The methods are summarised in **Table 1.2,** and the accuracy of these methods will be discussed in **Section 2.5.1.2** .

Table 1.2: Summary of the methods used for vertebral transverse rotation measurements on 2D images (Lam et al., 2008).		
Cobb's method (Cobb, 1948)	The body of the vertebra is split into six sections. The degree of rotation is determined by locating the section in which the spinous process is.	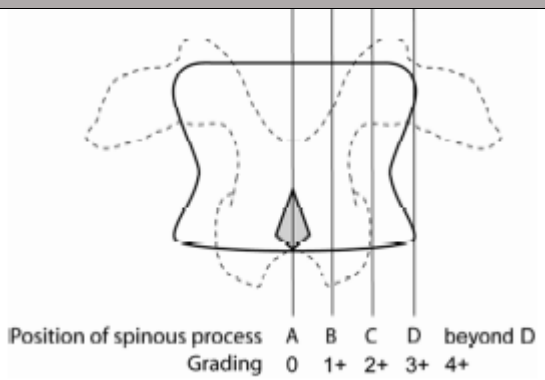
Nash–Moe method (Nash and Moe, 1969)	The angle of rotation is estimated by calculating the percentage of a pedicle's dislocation.	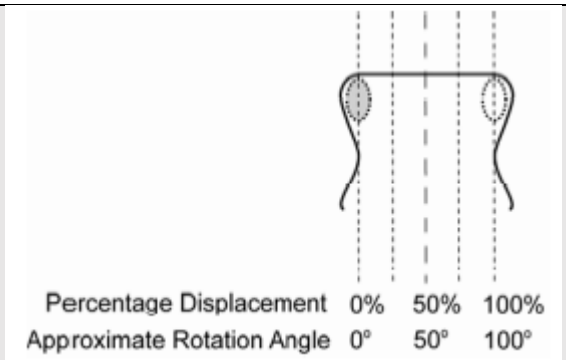
Perdriolle method (Perdriolle and Vidal, 1985)	The degree of rotation is measured by the Perdriolle torsion meter which uses the pedicle and vertebra's width for the measurements.	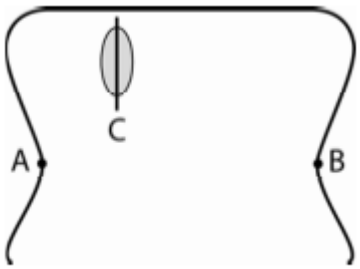
Stokes's method (Stokes et al., 1986)	The degree of rotation is calculated with Stokes's formula which uses the distance from the centre of a vertebra to both pedicles.	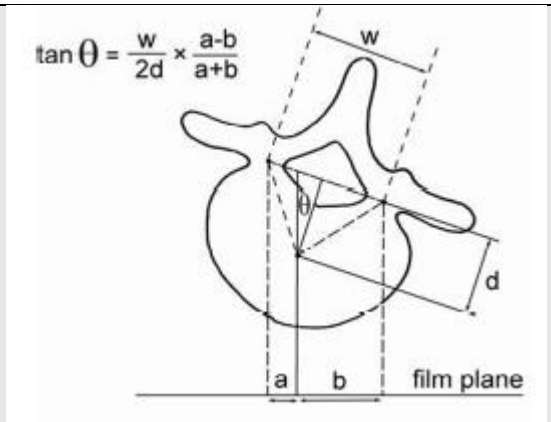

1.3.3 Skeletal maturity

The importance of quantifying skeletal maturity is that it shows the likelihood of deformity progression. As the skeleton matures, it is less likely that the deformity will progress. Skeletal maturity can be quantified from the iliac crest apophysis using the Risser classification system (Ng and Bettany-Saltikov, 2017; W. Kim et al., 2018; Blevins et al., 2018). The grading system has six stages (**Figure 1.4**):

- Stage 0: The iliac apophysis is not ossified.
- Stage 1: The apophysis is 25% ossified.
- Stage 2: The apophysis is 50% ossified.
- Stage 3: The apophysis is 75% ossified.
- Stage 4: The apophysis is 100% ossified but not fused with the iliac crest.
- Stage 5: The apophysis is 100% ossified and fused with the iliac crest.

Patients at stages 0–2 are at the highest risk of curve progression because their skeleton is not mature, whereas patients at stage 5 have the lowest risk (Ryan et al., 2007). This grading system is the US Risser staging system. However, an alternative grading system, i.e. the European Risser system, has a similar number of stages but instead divides the iliac crest into three segments instead of four. There is good agreement between the two systems (Kotwicki, 2008; Nault et al., 2010).

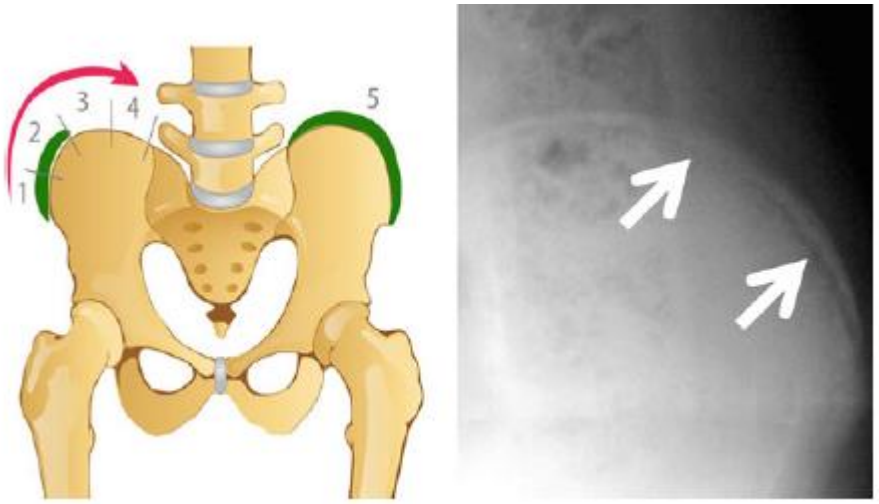

Figure 1.4: Risser staging system (left). The X-ray image shows Risser stage 4, where the apophysis is completely ossified but not fused with the iliac crest (Abdelgawad and Naga, 2014).

1.4 Rationale for the research in this thesis

X-ray images play a crucial role in the management of scoliosis by providing definitive diagnosis, grading its severity, assessing skeletal maturity and monitoring its progression. However, there are concerns about the potential for cancer induction associated with X-ray imaging. As discussed earlier, patients with scoliosis are often exposed to X-ray radiation on multiple occasions during management of the disorder. An X-ray is ionising radiation that can damage human tissues, and its effects might take years to appear (Pace et al., 2013). The induction of cancer and hereditary effects are the main concerns regarding the use of X-rays for evaluating scoliosis.

Despite recent advances in X-ray imaging technology, the risk of developing cancer due to exposure to ionising radiation persists. It is assumed that the risk increases as the amount of radiation increases (Chodick et al., 2007; Brenner and Hall, 2007; Johnson et al., 2014); however, the relationship between these elements is not wholly credible due to the random nature of X-rays. However, other factors might contribute to the incidence of cancer, such as

patients' age, gender and family history. Also, the risk of developing a certain type of cancer is associated with the type of X-ray examination (World Health Organization, 2016); in the case of AIS, breast cancer is always the main concern (Doody et al., 2000; Ronckers et al., 2008; Ronckers et al., 2010; Presciutti et al., 2014; Simony et al., 2016).

Several studies that followed patients with AIS for years after repeated X-ray examinations found an increased rate of breast cancer incidence in women who had scoliosis as compared with healthy women (John et al., 2007; Ronckers et al., 2008; Ronckers et al., 2010; Simony et al., 2016). However, these data are based on women who had undergone X-ray examinations for scoliosis assessment in 1912–1990. The imaging machines at that time delivered higher doses compared with the current machines, and there was a tendency to use X-ray imaging on a more frequent basis (Nash et al., 1979; Hoffman et al., 1989; Levy et al., 1996; Doody et al., 2000). The newer technologies in X-ray imaging, such as the image receptors in digital radiography (DR), are more dose efficient than the older technologies such as the traditional film (Korner et al., 2007; Seibert, 2008); in other words, the dose required to acquire an X-ray image today, with the same quality level, requires a lower dose in DR than when using the film screen. The imaging technology currently used for scoliosis assessment is different from the earlier versions of imaging machines in term of the irradiation technology, hence, using lower radiation dose to generate an X-ray image; however, it will likely require years to understand the effectiveness of the new imaging machines in reducing breast cancer incidence.

With the uncertainty regarding the risk of radiation on adolescents and the effectiveness of new X-ray imaging machines in mind, a few factors can be highlighted as to why breast cancer is more common in patients with AIS. Patient age at the time of radiation exposure has a critical influence on the incidence of breast cancer (Shuryak et al., 2010). The risk of

developing radiation-induced cancer decreases as the patient age increases. This can be due to the following: (1) younger patients are expected to have long lifespans, which increases the possibility of developing radiation-induced cancer later in life. Radiation-induced cancer has a long latency period that can be measured in decades (Shuryak et al., 2009; National Research Council, 2012; Carpenter and Bushkin-Bedient, 2013); and (2) radiation-induced cancer may develop in patients with AIS due to changes occurring in their bodies during adolescence. During this period, rapid cell replication takes place, and if the DNA is damaged, the effect can be permanent. Any DNA damage at this stage can lead to the development of cancer later in life (Shah et al., 2012; Carpenter and Bushkin-Bedient, 2013). The risk of developing radiation-induced cancer is difficult to predict, but the influence of patient age on increased risk can be observed.

There is another important factor that greatly influences the induction of breast cancer following radiation exposure: the sensitivity of breast tissue to radiation. Radiation is responsible for increasing the breast cancer incidence rate. The risk is higher for patients who are less than 20 years old at the time of exposure (Ng and Shuryak, 2015; Brenner et al., 2018). Breast tissues are composed of glandular and fatty tissues; the glandular tissue (i.e. the functional part) is the main component of a young female breast, and it is particularly sensitive to radiation (Ronckers et al., 2005). This explains the higher incidence rate of breast cancer in patients with AIS. As females age, fatty tissue becomes the main breast tissue component, rendering the breast less sensitive to radiation.

1.5 Study aim

As patients with AIS undergo repetitive X-ray examinations during the diagnosis and follow-up periods, it is necessary to minimise the risk from frequent exposure to radiation as far as

reasonably practicable. There are several X-ray imaging technologies that can be used to assess AIS, as discussed in **Sections 2.5.1** and **2.5.2**. Some of these, such as conventional radiography, have been used traditionally to assess AIS; others such as ultrasound scanning are still under investigation, but there is the potential to use other existing technologies to assess AIS which has not been used for this purpose before. The aim of this research is to evaluate the potential of using computed tomography (CT) scan projection radiography (SPR), a scanning mode used to plan the actual CT scan, in the assessment of AIS from radiation dosimetry and the accuracy of Cobb angle measurement perspectives. The aim and objectives will be discussed in detail in **Section 2.6** on **page 66**.

1.6 Thesis structure

This thesis is divided into six chapters, as illustrated in **Table 1.3** below.

Table 1.3: Thesis outline.

Chapter	Description
One	Provides an overview of AIS.
Two	Introduces radiation dose and the image quality (IQ) aspect and discusses the imaging modalities used in the evaluation of scoliosis from the following perspectives: • Imaging conditions • Accuracy of AIS measurements • Reproducibility and repeatability of the measurements • Radiation dose and risk • Image quality • Cost and availability.
Three	Provides a description of the method and materials used to achieve the aim, which includes using a dosimetry phantom to quantify radiation dose level, constructing a phantom with scoliosis spine and testing the accuracy of Cobb angle measurements on SPR images.
Four	Shows the result of the experiments that have been conducted to achieve the aim.
Five	Provides an overall discussion and the study's limitations.
Six	Reports the study's conclusion and provides recommendations for future work.

Chapter 2: Radiation dose and image quality in scoliosis imaging

2.1 Chapter overview

This chapter reviews AIS imaging modalities. The review is preceded by a discussion of radiation dose and IQ assessment methods. The chapter is divided into three sections: (1) radiation dose measurements, where radiation dose quantities, radiation dosimeters, and their applications in diagnostic radiography are discussed. This section ends with a review of the findings of previous studies that investigated radiation dose levels in AIS imaging; (2) IQ evaluation, where IQ parameters, the methods of evaluating IQ and the findings of previous studies that investigated IQ evaluation in scoliosis imaging are discussed. This is followed by a review of the relationship between IQ and radiation dose in diagnostic radiography; and (3) scoliosis image modalities, where the imaging modalities used to evaluate AIS are reviewed. The imaging conditions, accuracy of acquired measurements and their cost and availability are discussed. The aim and objectives of this thesis are stated at the end of this chapter.

2.2 Radiation dose measurements

Since its discovery, X-ray imaging has played an important role in medical diagnostics, but its association with the risk of causing secondary diseases (i.e. cancer) remains concerning. Possible biological damage from X-ray exposure can take the form of either stochastic (random) or deterministic (non-random) effects. The latter refers to a reaction that can occur after exposure to a certain level of X-radiation (threshold level). Examples of such reactions include nausea, vomiting, hair loss and skin burns, even death. These reactions might appear in the short term after exposure, and their magnitude increases as the dose increases. According to the International Commission on Radiological Protection (ICRP), the likelihood

of these reactions occurring increases after exposure to X-ray doses of >100 mSv (ICRP, 2007). Fortunately, these dose levels are far in excess of those used in diagnostic imaging.

Stochastic effects, on the other hand, refer to reactions that can occur after exposure to X-rays without a threshold level. In this case, X-rays can cause cancer or heritable diseases (Ron, 2003; Louis et al., 2006; Ronckers et al., 2008; Carpenter and Bushkin-Bedient, 2013; Hamada and Fujimichi, 2014), and the likelihood of these effects occurring is assumed to increase with the dose, but not in terms of their severity. This assumption is based on a linear no-threshold model (LNT) which is widely used for assessing the risk of radiation (**Figure 2.1**). Moreover, several factors increase the probability of stochastic effect occurrence, such as the radio sensitivity of tissues and the patient's gender and age. These are more concerning for patients with AIS who are young and most of whom are females.

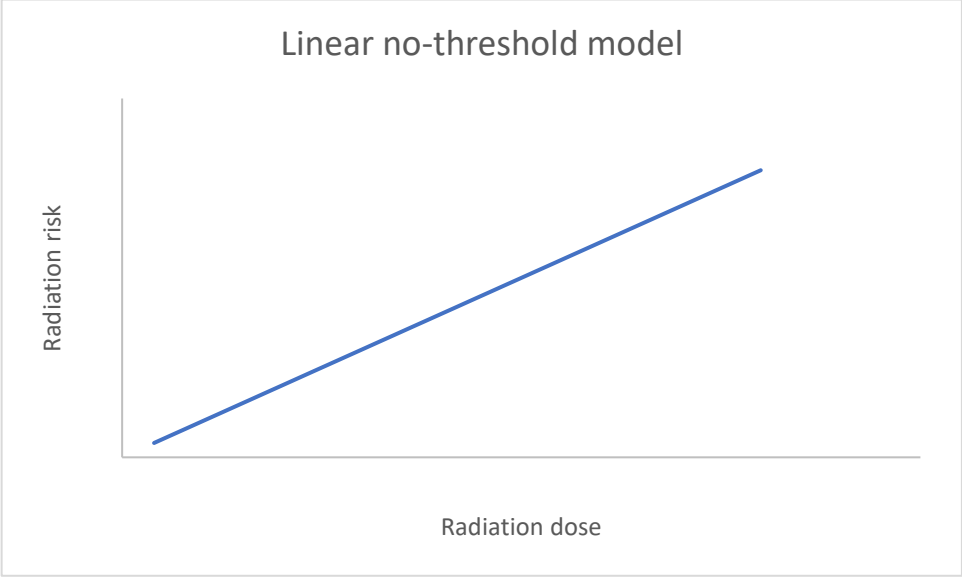

Figure 2.1: LNT assumes a proportional relationship between radiation dose and the risk of radiation. It is derived from high dose incidence (e.g. Hiroshima and Nagasaki incidents), and then the data are extrapolated to low dose incidence. The limitation of this model is discussed in the following section.

2.2.1 Radiation risk quantities and units

It is important that X-ray doses are monitored when used in medical imaging to minimise the risk of biological effects associated with X-ray use. Radiation dose monitoring enables the determination of the level where the benefits of undergoing X-ray examination outweigh the harms and enable the estimation of any potential risk. Two international bodies govern the radiation quantities in diagnostic imaging: The International Commission on Radiation Units (ICRU) and the ICRP. The ICRU focuses on the physical aspects of dosimetry (i.e. dose measurements), and the ICRP focuses on quantifying the risk from X-rays (i.e. radiation protection). The radiation dose can be quantified using two factors: (1) basic dosimetry quantities, or (2) application-specific quantities (sometimes termed patient dose quantities) (International Atomic Energy Agency [IAEA], 2014). The latter cannot be measured directly and are estimated from dosimetry quantities.

2.2.1.1 *Basic and application-specific dosimetry quantities*

In diagnostic radiography, the fundamental basic dosimetry quantity used to measure the patient dose is the absorbed dose (D), which is the amount of energy deposited in a unit of mass (joules/kg); its SI unit is the gray (Gy). It can be derived using the number of X-rays passing through the human body (i.e. fluence) and the quantity of energy required to charge particles in the body (i.e. kerma). However, it is not clinically possible to measure the absorbed dose in patients; instead, application-specific quantities are used to estimate the absorbed dose. The most common methods for estimating the absorbed dose are entrance surface air kerma (ESAK), air kerma–area product (P_{KA}) CT, air kerma–length product ($P_{KL,CT}$), CT dose index (CTDI), and organ dose (OD) (Mccollough and Schueler, 2000; Mettler et al., 2008; McCollough et al., 2010; Deak et al., 2010; Christner et al., 2010a;

Cynthia et al., 2011). The guidelines for these measurements have been published in the ICRP 103 and IAEA TRS457 reports. It is worth noting that the ICRU has unified the naming of these quantities; however, the terms entrance surface dose (ESD), dose–area product (DAP) and dose–length product are widely used in the literature instead of ESAK, P_{KA} and $P_{KL,CT}$, respectively.

Apart from the absorbed dose, the remaining quantities can be used within in vivo and in vitro studies to measure the absorbed dose. Using these quantities for measurement requires recording the 'irradiation conditions' (e.g. beam and detector sizes) and 'patient information' (e.g. height, weight, age). With this information, the absorbed dose can then be derived mathematically (i.e. indirect measurements) and Monte Carlo (MC) simulation software is mostly used to perform this type of measurement; this will be discussed in **Section 2.2.2**.

2.2.1.2 *Risk-related quantities*

The previous quantities quantify the amount of radiation patients are exposed to during X-ray examinations but do not provide information about the risk from the exposure. The risk is dependent on the type of radiation used and the type of tissue irradiated. The equivalent dose quantity (H_T) shows the amount of deposited radiation in a unit of mass and considers its type (e.g. X-rays, γ-rays or heavy particles) (**Equation 1**); in other words, it shows the biological effects of a certain type of radiation in a specific organ. The radiation weighting factors (W_R), which are determined by the ICRP, account for the relative biological damage from the corresponding radiation (**Table 2.1**) but not the radio sensitivity of the tissue; thus, H_T is used in radiation protection planning rather than in individual risk assessment (ICRP, 2007; Fisher and Fahey, 2017). The equivalent dose is defined by the same unit as the absorbed dose (joules/kg), but its SI unit is the Sievert (Sv):

$$H_T = \sum_R W_R D_T, \quad (1)$$

where R is the type of radiation, W_R is the radiation weighting factor (**Table 2.1**) and D is the absorbed dose.

Table 2.1: Recommended W_R (ICRP, 2007).	
Type of radiation	Radiation weighting factor (W_R)
X-rays, γ-rays and electrons	1
Protons	2
α-particles	20

To overcome the limited usage of the equivalent dose in assessing the risk of radiation to patients, another measure, called the effective dose (ED), is used. The ED is the sum of the equivalent doses if the whole body were to be irradiated and considers the difference in the tissues' radiosensitivities (**Equation 2**). This difference is represented by the tissue weighting factor (W_T), which is a measure of the risk of ionising radiation to a specific tissue (**Table 2.2**). The ED can be used to compare the risk of radiation of a specific X-ray examination with the risks from other sources of radiation (e.g. background radiation) or other X-ray examinations (e.g. PA vs. AP, or conventional spinal radiography vs. spinal CT) (McCollough et al., 2010; Fisher and Fahey, 2017). The ED has the same unit as the equivalent dose, i.e. the Sievert. In its Report 103, the ICRP recommends that the ED should be used for planning and optimisation in radiological protection, demonstrating dose limits for regulatory purposes and for comparing typical doses from different X-ray examinations, but not for assessing radiation doses to individual patients or for investigating individual risk:

$$ED = \sum_T W_T H_T, \quad (2)$$

where ED is the effective dose to the whole body, W_T is the tissue weighting factor (**Table 2.2**) and H_T is the equivalent dose absorbed by tissue (T).

Table 2.2: Tissue weighting factors from last two ICRP reports (ICRP, 1991; ICRP, 2007).

Organs/Tissue	Tissue weighting factor (W_T)	
	ICRP 60	ICRP 103
Gonads	0.20	0.08
Bone marrow	0.12	0.12
Colon	0.12	0.12
Lung	0.12	0.12
Stomach	0.12	0.12
Breast	0.05	0.12
Bladder	0.05	0.04
Liver	0.05	0.04
Oesophagus	0.05	0.04
Thyroid	0.05	0.04
Skin	0.01	0.01
Bone surface	0.01	0.01
Salivary glands	†	0.01
Brain	†	0.01
Remainder*	0.05	0.12

* Remainder tissues: adrenals, extrathoracic (ET) region, gall bladder, heart, kidneys, lymphatic nodes, muscle, oral mucosa, pancreas, prostate, small intestine, spleen, thymus and uterus/cervix.
† Not available.

The ED does not describe the risk of radiation to individual patients of a specific age, gender or genetic makeup. The ED estimates the risk to a reference person with an average characteristic (ICRP, 2007; McCollough et al., 2010; Wall et al., 2011; Tootell et al., 2014; Harrison and Lopez, 2015). The average characteristic is defined in the *ICRP Publication 89* as characteristics of a hypothetical gender-averaged adult person whose relevant anatomical and physiological parameters are at the 50th percentile of the population (ICRP, 2002). The purpose of introducing the ED was for setting limits for radiation protection (Paquet et al., 2016).

Another controversial aspect of the ED is the W_T, which, as can be seen in **Table 2.2**, has evolved over time. An expert panel calculated these factors based on the epidemiology of

Hiroshima and Nagasaki atomic bomb survivors (Lifespan Study [LSS]), and they represent the relative contribution of a specific tissue's radiosensitivities to the assumed total risk arising from stochastic effects for uniform irradiation to the entire body (IAEA, 2007; Fisher and Fahey, 2017). However, these factors do not reflect the best knowledge of radiation risks, but rather the experts' views on the stochastic endpoints of cancer incidence, cancer mortality, life-shortening and hereditary risk (Streffer, 2007; Brenner, 2008; Brenner, 2011; Brenner, 2012; Harrison and Lopez, 2015).

Given the limitations to the use of ED for assessing patient risk from radiation, the effective risk (ER) was proposed. Brenner (2008) suggested that it be used instead of the ED for assessing the radiation risk; he proposed replacing the W_T in the ED equation (**Equation 2**) with factors proposed by the US National Academy of Sciences (NAS) in its Biologic Effects of Ionizing Radiation (BEIR) VII report. The difference between the two sets of factors is that the NAS factors are not based solely on committee decision, but on more scientific methods. That is, they are based on the latest updates of the LSS (at that time), populations living in an environment with high background radiation, people who worked on the Chernobyl incident and, more importantly, medically exposed cohorts (NAS, 2006; Brenner, 2008; Rühm et al., 2015). The NAS factors also account for age, sex and tissue radiosensitivity (**Equation 3**) (NAS, 2006). The ER can be estimated using the following equation:

$$ER = \sum_{T} r_T \, H_{T,} \qquad (3)$$

where ER is the lifetime attributable risk, r_T is the lifetime radiation-attributable T-specific cancer risk (**Table 2.3**) and H_T is the equivalent dose absorbed by the tissue (T).

Table 2.3: The r_T of males and females by age (from birth to 30 years) (NAS, 2006).

Cancer	Risk coefficient (cases/1000,000 persons/Gy at different ages*											
	Male						Female					
	0	5	10	15	20	30	0	5	10	15	20	30
Stomach	0.76	0.65	0.55	0.46	0.40	0.28	1.01	0.85	0.72	0.61	0.52	0.36
Colon	3.36	2.85	2.41	2.04	1.73	1.25	2.20	1.87	1.58	1.34	1.14	0.82
Liver	0.61	0.50	0.43	0.36	0.30	0.22	0.28	0.23	0.20	0.16	0.14	0.10
Lung	3.14	2.61	2.16	1.80	1.49	1.05	7.33	6.08	5.04	4.17	3.46	2.42
Bladder	2.09	1.77	1.50	1.27	1.08	0.79	2.12	1.80	1.52	1.29	1.09	0.79
Thyroid	1.15	0.76	0.50	0.33	0.21	0.09	6.34	4.19	2.75	1.78	1.13	0.41
Remaining solid cancers	11.23	6.72	5.03	3.94	3.12	1.98	13.39	7.19	5.23	4.09	3.23	2.07
Leukaemia	2.37	1.49	1.20	1.05	0.96	0.84	1.85	1.12	0.86	0.76	0.71	0.63
Prostate	0.93	0.80	0.67	0.57	0.48	0.35	-	-	-	-	-	-
Breasts	-	-	-	-	-	-	11.71	9.14	7.12	5.53	4.29	2.53
Uterus	-	-	-	-	-	-	0.50	0.42	0.36	0.30	0.26	0.18
Ovary	-	-	-	-	-	-	1.04	0.87	0.73	0.60	0.50	0.34

* Number of cases per 1,000,000 persons exposed to a single dose of 0.1 Gy.

The ER is a useful measure for estimating the possible risks of using ionising radiation in medical imaging; however, some limitations remain. The r_T is built on the basic hypothesis of the LNT, which is a widely accepted model (Little et al., 2009; Tubiana et al., 2009). It is an assumption based on data from people who were exposed to high radiation doses (Boice, 2017; Tran and Seeram, 2017; Ulsh, 2018; Cardarelli and Ulsh, 2018), which means this is not the best model for assessing the risk of low-dose radiation (Cardarelli and Ulsh, 2018), with which the ICRP agrees. The linear-quadratic (LQ) model is more appropriate for estimating the risk than the LNT (Tran and Seeram, 2017; Cardarelli and Ulsh, 2018; Ulsh, 2018). Similar to the LNT, the LQ model suggests that the risk increases as the dose and has no threshold limit, but that it increases exponentially with repeated exposure (**Figure 2.2**). Despite this, several international bodies, including the ICRP, NAS, United Nations Scientific Committee on the Effects of Atomic Radiation (UNSCEAR) and Canadian Nuclear Safety Commission (CNSC), still use the LNT (Tran and Seeram, 2017). The ICRP claims that there is no significant difference between the models for estimating the risk of low-dose radiation, and that the LNT is the most cautious model.

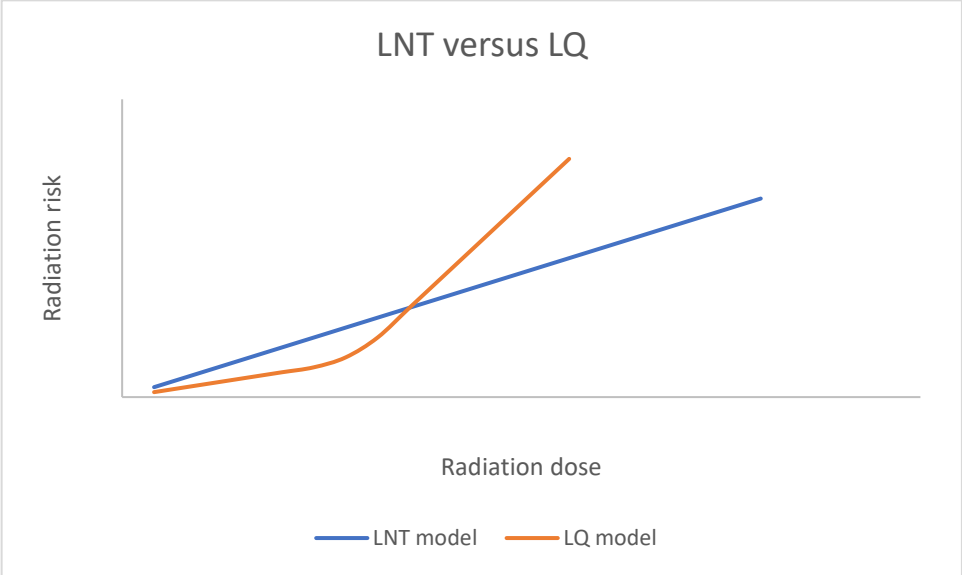

Figure 2.2: The difference between the LNT and LQ risk models.

Other methods can be used to estimate the risk of radiation, namely, the excess relative risk (ERR), excess absolute risk (EAR), lifetime attributable risk (LAR) and final risk model (NAS, 2006). The ERR and EAR, which are defined in **Equations 4** and **5**, respectively, allow estimation of the risk at a specific time after the exposure. While the ERR is suitable for estimating the risk for a specific population in specific conditions, it cannot be applied to a different population (O'Connor, 2017). For example, it can be used to estimate the risk of cancer in Japanese who lived in the wartime conditions of Nagasaki and Hiroshima, but not for any other populations. The EAR, on the other hand, is suitable for estimating the risk between two significantly different populations (e.g. Japanese and Europeans). The LAR is the summation of the ERR and EAR. Nevertheless, using the LAR to estimate risk has received criticism; first, the correlation between the ERR and EAR is weak, and second, it is difficult to estimate the risk of cancer of a single organ (O'Connor, 2017). To overcome these limitations, the NAS committee introduced the final risk model (**Equation 6**). However, this risk model has received the same criticism as the ED, for which the committee has proposed a subjective factor (x) to resolve the limitations of the LAR.

$$ERR = \frac{rate\ of\ disease\ in\ an\ exposed\ population}{rate\ of\ disease\ in\ an\ unexposed\ population} - 1 \quad (4)$$

$$EAR = rate\ of\ disease\ in\ an\ exposed\ population - rate\ of\ disease\ in\ an\ unexposed\ population \quad (5)$$

$$Final\ risk = x.ERR + (1 - x).EAR \quad (6)$$

2.2.2 Quantifying radiation dose: Direct versus indirect measurements

To estimate the risk of radiation in diagnostic imaging, the radiation dose is quantified either directly using radiation dosimeters or indirectly using mathematical simulation software. For

direct measurements, the most frequently used dosimeters are thermoluminescent dosimeters (TLDs), metal–oxide–semiconductor field-effect transistors (MOSFETs), ionisation chambers, silicon diodes and optically stimulated luminescence dosimeters (OSLDs) (Tootell et al., 2014; Koivisto et al., 2014; Cakmak et al., 2015). These dosimeters can be used on patients or in phantoms to measure the absorbed dose. On the other hand, MC mathematical simulation is widely used for estimating the absorbed dose in diagnostic radiography, and it is used for indirect measurements (Tapiovaara, 2012). The software requires that the users input some of the irradiation details, including ESD, DAP and imaging parameters, such as source-to-image receptor distance (SID), to estimate the risk.

Both direct and indirect measurements of radiation risk are valid for dose measurements in diagnostic radiography (IAEA, 2007). The main differences between the two methods are the accuracy of the measurements and the feasibility of performing the measurements. On one hand, direct measurement using dosimeters provides more accurate information when compared with the computational method (Lee et al., 2014; Shrimpton et al., 2014; Sinclair et al., 2015; Hayashi et al., 2017). MC, for example, underestimates the measurements for adults (Harmer et al., 2018; Borrego et al., 2018) and overestimates the measurements for children (Kiljunen et al., 2009; Borrego et al., 2018). There are different possible causes for these inaccurate measurements in MC software: the software utilises a mathematical phantom with unrealistic organ shape and size and it oversimplifies the anatomical structures and unrealistically adjusts the body for adults and children (**Figure 2.3**) (IAEA, 2013; Borrego et al., 2018). Second, the accuracy of the measurement is highly dependent on the accuracy of the reproduced beam size and location (IAEA, 2007; Allisy-Roberts and Williams, 2008; Podnieks and Negus, 2012). Failure to use the exact same beam size and location changes the outcomes of the calculation (i.e. measurements), which may yield inaccurate results. Lastly,

the software generates a uniform X-ray field, which does not simulate the actual X-ray beam (Kim et al., 2015).

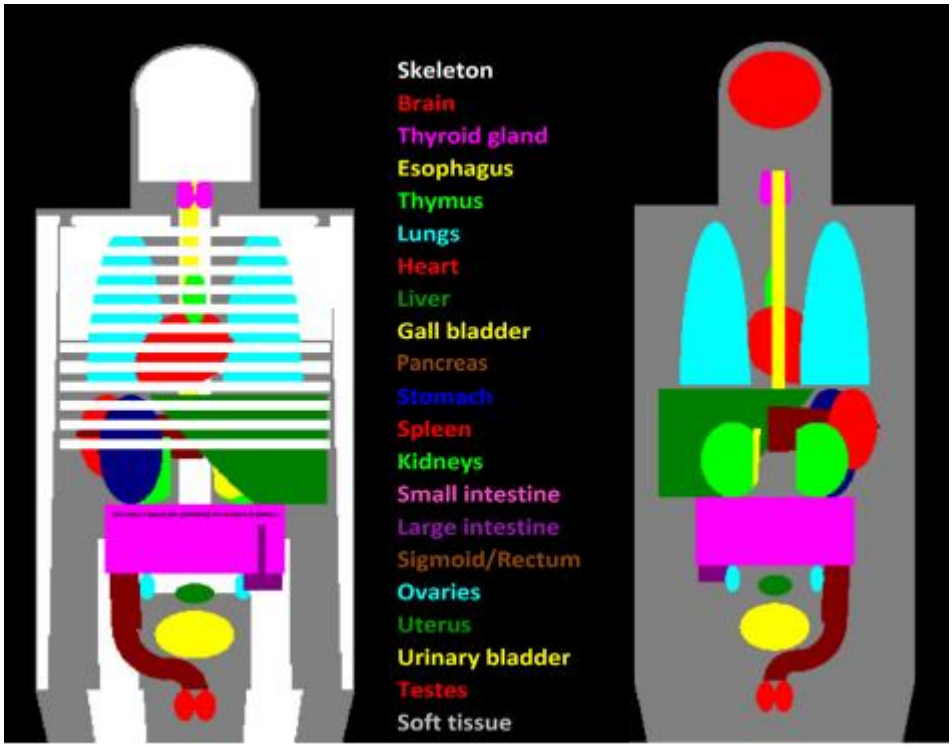

Figure 2.3: The mathematical phantom used in MC shown in PA view (left) and AP view (right) (image adopted from (Seidenbusch et al., 2014).

MC measurements, however, are easily performed compared with the direct methods. In general, dosimeter measurements are labour-intensive and time-consuming. The amount of labour and time varies between dosimeters based on their type and application. While active dosimeters, such as ionisation chambers and MOSFETs, display dose values directly, passive dosimeters, such as TLDs and OSLDs, do not provide immediate readouts; instead, they store the singles to be read later, which means extra work and more time are required to obtain the dose values.

2.2.3 Quantifying radiation dose: Measurement methods

For dose measurements in diagnostic radiography, the ideal dosimeter for direct measurement should have the following properties as stated in the IAEA handbook (2014):

1. High sensitivity, which refers to the lowest detectable signal. The higher the sensitivity, the higher the signal produced for the same dose.
2. Linearly proportional response to radiation dose.
3. Small energy dependence, which refers to low variation in a dosimeter response within a range of energies (i.e. radiation quality). In diagnostic radiography, this variation is limited by IEC 61674 to ±5% (International Electrotechnical Commission [IEC], an international body responsible for setting standards) (IEC, 2012).
4. Small angular dependence, which refers to the effect of a dosimeter response by its shape and size and by the incident X-rays. IEC 61674 limits variation in a dosimeter response to ±3% at an incident angle of 5° (IEC, 2012).
5. Small current leakage, which refers to any recorded signal that is not generated by radiation (e.g. electronic noise, environmental equilibrium). IEC 61674 limits this to 5% of effective air kerma for the range in use.

Other characteristics should also be considered when choosing a practical dosimeter, including low cost, excellent reproducibility, small size and an effective atomic number similar to that of human tissue (Koivisto et al., 2015). Moreover, the clinical or research applications of a dosimeter and the type of measurement should be taken into account when choosing the most suitable method.

Even though the previously mentioned dosimeters can be used for radiation risk assessment (Lemoigne and Caner, 2010), the variety can be limited because not all of them fulfil all

specifications of an ideal dosimeter. Ionisation chambers provide accurate and precise measurements and come in different forms; the most widely known form is the one mounted on the collimator of the X-ray tube. Ionisation chamber usage for dosimetry in diagnostic radiography is limited to the CTDI and DAP (Kramer et al., 2012) and to indirect measurements. Ionisation chambers are mostly used for quality assurance or to quantify basic dosimeter quantities (Meghzifene *et al.*, 2010; Kramer, Moores and Stieve, 2012; Mahmoud, Hamdy and Abaza, 2019). They cannot be used on patients because they are made from materials not equivalent to human tissue and can overlay image details (Kramer et al., 2012).

Semiconductor dosimeters (i.e. silicon diodes and MOSFETs) are smaller than ionisation chambers and can be used on patients and placed inside phantoms. They are active dosimeters; hence, they provide instant readout. One of their disadvantages is the relatively higher angular dependence as compared with other dosimeters (Dong et al., 2002; Wang et al., 2004; IAEA, 2014; Koivisto et al., 2015). A 21% difference in MOSFET readings was found when its orientation was changed; therefore, it is recommended that MOSFET dosimeters be placed with their flat side facing the X-ray tube when used on patients' skin or inside a phantom (Jones et al., 2005). In general, semiconductor dosimeters are sensitive to their positioning in the radiation field, especially the direction of the heel effect, and they have a short lifetime (IAEA, 2014). Silicon diodes do not record side scatter and backscatter radiation because they are absorbed by the dosimeter backing materials, which may affect measurement accuracy. Other disadvantages of silicon diodes include short lifetime and the requirement for frequent calibration.

The remaining dosimeters are solid-state dosimeters: TLDs and OSLDs. Their dose measurement principles are similar: when they are irradiated, they trap a charge for a time before the charge is released during the read-out. They are small and made from tissue-

equivalent materials, which makes them suitable for placement on patients or within phantoms. The main difference between these dosimeters is how the measurements are read out; TLDs use heat to release the trapped charge, whereas OSLDs use light. When the charge is released, light proportional to the amount of radiation is released. The response is linear in the energy range of the X-ray used in diagnostic radiography (IAEA, 2007; Meghzifene et al., 2010; Oliveira et al., 2010; Al-Senan and Hatab, 2011). Unlike the other dosimeters, acquiring dose measurements requires two steps: irradiation and read-out, which renders them less time-efficient and more labour-intensive. Their other weakness is sensitivity to the surrounding environment, and their sensitivity varies. Compared to TLDs, OSLDs have shorter lifetimes and require careful handling because they are light-sensitive (Alvarez et al., 2017).

2.3 Image quality

The definition of IQ is broad and cannot be easily integrated into the perspective of quantifying medical images for evaluation. It is also subjective, and a specific or widely accepted definition does not exist (Shet et al., 2011; Singh and Pradhan, 2015). This has led to enormous controversy in determining the optimum IQ. However, it is not necessary for X-ray images to be of optimum quality to be suitable for clinical use. In fact, a good X-ray image is characterized by the fact that it has all of the needed clinical details for diagnostic purposes. Sufficient IQ for clinical use might be acceptable if it is associated with a lower radiation dose to the patient (Russell et al., 2008; Seibert, 2008).

Patient dose and the IQ are correlated. In general, the highest IQ levels are associated with high radiation doses, because noise levels in the image tend to be low when the dose is high. However, obtaining high-quality images may not necessarily be ideal for certain cases, such as scanning for tumours, because higher radiation doses decrease the contrast of images. Therefore, it is important that an image has the right quality level for the task to be accomplished (**Table 2.4**) (ICRP, 2004; Busch and Faulkner, 2006). An example of this is the liver lesion in the two images shown in **Figure 2.4**: the lesion appears clearer on the image with the lower dose despite the other image being of higher quality (i.e. the dose was reduced by adjusting the tube potential). The trade-off between IQ and radiation dose should be examination-specific, as the IQ is determined by whether the purpose of the examination was achieved.

Table 2.4: Examples of different clinical indications and the suggested IQ needed for diagnostic purposes (Uffmann and Schaefer-Prokop, 2009).	
Image quality level	Clinical indication
High	• Primary bone tumour • Non-displaced fracture
Medium	• Control of a known displaced fracture • Back pain with no indication of infection or neoplasm (i.e. imaging lumbar spine)
Low	• Follow-up metal implantation for osteosynthesis • Follow-up for pneumonia • Follow-up for scoliosis

Figure 2.4: Liver lesion, circled, in left and right images. The image on the left was acquired at 120 kV; the image on the right was acquired at 80 kV (Fletcher, 2010).

2.3.1 IQ parameters

The quality of radiographic images can be characterised by spatial resolution, contrast and noise (Goldman, 2007; Alsleem and Davidson, 2013; Konstantinidis, 2014). The following provides an overview of these characteristics.

2.3.1.1 *Spatial resolution*

Spatial resolution is the ability of an imaging system to detect small objects with different contrast (e.g. bone–soft tissue interface). In general, it is limited by pixel size and by the

spacing between pixels. The smaller the pixel sizes, hence more pixels, the higher the spatial resolution. However, other factors influence the spatial resolution of an image: subject blur, receptor blur, motion blur and geometric blur (Williams et al., 2007; Alsleem and Davidson, 2013; Chow and Paramesran, 2016), which cause an object to appear in the image with poorly defined boundaries. While subject blur is caused by the superimposition of the objects or by their shape (e.g. an organ), receptor blur is caused by scattering radiation, generated when the incident X-rays react with image receptors. Motion blur, the most common source of blur, is caused by patient movement during the examination (Alsleem and Davidson, 2013): this blur includes both voluntary and involuntary motion (e.g. heartbeat). The effect of motion blur can be reduced by reducing the examination time (Alsleem and Davidson, 2013; Huda and Brad Abrahams, 2015). Lastly, geometric blur is caused by the physical size of the radiation source (i.e. focal spot), object-to-image receptor distance (OID) and SID (Kei Ma et al., 2014; Singh, 2016). Geometric blur increases with focal spot size and with SID **(Figure 2.5**).

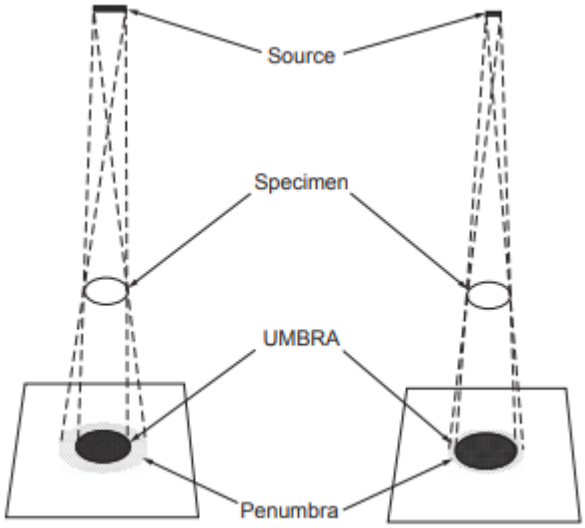

Figure 2.5: The effect of focal spot size on the blur (sharpness) of an object (Singh, 2016).

2.3.1.2 *Contrast*

Contrast refers to the ability of an imaging system to discriminate objects with small differences in grey scale. This slight difference is generated by the presence of slightly similar densities and effective atomic numbers; hence, slightly different X-ray attenuating properties (e.g. the appearance of liver and spleen in an X-ray image) (Bushberg et al., 2012). A high-contrast image is demonstrated by a sharp transition between light grey and dark grey (**Figure 2.6**). Generally, contrast is influenced by scatter radiation, beam filtration and collimation, image receptor properties and photon number (Williams et al., 2007; Alsleem and Davidson, 2013; Sossin et al., 2017). A high-contrast image allows better visualization of image details.

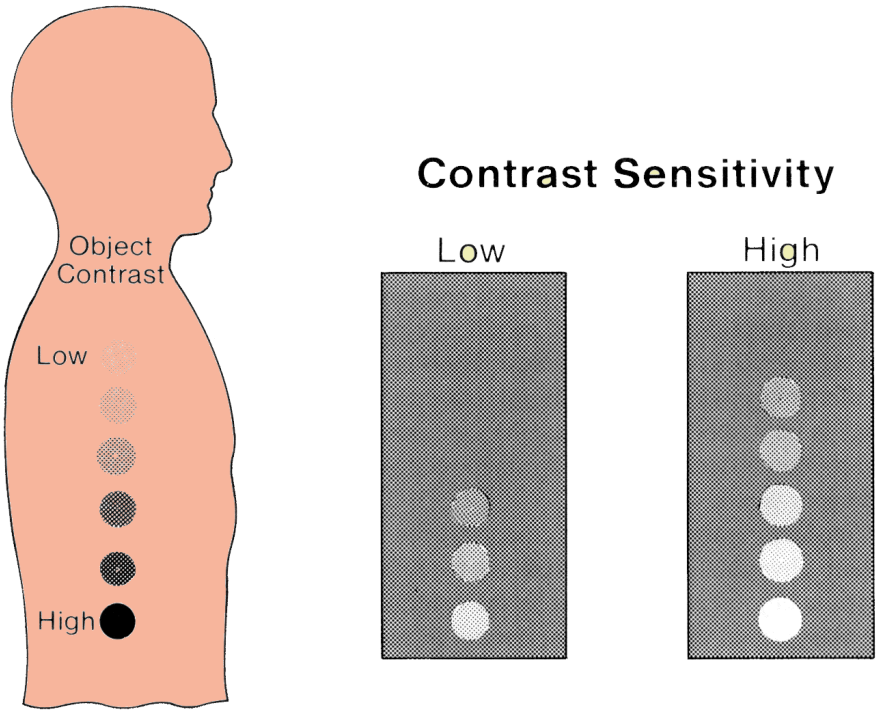

Figure 2.6: The difference between low and high contrast (Sprawls, 1995).

2.3.1.3 *Noise*

Noise refers to the unwanted details in an image that arise as random fluctuations in recorded X-rays. It is non-useful information and can be explained using the standard deviation (*SD*) to

show how distributed the recorded X-rays are (Alsleem and Davidson, 2013). Noise is influenced by the number of photons logged in each pixel; the higher the number of photons, the lower the noise level in an image (**Figure 2.7**). An X-ray image contains two types of noise. One is quantum noise, which appears when too few X-rays are recorded (i.e. reaching the image receptor) due to scatter radiation, decreasing pixel size or the size of anatomical structure (i.e. larger structures attenuate more radiation) (Bacher et al., 2006; Goldman, 2007). The other noise is caused by the imaging system itself (hence, it is termed system noise) during image formation (Goldman, 2007). The latter is less problematic than quantum noise and occurs less often (Huda and Abrahams, 2015).

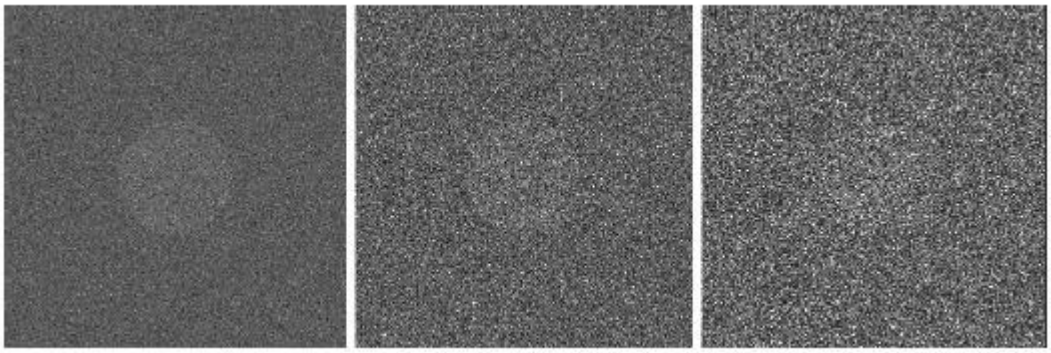

Figure 2.7: An image with different noise levels: noise levels increase from left to right (IAEA, 2014).

2.3.2 IQ assessment methods

Several methods can be used to assess the quality of X-ray images, and they fall into three broad categories (**Figure 2.8**): physical, clinical performance and psychophysical methods. While the physical methods focus on the physical aspects and performance of an imaging system, the psychophysical and clinical performance methods are used to assess the performance of the whole chain (i.e. imaging systems and image observers). The features, advantages and disadvantages of these methods will be discussed in the following sections.

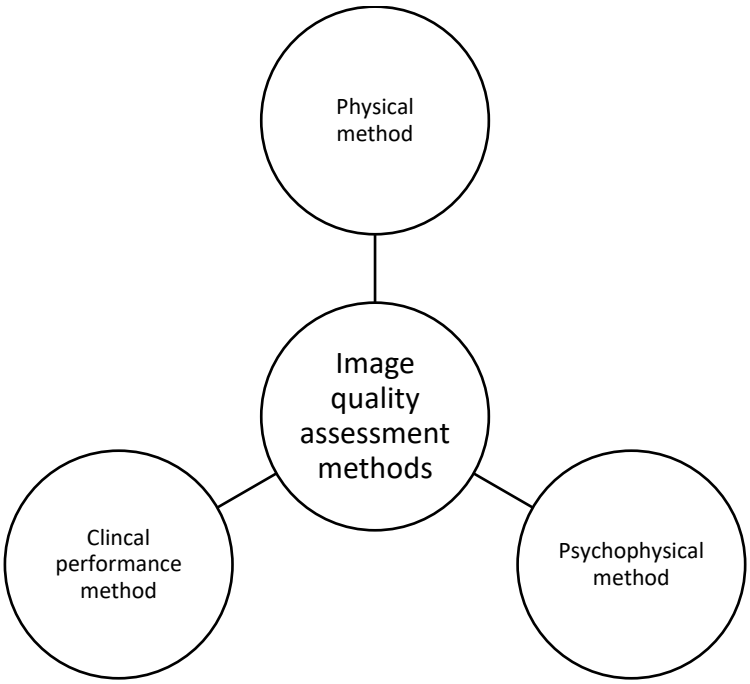

Figure 2.8: Summary of IQ assessment methods.

2.3.2.1 *Physical methods*

The physical methods are used to describe the physical characteristics of an imaging system. They quantitively describe the spatial resolution, contrast and noise. An example of their application is when a new image receptor is introduced. Spatial resolution can be quantified using point-spread function (PSF) or modulation transfer function (MTF) (Alsleem and Davidson, 2013; Konstantinidis, 2014). Noise can be quantified using the signal-to-noise ratio (SNR) or noise power spectrum (NPS) (Samei et al., 2005; Tasi and Matsuyama, 2015), and contrast is mostly quantified by the contrast-to-noise ratio (CNR) (Mori et al., 2013). Moreover, detective quantum efficiency (DQE) measures the efficiency of an imaging receptor in converting X-ray energy into an image. These physical measures provide more reliable and reproducible results when compared with the other methods (Yan et al., 2012; Vodovatov et al., 2017). However, they cannot be used individually to evaluate IQ because

they cannot quantify some of the clinical features in the images as an observer might (Bath, 2010).

2.3.2.2 *Clinical performance methods*

Clinical performance methods describe the effectiveness with which an image can be used for its intended purpose. The overall basis of this type of assessment is when experts provide their opinion of the quality of an image based on certain criteria. This is not as reliable as the physical methods due to the involvement of human subjectivity, but has higher validity than the physical methods for assessing the whole imaging system, including the observers themselves (Obuchowski, 2003; Bath, 2010; Ludewig et al., 2010; Liu et al., 2012; Bochud et al., 2015). Clinical performance measurement methods include examining receiver operating characteristics (ROC) and visual grading analysis (VGA) (Mansson, 2000; Båth and Månsson, 2007; Zarb et al., 2010). This type of measurement focuses on the appearance of normal or pathological structures in an image.

The ROC is a task-based method used to evaluate the imaging performance of an imaging system. Observers are asked to decide whether a pathological structure is present in an image; based on its grading system, the observers are able to state their level of confidence. ROC indicate the ability of observers to correctly detect pathological structures in an image by measuring the probability of identifying positive results (i.e. sensitivity) and the probability of identifying negative results (i.e. specificity) (Obuchowski, 2003; Florkowski, 2008; Ludewig et al., 2010; Alsleem and Davidson, 2013). Although ROC can be used for measuring the IQ to be evaluated, its main usage is for comparing the detectability of different imaging systems (or observers) for certain pathologies (Bath, 2010). In addition, ROC studies are difficult to perform because they are time-consuming and require large amounts of data to have adequate

statistical power (Bath, 2010; Alsleem and Davidson, 2013); therefore, evaluating a large number of images may cause observers to behave differently in the experimental environment compared with a real experience in the clinical environment (Gur et al., 2007; Bath, 2010), which consequently affects the accuracy of the measurements. Therefore, ROC is not recommended for finding the optimal imaging setting or dose level.

Unlike ROC, VGA utilises normal structures in X-ray images for IQ evaluation. The main theory of VGA is based on the ability to detect whether the pathological structure in an image correlates well with the precise anatomical demonstration (Båth and Månsson, 2007; Ludewig et al., 2010). It assesses IQ levels by evaluating the appearance of anatomical structures in the images based on the quality criteria recommended by the Commission of the European Communities (CEC) (CEC, 1996c; Engen et al., 2005). Observers are required to decide whether the criteria have been fulfilled. VGA can be performed in two ways: relative grading using reference images, and absolute grading without reference images. In comparison with ROC, VGA is easier to perform and has higher agreement with the physical methods (Båth and Månsson, 2007). In addition, it does not focus on the observers' performance, but rather the performance of the whole imaging chain. However, if a certain image is evaluated as poor quality because some or all criteria are not fulfilled, VGA does not identify the reasons related to the poor quality (i.e. the sources of poor IQ could be the imaging equipment, processing or the interpreters) (Ludewig et al., 2010). Lastly, it is less reliable than physical measurements due to the involvement of human subjectivity.

2.3.2.3 *Psychophysical methods*

This type of IQ assessment combines the features of the previous two methods. That is, it describes the physical characteristics of an imaging system from an observer's point of view.

The basic principle of psychophysical assessment is that observers are asked to evaluate the physical characteristic of an imaging system using test phantoms (Mansson, 2000; Yoshiura, 2012; Hardesty et al., 2013; Mraity et al., 2014; Zarb and Rainford, 2014). The difference between the physical and psychophysical methods is that subjectivity has less influence on the physical measurements. Nevertheless, human subjectivity can be eliminated entirely by performing the psychophysical measurements on software programs to automatically evaluate the quality of an image (Zarb and Rainford, 2014). Common examples of these measurements are line spread-function (LSF) for evaluating spatial resolution and contrast-detail analysis (CDA) for evaluating contrast (**Figure 2.9**). These measurements are easier to perform compared with the other methods, which renders them preferable for routine checks in hospitals (Hiles et al., 2005; Marshall et al., 2011). The disadvantages of these measurements is that they are less relevant to clinical practice than the clinical performance measurements due to the use of test phantoms that do not represent the human body (Mansson, 2000).

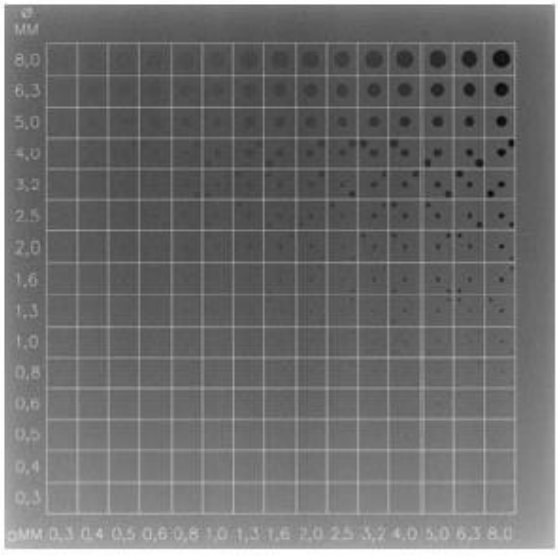

Figure 2.9: An X-ray image of a CDRAD phantom used for CDA studies.

2.4 Relationship between IQ and radiation dose

The relationship between IQ and radiation dose level is complicated. As noted in the earlier discussion (**Section 2.3** on **page 32**), the main goal of medical imaging using ionising radiation is to generate an image with sufficient IQ and minimum dose to patients for the task to be achieved. IQ is dependent on the quantity and quality of the X-rays absorbed in the image receptor (Martin, 2007; Sensakovic et al., 2017): Broadly, IQ improves as the dose increases. Several factors should be considered when balancing IQ and radiation dose, including: (1) tube kilovoltage peak (kVp), which controls the quality of the X-rays (i.e. their energy); (2) tube current (in milliamperes [mA]), which controls the quantity of X-ray photons; (3) time of exposure; (4) beam size (i.e. collimation); (5) SID; (6) OID; (7) focal spot; (8) grid; (9) pitch in CT; and (10) patient size (George et al., 2004; Ramanaidu et al., 2006; Ching et al., 2014; Mayo-Smith et al., 2014; Tavares et al., 2015; England et al., 2015; Ofori et al., 2016; Sensakovic et al., 2017; Jumriah et al., 2018; Wells, 2018). **Figure 2.10** shows a summary of the relationship among these factors and IQ and radiation dose.

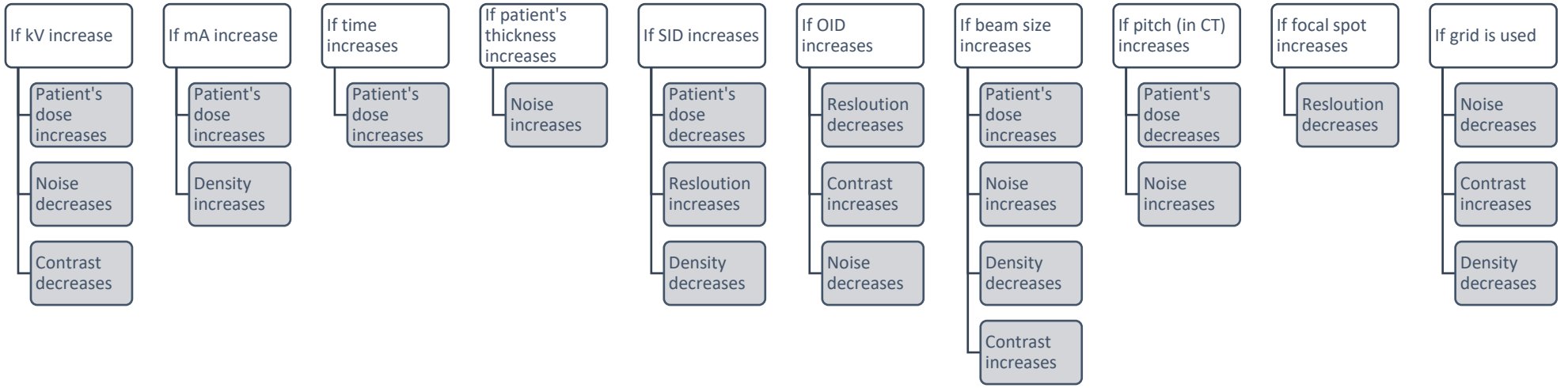

Figure 2.10: Summary of the effects of adjusting imaging factors on image quality and radiation dose. The effect of one factor shows when the other is constant.

As shown in **Figure 2.10**, these imaging parameters control both the radiation dose and IQ levels. For quantifying the curve in AIS, IQ level has less impact on the accuracy of the measurements because the curve is still discernible in low image quality (Uffmann and Schaefer-Prokop, 2009; Bonanni, 2017; Chung et al., 2018). Therefore, the main concern when irradiating AIS patients to assess spinal curve should be the dose level rather than the quality of the images. The accuracy of Cobb angle measurements using different images with different IQ levels and different imaging modalities are discussed in the following section.

2.5 Scoliosis imaging modalities

The importance of X-ray images in the diagnosis and management of scoliosis has been discussed in the previous chapter (**Section 1.3** on **page 8**). In addition to conventional projection radiography, other imaging systems can be used to evaluate spinal curvature. However, not all imaging methods use X-rays to generate an image of the spine. Images of the spine can be acquired using magnatic resonance (MR), ultrasound (U/S) or simply by taking a photo of the patient's back. The following sections outline these imaging systems in terms of their imaging characteristics/ applications, spinal curve measurement accuracy, radiation dose levels and risk, cost and availability. These imaging systems are categorised into ionising and non-ionising imaging modalities.

2.5.1 Ionising imaging modalities

Ionising imaging modalities use ionising radiation to generate an image (or a series of images) that fulfils its diagnostic purposes. In scoliosis evaluation, these can be conventional projection radiography, CT or EOS imaging systems (Ng and Bettany-Saltikov, 2017; W. Kim et al., 2018). Although these imaging modalities follow similar principles for generating

X-ray images, there are some differences among their imaging techniques and their usage for scoliosis management.

In conventional radiography, which is the gold standard for AIS assessment, patients stand against an image receptor for scoliosis imaging (**Figure 2.11**). For the equipment to capture the entire spine, it divides the region of interest (ROI) into two or three segments depending on the patient's length. Then, the X-ray tube and imaging receptor move simultaneously and irradiate each area separately (this is one of the DR features that was not available in earlier versions of the conventional system: computed radiography [CR] and screen-film [SF]). The resultant images are then stitched together to form one image of the spine. The images can be acquired in AP, PA or lateral positions. In scoliosis imaging using EOS, patients stand inside the imaging machine (**Figure 2.12**). Two X-ray tubes fitted perpendicular (i.e. at 90°) to each other and paired to two detectors acquire the images, which can be either in single projection: AP, PA or lateral or two images from different aspects, AP+Lateral or PA+Lateral, simultaneously. The resultant images can be software-processed to produce a three-dimensional (3D) model of the spine. Lastly, CT scanning involves patients lying in supine or prone positions on a CT table for the imaging (**Figure 2.13**). The X-ray tube rotates around the patient as the table moves horizontally while the images are acquired.

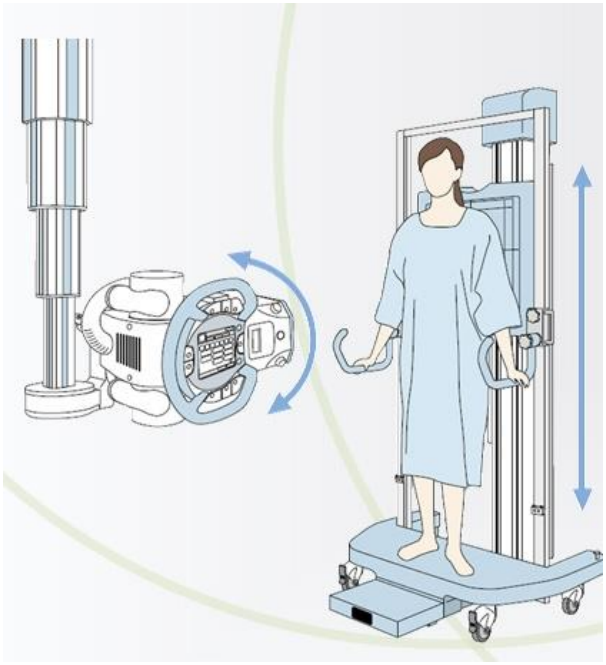

Figure 2.11: The image receptors move up and down behind the patient to capture parts of the spine (Shimadzu Europa GmbH, 2017).

Figure 2.12: The patient inside an EOS imaging system; the two white lines show the position of the X-ray tubes (EOS imaging, 2019).

Figure 2.13: A patient in a supine position on a CT table (Macmillan Cancer, 2019).

2.5.1.1 *Imaging conditions*

The gold standard for evaluating scoliosis curvature is to have patients stand during scanning. In this position, spinal curvatures have the highest degree of deviation due to the gravitational effect (Keenan et al., 2014; Vavruch and Tropp, 2016). AP, PA or lateral projection images can be obtained in a standing position using projection radiography and EOS. Such images can also be obtained using CT; however, for the current generation of CT scanners, scanning can only be performed in the supine/prone position, due to their design. Changes in patient positioning during imaging acquisition alters the shape of the spine due to a shift in the axial load and a change in the patient's posture (Yazici et al., 2001; Cheung et al., 2015). Even though the Cobb method can be applied to images in which patients are standing, the measurements taken using supine images will be underestimated (Keenan *et al.*, 2014; Brink *et al.*, 2017).

2.5.1.2 *Accuracy of scoliosis measurements*

The differences between Cobb angle measurements of images obtained in standing positions have been described in the literature. Torell *et al.* (1985) collected data from 287 female patients from 10 to 17 years of age who had been imaged in both the standing positions. The mean difference between the two measurements was approximately 9° higher in the standing images (*SD* = 6.2). In 93% of the patients, the difference between the standing and supine measurements was from 0° to 20°. The authors found that the difference between the two measurements was independent of the curve severity and that it decreased as the patient age increased due to stiffening of the bone. However, how the measurements were performed for the standing images is unclear: the authors did not state whether the most tilted vertebrae were pre-selected.

Keenan *et al.* (2014) investigated the effect of changing the patient's position on Cobb angle measurements and the effect of pre-selecting the most tilted vertebrae. They reported an 11° increase in the measurement, if the position was changed from supine to standing. They also reported minor changes in Cobb angle measurement when the most tilted vertebrae were pre-selected from a previous X-ray image; however, they noted that the difference was negligible. Similarly, Brink *et al.* (2017) reported an 11° increase in the measurements when the imaging position was changed from prone to standing. Unlike Torell *et al*. (1985) where the standing and supine images were taken on the same day, the last two studies had between-image intervals of up to 3 months. Interestingly, all studies reported a linear relationship between the weight-bearing and non-weight-bearing measurements. Although these studies examined the differences in Cobb angle measurements, the images used were intended for scoliosis treatment planning and not Cobb angle measurements. The patient position on the CT scan table, which influences the angle measurements, was not standardised as in standing imaging.

Vertebral rotation measurement, which is one of the diagnostic measurements for AIS, can be approximated from 2D radiography of the spine using spinal anatomical landmarks. **Table 1.2** (**page 11**) shows a summary of the widely used methods for measuring vertebral rotation on 2D images. These methods utilise the appearance of the spinous processes and pedicles to estimate the degree of rotation. They are simple to use and do not require exposing patients to additional radiation; the exception is the Stokes method, which requires two X-ray images to measure the degree of rotation. This can provide an indication of the vertebral rotation; however, the measurements are not as precise as those taken from CT images.

CT images have the advantage of showing the accurate and true shape of the spinal vertebrae. This accurate representation of the vertebrae allows more accurate measurements of vertebral rotation when compared to conventional radiography (Carlson et al., 2013). The measurements are performed using the methods summarised in **Table 2.5**. Although these methods are based on sectional CT images (i.e. 2D images), the ability to visualise the vertebrae in the transverse plane increases the accuracy of axial vertebral rotation measurements (Vrtovec et al., 2009); however, they are still limited by the possibility that a vertebra could be rotated in the coronal and sagittal planes. The assumption that the vertebra rotates in one direction is not true in scoliosis and could result in measurement errors. An alternative method for further improving the accuracy of vertebral rotation is to use 3D images.

Table 2.5: Summary of the methods used for vertebral rotation measurements on CT images (adopted from Lam *et al.*, 2008).		
Aaro–Dahlborn's method (Aaro et al., 1978)	The degree of vertebral rotation is the degree between two lines: (1) AB is drawn between the anterior midline of the body and vertebral foramen, and (2) BC is drawn through the midline of the vertebra.	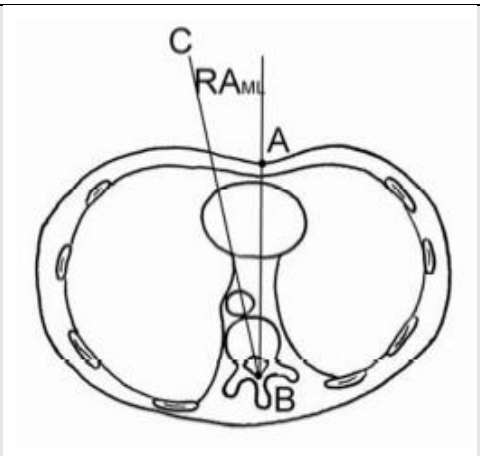
Ho's method (Ho et al., 1993)	The degree of vertebral rotation is the degree of the angle (ACV); AC bisects the angle BCB (i.e. the two lines between the pedicle and laminae), and a line runs through midline of the body (CV).	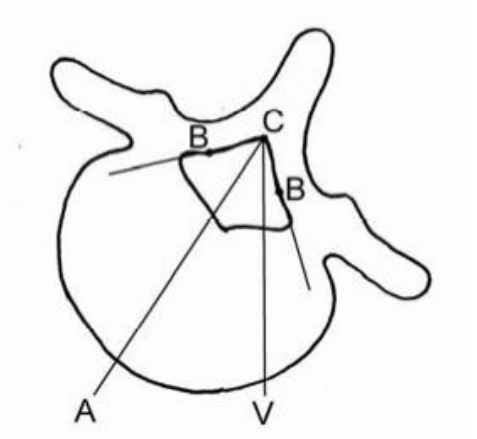

Spinal 3D images can be acquired using CT or EOS. CT images provide accurate and detailed information on the structure of the deformity (Lam *et al.*, 2008; Glaser, Doan and Newton, 2012; Brink *et al.*, 2017). Such images can be reconstructed to generate an accurate 3D image of the spine. EOS can also generate 3D images of the spine; however, the images do not truly represent the spine, as they are an approximate model. Unlike CT scanning, where the reconstructed images are based on true acquired data from every direction, EOS utilises software to create a 3D model of the spine based on two images. The software uses landmarks to estimate the location of each vertebra. The resultant images are not as accurate as CT images but provide comparable measures (Pomero et al., 2004; Rousseau et al., 2007;

Somoskeöy et al., 2012; Glaser et al., 2012; Wade et al., 2013; Courvoisier et al., 2013; Al-Aubaidi et al., 2013; Bagheri et al., 2018). Based on the foundation of generating 3D images using two images, Kim *et al.* (2018) used two conventional X-ray images (i.e. AP and lateral view images) to generate a 3D model of the spine. They found that it was possible to generate 3D images of the spine provided the images were acquired at 90° to each other; yet, the measurements were less accurate than EOS measurements. A major drawback of their technique is that it requires manual processing (i.e. segmentation of the vertebrae), which is time-consuming and labour-intensive.

2.5.1.3 *Reproducibility and repeatability of scoliosis radiologic measurements*

Reliable and accurate measurements of spinal deformity are important when assessing scoliosis. Decisions are made based on the findings of these measurements. As the Cobb angle is the standard measure for quantifying spinal curvature, errors are present in the measurements mostly due to patient positioning during the imaging session, the operator performing the measurements and how they are performed (Vrtovec et al., 2009; Maillot et al., 2015). As discussed in **Section 1.3.1** on **page 9**, the clinically accepted variation in Cobb angle measurement is 5°. The possible sources of the variation in the measurements can be due to changes in the patient's position between images or how the Cobb angle measurement is performed during the measurements. In conventional X-ray images, the variation caused by the changes in the patient's imaging position is from 2° to 7° (Goldberg et al., 1988; Pruijs et al., 1994). Surprisingly, the level of the observers' experience in performing Cobb angle measurements has no impact on the consistency of the findings (Ritter et al., 2016; Segundo et al., 2016). A major source of error in measurements may be incorrect definition of the vertebral endplates, which results in inaccurate drawing on the endplates, or measurement of the angle itself (Lechner et al., 2017). The last source of measurement variation, that is, how

the measurements are performed, can be affected by the format of the spine images (i.e. physical and digital images).

Cobb angle measurements performed manually on X-ray film images are linked to significant intra- and inter-measurement variations (Hwang et al., 2010; Vrtovec et al., 2013). The causes of these variations can be inaccurate selection of the most tilted vertebra, inaccurate line drawing on their endplates, inaccurate protractors and the use of different protractors and markers (i.e. different line thicknesses) (Tanure et al., 2010). Overall, manual Cobb angle measurements are subject to less intra-observer variation than inter-observer variation; variation is also less when constant protractors and markers are used and the most tilted vertebrae are pre-selected (i.e. when the observers are told which vertebrae they should use for the measurements) (Maillot et al., 2015). Measurements performed on digital images eliminate the variations from protractors and markers, but other factors such as the variation in defining the endplates can influence the measurements. The intra- and inter-observer measurements are improved on digital images (Dimar et al., 2008; Ritter et al., 2016). This has led to a slight enhancement in Cobb angle measurements on digital images (Tanure et al., 2010; Langensiepen et al., 2013). The difference between the two methods was up to 1.7° (Jones et al., 2008), and there is excellent agreement between the two measurements (Jones et al., 2008; Tanure et al., 2010; Somoskeöy et al., 2012; Langensiepen et al., 2013). A benefit from performing Cobb angle measurements on digital images is the ease of using image viewing software, which allows observers to manipulate the images (i.e. increase contrast or zoom) to gain better visualisation of spinal landmarks; moreover, the standardised measuring tools could be major contributors to the slight enhancement in the measurements.

So far, in this context, performing the measurements on digital images refers to the process of manually selecting the most tilted vertebra and drawing lines using a computer pointing

device (e.g. a computer mouse). Several studies have tested software to automatically or semi-automatically select the most tilted vertebra and measure the Cobb angle reference with minimum human intervention (Allen et al., 2008; Zhang, Lou, Hill, et al., 2010). For such measurements, observers highlight the ROI and, based on their entry point, develop a program to calculate the Cobb angle. Although this method is reliable, it is only applicable to certain types of spinal curvatures (i.e. moderate). Other studies have utilised smartphone applications to measure the Cobb angle on either physical or digital X-ray images and compare their measurements to manual measurements using a protractor. Measurements performed using smartphone applications are in excellent agreement with manual measurements (Qiao et al., 2012; Shaw et al., 2012). In summary, conventional X-ray images in both formats are reliable for Cobb angle measurements, with digital X-ray images having a slight advantage.

CT images are not widely used for Cobb angle measurements; therefore, there are very few studies investigating its reliability. Nevertheless, variations in Cobb angle measurement in the coronal plane in CT images are at the same level as that of X-ray images; the intra- and inter-observer variability is 2.6° and 3.8°, respectively (Adam et al., 2005). In addition, 3D images of the spine have high reliability in terms of Cobb angle measurements and selection of the most tilted vertebra (Tauchi et al., 2016; Lechner et al., 2017; Huo et al., 2017). The variability of Cobb angle measurements on 3D images is similar to that from conventional X-ray images: inter-observer variation for 3D CT images and X-ray images is 3.57° and 3.62°, respectively (Lechner et al., 2017).

There have been more investigations of the reliability of EOS imaging systems in Cobb angle measurements compared to CT. The 2D or 3D images of EOS are reliable in terms of Cobb angle measurements (Ilharreborde et al., 2011; Somoskeöy et al., 2012; Al-Aubaidi et al., 2013; Yvert et al., 2015; Melhem et al., 2016; Rehm et al., 2017; Bagheri et al., 2018). The

intra- and inter-observer variations of 3D measurements is 4.8° and 6.2°, respectively (Ilharreborde et al., 2011). There is no statistical difference between Cobb angle measurements performed on 2D and 3D EOS images (Somoskeöy et al., 2012), between 2D EOS images and conventional radiography images (Chung et al., 2018) or between 3D EOS images and 3D CT images (Glaser et al., 2012; Al-Aubaidi et al., 2013).

Unlike measuring the degree of spinal curvature, where the method is constant, vertebral rotation measurement uses different methods, as discussed earlier, which could contribute to the variation in the measurements. In terms of the accuracy of vertebral rotation measurements, the most accurate measurements can be obtained from 3D CT images (Vrtovec et al., 2009; Illés et al., 2011). This is because CT scanners can acquire true 3D images of the spine. Measurements obtained from EOS 3D images are comparable to CT measurements (Glaser et al., 2012; Al-Aubaidi et al., 2013); measurements performed on 2D images are the least accurate, because the methods mentioned in **Table 2.5** all use the appearance of a single landmark to determine the rotation, and it is usually linked to greater inter-observer variation due to the absence of a standardised method (Vrtovec et al., 2009).

2.5.1.4 *Radiation dose and risk*

The main concern when using the X-ray imaging machines (i.e. conventional radiography, CT, EOS) is the risk of ionising radiation, as patients with scoliosis undergo repeated exposures to manage the deformity. Systematic searches of the literature were conducted to identify studies that had investigated the radiation dose level from the range of X-ray modalities when used for AIS imaging. A variety of terms, identified through medical subject headings (MeSH), were considered to ensure an extensive search of the literature. **Table 2.6** summarises the findings of these studies. Besides showing the dose levels from CT and EOS,

the table shows the radiation dose levels from different technologies of conventional radiography (i.e. SF, CR, DR).

Table 2.6: Summaries of studies performed to measure the radiation dose in adolescent scoliosis imaging.				
Study	Type of measurement	Machine	Projection	ED (µSv)
Chamberlain *et al.* (2000)	Indirect measurements	SF	AP	140
Hensen *et al.* (2003)	Indirect measurements	SF	AP	800-1090
			PA	440-490
			Lateral	470-540
		CR	PA	30
			Lateral	36
Lee, McLean and Robinson (2005)	Indirect measurements	SF & CR	PA	81-123
			Lateral	124-207
Gialousis *et al.* (2008)	Indirect measurements	SF	AP	440-470
			PA	240-250
			Lateral	290-410
Abul-Kasim *et al.* (2008)	Indirect measurements	CT	Supine	380- 7760
Abul-Kasim *et al.* (2009)	Indirect measurements	CT	Supine	370
Abul-Kasim (2010)	Indirect measurements	CT	Supine	370
Deschênes *et al.* (2010)	Direct measurements	CR	PA+Lateral	Not stated [A]
		EOS		
Mogaadi, Ben Omrane and Hammou (2012)	Indirect measurements	SF	AP	678
			lateral	586
Kalra *et al.* (2013)	Indirect measurements	CT	Supine	100-600
Ben-Shlomo *et al.* (2013)	Indirect measurements	CR	AP	113-166
			PA	62-90
			Lateral	91-128
Damet *et al.* (2014)	Direct measurements [B]	EOS	AP+Lateral	200
Luo *et al.* (2015)	Indirect measurements	CR	PA	215 [C]
			Lateral	295 [C]

		EOS	AP	121
			PA	69
			Lateral	121
Hui *et al.* (2016)	Indirect measurements	EOS	PA	2.6
		DR	PA	67.5
Law *et al.* (2016)	Indirect measurements	DR	PA+Lateral	650-840
Pedersen *et al.* (2018)	Direct measurements [E]	CR	AP	545
			PA	495
		EOS	AP+Lateral	37 (adult phantom)
				29 (5-year old phantom)
Branchini *et al.* (2018)	Direct measurements [D]	EOS	PA+Lateral	430
		CR		870
Hwang *et al.* (2018)	Indirect measurements	DR	AP	188 - 300
Law *et al.* (2018)	Indirect measurements	EOS	PA+Lateral	2.82- 13.23

[A] Thirteen OSLDs were used to measure ESK instead of the ED to make the comparison. The average radiation dose measured with EOS was lower at each location where the OSLDs were used.
[B] Used 5-year-old phantom.
[C] This value reduced to 57 µSv for PA projection and 162 µSv for lateral projection when a lead acrylic filter was positioned at the X-ray collimator.
[D] Not all organs dose were measured using TLD; there was an assumption that some organ doses are equal to each other and they used on adult phantom.
[E] An adult phantom was used to represent 15-year old child used for the dose measurements.

The review indicates that EOS has the lowest dose and CT has the highest dose. A micro dose protocol is utilised in the EOS imaging system to further reduce the dose to patients. The micro dose protocol delivers 5.5 times lower radiation than the standard EOS imaging protocol and 45 times lower radiation than conventional radiography (Ilharreborde et al., 2016). However, it was not clear what type of conventional radiography (i.e. SF, CR or DR) was used in the comparison in Ilharreborde *et al.*'s (2016) work. Nevertheless, the dose ranged from 2.6–121 µSv for EOS and 370–7760 µSv for CT for a single frontal projection (i.e. AP or PA). On the other hand, the dose in conventional radiography is 81–1,090 µSv, 30–215 µSv and 188–300 µSv for SF, CR and DR, respectively. The DR values are from one work, and they are only for an AP projection. Nevertheless, direct comparison between these studies is difficult because the methods used differ in several aspects: (1) the dose measurement methods were not consistent: radiation dose was measured using direct and indirect methods; (2) the tissue weighting factors used to calculate the ED were not consistent because they are updated regularly. Using different weighting factors changes the values of the measured doses. The difference in measurements ranged from 7% to 25% when using the ICRP 103 weighting factor instead of the ICRP 60 weighting factor (Christner et al., 2010b; Huda et al., 2011); and (3) different imaging parameters and field sizes were used, and they affect radiation dose levels directly.

Most of the studies displayed in Table 2.6 calculated the ED indirectly by measuring the ESD or DAP using MC or conversion factors. Such measurements can indicate the radiation to which patients are exposed, but with less accuracy as compared with direct measurements because of the reasons mentioned in **Section 2.2.2** on **page 26**. The other studies either used an adult phantom (Damet et al., 2014; Branchini et al., 2018; Pedersen et al., 2018) or a phantom representing a 5-year-old child (Damet et al., 2014; Pedersen et al., 2018) to measure

the ED from scoliosis radiography for adolescents. In addition, Branchini *et al.* (2018) did not measure the absorbed dose for the entire body, that is, they did not measure the absorbed dose for all organs. Instead, they measured the absorbed dose for the most radiosensitive organs (i.e. sample of organ location); thus, they assumed that different organs receive the same amount of radiation. For example, the heart dose is similar to the oesophagus dose, whereas the pancreas, spleen and gall bladder dose are similar to the stomach dose. This is not necessarily accurate, as these organs are located at different levels and depths in the human body and therefore receive different amounts of radiation which can be significantly biased due to where the dosimeters are located (Clavel et al., 2016). Damet *et al.* (2014) managed to measure the absorbed dose for all organs but failed to use the locations recommended by the manufacturer of the phantom by reducing the number of detectors used from 273 locations to 58 (CIRS, 2016). Using these techniques to estimate the ED reduces the accuracy of the measurements and affects the overall measurements. Lastly, Deschênes *et al.* (2010) did not use a phantom nor measure the ED; instead, they placed several detectors on patients and measured the ESD to compare CR and EOS in scoliosis radiographs. The ESD is a poor indicator of the risk of radiation because it does not take into account the irradiated area, the type of irradiated tissue and the penetrating power of X-rays (Chamberlain et al., 2000).

2.5.1.5 *Image quality*

Another systematic search of the literature was conducted to identify studies that had investigated the IQ of conventional radiography, CT and EOS in scoliosis radiography. The search terms were identified through MeSH. **Table 2.7** summarises the findings. When evaluating the IQ, the images from EOS had better IQ compared with the images from DR and CR (Deschênes et al., 2010; Yvert et al., 2015). However, assessing AIS does not necessarily require high-quality images, because the spine is discernible in low IQ, as

indicated earlier. When Hui *et al.*, (2016) compared the accuracy of Cobb angle measurements of EOS images to those of DR, no significant difference was found between their measurements.

Table 2.7: Summary of studies investigating IQ in scoliosis radiography.

Study	Type of measurement	Machine	Image source	Summary of findings
Deschênes *et al.*, (2010)	VGA	CR EOS	Patients' images	EOS was superior or equivalent to CR in terms of image quality.
Kalra *et al.*, (2013)	SNR VGA	CT	Patients' images	Images had excellent image quality.
Damet *et al.*, (2014)	MTF & NPS	EOS	Patients' images	Physical characteristics of the machine were assessed and found comparable to conventional radiography.
Yvert *et al.*, (2015)	CDA	DR EOS	CDRAD	EOS had better image quality.
Hui *et al.*, (2016)	VGA	DR EOS	Patients' images	No significant difference was found in the overall rating of image quality between DR and EOS.

2.5.1.6 *Cost and availability*

Data on the cost of installing and operating conventional X-ray, CT and EOS machines are limited. In general, the initial installation, maintenance and operation costs of an EOS imaging system are twice that of DR and four times that of CR (McKenna et al., 2012; Faria et al., 2013; Mahboub-Ahari et al., 2016). No direct comparison between CT and other machines was found; however, the National Institute for Health and Care Excellence (NICE), an organisation that provides national guidance and advice for improving health and social care in the UK, estimates that the initial installation cost of a new CT scanner is £350,000–500,000 and is around £400,000 for a new EOS system (NICE, 2011; NICE, 2016). EOS is unlike the other machines, which are multipurpose; EOS usage is limited to orthotists. A few studies have investigated the cost effectiveness of EOS imaging systems and have

acknowledged that dose reduction can be achieved using EOS, but that it is less cost-effective compared with the conventional radiography imaging machines (McKenna et al., 2012; Faria et al., 2013; Wade et al., 2013). It is worth noting that these separate studies were conducted by the same authors; therefore, due to the lack of more recent evidence, conclusions cannot be drawn from these studies. In terms of availability, conventional radiography machines and CT scanners are more widely available than EOS systems (the availability of CT scan and EOS imaging systems is discussed further in Chapter 5 [Discussion]).

2.5.2 Non-ionising imaging modalities

Non-ionising imaging modalities utilise other procedures rather than X-rays to generate diagnostic images such as sound and magnetic waves. Therefore, they do not pose radiation risks to patients. In scoliosis imaging, several radiation-free machines can be used to evaluate spinal deformity, namely, magnetic resonance imaging (MRI), U/S and surface topography (ST) machines (Adam et al., 2010; Cheung et al., 2015; Shi et al., 2015; Ng and Bettany-Saltikov, 2017). These imaging machines function differently from the machines that use X-rays; each works based on different principles. Therefore, the following sections discuss how they work, how they can be used for scoliosis evaluation and the accuracy of their measurements.

2.5.2.1 *Basic principles of MRI, U/S and ST and their imaging conditions*

MRI uses radio waves and magnetic fields to produce a diagnosable image. First, the machine sends radio waves to a patient sitting in a magnetic field, which are absorbed by hydrogen atoms in the body; then, the hydrogen atoms re-emit the absorbed radio waves, which are captured by the system to form an image (Allisy-Roberts and Williams, 2008). During an MRI scan, patients are in a supine position on a table; MRI cannot be performed in a standing

position. In U/S imaging, high-frequency sound waves are sent through the body; the waves are reflected when they hit a surface between tissues of different density. The reflections are recorded to produce a U/S image. For scoliosis imaging, a standing U/S scan can be used (**Figure 2.14**). Lastly, ST produces an image of the spine by projecting stripes of light on the back of a patient, and then a camera captures a series of photos of the back to assess the surface asymmetry and bony landmarks (**Figure 2.15**) (Frerich et al., 2012). The scan is performed in a standing position. All of these imaging machines can produce 3D images of the spine.

Figure 2.14: The newly emerging Scolioscan (Telefield Medical Imaging Ltd., 2019).

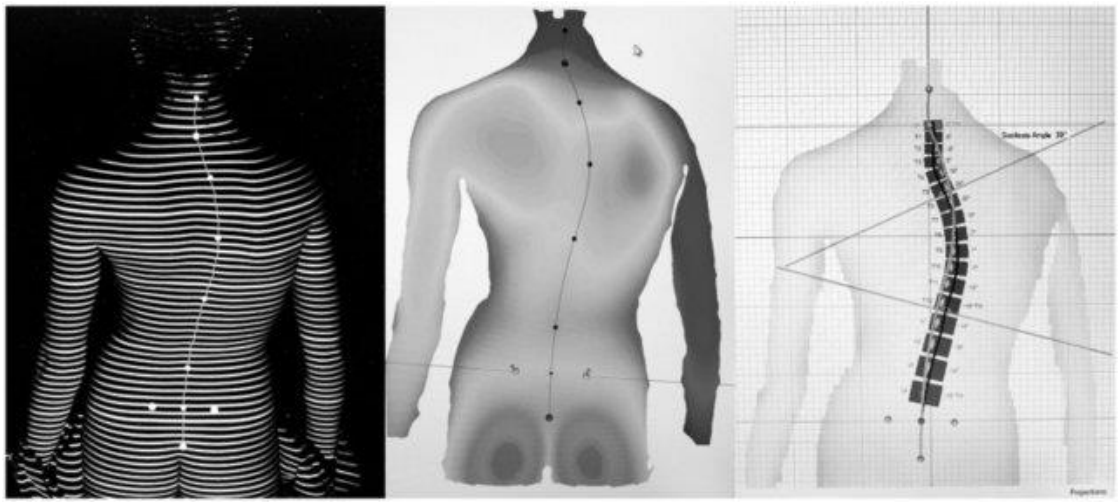

Figure 2.15: An illustration of how ST produces an image of the spine. Light is projected (left) and then a photo is captured (middle), and based on the surface asymmetry and bony landmark, an image (right) is produced (Frerich et al., 2012).

2.5.2.2 *MRI, U/S and ST usage in scoliosis measurements*

MRI and U/S are not commonly used to assess spinal curvature for several reasons. MRI scans are expensive and time-consuming, and MR images are inferior in terms of the reproduction of bony structures (Cheung et al., 2015; K. Kim et al., 2018; Brink et al., 2018). The scanning time is increased further if vertebral rotation measurements are required, as the scanner requires repeated sending and receiving of radio waves to cover the whole spine (Brink, Schlösser, et al., 2017). Additionally, the scan is not performed in the standing position, which has effects on the Cobb angle as discussed earlier. MRI is mostly used in scoliosis to diagnose the underlying causes of the deformity and investigate irregular curve patterns for treatment planning and for following up after treatment rather than for evaluating the curvature itself (Kim et al., 2010; Ozturk et al., 2010). Nevertheless, MRI cannot be used in treatment follow-ups when pedicle screws are used to correct the curvature, as these cause artefacts in MR images.

Using U/S for scoliosis assessment is still under investigation because the concept of using U/S is relatively new. Currently, a clinical trial is underway in the US, and its outcome is

expected to be realised towards the end of 2021. A major drawback to using U/S for scoliosis evaluation is that it provides limited detail of the anatomical structures (**Figure 2.16**). This is because the human back is not flat, and the transducer loses contact with the body.

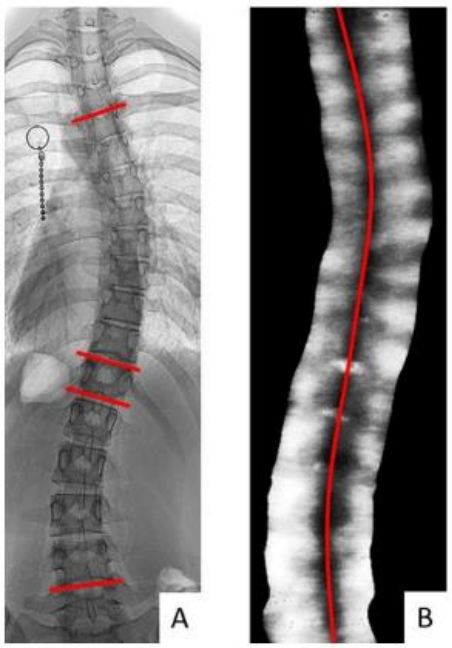

Figure 2.16: An X-ray image of the spine (A) and the corresponding U/S image (B) (Brink et al., 2018).

Unlike MRI and U/S, ST is used more than the other machines in scoliosis evaluation. Scanning requires a shorter time than the other approaches. ST has been developed to become more operator-independent than its previous versions, which has aided the reduction of the scan time and has improved the accuracy of the measurements. In scoliosis evaluation, ST is used to monitor the progress of the curvature (Knott et al., 2010; Frerich et al., 2012; Ng and Bettany-Saltikov, 2017), and when a change in Cobb angle measurement is noted, patients are referred to conventional radiography.

2.5.2.3 *Accuracy of scoliosis measurements*

Because of their lack of popularity, or because they were recently developed, few published works have investigated the reproducibility and reliability of these machines for evaluating

scoliosis. MRI underestimates the Cobb angle because the scan is performed in the supine/prone positions; however, its measurement correlates with measurements of the standing position, and the correlation is more reliable in severe cases (Wessberg et al., 2006; Shi et al., 2015; Brink, Colo, et al., 2017). The causes of underestimation are similar to those for CT measurements, which have been discussed in **Section 2.5.1.1** on **page 46**. For vertebral rotation, which can be measured on MRI using the methods used in CT imaging (**Table 2.5** on **page 49**), the measurements are comparable to those from CT images (Abul-Kasim et al., 2010). As with CT measurements, vertebral rotation measurement in axial MRI is more accurate than that from 2D radiography.

The use of U/S for assessing scoliosis has not been widely investigated because the technology is relatively new. The degree of the curvature is determined using the spinous process, transverse process or vertebral lamina (Chen et al., 2013; Zheng et al., 2015; Brink et al., 2018). U/S measurements have good agreement with measurements from radiography; however, when compared with conventional radiography, the angle is underestimated for moderate and severe cases (Y. Zheng et al., 2016; Zheng et al., 2018) and is overestimated for mild cases (Zheng et al., 2018). The accuracy of measurements can be improved by using previous radiography to select the most tilted vertebra (Young et al., 2015; R. Zheng et al., 2016). The accuracy of the measurements is greatly affected by the operator's level of experience and, most importantly, by the pressure applied to the patient's back by the U/S transducer, which could change the patient's posture (Zheng et al., 2018).

Lastly, ST is similar to MRI and U/S in terms of its inability to accurately determine the degree of the curvature, but it can provide measurements that correlate with the measurements from radiography (**Figure 2.17**) (Frerich et al., 2012; De Sèze et al., 2013; Mangone et al., 2013; Knott et al., 2016; Ng and Bettany-Saltikov, 2017); the correlation is weaker for curves

in the lumbar area than the other areas (intraclass correlation [ICC] = 0.492) (Knott et al., 2016). The Cobb angle measurements of ST can be 10° less than that of radiographic measurements for the same case (Frerich et al., 2012; De Sèze et al., 2013; Knott et al., 2016); and, ST can be used independently to evaluate scoliosis.

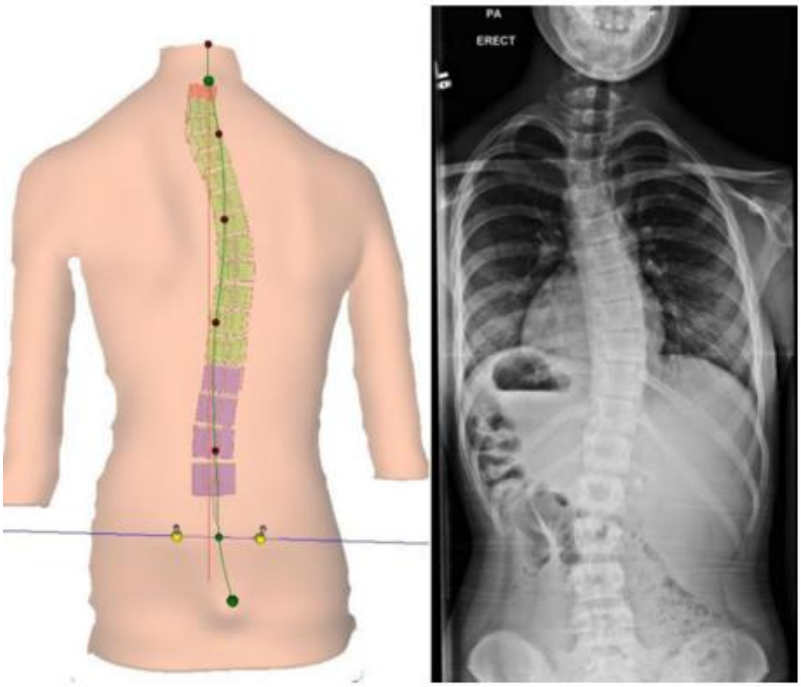

Figure 2.17: Images taken by 3D topographic camera (left) and a standard X-ray imaging machine (right) showing the shape of the same spine (Knott et al., 2016).

2.6 Study aim and objectives

Adolescents diagnosed with scoliosis undergo frequent radiographic examinations of the spine to monitor curve progression. The repeated examinations pose the risk of the patient developing radiation-induced cancer later in life. As discussed earlier, much effort has been made to develop technologies that reduce the risk of radiation to patients with AIS and improve the outcomes of the examination. Nevertheless, no machine can provide accurate Cobb angle measurements other than the gold standard for evaluating scoliosis, that is, conventional radiography, except EOS, but its availability is very limited. In light of this, there are potential benefits to using SPR in CT scanning for evaluating scoliosis.

SPR is a CT scanning mode that is used prior to the clinical CT scan to set the acquisition parameters. For example, it is used to identify where the scan starts and ends and to calculate and vary the tube mA value (mA modulation) (Dowsett et al., 2006; Nauer et al., 2009). It is more commonly referred to as the scout view or scanogram. Other terms, such as localiser radiograph and tomogram, are used in the literature. Unlike clinical scans, where the X-ray tube moves around the patient while the CT table is moving, the tube is fixed in SPR, and the patient is moved through a projected fan-beam X-ray. It can acquire images in AP, PA and lateral projections based on the tube position (i.e. above the patient for AP or underneath for PA). The radiation dose required to acquire these images is very low when compared with that of conventional radiography or the CT examination itself: the ED ranges from 1.9–27.7 µSv (Dowsett et al., 2006; Nauer et al., 2009), depending on the examination. The use of SPR images to assess AIS is not reported in the literature; consequently, the ED and the associated risk from using SPR to evaluate AIS has not been investigated.

Several studies have reported that SPR can provide diagnostic information and identify abnormalities, such as spinal stenosis and bony metastasis (Nuri Sener et al., 1993; Brook et al., 2007). Zhang *et al.* (2016) found that the spine and vertebrae are easily identifiable in SPR images. However, one study in the literature measured Cobb angle measurements on CT SPR images and compared them with those on conventional X-ray images. The study concluded that the Cobb angles on SPR were less by an average 11° (*SD* = 5.2, range 1.9–27°), but were strongly correlated to the measurements of conventional radiography (Vavruch and Tropp, 2016). Nevertheless, the study was retrospective; hence, the images used in the study were not intended for Cobb angle measurements. Moreover, the study included only severe cases (>40°); minor and moderate AIS cases, which are more common, were not compared with conventional radiography.

The above suggests that SPR images might not determine Cobb angle measurements as accurately as the gold standard of the conventional radiography images, but they could be similar to ST, U/S, CT and MRI measurements used for scoliosis assessment, which in turn suggests that reliable conversion of the parameters between the different measurements is possible. Moreover, because SPR uses lower radiation than conventional radiography, there is the potential for dose reduction when SPR images are used to monitor scoliosis curve progression when EOS is not available. Additionally, CT scanners are widely available, which means that dose reduction can be achieved at no extra cost to healthcare providers.

Radiation dose levels and the risk associated with using SPR for AIS assessment have not been investigated. The aim of this study was to investigate the ability to use SPR mode in CT scan to assess scoliosis by achieving the following objectives:

1. Calculating the ER and ED for SPR when used for AIS assessment and comparing them with ER and ED from DR and EOS.
2. Investigating the accuracy of Cobb angle measurements on SPR images.

2.7 Chapter summary

This chapter has reviewed radiation dose quantities, IQ parameters and the imaging modalities used for scoliosis assessment. SPR uses low-radiation doses and presents the potential for dose reduction and thereby reduces risk of developing radiation-induced cancer in patients with AIS. Its limitation is that the scan is performed where axial loading is absent. However, a reliable conversion factor can be achieved because of the strong correlation that its measurements have with the measurements of the gold standard. Therefore, the aim of this study was to measure the radiation dose levels from the SPR mode when used for Cobb angle measurements and to compare them with those of the other X-ray imaging machines, namely, DR and EOS. Moreover, the accuracy of its Cobb angle measurements was tested.

Chapter 3: Methods and material

3.1 Chapter overview

This chapter outlines the method and materials used to determine the capability of SPR in CT for assessing scoliosis. In addition to quantifying radiation dose from SPR, DR and EOS, this study tested the accuracy of Cobb angle measurements on SPR images. To test the accuracy, a novel phantom was built for this purpose. For better presentation, this chapter is divided into three main sections: (1) radiation dose measurements, where SPR, DR and EOS radiation is quantified and compared; (2) construction of a phantom; a detailed description of the construction of a novel phantom with a scoliotic spine; and (3) the accuracy of Cobb angle measurement evaluation when using SPR images. **Figure 3.1** provides an outline of the method.

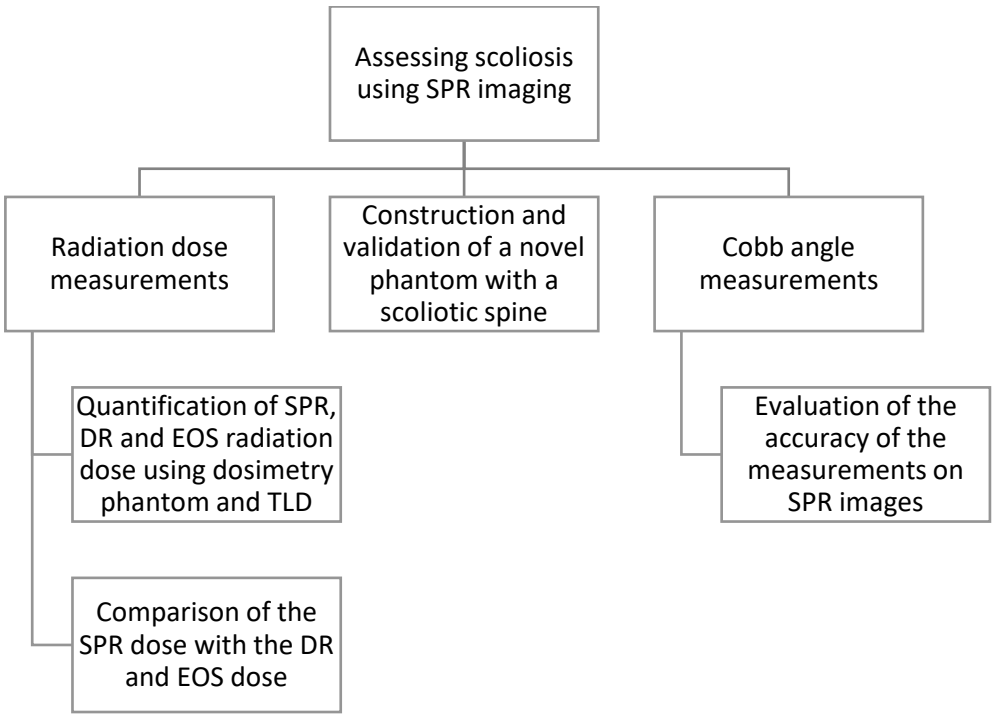

Figure 3.1: Summary of the method used for assessing the use of SPR images for Cobb angle measurements.

3.2 Radiation dose measurements

In this study, radiation was quantified via direct measurements of the radiation dose. As discussed in **Section 2.2.2** on **page 26**, this enabled a more precise determination of the radiation risk compared with indirect measurements through mathematical modelling, using software such as the 'industry standard' MC code PCXMC for projection radiography and ImPACT for CT scanners (ImPACT, 2002; Visvikis et al., 2006; Tapiovaara and Siiskonen, 2008), as SPR (CT), DR and EOS use different technologies. Using PCXMC to estimate the risk from SPR is not possible because it does not account for a bowtie filter that is used in CT scanners (Tapiovaara, 2012). Moreover, PCXMC cannot be used for EOS dose estimation because the EOS beam geometry is different from that of DR, and PCXMC has not demonstrated validity for this type of beam (Clavel et al., 2016). Despite this, several studies in the literature have used PCXMC for EOS dose estimation (Hui *et al.*, 2016; Ben Abdennebi *et al.*, 2017; Law, Ma, Chan, Lau, *et al.*, 2017; Law *et al.*, 2018). ImPACT, on the other hand, could not be used for SPR dose estimation in this study because it does not estimate the dose in paediatric patients (IAEA, 2013). Direct measurement using a dosimetry phantom enables standardisation of the materials used for the dose measurements, provides solutions to overcoming the drawbacks of using indirect measurements and ultimately improves the validity of the measurements.

3.2.1 Materials for dose measurements

Dose measurements were performed using a dosimetry anthropomorphic ATOM® phantom (CIRS, Norfolk, VA, US) and TLD because it is not feasible or ethical in radiography research to conduct *in vivo* dosimetry on patients. The following sections list the materials and their preparation and use in the dose measurements.

3.2.1.1 *The phantom*

The dosimetry phantom is constructed from tissue-equivalent materials and is used to provide a physical representation of the human body's anatomy and attenuation characteristics for radiation dosimetry studies. To provide a representation of the human anatomy, these commercially available phantoms typically use three tissue-equivalent materials, imitating bone, lung and soft tissue. The present study used a dosimetry phantom Model 706 (height, 140 cm; weight, 32 kg; thorax dimensions, 17 × 20 cm), representing a 10-year-old child (CIRS, Norfolk, VA, USA). The phantom spans the head to the top third of the thigh but not the legs or arms (**Figure 3.2**). To allow access to the organ locations for dosimeter placement, phantoms are assembled in 32, 25-mm thick axial slices. The locations are drilled with 5-mm holes and have 15 mm × 15 mm organ dosimetry spacing (**Figure 3.3**).

Figure 3.2: The ATOM® phantom that represents a 10-year-old child (CIRS, 2016).

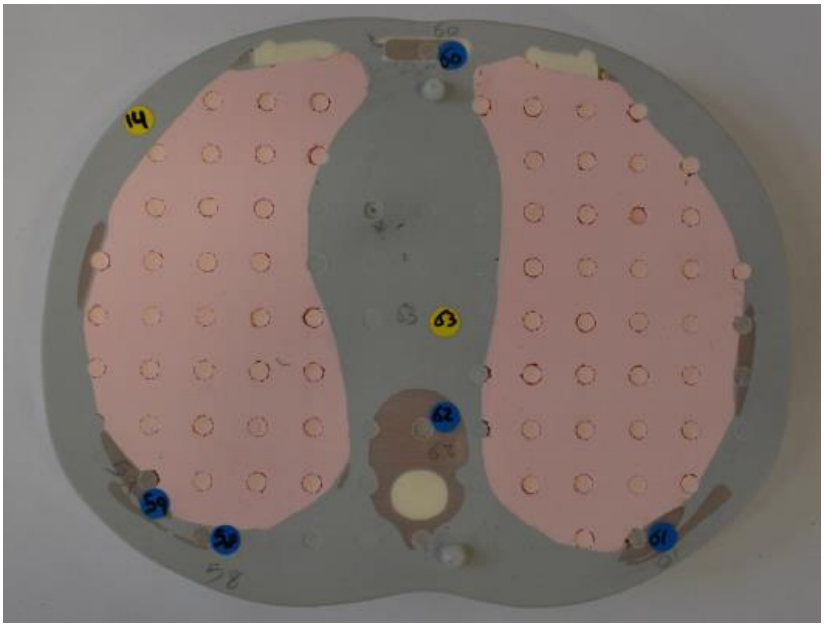

Figure 3.3: A slice from the phantom showing different tissue-equivalent materials: lung (pink), bone (brown) and soft tissue (grey).

The phantom is made from epoxy resins, with photon attenuation values within 1% for bone and soft tissue and 3% for lung tissue at photon energies of 30 keV to 20 MeV, as stated by the manufacturer (CIRS, 2013; CIRS, 2016). The phantom contains 198 locations for dosimetry detectors in 21 internal organs (**Table 3.1**). These are located based on holes in the slices (which are plugged when not in use) with tissue-, bone-, and lung-equivalent material depending on their locations. The plugs are 5 mm wide × 25 mm long. Specifically machined plugs were used to secure the dosimeters inside the phantom (**Figure 3.4**). The dosimeter locations inside the phantom are based on a map provided by the manufacturer, which outlines the most frequently observed organ locations and the optimised detector hole distributions within each organ. However, these locations are spread based on the normal anatomy of a 10-year-old child and do not account for the dislocation of some organs that might occur in the case of scoliosis.

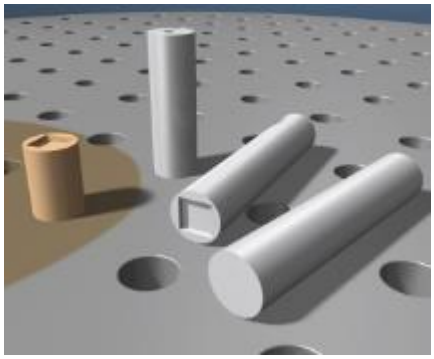

Figure 3.4: The plugs designed to hold the TLDs inside the phantom.

Table 3.1: The organs and number of dosimeter locations inside the phantom (CIRS, 2016).

Organ	TLD holes, *n*	Organ	TLD holes, *n*
Eyes	2	Pancreas	3
Brain	13	Kidneys	8
Thyroid	4	Adrenals	2
Heart	2	Intestine	11
Thymus	3	Ovaries	2
Lungs	24	Uterus	2
Liver	22	Urinary bladder	6
Gall bladder	3	Testes	2
Spleen	6	Prostate	1
Oesophagus	5	Breasts	2
Stomach	10	Active bone marrow	65

The provided map does not differentiate among the quantities of active bone marrow (ABM) in the phantom. ABM is distributed in nine bone tissues in the human body: cranium, mandible, cervical spine, clavicle, sternum, thoracolumbar spine, ribs, pelvis and femora, and the quantity of marrow in each bone differs, as reported previously (Cristy, 1981). Consequently, the absorbed dose to the ABM is calculated using the ABM distribution data from Cristy (1981) by averaging the absorbed radiation dose to each of the bone marrow tissues and multiplying this by their percentage of ABM. Then, the overall ABM dose is added and multiplied by its tissue weighting factor.

Additionally, the map does not specify the locations of some organs that require risk assessment. For example, it does not differentiate between the large and small intestines. In addition, it does not show specific locations for the oral mucosa, salivary glands and extrathoracic region. Therefore, a previously described method (Tootell et al., 2014; Ali et al., 2015; Mraity, 2015; Ali, 2016; Robinson et al., 2017; Tootell, 2018) was used to measure the doses to these tissues. Instead of adding more dosimeters to calculate the dose, existing locations (filled with dosimeters) were used as the equivalent locations for the missing organs based on the cross anatomy of the human body, as illustrated in **Table 3.2**.

Table 3.2: The equivalent locations for missing organs from the phantom map.

Organ	Equivalent locations
Salivary Gland	Left and right of the lingula of the mandible and sublingual fossa
Oral Mucosa	Left and right of the lingula of the mandible
Extrathoracic Region	Anterior aspect of C2 and upper part of the oesophagus

The Model 706 phantom was used for measuring radiation doses. It represents a 10-year-old child and is not gender-specific; the manufacturer only produces adult gender-specific phantoms. In general, the main anatomical differences between female and male bodies are the size of the breast and the reproductive system organs. Females, on average, have larger breasts compared with the males, and their breasts have glandular tissue. According to the Tanner staging system (also known as the sexual maturity rating), which divides puberty into five stages and tracks the changes in the gender characteristics of children during this period, female breasts begin to enlarge at stage 2, with a rapid increase in size at stage 3 (Marshall and Tanner, 1969); this means that the changes occur any time from the ages of 10 to 15 years. Therefore, it was assumed that there is no difference in breast size between male and

female 10-year-old children, as there is no specific time to which the changes can be assigned. Second, the reproductive organs, namely the prostate, testes, ovaries and uterus, are in different locations in the body; therefore, it was possible to measure the dose for these organs in one irradiation cycle rather than performing gender-specific measurements. The calculation, on the other hand, was gender-specific, where the prostate and testes doses were discarded when calculating the risk for a female patient, and vice versa.

3.2.1.2 *Thermoluminescent dosimeters*

As discussed in **Section 2.2.3** on **page 29**, multiple types of radiation dosimeters can be used to quantify the radiation dose in the diagnostic radiography range. However, only a few can be used for organ doses and placed inside a phantom, namely, the TLD, OSLD and MOSFET. The ionisation chamber and silicon diodes cannot be placed inside a standard dosimetry phantom but require a specialised phantom with a different hole design to accommodate them. In this research, TLDs were selected for use in the experiments for the following reasons:

1. A MOSFET reader can be linked to up to five MOSFET detectors; as there are 198 dosimeter locations for the measurements, 40 readers would be required, the acquisition of which would be cost prohibitive for this study;
2. Fewer MOSFET readers can be used for the measurements; however, this would not be practical because it requires irradiating the phantom and then moving the detectors to other locations until all 198 locations are covered. This would be impractical because it requires the phantom to be disassembled and reassembled at each irradiation, especially when the measurements are carried out on imaging machines at fully working hospitals. In addition, there is the possibility of altering the phantom's position when moving the MOSFET detectors, which could affect the accuracy of the measurements;

3. OSLDs also would be impractical because they are very sensitive to light. For the DR and EOS dose measurements, the irradiation was carried out at two children's hospitals, where adolescents undergo X-ray examinations. This meant that the phantom had to be transported to the two hospitals and the dosimeters could have been exposed to sunlight, consequently affecting the accuracy of their measurements (Pinto et al., 2014). This could be avoided by transporting the dosimeters in a protective case; however, this would mean placing them inside the phantom at the hospitals, where space and time are limited.

TLD chips satisfy all the criteria of an ideal detector that are mentioned in **Section 2.2.3** on **page 29**. They are tissue-equivalent, small and sensitive to the X-ray energy range used in diagnostic radiography, and they have a measurement range of 10 pGy to 10 Gy (Thermo Fisher Scientific Inc., 2016). TLDs have an effective atomic number (Z_{eff}) of 8.04 that is very close to that of human tissue (Z_{eff} = 7.42), which renders their interaction with X-rays similar to that of human tissue (Dong et al., 2002; Oliveira et al., 2010). Additionally, they are small (3.2 × 3.2 × 0.89 mm), making them suitable for placement inside the phantom. They also have a very low fading rate (approximately 3% per year) and are relatively inexpensive; one TLD, the Harshaw TLD-100H (LiF: Mg, Cu, P) (Thermo Scientific, USA) costs around £5. The main weakness of TLDs is their sensitivity to scratches and surface contamination, which could affect measurement accuracy. To avoid scratching them, Dymax 5 vacuum tweezers (Charles Austen Pumps, Surrey, UK) were used to move the TLDs (**Figure 3.5**). To reduce the possibility of contamination, the TLDs were always kept in their original packaging when not used. Additionally, the trays that were used to hold the TLDs during annealing were cleaned regularly with alcohol spray. Another weakness of the TLDs is the variation in their response to X-rays; the differing responses were overcome by obtaining calibration factors as illustrated in the following paragraphs.

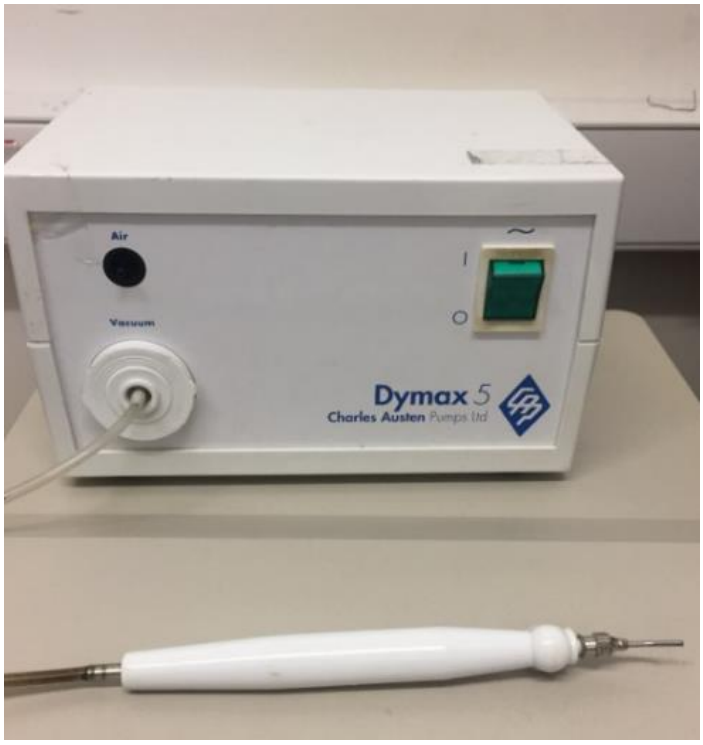

Figure 3.5: The vacuum tweezer that was used to carefully handle the TLD.

As discussed in **Section 2.2.3** on **page 29**, the TLD is a passive dosimeter, which means it does not provide an instant measurement of the radiation dose, but stores it instead. TLDs are made of inorganic crystals; when they are irradiated, they store part of the incident photon energy. During the read-out, the energy from the incident photons is released by heating. During heating, thermoluminescence occurs in proportion to the amount of absorbed energy (Yu and Luxton, 1999). As the signal may remain in the TLD crystals after the heating (i.e. after the read-out), the TLDs were annealed after each read-out to avoid residual signals that could affect the accuracy of subsequent measurements (Yifrah et al., 2014). **Figure 3.6** shows the cycle of using TLDs in the dose measurements.

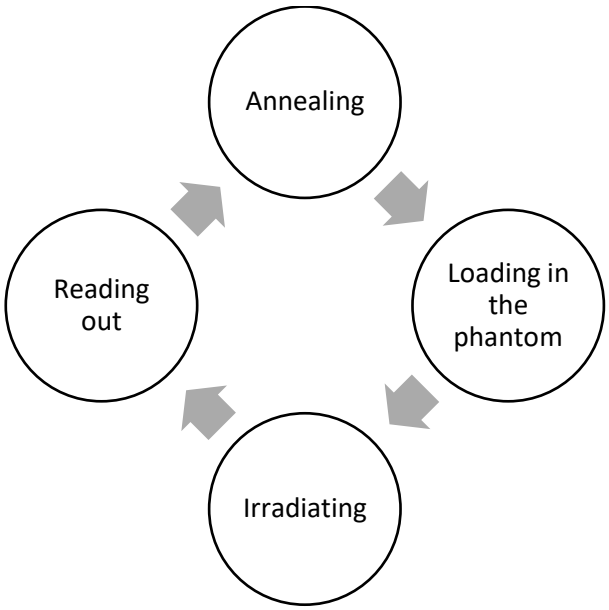

Figure 3.6: The cycle of dose measurements using TLD.

A fresh batch of 250 TLD chips was purchased specifically for the dose measurements. The sensitivity and consistency of the new TLDs were tested to ensure that the variation in their response to X-rays was within acceptable limits. The uncertainty of TLD measurements should be within ±10% (Allisy-Roberts and Williams, 2008). The TLDs were annealed at 240° for 10 min in temperature-controlled oven trays (**Figure 3.7**), and then each TLD was assigned a code by placing it on a tray with coded spaces (**Figure 3.8**). Next, the tray was irradiated using a general radiography X-ray machine (Konica Minolta Medical Imaging, Ramsey, NJ, USA). The irradiation was repeated three times. The TLDs then were read out using a Harshaw TLD model 3500 reader (Thermo Fisher Scientific, Waltham, MA, USA) (**Figure 3.9**). Based on the average readings, the TLDs were divided into two groups: A and B; where TLDs with similar responses to radiation were placed together following the method developed by Tootell *et al.* (2012). The difference in sensitivity between TLDs in the same group was calculated using the coefficient of variation (CV) (**Equation 7**). The CV of both groups was < 3%, which was achieved by removing the TLDs with extreme measurements. In

group A, 118 TLDs had a CV of 2.87%; in group B, 103 TLDs had a CV of 2.63%. The consistency of the measurements was tested after the TLDs had been calibrated, using the following equation:

$$CV = \frac{\sigma}{\mu}. \tag{7}$$

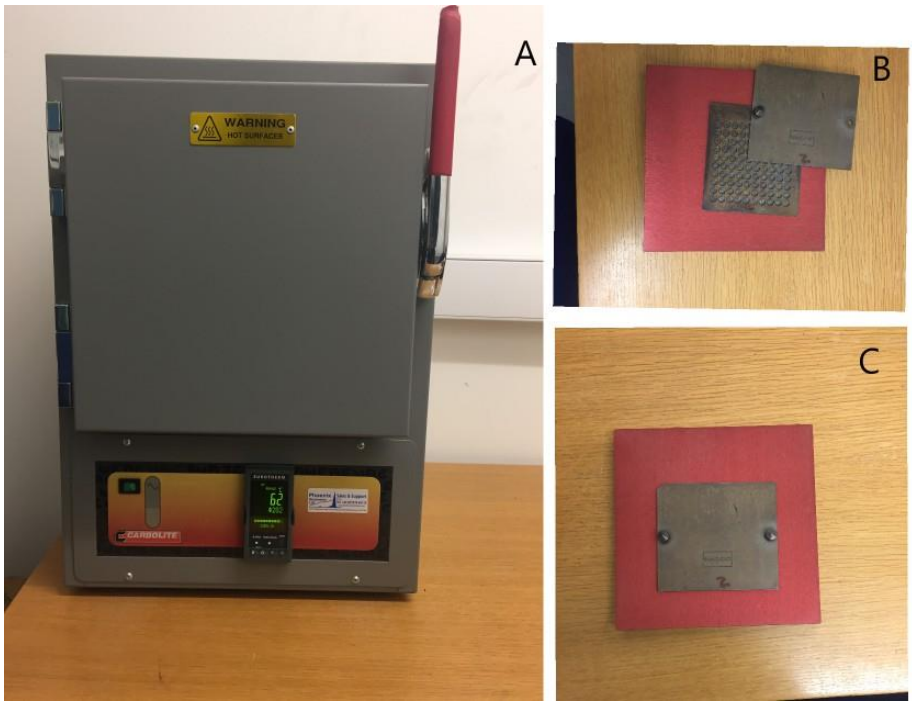

Figure 3.7: The oven (A) and the trays (B and C) used for annealing the TLDs.

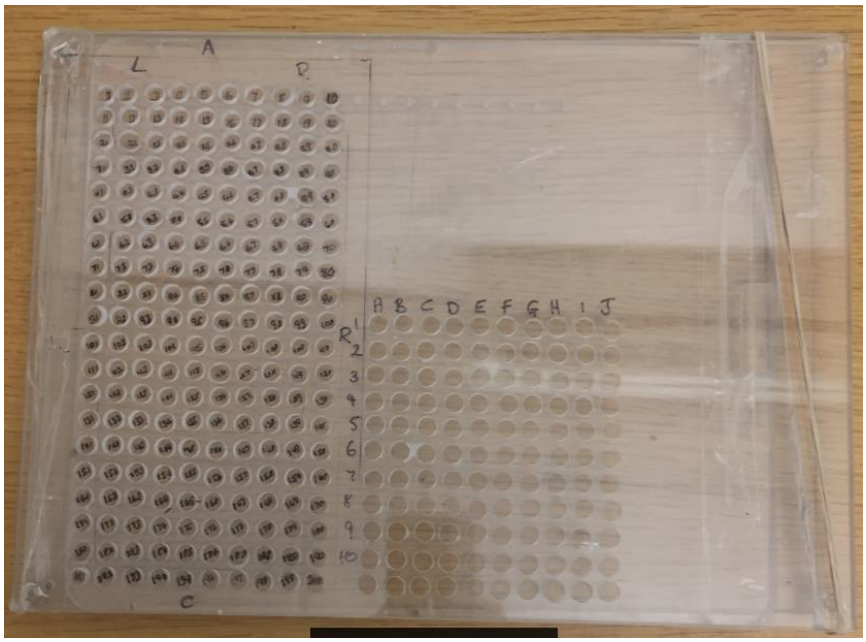

Figure 3.8: The tray used in the sensitivity test. Each TLD was assigned a code for the grouping.

Figure 3.9: Harshaw TLD model 3500 reader.

The TLDs were calibrated to minimise systematic errors that may have arisen from the TLDs and to improve the accuracy of their measurements. However, it was impractical to calibrate

each TLD individually due to time resources and the limited impact on accuracy, as the sensitivity difference of both groups was < 3%; this is below the 15% of batch variance suggested by the international standards for photon dosimeters (European Commission, 2009). Instead, 18 TLDs from each group were selected randomly for calibration following a previously used method (Ali et al., 2015). The calibration factor was obtained using the dose–TLD response curve (**Figure 3.10**). Establishing the curve requires at least five points (Shirazi et al., 2008); therefore, six TLDs (three from each group: A and B) were irradiated at five levels of radiation quantities (i.e. 10, 20, 40, 80, and 160 mA, which were randomly selected), but X-ray beam quality was kept constant at 90 kV. This kV was chosen based on the imaging factors for scoliosis in an average child. Three measurements at each mA level were averaged to minimise random error. Three TLDs were used to measure the background radiation. The R-squared (R^2) value in the figure (R^2 = 99.5%) shows the linearity in the TLD response at this energy range.

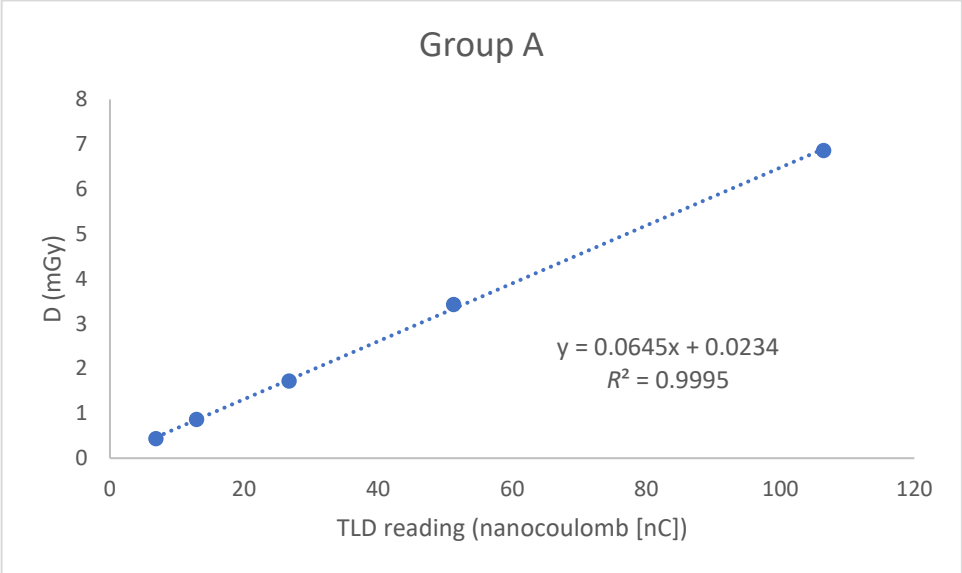

Figure 3.10: A plot of TLD measurements against the dose.

3.2.1.3 *Scoliosis shawl*

As part of the study, the efficacy of a scoliosis shawl (Rothband, Burnley, UK) for reducing the risk of radiation-induced cancer in patients with AIS was tested. The shawl (85 cm × 20 cm) is made of thin layers of protective sheets with 0.5-mm lead equivalence and weighs 1.2 kg. It is specifically designed to protect the breast tissues when patients undergo spinal examinations (**Figure 3.11**). The shawl was used during DR and SPR imaging examinations but not in EOS, as the radiation risk EOS poses is very low (EOS imaging protocol is discussed further in **Section 3.2.2.3** on **page 87**). Before using the shawl, the phantom was scanned several times, and shawl positions were adjusted to ensure that it did not cover the spine. When the desired location was detected, markers were placed on the phantom to ensure that the shawl was placed in the same place every time.

Figure 3.11: The scoliosis shawl.

3.2.2 Imaging conditions

Prior to each irradiation, the TLDs were annealed and placed in the phantom. Each TLD group was annealed in a separate tray to ensure that the groups were not mixed up. The TLDs

were placed inside the phantom starting from the bottom (i.e. slice 32) and moving upward until they reached the head (i.e. slice 1). Locations 101–198 were filled with group B TLDs; locations 1–100 were filled with group A TLDs.

Prior to conducting the experiments, the CT, DR and EOS had undergone quality testing in accordance with Institute of Physics and Engineering in Medicine (IPEM) Report 91 (Hiles, 2014), which relates primarily to imaging performance and radiation safety checks; the results were within manufacturer tolerances. The phantom was then irradiated as described in the following sections.

3.2.2.1 *Scan projection radiography*

The phantom was placed on the imaging couch of a third-generation 16-slice CT scanner (Toshiba Aquilion; Toshiba Medical Systems, Tokyo, Japan) in the supine position with the head towards the gantry (**Figure 3.12**). The scan range was set to cover the area from the intersection between cervical vertebrae C3/C4 to the iliac crests (Whitley et al., 2005). Tape markers were placed on the phantom and the CT imaging couch to ensure that the phantom was in exactly the same position for each exposure. Lateral alteration of the radiation field was not permitted in SPR mode.

Thirty-six SPR exposures were made: 18 in AP and PA positions without the scoliosis shawl, 9 in AP positions with the scoliosis shawl and 9 in lateral positions using combinations of 80, 100 and 120 kV and three mA values (10, 20, 30 mA) (**Table 3.3**). Each imaging protocol was given a code to be used in the comparison with the other machine. The exposure factors were selected based on the local teaching hospital guidelines for imaging an average 10-year-old child. The X-ray tube position was adjusted according to the desired projection as follows: above the phantom for AP, below the phantom for PA and to the right of the phantom (i.e.

right lateral) because it imposes lower risk than left lateral irradiation (Ben-Shlomo et al., 2013). With each imaging protocol, the phantom was irradiated three times to minimise random error. The shawl was not used during PA and lateral positions because it is not designed to shield breast tissue from a radiation beam from the back and the side. To test the consistency of the measurements, the phantom was irradiated three times at one-week intervals using the same projection and imaging factors.

Figure 3.12: Left: The phantom on the CT table. Right: The shawl on the phantom.

Table 3.3: Imaging factors and projections used for irradiating the phantom in SPR mode.

Imaging protocol	Imaging projection	kV	mA
CT1	AP	120	10
CT2	AP	120	20
CT3	AP	120	30
CT4	PA	120	10
CT5	PA	120	20
CT6	PA	120	30
CT7	AP	100	10
CT8	AP	100	20
CT9	AP	100	30
CT10	PA	100	10
CT11	PA	100	20
CT12	PA	100	30

Table 3.3: Imaging factors and projections used for irradiating the phantom in SPR mode.			
Imaging protocol	Imaging projection	kV	mA
CT13	AP	80	10
CT14	AP	80	20
CT15	AP	80	30
CT16	PA	80	10
CT17	PA	80	20
CT18	PA	80	30
CT19	Lateral	120	10
CT20	Lateral	120	20
CT21	Lateral	120	30
CT22	Lateral	100	10
CT23	Lateral	100	20
CT24	Lateral	100	30
CT25	Lateral	80	10
CT26	Lateral	80	20
CT27	Lateral	80	30
To distinguish the AP imaging protocols with the scoliosis shawl from the AP imaging protocols without scoliosis shawl in the Chapter 4 (Results), the term (scoliosis shawl) was used with the codes.			

3.2.2.2 *Digital radiography*

The TLDs were prepared and placed inside the phantom at the university laboratory. Then, the phantom was transported to a local children's hospital to be irradiated by a radiographer at the hospital. The phantom was irradiated using a Digital Diagnost X-ray imaging machine (Philips Healthcare, Best, the Netherlands) (**Figure 3.13**) at 85 kV for AP and PA projections and at 90 kV for the lateral projection, with automatic selection of the mA value (**Table 3.4**). The SID was 180 cm. The primary radiation field was set to cover the same area imaged using CT SPR. As the area of interest was large, the imaging system automatically divided the acquisition into upper and lower regions; hence, two exposures were needed to capture the whole spine, which were digitally stitched together post-acquisition. The phantom was then transported back to the laboratory for the TLDs to be read out and prepared for the following irradiating cycle. In total, four irradiations took place at the hospital: AP without scoliosis

shawl, AP with scoliosis shawl, PA and lateral; also, similar to SPR, the phantom was irradiated three times in each irradiation.

Figure 3.13: The phantom positioned for DR imaging.

Table 3.4: Imaging factors and projections used for acquiring DR images.

Imaging protocol	Imaging projection	kV	mAs	DAP (µGy.m^2)
DR1	AP_1	85	5	6.67
	AP_2	85	16.9	15.77
DR2	PA_1	85	5.9	9.88
	PA_2	85	14.5	14.09
DR3	$Lateral_1$	90	5	8.61
	$Lateral_2$	90	11	10.39
DR1*	AP_1	85	5	6.65
	AP_2	85	17	15.86

$_1$ refers to the upper image; $_2$ refers to the lower image:* scoliosis shawl was used.

The acquisition parameters for DR were selected based on the local guidelines for imaging an average 10-year-old child. The DAP values shown in **Table 3.4** are below the suggested local diagnostic reference level (LDRL), which is 180 µGy.m^2 for imaging the whole spine for children from 9 to 11 years of age (The Christie, 2018). Nevertheless, the values could not be

compared with the UK national DRL because paediatric DRLs for the whole spine are not reported (Hart et al., 2010).

3.2.2.3 *EOS*

The TLDs were prepared and loaded into the phantom and transported to a children's teaching hospital for the scanning; the phantom was imaged using the EOS imaging system (EOS Imaging, Paris, France) (**Figure 3.14**) and with automatic exposure factors for an average 10-year-old child (**Table 3.5**). It was then irradiated by a radiographer at the hospital on three separate occasions in different positions: (1) in the AP and lateral projections simultaneously, (2) in the AP position and (3) in the lateral position. The irradiation was made using the micro dose protocol, and similar to using DR, the acquisition parameters for the EOS were selected based on the local guidelines for imaging a 10-year-old child. However, there are no published DRL values for using the EOS for imaging the whole spine, so a comparison with the DRL was not possible.

Figure 3.14: The phantom in the EOS imaging system.

Table 3.5: Imaging factors and projections used for acquiring EOS images.				
Imaging protocol	Imaging projection	kV	mA	DAP (μGy.m^2)
EOS1	AP *	75	200	10.003
	Lateral *	95	200	14.282
EOS2	AP	75	200	8.347
EOS3	Lateral	80	80	4.253
* Indicates that imaging projections were acquired simultaneously.				

3.2.3 Thermoluminescent dosimeter readings

After each irradiation, the phantom was disassembled in the university laboratory to remove the TLDs. The removal began with the head, where TLD number 1 had been placed: the slices were not detached from the phantom until all TLDs inside had been read. In addition, the TLDs were removed in order, beginning with TLD number 1 and ending with TLD number 198. The TLD reader is operated with software (WinREMS, Thermo Fisher Scientific) that saves the TLD numbers and their readings automatically to an Excel file (Microsoft, Redmond, WA, USA).

3.2.4 Data analysis

The readings of each imaging protocol of the three imaging machines were stored in separate Excel sheets. First, the background radiation was subtracted from TLD readings, and the results were averaged. Then, the values were multiplied by their corresponding calibration factors. The absorbed dose in each organ was calculated by adding the results read from the corresponding TLDs and then averaged. The absorbed dose was then multiplied by W_T and W_R to calculate the ED and ER, respectively. Data were tested for normality based on Shapiro-Wilk test, and *p*-values greater than 0.05 represented normally distributed data. To compare SPR with the other machines, the mean absorbed dose of each SPR imaging protocol was

compared with the DR and EOS imaging protocols using the *t*-test and SPSS v25.0 (IBM, Armonk, NY, USA). The comparisons were used to show significant differences among the imaging protocols in terms of radiation dose levels; $p < 0.05$ was considered to represent a significant result.

The consistency of the measurements (i.e. reliability) was evaluated using an ICC two-way mixed model (Rosner, 2016). The ICC demonstrates the degree of correlation and agreement between the measurements. ICC <0.5 indicates poor reliability, ICC from 0.5 to 0.74 indicates moderate reliability, ICC from 0.75 to 0.89 indicates good reliability and ICC >0.90 indicates excellent reliability (Portney and Watkins, 2000; Koo and Li, 2016).

3.3 Construction and validation of a phantom with scoliotic spine

The suitability of SPR images for assessing scoliosis were examined. To achieve this goal, an SPR image of scoliotic spine had to be acquired, and for ethical considerations, this could not be performed on a human. An alternative was to use an imaging phantom to acquire SPR images. Typically, such phantoms have a normal (i.e. without scoliosis) spine, which does not fit the purpose of the present research (i.e. assessing the degree of the curvature on SPR images). Another possible approach was to use a curved spine model (**Figure 3.15**) similar to that used by Chung *et al.* (2018). However, their phantom lacked soft tissue, meaning the effect of scatter radiation was missing. This study required a phantom that represented the spine of patients with AIS as closely as possible. Therefore, a novel phantom representing a 10-year-old female with AIS was designed and then constructed.

Figure 3.15: The phantom used by Chung et al. (2018).

3.3.1 Phantom design and construction

Due to the complexity of the internal tissues and their shape, it is not easy to simulate the human body. The human body contains several types of tissue that interact differently with X-ray photons. Therefore, a phantom to be used in diagnostic radiography applications should have materials with photon mass attenuation and mass absorption coefficients similar to that of human tissue (White and Constantinou, 1982; Watanabe and Constantinou, 2006). In the energy range used in diagnostic radiography (i.e. up to 150 keV), X-ray photons interact with the materials in two ways: the photoelectric effect and Compton effect (Aichinger et al., 2012; IAEA, 2014). These interactions are dependent on the materials' density (ρ), atomic number (Z), and photon energy (the Compton effect is independent of Z) (Allisy-Roberts and Williams, 2008). The phantom should also mimic the size and shape of the human body (Dewerd and Kissick, 2014).

According to ICRU Report 44, which addresses tissue substitutes in radiation dosimetry and measurement, several materials can be used as human tissue-mimicking materials. Examples of the soft tissue materials that have been used in radiography studies are water, urethane, poly (methyl methacrylate) (PMMA) and wax (Regulla et al., 1998; Sanada et al., 1999; D'Souza et al., 2001; Jones et al., 2003; Winslow et al., 2009; Caldas et al., 2011; Schropp et al., 2012; Mann et al., 2012; Farrer et al., 2015); examples of bone tissue-mimicking materials are polyvinyl chloride, aluminium and plaster of Paris (PoP) (Pina et al., 2009; Singh et al., 2014; Mohammed Ali et al., 2018). Air is widely used to simulate lung tissue (Vassileva, 2002).

The materials used for constructing the phantom were PMMA and PoP, representing soft tissue and bone tissue, respectively. The choice was based on the following: (1) PMMA is

commonly used as a soft tissue substitute in diagnostic radiology studies, especially for non-dosimetry phantoms (Lofthag-Hansen, 2010; Chung et al., 2010; Garcia et al., 2010; Barnes and Temperton, 2011; McCullagh et al., 2011; Koivisto et al., 2013; Chambers, 2014; Yvert et al., 2015; Sossin et al., 2017); (2) PMMA has similar physical properties to human tissues (**Table 3.6**), and it has a mass attenuation coefficient (μ/ρ) similar to that of soft tissue in the diagnostic energy range (Russo, 2014) (**Figure 3.16**); (4) PoP has been used medically as a bone tissue substitute (e.g. to fill in bone defects) (Sharma and Prabu, 2013), and its mass attenuation coefficient is similar to that of bone (**Figure 3.17**); and (5) PMMA and PoP are inexpensive and easy to use. The construction of the phantom consisted of two steps: (1) building a curved spine model to be used as a template for the phantom, and (2) constructing the remaining part of the phantom.

Table 3.6: Mean values of some of the physical properties of human tissue and PMMA (Hubbell and Seltzer, 2004).

Material	ρ (kg/m^3)	Z/mass ratio	Mean excitation energy (eV)
Human Tissue	1060	0.53937	74.0
PMMA	1190	0.5499	74.7

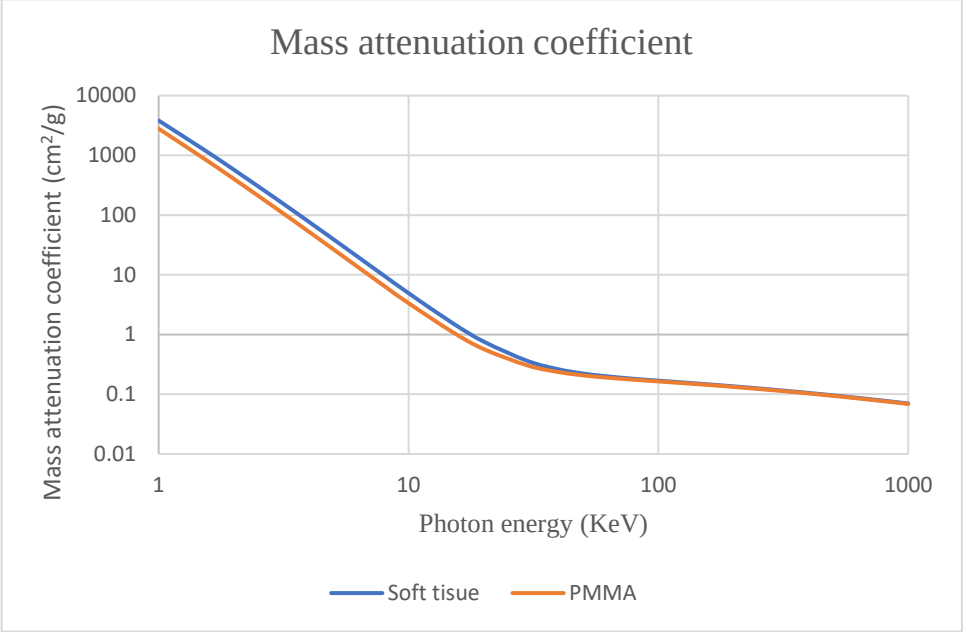

Figure 3.16: X-ray attenuation in soft tissue and PMMA (Hubbell and Seltzer, 2004).

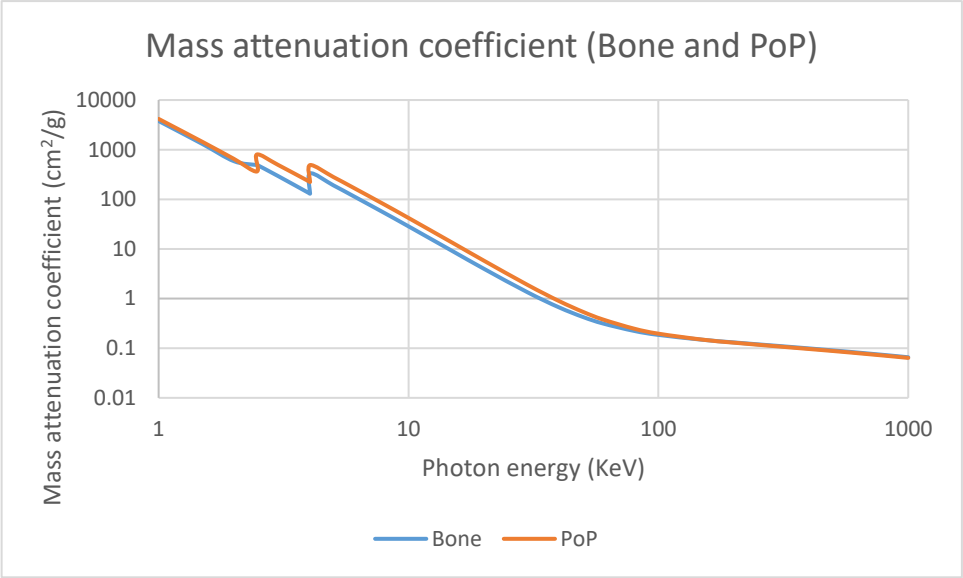

Figure 3.17: X-ray attenuation in bone and PoP (Hubbell and Seltzer, 2004).

3.3.1.1 *Building a template for the phantom*

The bony compartment of the spine was cut into PMMA slabs and filled with PoP. One of the simplest methods for building a phantom using these materials is using CT images as a guide to cut the bony compartments into the PMMA slabs (Jones, 2006; Harrison et al., 2011; Chan and Fung, 2015; Mraity, 2015; Mohammed Ali, 2019). As discussed earlier, CT images

provide accurate representation and measurements of the internal parts of the human body. However, CT images of AIS are lacking because CT scanning is not widely used for scoliosis assessment due to the higher radiation dose. Instead, a method was developed to create CT images of the scoliotic spine. This was achieved by bending a spine model, scanning it and then using the CT images as a guide for the cutting.

The spine model was of an adult life-size spine (**Figure 3.18**) and its vertebrae were mounted on an aluminium rod (**Figure 3.19**). The vertebrae were removed from the rod after they had been labelled to ensure that they were placed in the correct order. Another rod was bent in two steps to form the base of the scoliotic spine: (1) the normal concave and convex curves in the thoracic and lumbar regions, which were copied from the original rod; and (2) the lateral curve, which was made based on a calculation, as illustrated in the following section. The two steps were performed using standard bending irons.

Figure 3.18: Skeleton model used for educational purposes.

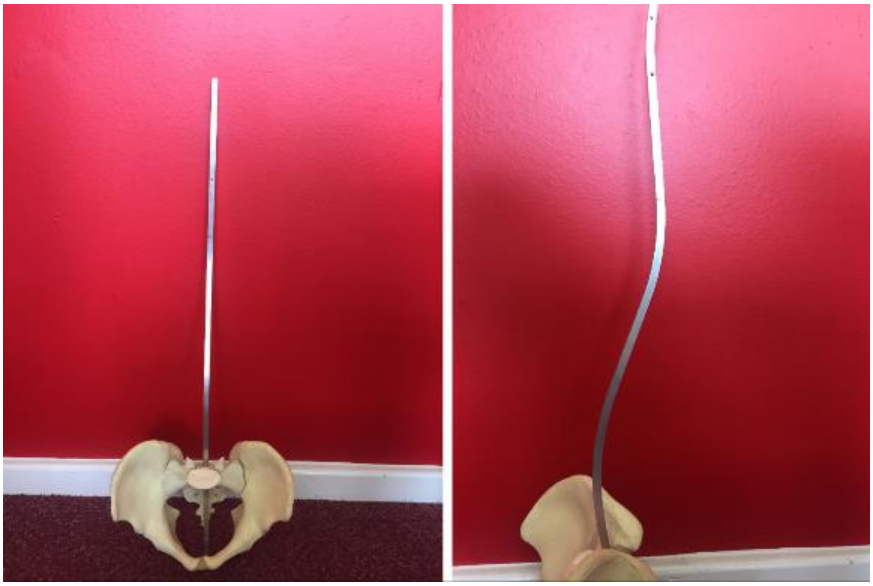

Figure 3.19: Aluminium rod in frontal (left) and lateral (right) views.

From the screen programs, summarised in (**Table 1.1** on **page 6**), the most common degrees of curvature in AIS are 10° to 20°. Consequently, 15° was selected as the degree of curvature on the phantom. To find the offset (A) between the aluminium rod when it is straight (representing a straight spine) and then bent (representing a scoliotic spine with angle [β] 15°) (**Figure 3.20**), the following calculations were performed:

1) Calculating the radius (R) of the circle that defines the curve of the scoliotic spine model:

$$R = \frac{C}{sin\,\alpha} \Rightarrow R = \frac{0.15m}{sin\,7.5^\circ} = 1.15m$$

2) Calculating Ɛ:

$$\text{Ɛ} = \delta - \gamma \Rightarrow \text{Ɛ} = \frac{180^\circ - \alpha}{2} - (180^\circ - 90^\circ - \alpha) \Rightarrow \text{Ɛ} = \frac{180^\circ - 7.5^\circ}{2} - (180^\circ - 90^\circ - 7.5^\circ) \Rightarrow \text{Ɛ} \approx 4^\circ$$

3) Calculating A:

$$\tan \text{Ɛ} = \frac{A}{C} \Rightarrow A = \tan \text{Ɛ} \times C \Rightarrow A = \tan 4^\circ \times 0.15m \Rightarrow A \approx 0.01m = 1cm\,.$$

Therefore, the rod was bent laterally by 1 cm (**Figure 3.21**). Next, the labelled vertebrae were mounted on the bent rod (**Figure 3.22**).

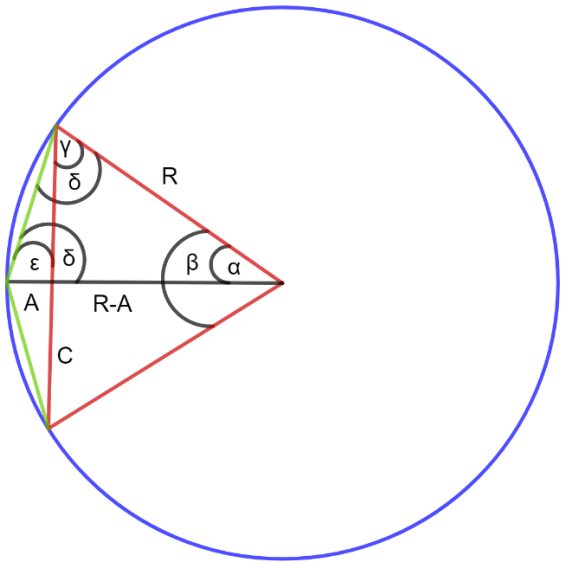

Figure 3.20: Diagram illustrating the amount of bending (A) needed to produce a scoliotic spine of angle (β) 15°.

Figure 3.21: The bent aluminium rod in frontal (left) and lateral (right) views.

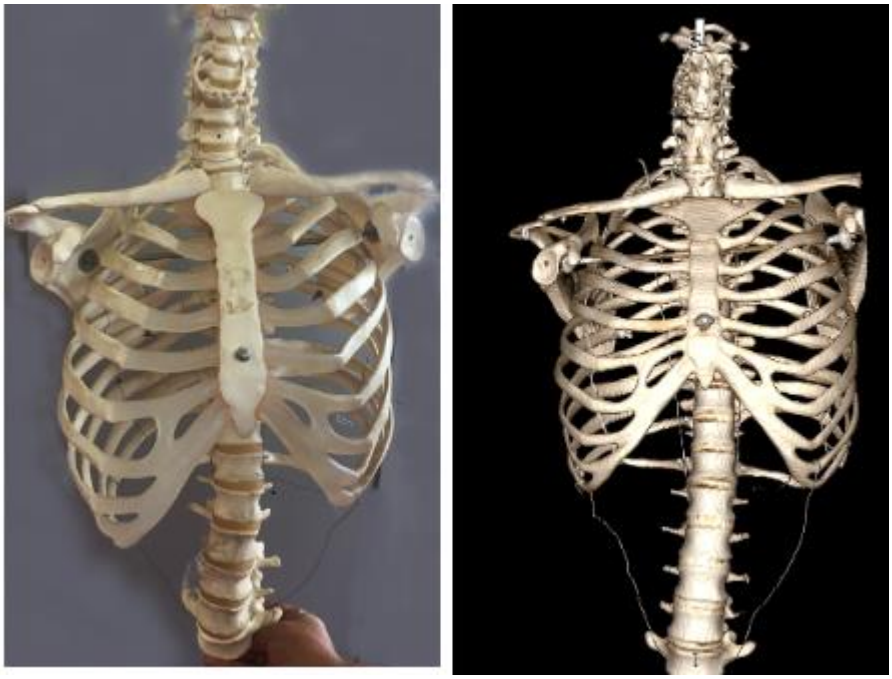

Figure 3.22: Left: the model with a bent spine; right: its 3D image.

3.3.1.2 *Designing the phantom*

PMMA slabs can be obtained in various dimensions. Accordingly, the craniocaudal length and the side to side width of the stack of slabs were chosen based on the size of an average 10-year-old girl: 50 cm and 25 cm, respectively. Two sizes were chosen for the thickness of the slabs: 2 mm and 10 mm, to be stacked together to form a total of 18 cm anterior to posterior thickness (the reason for choosing these thicknesses is discussed in the following paragraph). The phantom torso size was extracted from CT images of a 10-year-old girl. The images were anonymised, stored on an educational file at the Directorate of Radiography at the University of Salford and used for educational purposes, so no ethical approval was needed. The girl's chest and waist circumferences were 62 cm and 57 cm, respectively, which are within the anatomical reference data (ICRU, 1992; Mertz et al., 2001; ICRP, 2002; Kuba et al., 2013). Thus, the phantom would be used to represent an average 10-year-old girl.

The phantom was designed for Cobb angle measurements on SPR images; therefore the AP/PA view of the phantom could be acquired to perform the measurements. This had an important influence on designing the phantom, because constructing the phantom based on axial or sagittal CT images would have resulted in image artefacts. The air gap between the slabs would appear as black lines in the SPR images; therefore, the phantom was designed based on coronal images of the bent phantom as used previously (Harrison et al., 2011; Mohammed Ali et al., 2018). Another factor that influenced the design of the phantom was the thickness of the slabs; the chosen thicknesses were 2 mm and 10 mm: the thinner slabs were used in the spine area to maintain finer anatomical detail, and the thicker slabs were used for the remaining areas of the phantom to speed up construction and where finer anatomical detail was not present and thus not needed.

With the phantom design ready, the next step was to acquire CT images of the bent-spine phantom, which was scanned using the same CT scanner used for the dose measurements. The image orientation was adjusted to coronal images, and two sets of images based on the desired thickness were produced: 2 mm and 10 mm. As stated earlier, the bent-spine phantom had adult vertebrae; therefore, the images were scaled to match the vertebrae size of a 10-year-old girl (approximately 2 cm long and 4 cm wide) to ensure that the phantom was as close a representation of a 10-year-old girl as possible. After obtaining the required vertebrae size, the images were printed on A3 paper (29.7 cm × 42 cm). Each image was then aligned to its corresponding PMMA slab, and the details were drawn onto the slabs (**Figure 3.23**).

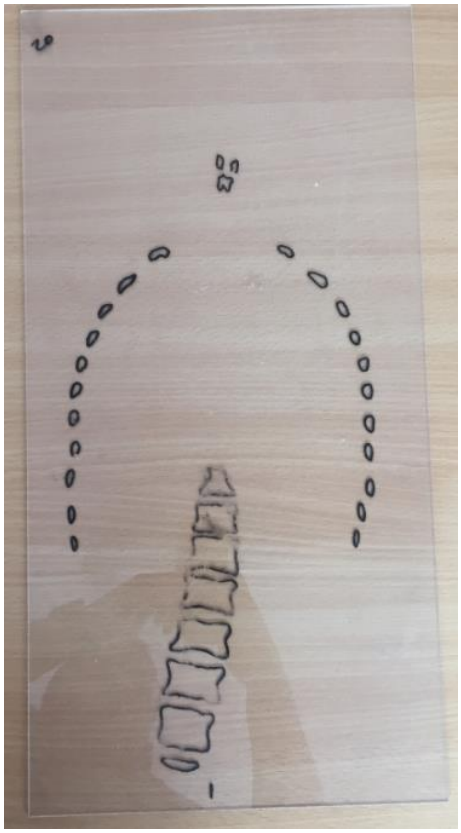

Figure 3.23: An example of a pre-drilled PMMA slab, with the shape of the lower vertebrae and ribs.

The next step was to cut the shape of the bony compartment into the slabs. The cutting was performed manually with a hand milling machine (**Figure 3.24**). After cutting the vertebrae and the lung shapes, the slabs were combined with each, every three, four or five adjacent slabs, depending on the formed shape. The edges of the drilled shapes in the combined slabs were smoothed; this ensured that the holes in the slabs were connected and improved the accuracy of the anatomical shape (Mohammed Ali, 2019). After smoothing the edges of the combined slabs, the slabs were placed together for further smoothing. Finally, each slab was marked at common points in two corners (opposite corners) to be drilled for plastic screws to hold the slabs together. Additionally, a space was drilled into the slabs in the middle of the phantom at the level of the lumbar spine to house a sheep vertebra to be used in the validation of the phantom. This particular animal vertebra was chosen because it shares some structural features with a human vertebra and can be used as an alternative to a human vertebra in

radiographic research (Sheng et al., 2010). The sheep vertebra was acquired from a local abattoir; thus, no ethical approval was required as the animal had been slaughtered for human consumption.

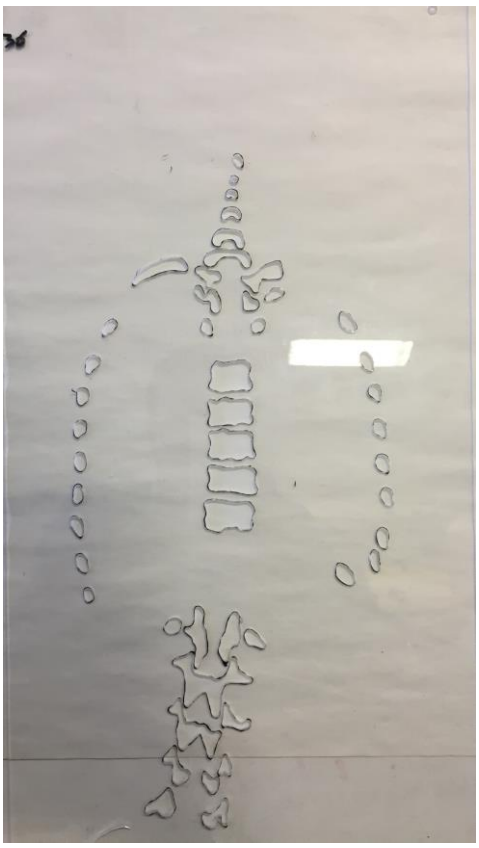

Figure 3.24: The bony compartments of the ribs and spine cut in slab #36.

After cutting the bony compartments in the slabs, the cavities were filled with PoP to simulate the bone tissue. PoP is a dry powder and must be mixed with water to form a workable paste. However, the water-to-plaster ratio affects its density; more water makes the paste less dense (Madu et al., 2016; Mohammed Ali et al., 2018). To identify the ratio that produces a paste with radiological properties similar to the vertebrae of a 10-year-old girl, several mixtures with different ratios were made and scanned with a CT scanner, while they were drying for 14 days (Table 3.7). CT scan images were used to calculate the attenuation coefficients of the mixtures using Hounsfield units (HUs) (Homolka et al., 2002; Homolka and Nowotny, 2002;

Gücük and Uyetürk, 2014). Three samples of each mixture were made to ensure the accuracy of the density. The 14-day period is required for the water to escape from the paste at room temperature and for its density become constant, as determined by Mohammed Ali *et al.* (2018).

Table 3.7: Water-to-plaster ratios used to identify the correct density.

Batch	Sample	Water (ml)	Plaster (g)
1	1	20	50
	2	30	50
	3	40	50
2	1	42	50
	2	44	50
	3	46	50
	4	48	50

The attenuation coefficients of the 10-year-old girl's vertebrae was extracted from the CT images. The vertebrae consist of two types of bone tissue: trabecular and cortical. The latter is denser and forms the endplates of the vertebra, and because the Cobb angle measurement is performed using the vertebral endplates, the HU of the girl's vertebral endplates was calculated and found to be 598 (*SD* = 79) (**Figure 3.25**). The HU of the water-to-plaster ratio of 48:50 was the closest to that of the 10-year-old girl's vertebrae. Prior to irradiating the PoP samples, the CT scan was checked for the accuracy of HUs, and the results were within the acceptable tolerance (CEC, 1996a; Cropp et al., 2013)

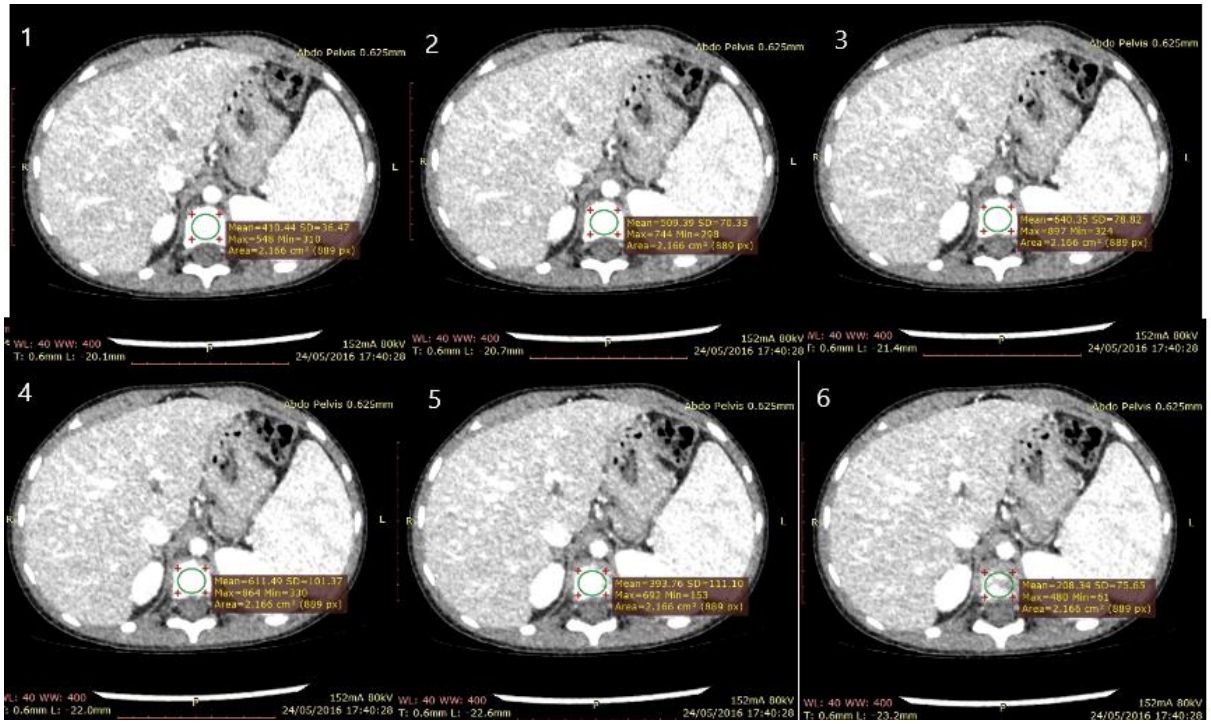

Figure 3.25: A series of CT slices shows the variation in the density of a vertebra. The series starts from the top left at image 1 and ends at the right bottom at image 6; images 4 and 5 are at the edge of the vertebra.

Two adjacent slabs were combined in preparation for the PoP filling. The combined slabs were weighted to ensure that the PoP would not go between the slabs. The PoP powder had been prepared in small cups in 50-g portions (**Figure 3.26**); water was added only when the portion was about to be used for filling. After the water was added, the mixture was stirred until the desired consistency was obtained just when it was about to solidify. It was not practical to use a loose mixture because it would go between the slabs even with pressure applied on the combined slabs. The mixture was then poured into the cavities and pushed inside them to ensure that the cavity areas were entirely filled. Then, the mixture was flattened, and the excess was removed. Finally, the PoP was left to dry for 6 days before HU monitoring began. During this process, a problem was encountered; the PoP was not drying at the anticipated rate because the slabs of the phantom had been combined, which prolonged the drying period before the phantom would be ready for the experiments. Therefore, the phantom was disassembled and left to dry; the phantom was reassembled only to be scanned. The PoP

had dried by around day 25; however, it was left for more than one month to ensure that it was completely dry, before commencing imaging (**Figure 3.27**).

Figure 3.26: The PoP was prepared in small cups.

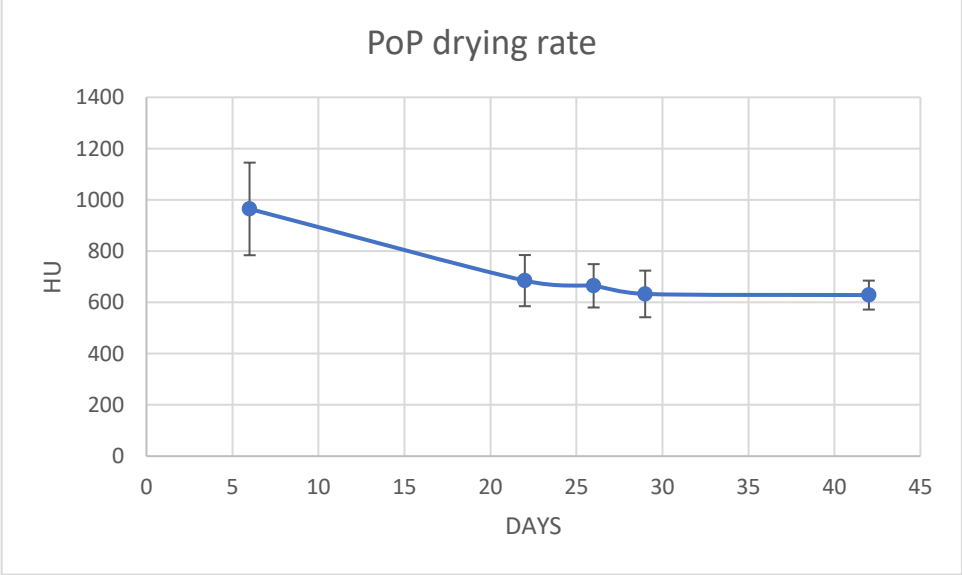

Figure 3.27: Drying rate of PoP after being poured into the phantom.

3.3.1.3 *Validation of the phantom*

The phantom was built to provide a tool for measuring the Cobb angle on SPR images. However, before experiments could be carried out on the newly constructed phantom, it had to be validated for representing the human body and fulfilling the purpose for which it had been designed. This included comparing the density of the phantom's spine with that of the 10-year-old girl and the sheep vertebra. It also included comparing the phantom's pixel values with those of a commercially available phantom (with a normal spine) to ensure that the constructed phantom delivered a similar response.

The HU of the simulated bone and PMMA in the PoP phantom were compared with the spine and the soft tissue of the 10-year old girl, respectively. The comparison was made using the HU because it shows the attenuation characteristic of materials. The HU is an accepted measure for identifying the density of materials (Homolka and Nowotny, 2002; Mattsson and Thomas, 2006). The phantom was scanned using CT and the acquisition parameters used were similar to those used to scan the girl because the HU is affected by the quality of the radiation (i.e. kV) (Zurl et al., 2014). In addition to the density, bone homogeneity was evaluated using the *SD* of the HU values. All HU measurements were performed using RadiAnt image viewing software v4.6.9 (Medixant, Poland) (**Figure 3.28**).

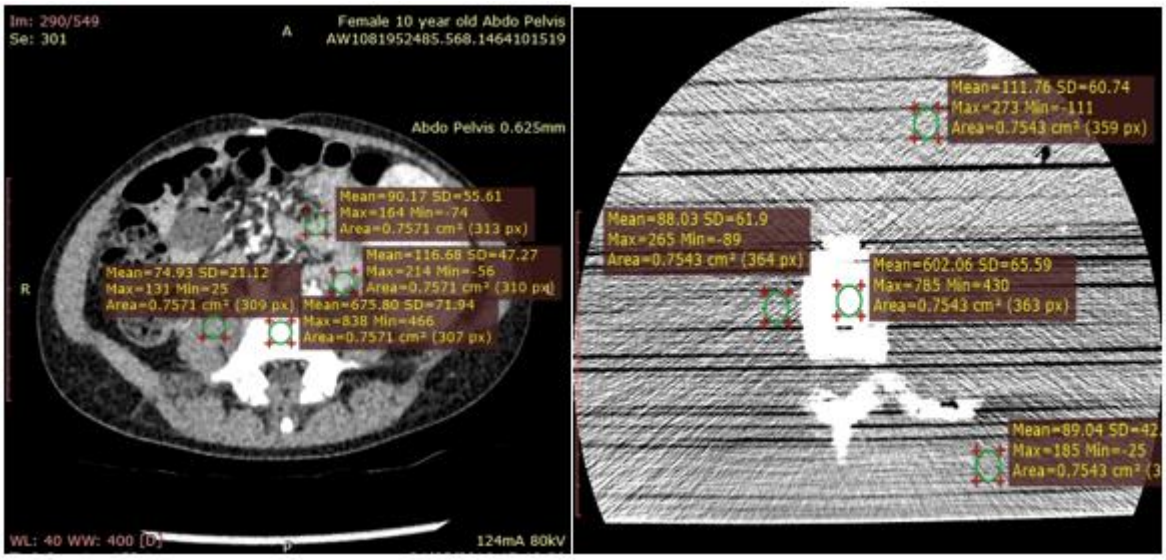

Figure 3.28: HU measurements on the 10-year old girl image (left) and PoP phantom (right).

The other measure used to validate the phantom was pixel values. Here, the signal and noise level in the phantom's images were compared with that of a commercially available and validated phantom: a multipurpose anthropomorphic chest phantom (Lungman; Kyoto Kagaku Co., Kyoto, Japan). This phantom represents a male chest torso and has an embedded portion of a synthetic spine (i.e. epoxy resin) that is similar to human bone (Dewerd and Kissick, 2014). The images of the two phantoms were acquired with an Aero DR system (Konica Minolta Medical Imaging, Ramsey, NJ, USA) using a range of kV and mA values (**Table 3.8**). The kV values were selected based on local diagnostic reference figures, and the selected range of mAs values would cover the possible values of automatic exposure control when irradiating a 10-year old child.

Table 3.8: The variation of kV and mAs values used to acquire the two phantom images for SNR calculation.	
kV	mAs
75	1
80	2
85	3.2
90	4
95	5
100	6.3
105	7.1
110	8
115	9
120	10
	11
	12.5
	14
	16
	18
	20

For SNR calculation, the post-processing of the acquired images was set to quality control to avoid any manipulation in the pixel values. SNR was calculated using ImageJ (Rueden et al., 2017). The average pixel values (i.e. the signal) of several vertebrae and the noise were calculated from the background (**Figure 3.29**). The ROI used for the calculation had a similar size and location for all images. The SNR was calculated as the ratio of singles to noise (Smans et al., 2010).

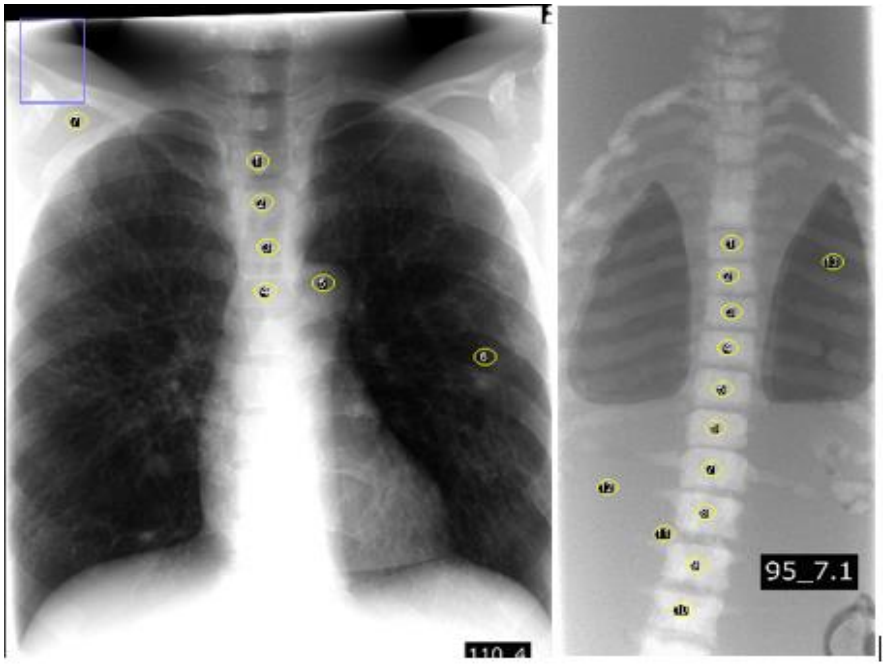

Figure 3.29: ROI used to calculate SNR; Lungman (left) and PoP phantom (right).

In addition, the appearance of the spine and its vertebrae of the PoP phantom (**Figure 3.30**) was compared against CT based date of a 10-year old female patient (**Figure 3.31**). The images of the PoP phantom and the patient were reconstructed using RadiAnt image viewing software v4.6.9 (Medixant, Poland). The comparison was made against a normal spine and only with the lumbar vertebrae and part of the thoracic vertebrae due to the lack of CT image of an entire spine. As mentioned previously, the images of the 10-year old female were anonymised, stored on an educational file at the Directorate of Radiography at the University of Salford and used for educational purposes, so no ethical approval was needed. An AP view of the PoP was compared with an AP image of a 10-year old female patient with AIS as shown in **Figure 3.32**. Lastly, the Cobb method was performed directly on the phantom. This was possible because the PMMA is transparent and the PoP vertebrae were visible. The reason for performing the measurement on the phantom was to confirm that the spinal curvature angle was 15°.

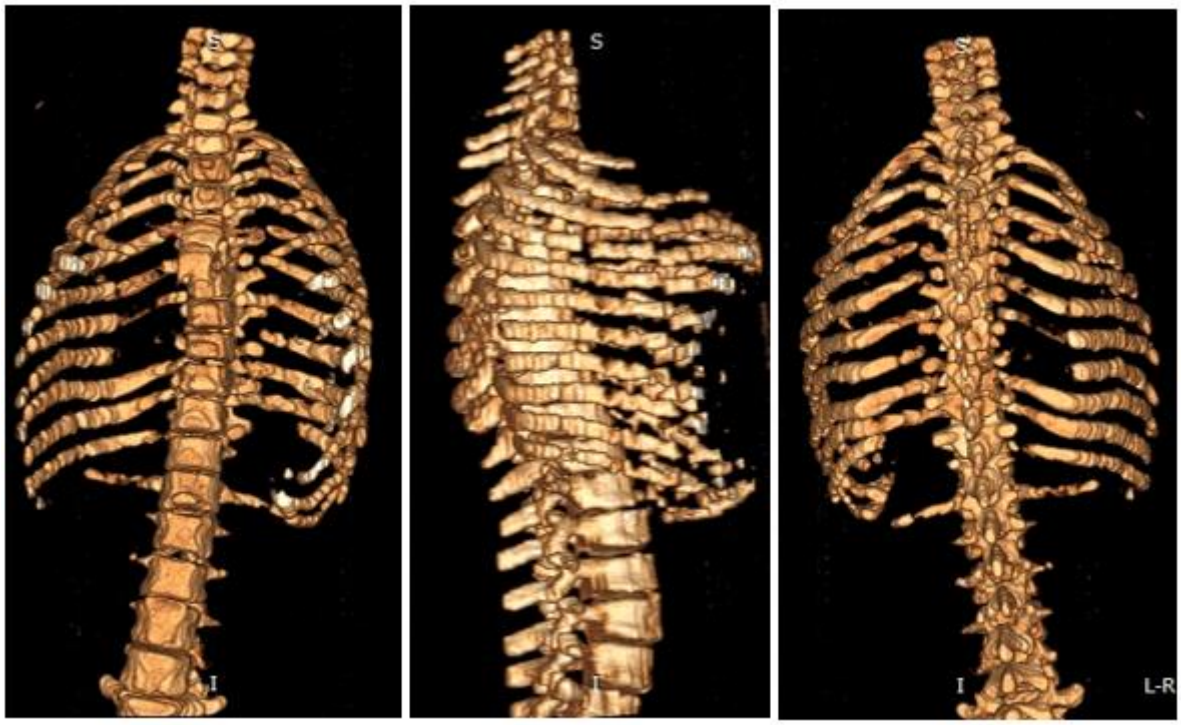

Figure 3.30: 3D images of the PoP phantom: AP view (left), lateral view (middle) and PA view (right).

Figure 3.31: 3D images of the abdominopelvic region of a 10-year old female patient: AP view (left), lateral view (middle) and PA view (right).

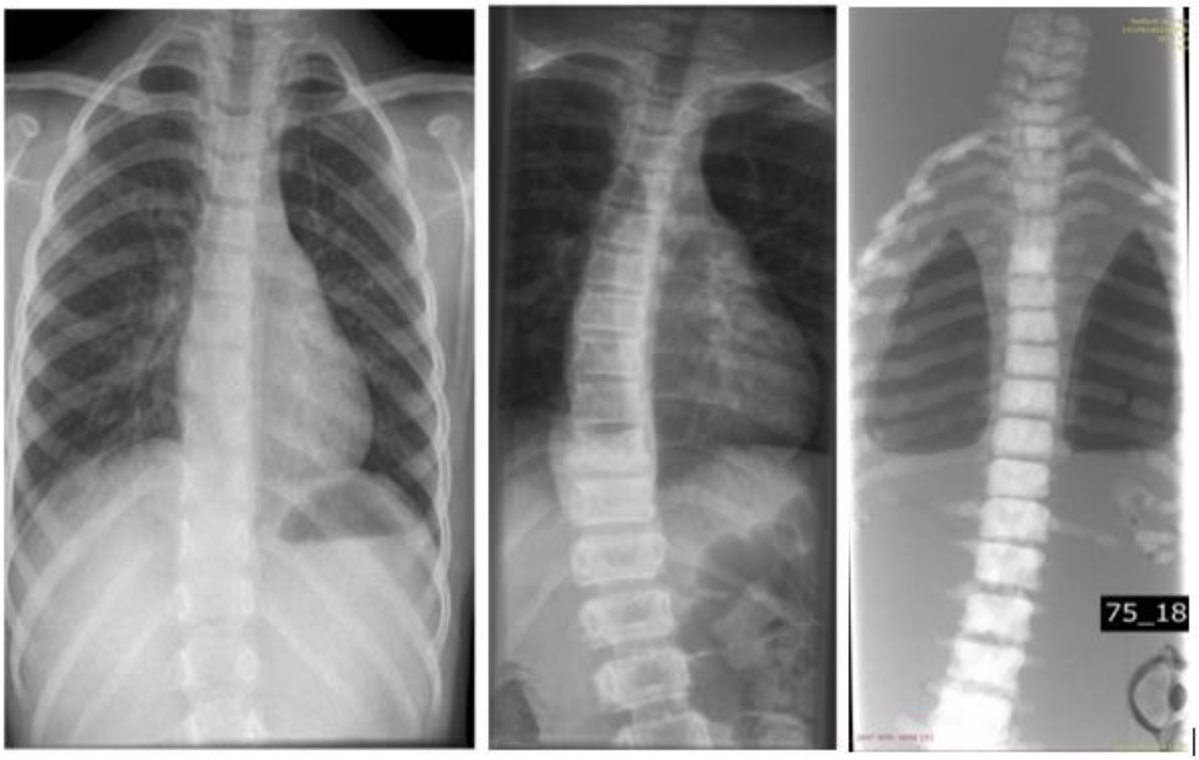

Figure 3.32: AP view images of the spine: a 10-year-old female patient with no sign of AIS (left), AP view image of a 10-year old with AIS (middle) and AP view image of the PoP phantom (right). Patients images were adopted from Deogaonkar *et al.* (2008).

3.3.2 Initial visual evaluation of the PoP phantom images to determine suitability for inclusion in Cobb angle analysis

The PoP phantom was scanned in SPR mode in the CT using the imaging parameters applied for the dose measurements (**Table 3.3** on **page 84**). As the images were intended for Cobb angle measurements, only AP and PA projections were acquired; additionally, the design of the phantom did not permit lateral images (**Figure 3.33**). In total, 18 SPR images were acquired. Each image was assigned a code so that, when evaluated later, observers would be blinded to the imaging parameters.

Figure 3.33: The PoP phantom on the CT table.

As discussed earlier, Cobb angle measurements depend on locating the endplates of the most tilted vertebrae. Therefore, the 18 images were inspected visually to determine the eligibility of an image for Cobb angle measurements. A 5-megapixel monochrome reporting monitor (DOME E5; NDSsi, Santa Rosa, CA, USA), calibrated in accordance with Royal College of Radiologists (RCRs) guidelines (RCRs, 2019), was used for the evaluation. Two radiographers with at least two years' experience and two medical physicists with experience in evaluating medical images through their work in radiation dose optimisation evaluated the clarity of the endplates based on the European guidelines on quality criteria for diagnostic radiographic images (CEC, 1996b). The guidelines recommend evaluating seven areas in the region; however, these criteria are not specific for scoliosis imaging, but for spine images in general. Therefore, most of the areas are irrelevant to Cobb angle measurement, which was the purpose of constructing the phantom. Consequently, the observers were asked to evaluate the appearance of the upper and lower endplates of all vertebrae in the images. The evaluation involved a strict scale similar to that used by AlQaroot (2012): if an endplate was not clear in the image, then the entire image would be marked as illegible for Cobb angle measurements. Ultimately, only images that had been marked as eligible for measurement by the four

observers were selected for the next stage. The use of the strict scale ensured that only images with good quality for Cobb angle measurements were selected. Ethical approval was obtained from the university for this evaluation (HSR1718-104).

3.3.3 Data analysis

SNR values were tested for normality based on the Shapiro-Wilk test, and *p*-values greater than 0.05 represented normally distributed data. The relationship between the SNR values of the PoP phantom and the Lungman phantom was analysed using Pearson's correlation test (r) for normally parametric data and Spearman's test (ρ) for non-parametric data. A correlation coefficient <0.20 is considered very weak, 0.20 to 0.39 is weak, 0.40 to 0.59 is moderate, 0.60 to 0.79 is strong and 0.80 or greater is a very strong correlation (Evans, 1996). ICC was used to analyse the agreement between the observers, who evaluated the SPR images visually.

3.4 The task: Cobb angle measurements

Thirteen observers (seven radiographers and six orthotists) were invited to perform Cobb angle measurements on the 5-megapixel monochrome reporting monitor (DOME E5, NDSsi). The monitor had been calibrated in accordance with the RCRs guidelines (RCR, 2019). The Cobb angle was measured digitally using RadiAnt image view software v4.6.9 (Medixant, Poland) to simulate the clinical environment. The observers' level of experience varied: the radiographers had at least two years' experience; however, four of the orthotists were mostly prosthetics and orthotics students, and their experience ranged from low (year-one students) to students who had practiced the measurement in a hospital (year-three students), and two were academics. The reason for choosing radiographers and orthotists is that in clinical practice, Cobb angle measurements are performed by orthotists. Moreover, orthotists and radiographers have done the measurements in previous studies (Shea et al., 1998; Cheung et al., 2002; Gstoettner et al., 2007; Shaw et al., 2012; Melhem et al., 2016; Vavruch and Tropp, 2016; Chung et al., 2018). The level of experience also varied among the observers; however, this should not have had an impact on the accuracy of Cobb angle measurements as mentioned in **Section 2.5.1.3** on **page 50**. Nevertheless, all observers were given the same half-hour training session to ensure that they were familiar with the measuring software and, importantly, how to place 'lines' on the image in order to calculate the Cobb angle.

In the training sessions, which were delivered individually to each observer before the Cobb angle was measured, the basic concepts of the Cobb method were explained, and the observers were familiarised with the software. One important part of the Cobb method is identifying the most tilted vertebrae; therefore, the observers were trained to identify the most tilted vertebrae. To do so, the observers had to select all possible tilted vertebrae and perform the Cobb method on each two vertebrae. For example, if they selected T5, T6 and T7 as the

possibly most tilted superior vertebrae, and L1, L2 and L3 as the possibly most tilted inferior vertebrae, they had to perform the angle measurements nine times as follows: T5 and L1, T5 and L2, T5 and L3, T6 and L1, T6 and L2, T6 and L3, T7 and L1, T7 and L2, and T7 and L3. Then, the measurements were compared, and the pair of vertebrae with the highest angle value was selected as the most tilted vertebrae. This step was introduced to increase the accuracy of the measurements and to ensure that the most tilted vertebrae were selected. The second part of the training session was to perform the measurements on two conventional radiography images of patients with AIS that had been downloaded from an online library and anonymised (Science Photo Library Limited, 2018). After finishing the training session, the observers were asked to determine the degree of the curve in the images of the PoP phantom. The observers were blinded to the imaging parameters, and the vertebrae in the images were numbered so that the observer could track their progress easily. The measurements were performed once in an attempt to reflect clinical practice and increase the validity of the outcomes. All measurements from the training session and the actual measurement were recoded. The university had granted ethical approval for this study (HSD1718-104).

3.5 Data analysis

The number of observers (N = 13) needed for the study was determined using G*power (Faul et al., 2007), with 90% power to detect the difference from a constant with α-error of 5%. The agreement between the observers' Cobb angle measurements was analysed using ICC.

3.6 Chapter summary

This chapter details the method used to test the suitability of SPR images for assessing AIS. First, a dosimetry phantom, representing a 10-year-old child, and TLDs were used to quantify

the radiation dose levels of the SPR mode in CT when used for assessing scoliosis. The amount of radiation was compared with the dose levels from the commonly used scoliosis assessment imaging machines, DR and EOS. Then, the building and validating of a novel phantom with a scoliotic spine were described. Finally, the accuracy of Cobb angle measurements was assessed using SPR images of the PoP phantom.

Chapter 4: Results

4.1 Chapter overview

This chapter reports the results of the experiments carried out to investigate the possibility of using SPR imaging for assessing AIS. It is divided into three sections to correspond with the sections in Chapter 3 (Methods and material). In the first section, the SPR radiation dose levels are analysed and compared with those of DR and EOS. The second section presents the findings of the building and validating of a novel phantom with a scoliotic spine. In the last section, the accuracy of Cobb angle measurements using SPR images is reported.

4.2 Radiation dose measurements

This section reports the finding of the dose measurement experiments that were carried out to quantify the radiation dose from SPR, DR and EOS when used to assess AIS. It reports the organ dose (OD) values (i.e. TLD readings for the evaluated organs) for SPR with and without using the scoliosis shawl. Then, it compares them to the OD values of DR and EOS. This is followed by the ED and ER from using SPR, DR and EOS to assess AIS, respectively.

4.2.1 OD for SPR exposures

As a quality control step, the reliability of the dose measurements was assessed by irradiating the phantom three times at one-week intervals using the same projection and imaging factors. **Table 4.1** shows the results of the repeated exposures. The assessment revealed a high level of consistency for the method used for measuring OD with ICC value of 0.994 (p <0.001).

Table 4.1: OD values (mGy) of the reliability test results that was performed using SPR.					
Organs	First scan	Second scan	Third scan	Average	*SD*
Thyroid	0.279	0.237	0.244	0.253	0.022
Oesophagus	0.178	0.156	0.153	0.162	0.014
Lungs	0.105	0.087	0.094	0.095	0.009
Breasts	0.073	0.066	0.066	0.068	0.004
Liver	0.156	0.121	0.132	0.136	0.018
Stomach	0.119	0.086	0.111	0.105	0.018
Bladder	0.198	0.138	0.165	0.167	0.030
Colon	0.153	0.106	0.106	0.121	0.027
Ovaries	0.032	0.028	0.028	0.029	0.002
Salivary Glands	0.003	0.002	0.003	0.003	0.000
Thymus	0.430	0.392	0.391	0.405	0.022
Spleen	0.057	0.033	0.046	0.045	0.012
Kidneys	0.042	0.028	0.032	0.034	0.008
Adrenals	0.071	0.050	0.054	0.058	0.011
Heart	0.257	0.246	0.241	0.248	0.008
Pancreas	0.178	0.107	0.145	0.144	0.036
Gall Bladder	0.075	0.049	0.041	0.055	0.018
Uterus	0.036	0.029	0.030	0.032	0.004
Oral Mucosa	0.005	0.004	0.005	0.005	0.000
Small Intestine	0.199	0.130	0.170	0.166	0.035
Extrathoracic Region	0.199	0.130	0.170	0.166	0.035

Figure 4.1–**Figure 4.5** show the OD values for the critical organs (thymus, breasts, heart, thyroid and stomach) of the phantom that represent a 10-year-old child without using the scoliosis shawl. The figures present the data in terms of the imaging projections and acquisition parameters that were used to irradiate the phantom in order to illustrate the changes in the OD values as these factors change. The data in the figures are sampled from the overall OD data. The figures show the OD values of the most radio sensitive organs (i.e. the breasts and thyroid) and the other organs that received the highest radiation dose, which are the thymus, heart and stomach. All the OD data are presented in **Tables I-III** on **pages 186-188**. The highest measured OD values were 0.480 mGy (thymus), 0.436 mGy (breasts), 0.369 mGy (heart), 0.359 mGy (thyroid) and 0.344 mGy (stomach).

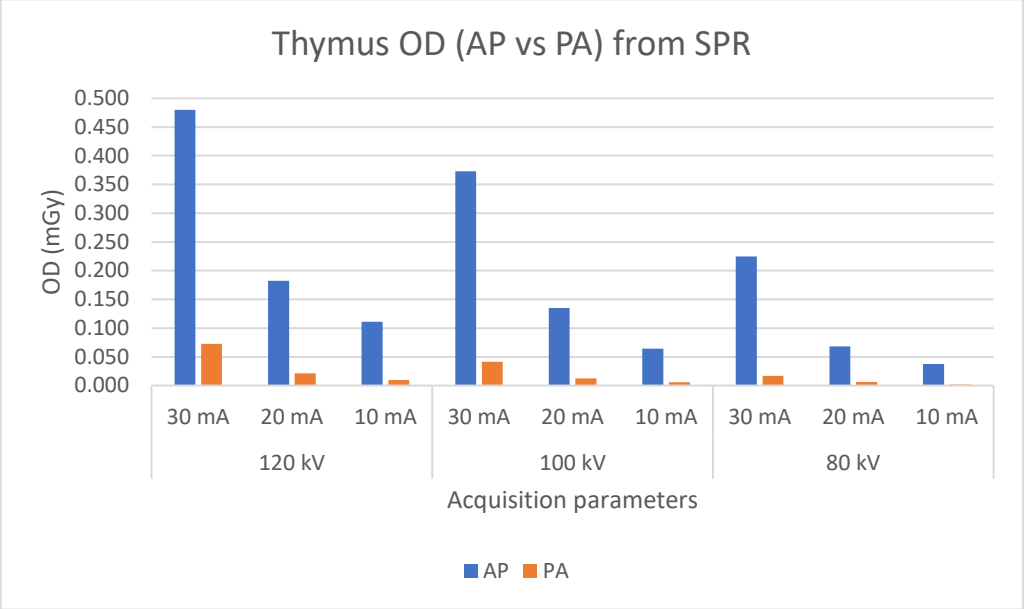

Figure 4.1: The thymus OD from different SPR imaging protocols.

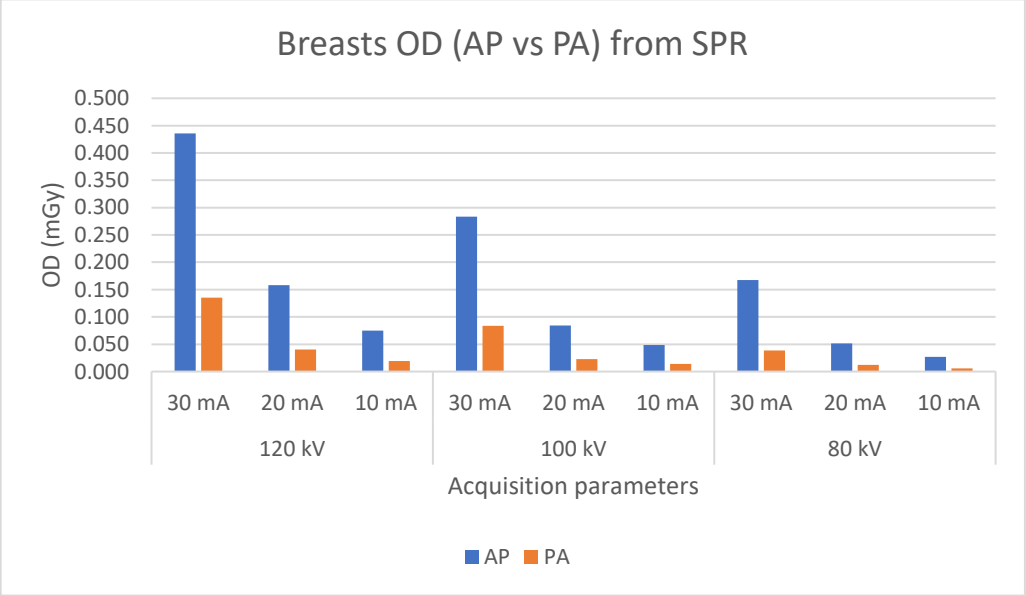

Figure 4.2: The breasts OD from different SPR imaging protocols.

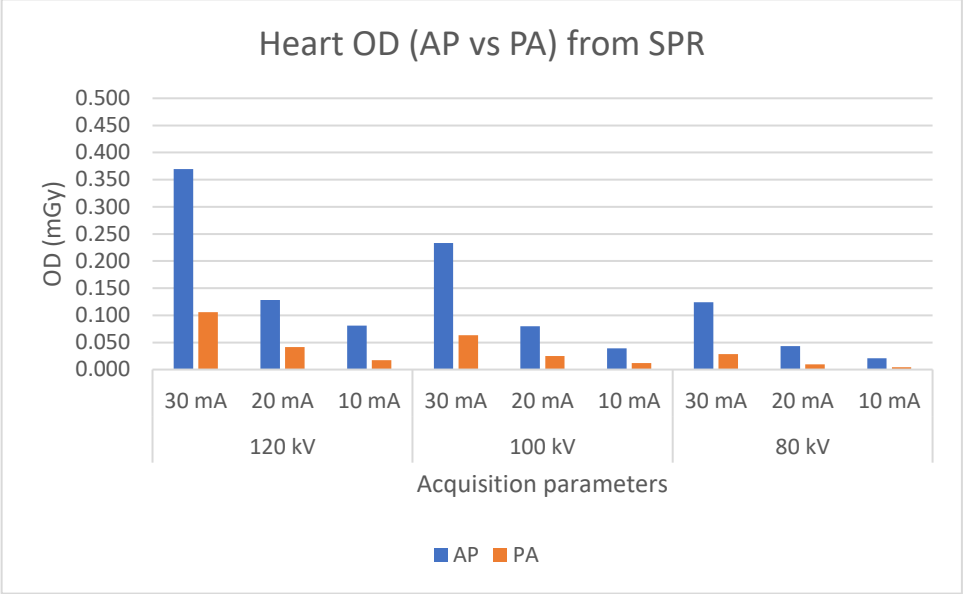

Figure 4.3: The heart OD from different SPR imaging protocols.

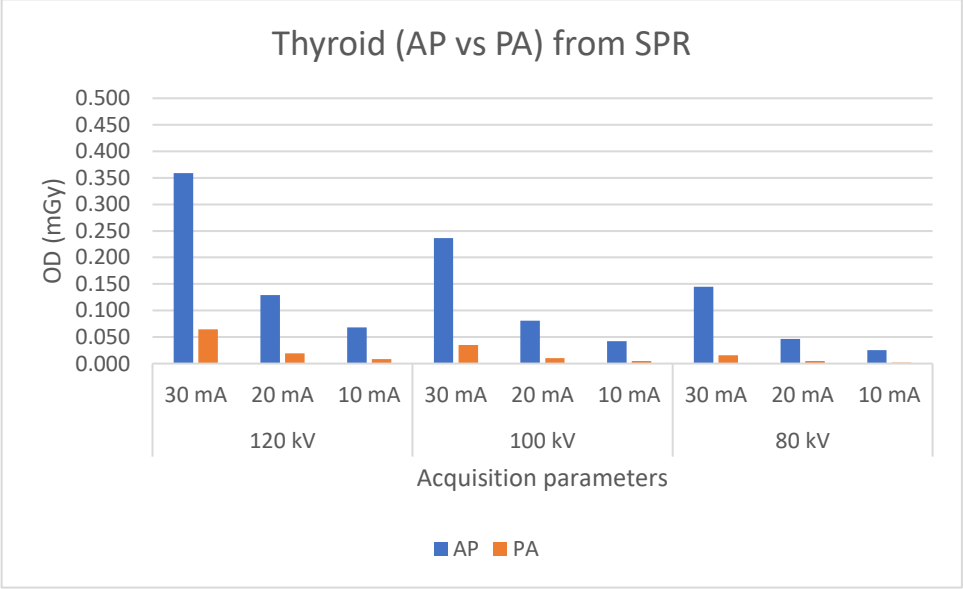

Figure 4.4: The thyroid OD from different SPR imaging protocols.

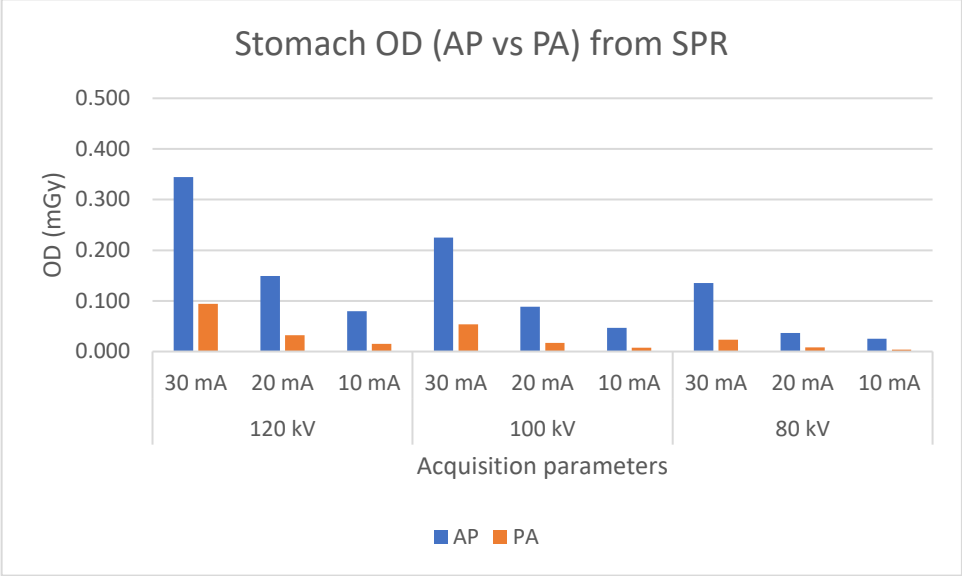

Figure 4.5: The stomach OD from different SPR imaging protocols.

There was a significant difference among the OD values for all imaging protocols between AP and PA ($p < 0.05$). The OD for most organs was lower in PA than in AP. In line with expectations, organs closer to the X-ray tube received a higher dose compared with organs that were farther away. For example, based on the imaging protocol, the breasts received, on average in the AP projection, 0.148 mGy (*SD* = 0.134, range 0.027 to 0.436 mGy) and in the PA projections, 0.041 mGy (*SD* = 0.042, range 0.006 to 0.135 mGy) (**Figure 4.2**); that was, on average, a dose that was 73.78% (*SD* = 3.05) higher in the AP projection compared with the PA projection (**Figure 4.2**). The kidneys, on the other hand, received, on average in the PA projection, 0.086 mGy (*SD* = 0.078, range 0.016 to 0.256) and in the AP projection, 0.036 mGy (*SD* = 0.031, range 0.005 to 0.101) (**Figure 4.6)**, which is a dose that was 58.20% (*SD* = 10.98) lower in the AP projection compared with the PA projection.

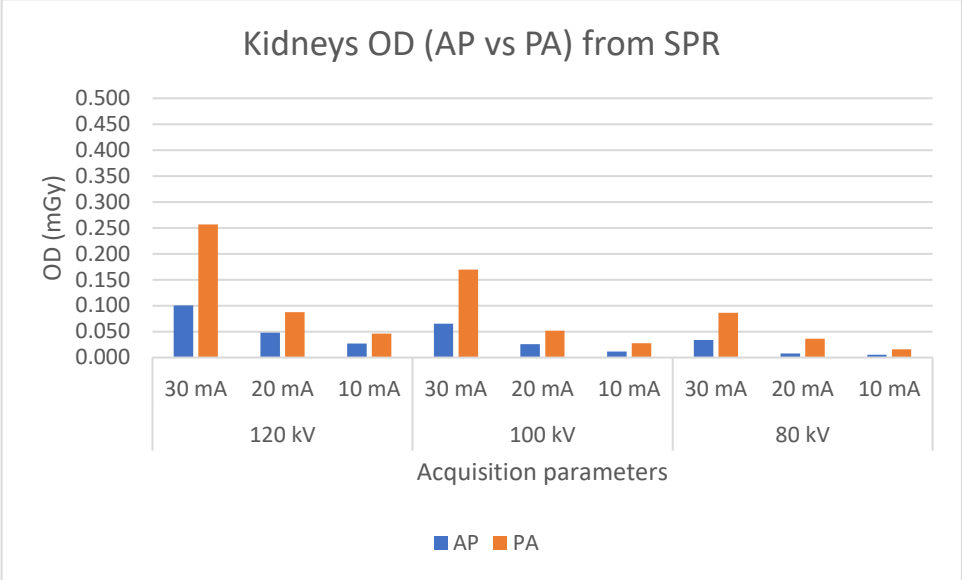

Figure 4.6: The kidneys OD from different SPR imaging protocols.

Organs located outside the primary beam while irradiating the phantom received fewer photons, as expected compared with the organs inside the primary beam. For example, the brain, eyes and testes, each received, on average, 0.001 mGy (*SD* = 0.0001 [brain], 0.0005 [eyes], and 0.0009 [testes]) when using imaging protocol CT 3 (AP, 120 kV, 30 mA), which as shown later in **Table 4.8**, is the SPR imaging protocol that had the highest effective dose compared with the other imaging protocols. **Figure 4.7** shows the OD of several organs inside and outside the primary beam to illustrate the difference in dose levels among these organs.

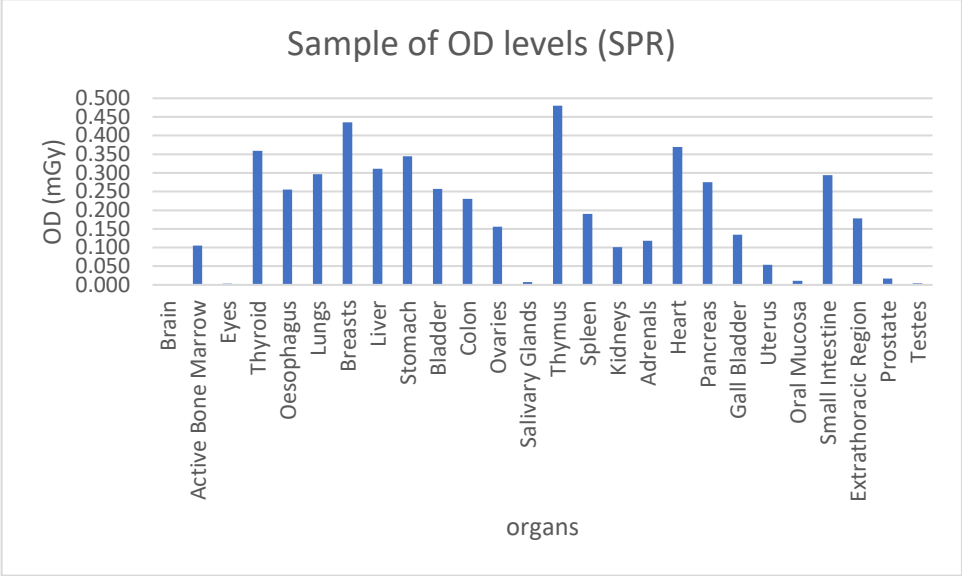

Figure 4.7: The OD levels of several organs when using CT 3 imaging protocol, which had the highest ED (as will be discussed later in section 4.2.2 on page 136).

The OD values from lateral projection radiation were low compared with those of AP and PA projections. The highest measured OD of lateral projection was 0.135 mGy, which represented the amount the spleen received when using imaging protocol CT21 (lateral, 120 kV, 30 mA). The breasts received, on average, 0.028 mGy (*SD* = 0.017) (range 0.006 to 0.061 mGy). **Figure 4.8** and **Figure 4.9** show the OD levels of the spleen and breasts, respectively, of lateral projection imaging when using SPR. The data in the figures are presented in term of the acquisition parameters. All the OD data of the remaining organs of lateral projections are presented in **Table V** on **page 189**.

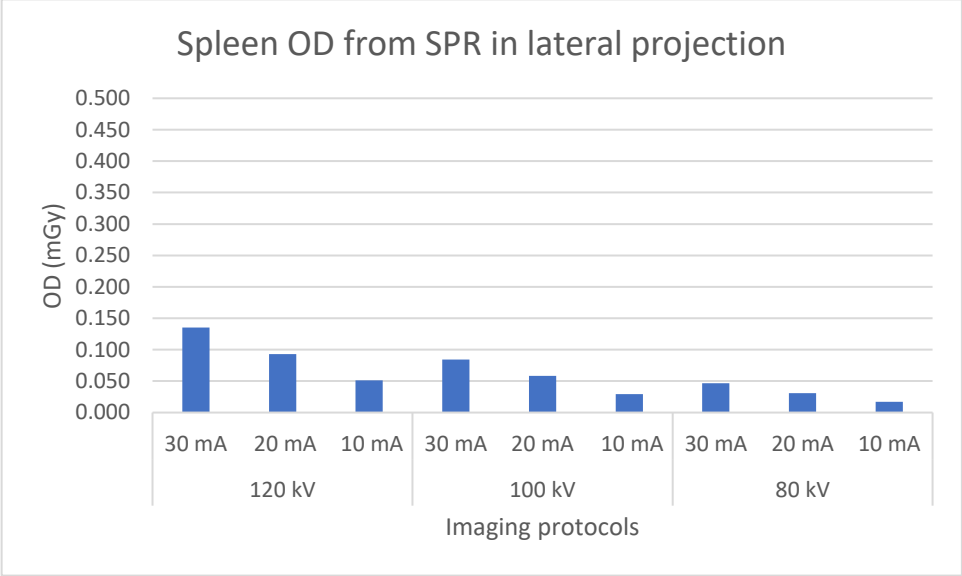

Figure 4.8: The OD of the spleen from the SPR imaging protocol with lateral imaging projection.

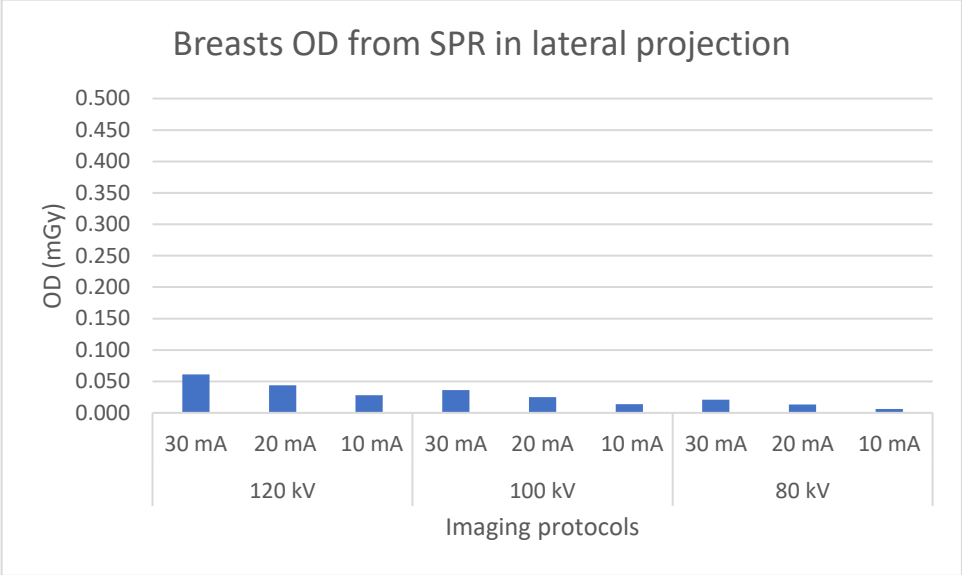

Figure 4.9: The OD of the breasts from the SPR imaging protocol with lateral imaging projection.

Figure 4.10–**Figure 4.12** show the effect of using the scoliosis shawl on the OD values of the breasts, lungs and kidneys. The shawl significantly reduced the radiation dose to these organs ($p < 0.05$); it reduced the dose to the breasts from an average of 0.148 mGy (*SD* = 0.134, range 0.027 to 0.436 mGy) to an average of 0.021 (*SD* = 0.021, range 0.002 to 0.073 mGy), which was, on average, an 87.15% (*SD* = 3.29, range 83.16 to 94.26 %) dose reduction. The

lungs also received a lower dose when the shawl was used; the dose was reduced from an average 0.102 mGy (*SD* = 0.089, range 0.020 to 0.297 mGy) when the shawl was not used to an average of 0.029 mGy (*SD* = 0.031, range 0.004 to 0.105 mGy), which was, on average, a 73.42% (*SD* = 3.83, range 64.79 to 79 %) dose reduction when the shawl was used. Additionally, with the scoliosis shawl, there was no statistical difference ($p > 0.05$) between PA and AP with the scoliosis shawl for all the imaging protocols except for imaging protocol CT 2. However, for the breasts and lung ODs, it was significantly lower in AP projections when using the scoliosis shawl compared with that of PA ($p < 0.05$). **Figure 4.13** and **Figure 4.14** compare the breast and lung ODs in the SPR PA projection with the SPR AP projection when using the scoliosis shawl, respectively. All the OD data of the remining organs are presented in **Table IV** on **page 189**

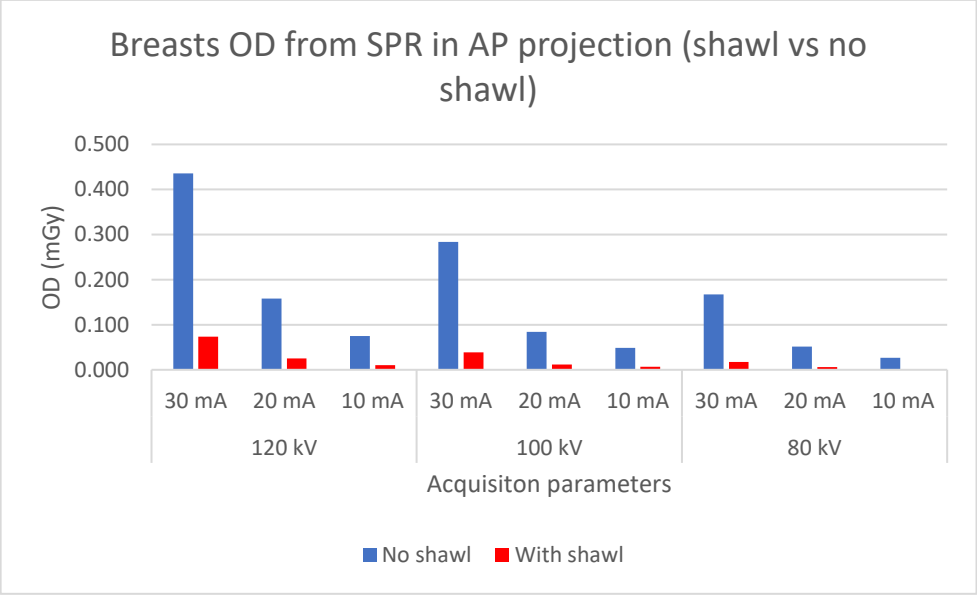

Figure 4.10: The effect of using the scoliosis shawl on the breasts OD in different SPR imaging protocols.

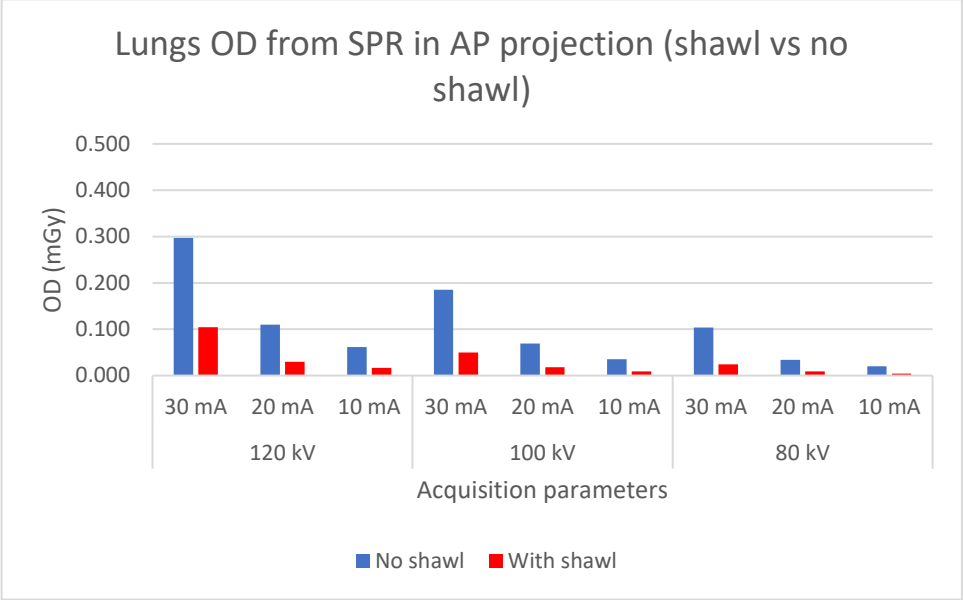

Figure 4.11: The effect of using the scoliosis shawl on the lungs OD in different SPR imaging protocols.

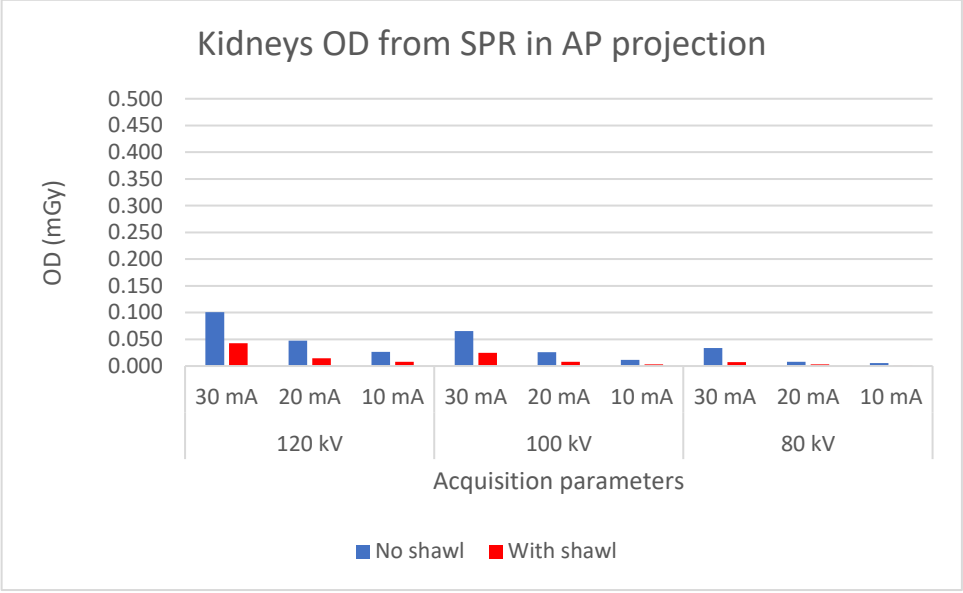

Figure 4.12: The effect of using the scoliosis shawl on the kidneys OD in different SPR imaging protocols.

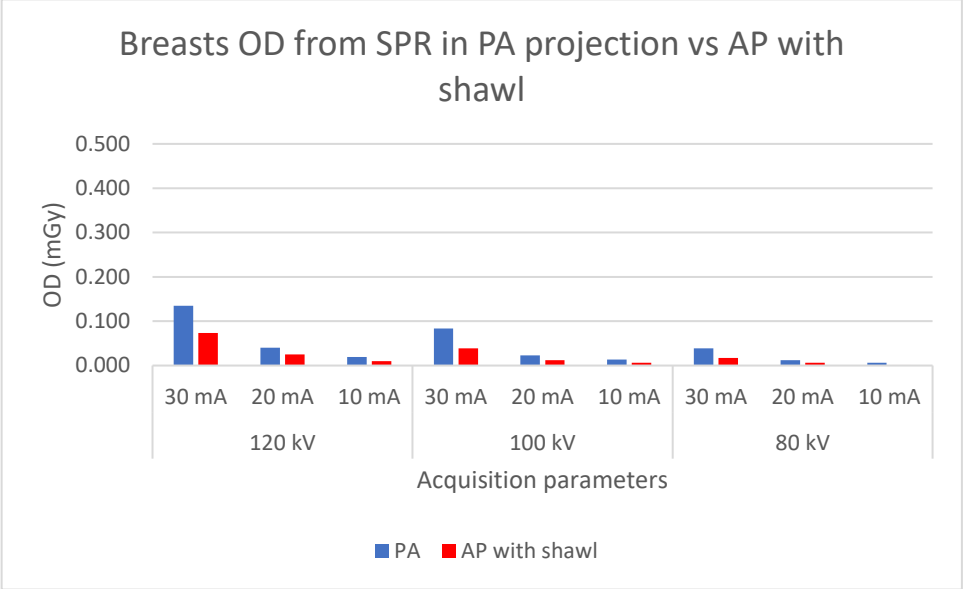

Figure 4.13: Breasts OD in PA projections in comparison with AP with scoliosis shawl.

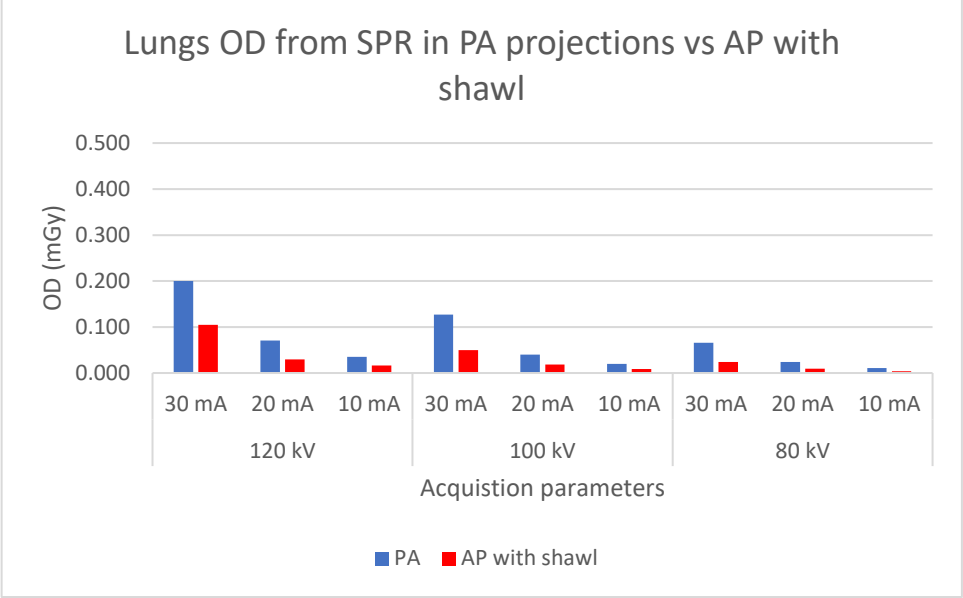

Figure 4.14: Lungs OD in PA projections in comparison with AP with scoliosis shawl.

4.2.1.1 *Comparison of SPR OD with DR and EOS*

Unlike SPR, where several acquisition parameters were used to irradiate the dosimetry phantom, only one set of acquisition parameters per projection was used to irradiate the phantom when using DR and EOS. These acquisition parameters were based on the local guidelines of the hospitals where the dose measurements were carried out. **Table 4.2** reports

the OD values when using DR to irradiate the dosimetry phantom with the following protocols: DR1 (AP), DR2 (PA) and DR1 (AP with scoliosis shawl) and when using the EOS with the following protocols: EOS1 (AP+Lateral) and EOS2 (AP).

Table 4.2: OD values (mGy) when using different imaging projections in DR and the EOS.

Organ	DR1 (AP)	DR2 (PA)	DR1 (AP with scoliosis shawl)	EOS1 (AP+Lateral)	EOS2 (AP)
Active Bone Marrow	0.028	0.026	0.010	0.015	0.003
Thyroid	0.108	0.012	0.067	0.049	0.016
Oesophagus	0.035	0.023	0.026	0.033	0.006
Lungs	0.055	0.056	0.017	0.033	0.009
Breasts	0.119	0.028	0.009	0.039	0.015
Liver	0.120	0.047	0.070	0.027	0.008
Stomach	0.167	0.037	0.058	0.045	0.010
Urinary Bladder	0.121	0.014	0.089	0.028	0.006
Colon	0.087	0.039	0.067	0.028	0.006
Ovaries	0.084	0.019	0.012	0.028	0.005
Salivary Glands	0.001	0.004	0.041	0.031	0.011
Thymus	0.071	0.008	0.047	0.034	0.014
Spleen	0.080	0.091	0.020	0.044	0.005
Kidneys	0.039	0.147	0.014	0.021	0.002
Adrenals	0.033	0.143	0.021	0.024	0.002
Heart	0.053	0.032	0.090	0.037	0.009
Pancreas	0.092	0.053	0.070	0.025	0.006
Gall Bladder	0.055	0.009	0.024	0.008	0.003
Uterus	0.081	0.014	0.013	0.021	0.005
Oral Mucosa	0.002	0.006	0.036	0.026	0.009
Small Intestine	0.118	0.035	0.096	0.030	0.006
Extrathoracic Region	0.028	0.025	0.009	0.026	0.005
Prostate	0.051	0.006	0.003	0.016	0.007

For DR, the stomach, urinary bladder, liver, breasts and thyroid received the highest radiation dose in the AP projection, whilst in the PA projection, the kidneys received the highest dose. When using the EOS to acquire two projections (i.e. AP and lateral) simultaneously, the thyroid, stomach, spleen and breasts received the highest radiation dose. However, when the EOS was used to acquire an AP projection, the thyroid, breasts and thymus received the

highest dose. In general, the EOS delivered a significantly lower OD than DR when they were used to acquire AP projections ($p < 0.05$). Similarly, the EOS delivered a significantly lower radiation dose than DR when they were used to acquire lateral projections ($p < 0.05$).

Figure 4.15 - Figure 4.19 compare the OD values of stomach, liver, breasts, thyroid and kidneys of SPR imaging protocols, respectively, with those of DR and EOS. For example, the breasts received lower radiation dose when using CT10 (PA, 100 kV, 10 mA) (0.014 mGy), CT16 (PA, 80 kV, 10 mA) (0.006 mGy) and CT17 (PA, 80 kV, 20 mA) (0.012 mGy) compared with using EOS2 (AP) (0.015 mGy), as shown in **Figure 4.17**. More interestingly, the breast OD when using CT13 (AP, 80 kV, 10 mA) (0.027 mGy) and DR2 (PA) (0.028 mGy) were almost equal. **Figure 4.20** and **Figure 4.21** show the OD values of the breast and stomach when the scoliosis shawl was used and compare them with the values from using DR and EOS. As shown in **Figure 4.20**, the breast OD when using the scoliosis shawl with these imaging protocols: DR1 (AP) (0.009 mGy), CT7 (AP, 100 kV, 10 mA) (0.006 mGy), CT13 (AP, 80 kV, 10 mA) (0.002 mGy) and CT14 (AP, 80 kV, 10 mA) (0.006 mGy) were lower than the breast OD when using EOS2 (AP) (0.015 mGy).

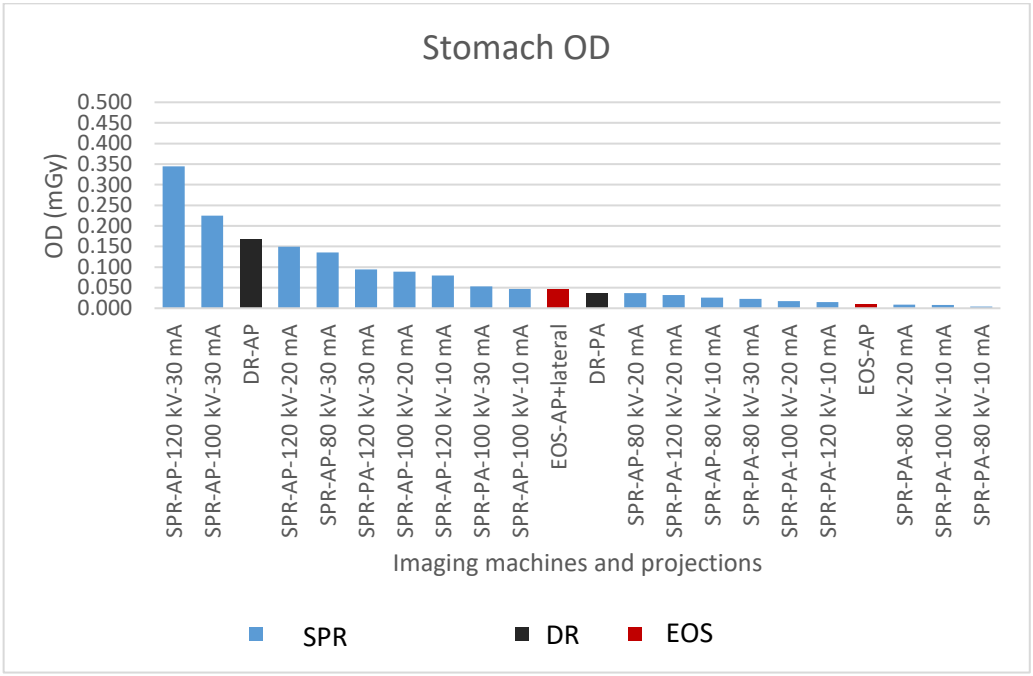

Figure 4.15: The stomach OD when irradiating the phantom using SPR, DR and EOS without using the scoliosis shawl.

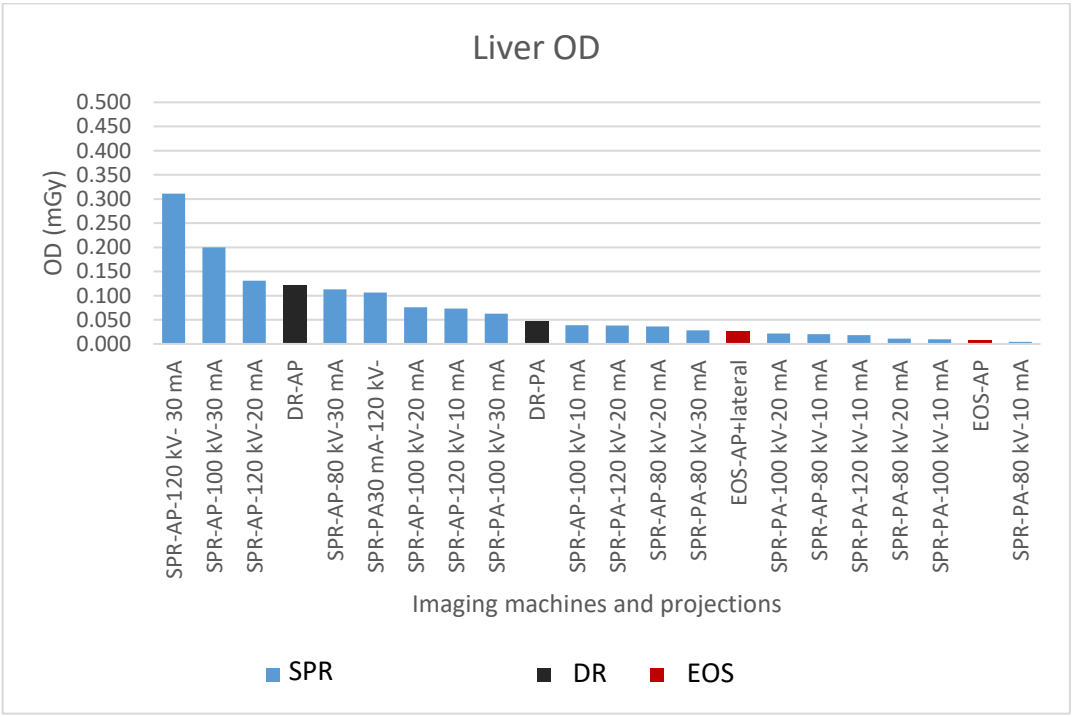

Figure 4.16: The liver OD when irradiating the phantom using SPR, DR and EOS without using the scoliosis shawl.

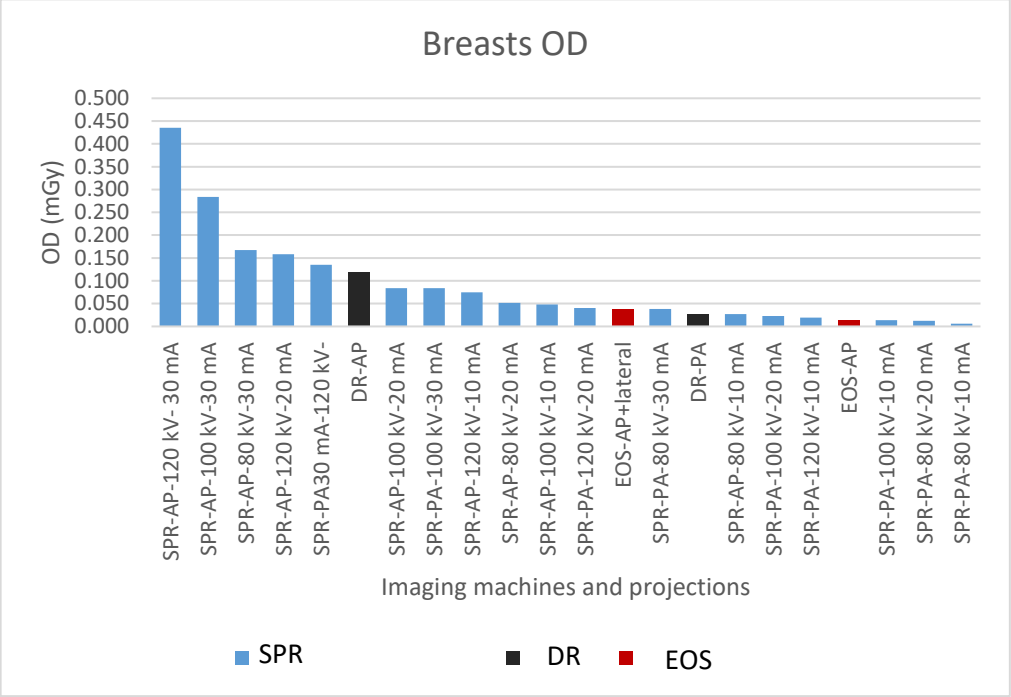

Figure 4.17: The breasts OD when irradiating the phantom using SPR, DR and EOS without using the scoliosis shawl.

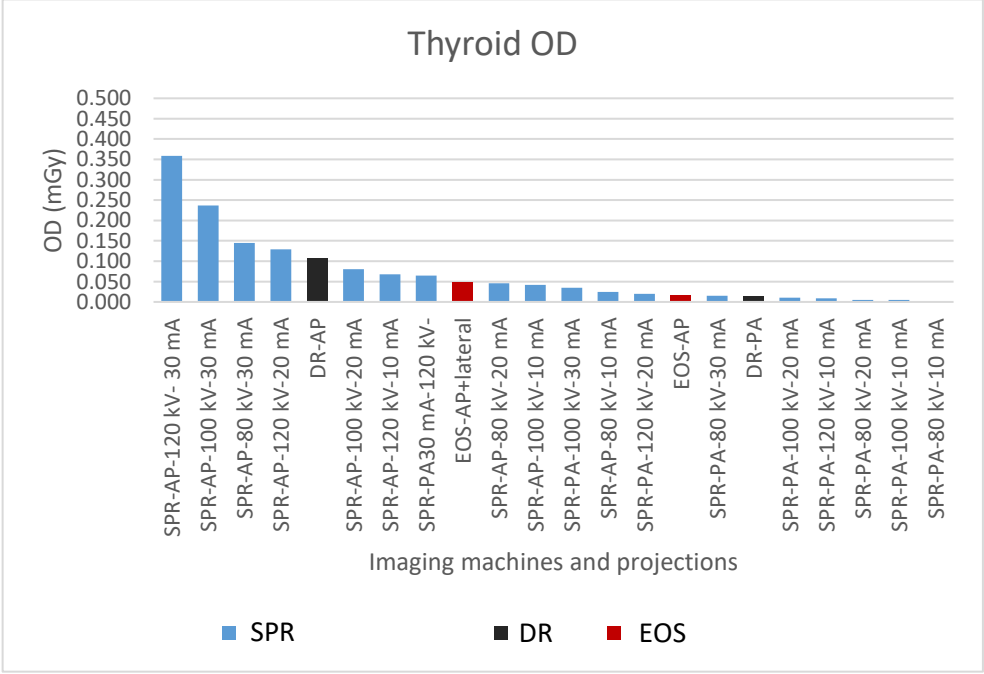

Figure 4.18: The thyroid OD when irradiating the phantom using SPR, DR and EOS without using the scoliosis shawl.

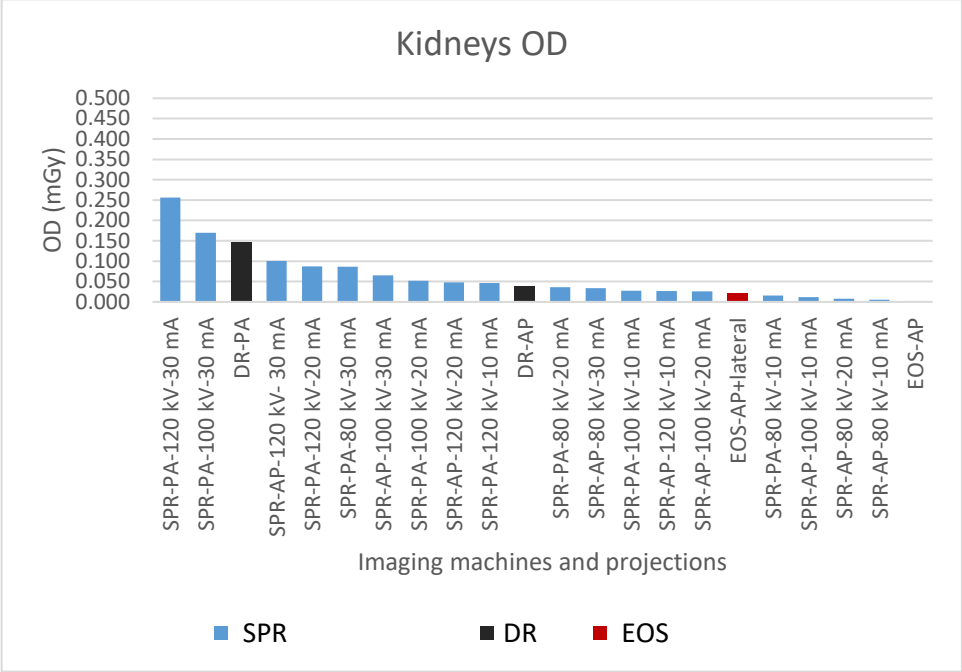

Figure 4.19: The kidneys OD when irradiating the phantom using SPR, DR and EOS and without using the scoliosis shawl.

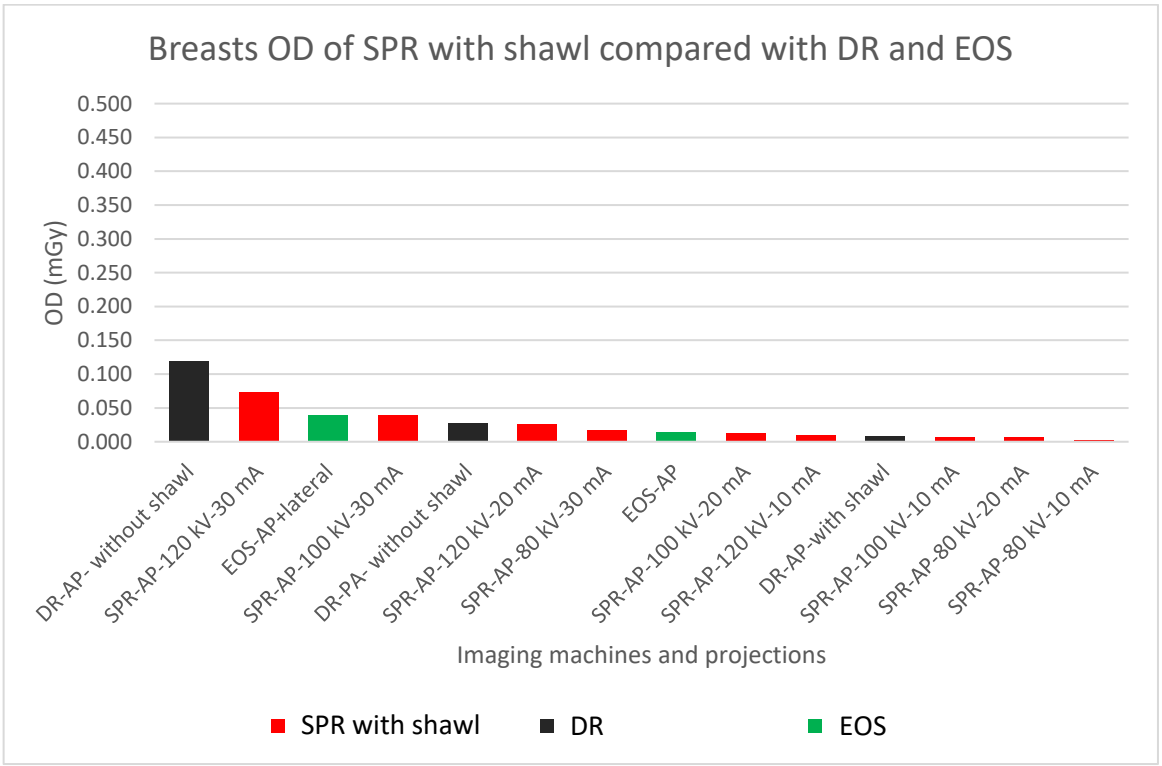

Figure 4.20: The breasts OD when irradiating the phantom using SPR, DR and EOS and using the scoliosis shawl.

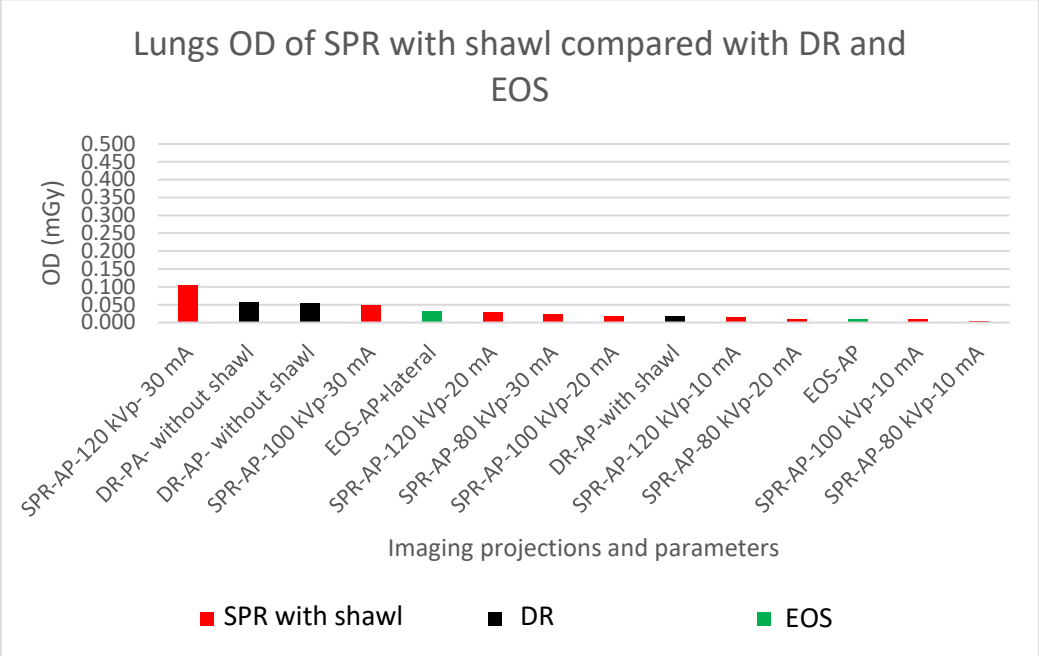

Figure 4.21: The lungs OD when irradiating the phantom using SPR, DR and EOS and using the scoliosis shawl.

Table 4.3 and **Table 4.4** report a summary of the OD values of the imaging protocols used to irradiate the dosimetry phantom without and with the scoliosis shawl, respectively. **Table 4.5** reports a summary of the OD values when using DR and EOS to irradiate the dosimetry phantom. Compared with DR, five SPR imaging protocols that were used to acquire AP, namely, CT1, 7, 8, 13 and 14, delivered overall significantly ($p < 0.05$) lower radiation dose to the phantom than DR when used to acquire an AP image. No SPR AP imaging protocol delivered a radiation dose lower than the EOS when it was used to acquire an AP image. However, seven SPR PA imaging protocols: CT4, 5, 10, 11, 16, 17 and 18 delivered, in total, significantly ($p < 0.05$) lower radiation dose than DR when used to acquire a PA image. When comparing AP and PA imaging protocols of SPR to the PA of DR, only CT13 (AP) delivered a significantly lower radiation dose than DR (PA). However, seven SPR PA imaging protocols: CT4, 5, 10, 11, 16, 17 and 18 delivered significantly lower radiation dose than DR AP with and without the scoliosis shawl.

Compared with the DR imaging protocol (AP) where the scoliosis shawl was used, six SPR imaging protocols with the scoliosis shawl: CT1, 7, 8, 13, 14 and 15 delivered significantly ($p < 0.05$) lower radiation dose. Interestingly, three SPR imaging protocols without the scoliosis shawl: CT7, 13 and 14 delivered significantly ($p < 0.05$) lower radiation dose than DR (AP) with the scoliosis shawl. Additionally, imaging protocol CT13 with the scoliosis shawl delivered a radiation dose to the phantom similar to that of the EOS (AP) with no significant difference ($p > 0.05$) .

Table 4.3: Summary of the SPR OD values in AP and PA imaging projection without using the scoliosis shawl.

Imaging protocols	Imaging projection	kV	mA	Average (mGy)	*SD*	Highest (mGy)
CT1	AP	120	10	0.044	0.032	0.111
CT2	AP	120	20	0.079	0.057	0.183
CT3	AP	120	30	0.192	0.145	0.480
CT4	PA	120	10	0.014	0.013	0.049
CT5	PA	120	20	0.031	0.027	0.102
CT6	PA	120	30	0.089	0.078	0.293
CT7	AP	100	10	0.024	0.018	0.064
CT8	AP	100	20	0.048	0.036	0.135
CT9	AP	100	30	0.124	0.100	0.373
CT10	PA	100	10	0.009	0.008	0.030
CT11	PA	100	20	0.016	0.016	0.062
CT12	PA	100	30	0.053	0.050	0.189
CT13	AP	80	10	0.013	0.010	0.037
CT14	AP	80	20	0.021	0.018	0.068
CT15	AP	80	30	0.072	0.060	0.224
CT16	PA	80	10	0.004	0.004	0.020
CT17	PA	80	20	0.009	0.009	0.037
CT18	PA	80	30	0.025	0.027	0.108

Table 4.4: Summary of the SPR OD values in AP projections when using the scoliosis shawl.					
Imaging protocols	kV	mA	Average (mGy)	*SD*	Highest (mGy)
CT1	120	10	0.020	0.018	0.070
CT2	120	20	0.036	0.034	0.141
CT3	120	30	0.109	0.104	0.430
CT7	100	10	0.011	0.011	0.04
CT8	100	20	0.022	0.022	0.09
CT9	100	30	0.068	0.070	0.294
CT13	80	10	0.006	0.006	0.027
CT14	80	20	0.012	0.013	0.054
CT15	80	30	0.033	0.406	0.177

Table 4.5: Summary of DR and EOS OD in AP and PA projections.						
Imaging protocols	Imaging projection	kV	mA	Average (mGy)	*SD*	Highest (mGy)
DR1	AP	85	(5.9, 9.5)*	0.063	0.045	0.167
DR2	PA	85	(4.3, 12.2)*	0.033	0.38	0.147
DR1 (with scoliosis shawl)	AP	85	(5, 17)*	0.035	0.030	0.096
EOS1	AP+ Lateral	75 (AP), 95 (lateral)	200	0.026	0.012	0.049
EOS2	AP	75	200	0.007	0.004	0.016
* DR acquired spine images in two irradiations and stitched the images together.						

Table 4.6 reports the OD when DR and EOS were used for acquiring lateral images. **Figure 4.22** and **Figure 4.23** show the breasts and spleen OD values when using SPR, DR, and EOS to irradiate the phantom in lateral projections. The spleen OD values were presented because the spleen received the highest dose in the lateral projection among all the used imaging machines. **Table 4.7** shows a summary of the OD values of SPR, DR and EOS when used to acquire lateral images. EOS delivered the lowest dose, whereas all the SPR imaging protocols except CT21 delivered significantly lower radiation dose than the DR ($p < 0.05$).

Table 4.6: OD level (mGy) when using DR and the EOS to acquire lateral images.		
Organ	DR (lateral)	EOS (lateral)
Active Bone Marrow	0.028	0.001
Thyroid	0.042	0.004
Oesophagus	0.052	0.004
Lungs	0.063	0.003
Breasts	0.033	0.003
Liver	0.119	0.002
Stomach	0.033	0.004
Urinary Bladder	0.041	0.001
Colon	0.053	0.002
Ovaries	0.049	0.002
Salivary Glands	0.017	0.003
Thymus	0.026	0.002
Spleen	0.027	0.005
Kidneys	0.078	0.002
Adrenals	0.065	0.004
Heart	0.062	0.004
Pancreas	0.092	0.002
Gall Bladder	0.037	0.000
Uterus	0.023	0.001
Oral Mucosa	0.025	0.002
Small Intestine	0.068	0.002
Extrathoracic Region	0.025	0.003
Prostate	0.009	0.001

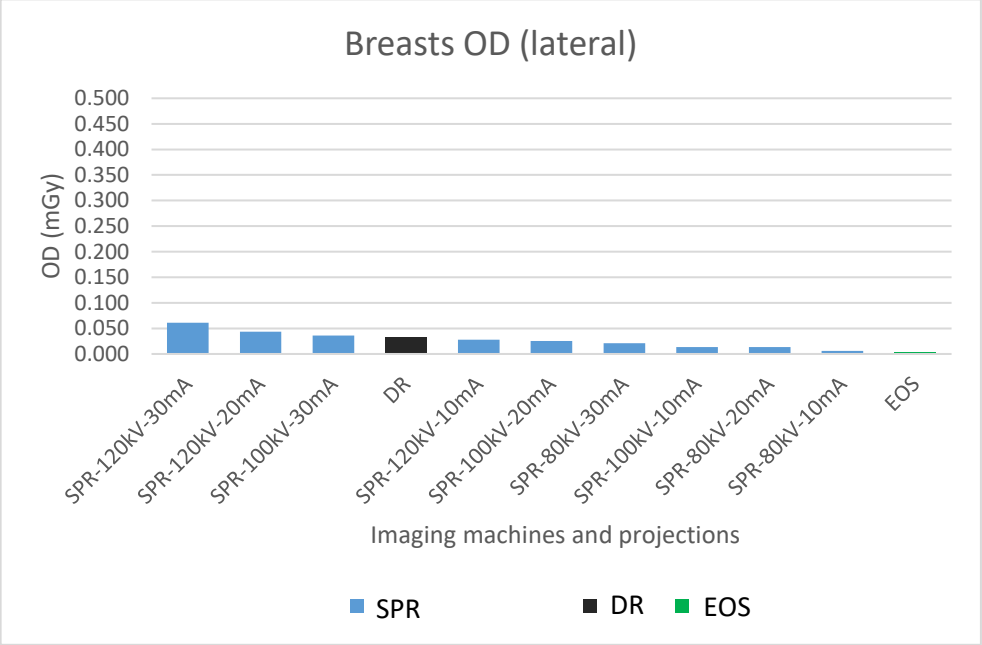

Figure 4.22: The breasts OD when irradiating the phantom using SPR, DR and EOS in lateral projections.

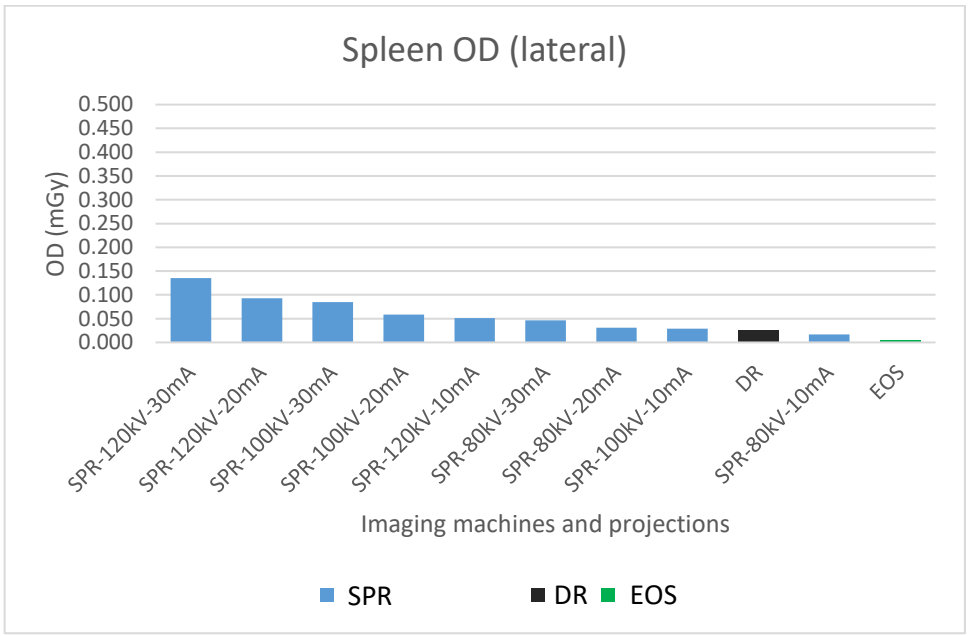

Figure 4.23: The spleen OD when irradiating the phantom using SPR, DR and EOS in lateral projections.

Table 4.7: Summary of the SPR, DR and EOS OD values in lateral projections					
Imaging protocols	kV	mA	Average (mGy)	*SD*	Highest (mGy)
CT19	120	10	0.016	0.013	0.051
CT20	120	20	0.030	0.025	0.093
CT21	120	30	0.043	0.035	0.135
CT22	100	10	0.008	0.007	0.029
CT23	100	20	0.017	0.015	0.058
CT24	100	30	0.026	0.022	0.085
CT25	80	10	0.004	0.004	0.017
CT26	80	20	0.008	0.008	0.030
CT27	80	30	0.013	0.012	0.046
DR3	90	(5, 11)*	0.042	0.028	0.119
EOS3	80	80	0.002	0.001	0.005
* DR acquired spine images in two irradiations and stitched the images together.					

4.2.2 ED

Table 4.8–Table 4.11 show the ED for patients when using SPR, DR and EOS for assessing AIS. The EOS delivered the lowest dose compared with the other machines. The EOS ED of the AP projection was 0.01 mSv, and the DR ED of the AP projection was 0.08 mSv, while the SPR ED was, on average, 0.09 (*SD* = 0.07, range 0.02 to 0.25 mSv). For PA projections, the EOS ED was not calculated (this imaging projection is not used where the measurements were performed), the DR ED of the PA projection was 0.03 mSv and the SPR ED was, on average, 0.03 mSv (*SD* = 0.03, range 0.001 to 0.10 mSv). Using the scoliosis shawl further reduced the SPR and the DR ED significantly ($p < 0.05$): the SPR ED was reduced by an average of 62.5% (*SD*= 6.75), and the DR dose was reduced by 50%. **Figure 4.24** on **page 139** shows the ED values of SPR (with and without using the scoliosis shawl), DR (with and without using the scoliosis shawl) and the EOS.

Table 4.8: The ED using AP and PA projections when using SPR mode with and without the scoliosis shawl.

Imaging protocol	Imaging projection	kV	mA	ED (mSv) without the scoliosis shawl	ED (mSv) with the scoliosis shawl
CT1	AP	120	10	0.06	0.02
CT2	AP	120	20	0.11	0.04
CT3	AP	120	30	0.25	0.11
CT4	PA	120	10	0.02	Not measured*
CT5	PA	120	20	0.04	Not measured*
CT6	PA	120	30	0.10	Not measured*
CT7	AP	100	10	0.03	0.01
CT8	AP	100	20	0.06	0.02
CT9	AP	100	30	0.16	0.07
CT10	PA	100	10	0.01	Not measured*
CT11	PA	100	20	0.02	Not measured*
CT12	PA	100	30	0.06	Not measured*
CT13	AP	80	10	0.02	0.01
CT14	AP	80	20	0.03	0.01
CT15	AP	80	30	0.1	0.03
CT16	PA	80	10	>0.01	Not measured*
CT17	PA	80	20	0.01	Not measured*
CT18	PA	80	30	0.03	Not measured*

* The scoliosis shawl was not used in the PA projection because it is not designed to protect the breasts in this projection.

The ED values of lateral projection in SPR, DR and EOS were, in general, lower than the AP and PA projections. On average, the SPR ED from the lateral projection was lower than that of DR but higher than that of the EOS.

Table 4.9: The ED from using lateral projection in SPR mode.

Imaging protocol	Imaging projection	kV	mA	ED (mSv)
CT19	Lateral	120	10	0.02
CT20	Lateral	120	20	0.04
CT21	Lateral	120	30	0.06
CT22	Lateral	100	10	0.01
CT23	Lateral	100	20	0.02
CT24	Lateral	100	30	0.03
CT25	Lateral	80	10	0.01
CT26	Lateral	80	20	0.01
CT27	Lateral	80	30	0.02

Table 4.10: The ED from using DR with and without the scoliosis shawl.					
Imaging protocol	Imaging projection	Acquisition parameter		ED (mSv) without the scoliosis shawl	ED (mSv) with the scoliosis shawl
		kV	mAs		
DR1	AP_1	85	5.9	0.08	0.04
	AP_2	85	9.5		
DR2	PA_1	85	4.3	0.03	Not measured*
	PA_2	85	12.2		
DR3	$Lateral_1$	90	5	0.05	Not measured*
	$Lateral_2$	90	11		
$_1$ Refers to the top image; $_2$ refers to the bottom image (i.e. DR takes two images in order to capture the entire spine and then stitches them together). * The scoliosis shawl was not used in the PA projection because it is not designed to protect the breasts in this projection.					

Table 4.11: The ED from using the EOS imaging system.				
Imaging protocol	Imaging projection	Acquisition parameter		ED (mSv)
		kV	mA	
EOS1	AP*	75	200	0.03
	Lateral *	95	200	
EOS2	AP	75	200	0.01
EOS3	Lateral	80	80	<0.01
* Indicates that the imaging projections were acquired simultaneously.				

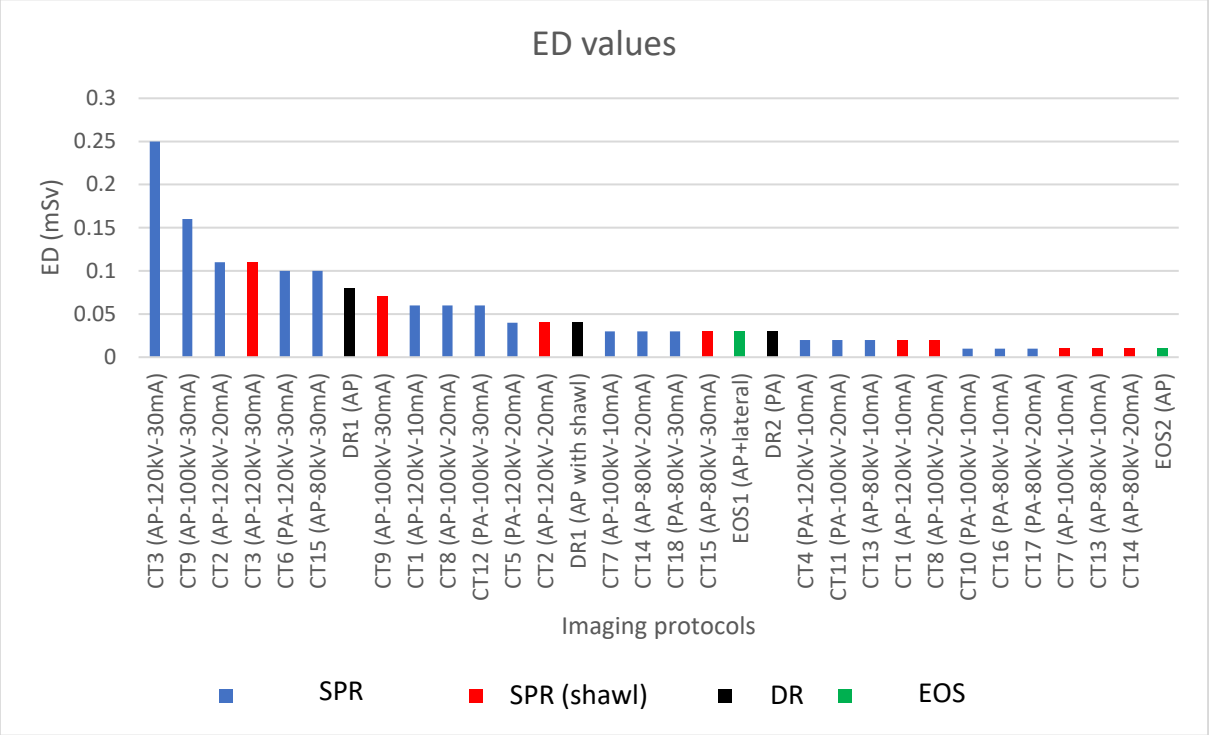

Figure 4.24: The ED values when irradiating the phantom using SPR, DR and EOS in AP, AP with scoliosis shawl and PA.

4.2.3 ER

Table 4.12–Table 4.15 show the ER for developing radiation-induced cancer from exposure to X-rays from SPR, DR and the EOS. In general, females were found to be at higher risk than males, and a statistical difference was observed ($p < 0.05$). In AP projections, the SPR ER for females was, on average, 2.75 cases/10^6 (*SD* = 2.39, range 0.53 to 7.9 cases/10^6), and SPR for males was, on average, 1.14 cases/10^6 (*SD* = 0.95, range 0.23 to 3.17 cases/10^6). In PA projections, the SPR ER for females was, on average, 0.97 cases/10^6 (*SD* = 0.95, range 0.14 to 3.10 cases/10^6), and SPR for males was, on average, 0.45 cases/10^6 (*SD* = 0.43, range 0.06 to 1.40 cases/10^6). By comparison, the DR ERs for females and males were 2.26 and 1.03 cases/10^6, respectively, for acquiring AP projections, and 0.92 and 0.52 cases/10^6, respectively, for acquiring PA projections. The EOS ER for acquiring the AP projection was 0.25 and 0.09 cases/10^6 for females and males, respectively. Using the scoliosis shawl reduced the ER significantly for both females and males ($p < 0.05$); however, the reduction was more noticeable for females than for males. On average, ER was reduced by 64.5% (*SD* = 3.83, range 58.88 to 69.81%) for females and by 51.5% (*SD* = 8.05, range 35.05 to 60%) for males.

Table 4.12: The ER from using AP and PA projections in SPR with and without the scoliosis shawl.

Imaging protocol	Imaging projection	kV	mA	ER (female patients/10^6) without the scoliosis shawl	ER (female patients/10^6) with the scoliosis shawl	ER (male patients/10^6) without the scoliosis shawl	ER (male patient/10^6) with the scoliosis shawl
CT1	AP	120	10	1.61	0.56	0.75	0.34
CT2	AP	120	20	3.07	1.03	1.35	0.57
CT3	AP	120	30	7.9	3.22	3.17	1.78
CT4	PA	120	10	0.50	Not measured*	0.24	Not measured*
CT5	PA	120	20	1.04	Not measured*	0.49	Not measured*
CT6	PA	120	30	3.10	Not measured*	1.40	Not measured*
CT7	AP	100	10	0.94	0.32	0.4	0.18
CT8	AP	100	20	1.81	0.64	0.82	0.37
CT9	AP	100	30	5.07	1.92	2.03	1.09
CT10	PA	100	10	0.3	Not measured*	0.13	Not measured*
CT11	PA	100	20	0.58	Not measured*	0.27	Not measured*
CT12	PA	100	30	1.9	Not measured*	0.85	Not measured*
CT13	AP	80	10	0.53	0.16	0.23	0.1
CT14	AP	80	20	0.9	0.37	0.34	0.22
CT15	AP	80	30	3	0.94	1.2	0.48
CT16	PA	80	10	0.14	Not measured*	0.06	Not measured*
CT17	PA	80	20	0.32	Not measured*	0.15	Not measured*
CT18	PA	80	30	0.91	Not measured*	0.41	Not measured*

* The scoliosis shawl was not used in PA projections because it is not designed to protect the breasts in this projection.

Table 4.13: The ER from using lateral projections in SPR.

Imaging protocol	Imaging projection	kV	mA	ER (female patients/10^6)	ER (male patients/10^6)
CT19	Lateral	120	10	0.59	0.25
CT20	Lateral	120	20	1.03	0.47
CT21	Lateral	120	30	1.45	0.66
CT22	Lateral	100	10	0.31	0.13
CT23	Lateral	100	20	0.59	0.26
CT24	Lateral	100	30	0.88	0.40
CT25	Lateral	80	10	0.15	0.07
CT26	Lateral	80	20	0.31	0.13
CT27	Lateral	80	30	0.47	0.20

Table 4.14: The ER from using DR.

Imaging protocol	Imaging projection	Acquisition parameter		ER (female patients/10^6) without the scoliosis shawl	ER (female patients/10^6) with the scoliosis shawl	ER (male patients/10^6) without the scoliosis shawl	ER (male patients/10^6) with the scoliosis shawl
		kV	mAs				
DR1	AP_1	85	5.9	2.26	0.84	1.03	0.59
	AP_2	85	9.5				
DR2	PA_1	85	4.3	0.92	Not measured*	0.52	Not measured*
	PA_2	85	12.2				
DR3	$Lateral_1$	90	5	1.15	Not measured*	0.64	Not measured*
	$Lateral_2$	90	11				

[1] Refers to the top image; [2] refers to the bottom image (i.e. DR takes two images in order to capture the entire spine and then stitches them together).
* The scoliosis shawl was not used in the PA projection because it is not designed to protect the breasts in this projection.

Table 4.15: The ER from using EOS imaging system.					
Imaging protocol	Imaging projection	Acquisition parameter		ER (10-year-old female patients/10^6)	ER (10-year-old male patients/10^6)
		kV	mA		
EOS1	AP*	75	200	0.86	0.37
	Lateral*	95	200		
EOS2	AP	75	200	0.25	0.09
EOS3	Lateral	80	80	0.07	0.03
* Indicates that these imaging projections were acquired simultaneously.					

Figure 4.25 shows the ER for females, and **Figure 4.26** shows the ER for males when using SPR (with and without scoliosis shawl), DR (with and without scoliosis shawl) and EOS. Compared with DR and EOS, five SPR AP imaging protocols CT1, CT7, CT8, CT13 and CT14 posed lower risk of developing radiation-induced cancer than DR1 (AP) for both males and females. On the other hand, six SPR PA imaging protocols CT4, CT10, CT11, CT16, CT17 and CT18 posed lower risk than DR2 (PA) for both males and females. However, CT5 (PA) posed a lower risk than DR2 (PA) for male patients only.

When using the scoliosis shawl, the risk from radiation was lower for male patients when using CT1, CT2, CT7, CT8, CT13, CT14 and CT15 compared with DR1 (AP with shawl); the OD values of these imaging protocols were significantly lower than those of DR ($p < 0.05$) except for CT2. On the other hand, the risk for female patients was lower than those of DR1 (AP with shawl) when using CT1, CT7, CT8, CT13, and CT14, whose OD values were significantly ($p < 0.05$) lower than those of DR. EOS had the lowest risk; however, lower levels could be achieved by using CT13 (AP) with the scoliosis shawl and CT16 (PA) for female patients and CT16 for male patients.

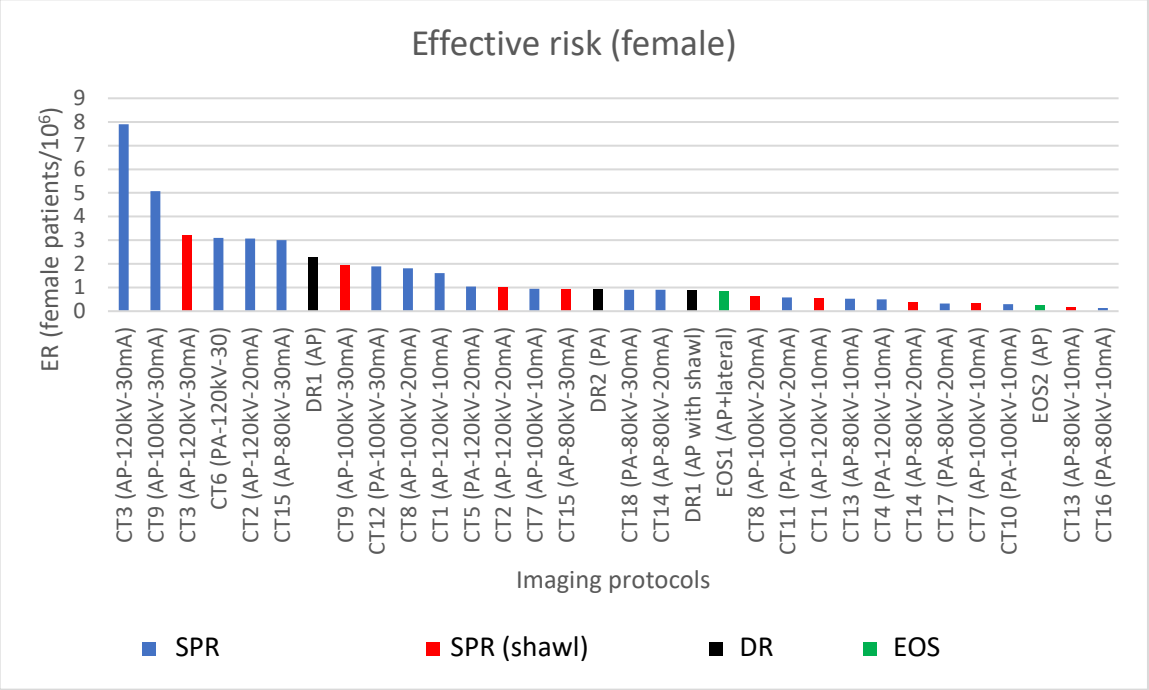

Figure 4.25: The ER for females from using SPR, DR and EOS.

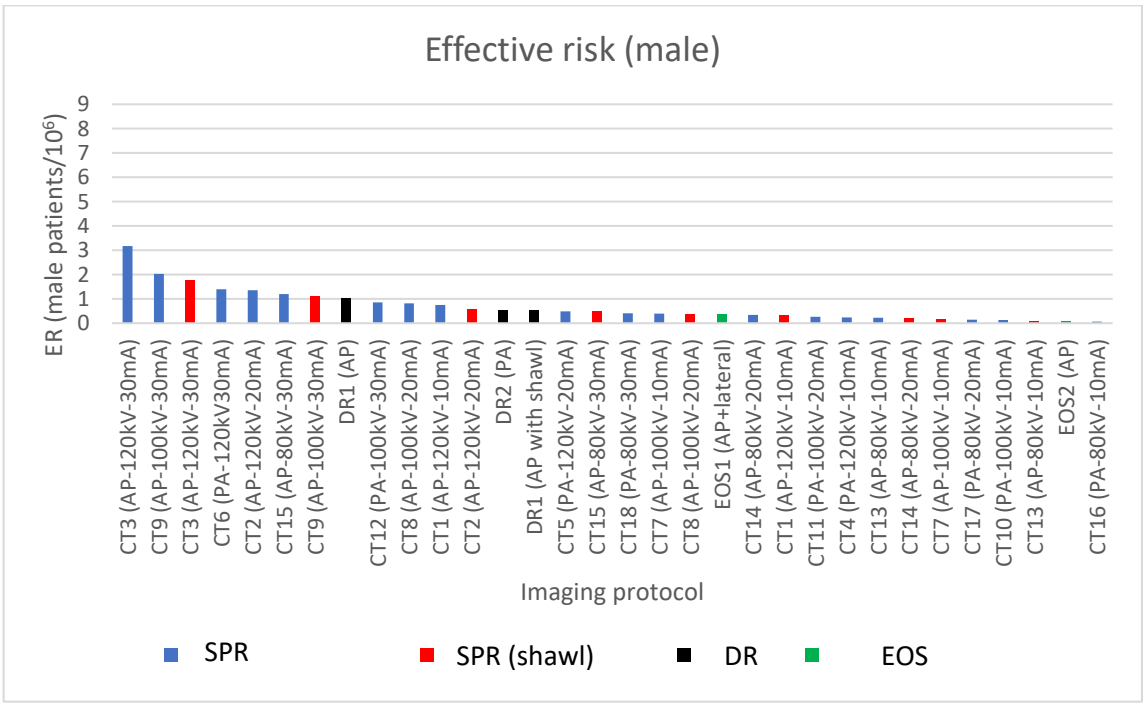

Figure 4.26: The ER for males from using SPR, DR and EOS.

4.3 Construction and validation of a phantom with scoliotic spine

4.3.1 Validation of the PMMA/PoP phantom with AIS

The phantom that was constructed to represent a 10-year old child with AIS needed to be validated. For this, HU and SNR values and visual inspection of the PoP phantom were used; a HU shows the attenuation properties of the materials used to build the phantom, and SNR allows comparing the phantom response to the X-ray. The HU of the PoP was compared with the HU of the spine of a 10-year human female and the HU of a vertebra from a sheep spine, whereas the SNR from the PoP phantom was compared with a commercially available phantom that was used for IQ evaluation.

Table 4.16 reports the HU for the human vertebra, sheep vertebra and vertebra made of PoP. The correlation between the HU of the vertebra made of PoP and the HU of the human vertebra was strong ($r = 0.90$, $p < 0.05$) and the correlation between the HU of the PoP vertebra and the HU of the sheep vertebra was also strong ($r = 0.88$, $p < 0.05$). **Table 4.17** reports the HU values of PMMA and that of the 10-year old girl (soft tissue). **Table 4.18** and **Table 4.19** show the relationship between the SNR values of the PMMA/PoP phantom and Lungman phantom over a range of kV and mA values (**Table 3.8** on **page 106**). The correlation was strong and positive ($r = 0.93$, $p < 0.05$). **Figure 3.30–Figure 3.32** on **pages 108–110** confirmed that the PoP phantom had a spine that was a close representation of the shape of that a 10-year-old girl. Lastly, Cobb angle measurement on the phantom confirmed that the constructed scoliosis curve was 14°, which was 1° lower than the target angle. The vertebrae pairs that formed the angle were T5 and L2, T5 and L3 and T6 and L3.

Table 4.16: Comparison of HU of different bone tissue with HU of PoP.

Vertebra	Real spine (whole)	Real spine (endplates*)	Sheep (whole)	Sheep (endplates*)	PoP vertebra
Mean HU	460	598	116	605	628
SD	107	79	155	83	56

* Measurements preformed only on the endplates.

Table 4.17: Comparison of HU of PMMA the soft tissue of the 10-year old girl.

	PMMA	Soft tissue (10-year-old girl)
Average	85.38	78.83*
SD	27.95	56

Huge variation was observed due to the heterogeneity of the human body (further discussion is in Section 5.3.1 on page 169.

Table 4.18: The correlation between the SNR values of the PMMA/PoP phantom and Lungman phantom across a range of kV values when changing mAs value.

kV	Spearman correlation	*p*-value
75	0.99	<0.001
80	0.99	<0.001
85	0.99	<0.001
90	0.97	<0.001
95	0.95	<0.001
100	0.97	<0.001
105	0.97	<0.001
110	0.97	<0.001
115	0.72	<0.001
120	0.91	<0.001

Table 4.19: The correlation between the SNR values of PMMA/PoP phantom and Lungman phantom across a range of mAs values when changing kV values.		
mAs	Pearson correlation	*p*-value
1	0.88	<0.001
2	0.88	<0.001
3.2	0.97	<0.001
4	0.95	<0.001
5	0.96	<0.001
6.3	0.97	<0.001
7.1	0.99	<0.001
8	0.90	<0.001
9	0.98	<0.001
10	0.98	<0.001
11	0.95	<0.001
12.5	0.99	<0.001
14	0.94	<0.001
16	0.96	<0.001
18	0.97	<0.001
20	0.97	<0.001

4.3.2 Initial visual evaluation of the PoP phantom images to determine suitability for inclusion in Cobb angle analysis

The observers (N = 4) marked 10 of the 18 images as suitable for Cobb angle measurements based on the clarity of the endplates. The 10 images and their imaging protocols are shown in **Table 4.20**. Inter-observer reliability was good, as shown by the ICC value of 0.76 with a 95% confidence interval (CI) between 0.60 and 0.86.

Table 4.20: The 10 images that were indicated by observers as eligible for Cobb angle measurements, based on endplate clarity.			
Imaging protocol	Imaging projection	kV	mA
CT3	AP	120	30
CT4	PA	120	10
CT5	PA	120	20
CT6	PA	120	30
CT8	AP	100	20
CT9	AP	100	30
CT10	PA	100	10
CT11	PA	100	20
CT12	PA	100	30
CT15	AP	80	30

4.4 Cobb angle measurements

The observers (n = 13) trained to perform the angle measurements using Cobb's method on two images of AIS patients. The inter-observer variation was within the 5°, except for observer 10 in image 1 and observer 13 in image 2. **Table 4.21** shows a summary of Cobb angle measurements of the two training images, which the participants did prior to doing the experimental images. For the PoP phantom images, the average difference from the true angle of the phantom spine (i.e. 14°) was –2.75° (*SD* = 1.46, range –4.26° to 0.90°) and the inter-observer agreement was good, that is, 0.861 (95% CI [0.70–0.95]). **Table 4.22** reports the measured Cobb angle for each image, **Figure 4.27** shows the average measured Cobb angles in each image and **Figure 4.28** shows them in the order of radiation dose level.

Table 4.21: Cobb angle measurement on the training images.		
	Image 1	Image 2
Average	87.7°	50.9°
SD	1.8°	2.8°
Maximum	89.8°	56.5°
Minimum	82.5°	45.6°

Table 4.22: The measured Cobb angle in each image.										
Imaging protocol	CT3	CT4*	CT5	CT6	CT8*	CT9	CT10	CT11	CT12	CT15*
Projection	AP	PA	PA	PA	AP	AP	PA	PA	PA	AP
kVp	120	120	120	120	100	100	100	100	100	80
mA	30	10	20	30	20	30	10	20	30	30
Average angle (degrees)	9.84	11.31	14.91	11.69	11.48	10.28	9.74	11.15	10.53	11.48
SD	2.81	1.30	1.69	1.50	2.38	1.93	1.30	1.62	2.12	1.85
Maximum	15.9	13.5	17.2	14.6	16	13.1	11.8	15	15.2	14.7
Minimum	6.2	8.6	12.1	8.6	7	6.1	7.2	9.1	7	7
* Indicates that the dose in these SPR imaging protocols is significantly ($p < 0.05$) lower than their corresponding positions in DR.										

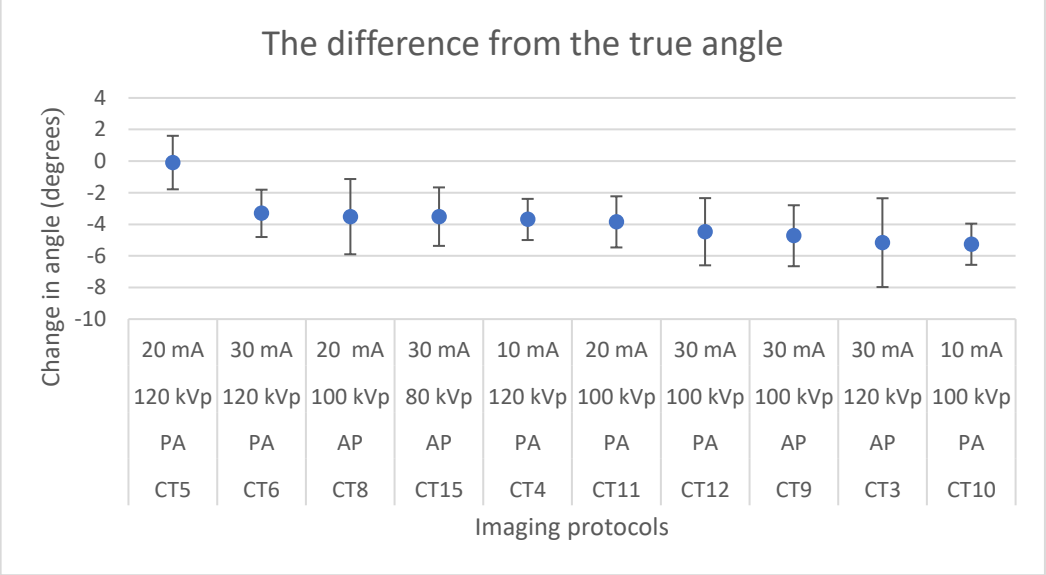

Figure 4.27: The average difference of the measured angle from the true angle per image in order measurement accuracy.

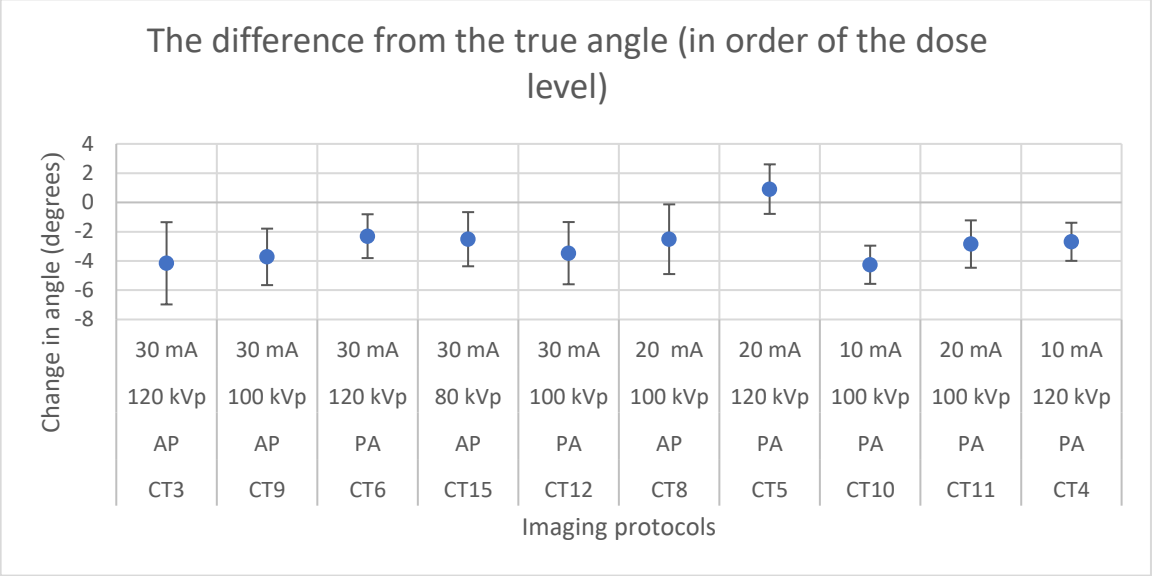

Figure 4.28: The average difference of the measured angle from the true angle per image in order of radiation dose in which the highest level dose is on the left.

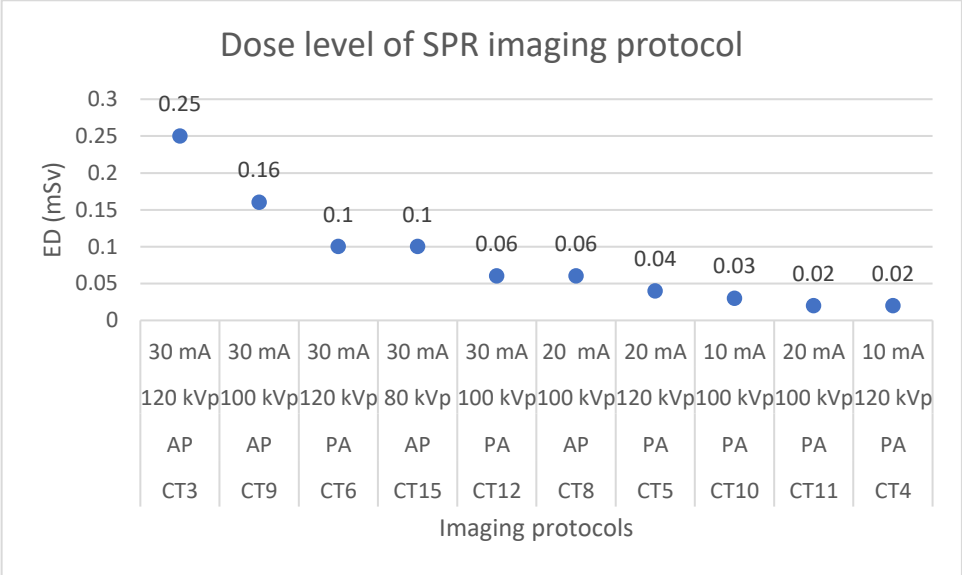

Figure 4.29: Radiation dose level of each imaging protocol used to acquire the 10 selected images for Cobb angle measurements.

In conclusion, Cobb angle measurements on all SPR images used in this part of the experiment had less than a 5° difference from the constructed angle (14°). The difference varied based on the imaging protocols. The image that was acquired using CT5 provided the most accurate Cobb angle measurements compared with the images (+0.9°), and its ER (0.49 cases/10^6) was slightly lower than DR2 (PA) (0.52 cases/10^6) for males only. The most

accurate Cobb angle measurements with the lowest risk for both genders were achieved using the images that were acquired using CT4, 8 and 11.

4.5 Chapter summary

This chapter reported the results of this study. The radiation dose level of SPR mode in CT scanning was compared to that of the two imaging machines currently used for assessing AIS, namely DR and EOS. The EOS had the lowest radiation dose; however, for females and males, AP imaging protocols CT1, CT7, CT8, CT13 and 14 had lower risk than DR (AP), and PA imaging CT4, CT10, CT11, CT16, CT17 and 18 had lower ER than DR2 (PA) protocols; the OD values of the SPR were significantly lower than that of DR. Using the scoliosis shawl reduced the dose significantly. Using the shawl with CT13 had a lower risk than EOS2 (AP) for female patients only.

To test the accuracy of the Cobb angle measurements on SPR images, a phantom with scoliotic spine was constructed from tissue-equivalent materials and validated. The phantom was then irradiated using the SPR mode in CT to acquire images for Cobb angle measurements. The images were visually evaluated, and 10 images were chosen for Cobb angle measurements.

The accuracy of measuring Cobb angle measurements on SPR images was reported and showed that the images can provide results within the clinically acceptable margin for error. Overall, the difference from the true angle was –2.75°. The most accurate Cobb angle measurements were obtained from CT5 (PA), which had lower radiation risk than DR2 (PA) for male patients. CT4, 8 and 11 were among the imaging protocols that had lower risk than their corresponding imaging protocols in DR, and they provided Cobb angle measurements within the clinically acceptable error.

Chapter 5: Discussion

5.1 Chapter overview

The use of ionising radiation in medical imaging plays an essential role in medicine. For patients with AIS, X-ray images enable the determination of the severity of the spinal deformity and the monitoring of its progression. This means that patients with AIS undergo several X-ray examinations during the management of their deformity. These repeated examinations bring with them an amount of radiation dose and subsequent increased risk of developing radiation-induced cancer. The aim of this study was to investigate the use of the SPR mode in CT scanning for assessing AIS to reduce the risk associated with using ionising radiation in such patients. This scanning mode is known for delivering a low radiation dose and, most importantly, is available at most hospitals, which means that, if proven to be valid, not only will it benefit patients by reducing the risk from radiation, it will also benefit health providers by reducing the cost of installing specialised imaging machines, such as the EOS, and consequently the staff will require minimal additional training.

This study represents the first investigation into the possibility of using SPR mode of CT scanners for the assessment of AIS by establishing the organ-specific radiation dose using direct measurement. Moreover, the accuracy of Cobb angle measurements on SPR images was also assessed by building a novel phantom to represent an adolescent patient with scoliosis.

The present chapter discusses the results of the experiments of this study and uses the same structure used in Chapters 3 (Method and materials) on **page 69** and 4 (Results) on **page 115**. First, the dose measurements are discussed, in which the radiation dose from SPR, DR and

EOS are quantified. This is followed by a discussion of the construction and validation of the phantom with a curved spine, and the accuracy of Cobb angle measurements on SPR images is discussed. At the end of this chapter, the implications of using SPR to assess AIS in clinical practice are discussed. That includes looking at the features of the currently used CT scanners and the possibility of the optimisation for assessing AIS. Lastly, the limitations encountered in this study are discussed.

5.2 Radiation dose measurements

The radiation dose from using SPR for assessing AIS was quantified, analysed and compared with those from DR and EOS. For this purpose, a dosimetry phantom representing a 10-year-old child and TLDs were used. Unlike many published studies that estimated the risk associated with AIS imaging using indirect mathematical measurements (i.e. PCXMC) or using a sample of organ locations to measure the OD, this study measured the radiation dose to all organs, as indicated in the ICRP report 103 (2007) using TLDs. Using all the dosimetric locations inside the dosimetry phantom allowed for more precise evaluation of the OD compared with assessing the OD by a sample of locations (Clavel et al., 2016). The benefit of measuring the radiation dose to all organs for SPR, DR and EOS is that it reduces the potential of introducing errors in the dose estimation.

As discussed in **Section 2.2.2** on **page 26**, quantifying radiation dose using direct measurements provides more accurate information compared with the computational methods. Moreover, the computational methods are usually designed for calculation of the radiation dose from a specific machine since the operating principles and the geometry of imaging varies with the technology. In this study, the radiation dose from SPR, DR and EOS were compared. Therefore, using one modelling software to estimate the risk from these

imaging machines might have introduced inaccurate measurements. For example, PCXMC, which is designed for dose calculation for projection radiography, is not valid for EOS dose calculation because of how X-rays are projected differently by projection radiography (Clavel et al., 2016), and it does not account for the bowtie filter in CT scanners (Tapiovaara, 2012) as discussed in **Section 3.2** on **page 70**. The outcomes of the dose measurements are more likely to represent reality in comparison with work already published that used indirect mathematical measurements.

Performing radiation dose measurements is complicated and requires time and resources, which are often lacking. Several previous studies (Chamberlain *et al.*, 2000; Hensen *et al.*, 2003; Lee, McLean and Robinson, 2005; Abul-Kasim *et al.*, 2008, 2010; Gialousis *et al.*, 2008; Abul-Kasim *et al.*, 2009; Deschênes *et al.*, 2010; Mogaadi, Ben Omrane and Hammou, 2012; Ben-Shlomo *et al.*, 2013; Ilharreborde *et al.*, 2013; Kalra *et al.*, 2013; Damet *et al.*, 2014; Luo *et al.*, 2015; Hui *et al.*, 2016; Law *et al.*, 2016, 2018; Branchini *et al.*, 2018; Hwang *et al.*, 2018) were carried out using conventional radiography imaging machines (i.e. SF, CR, DR) and EOS; however, direct comparison between data in this study and those in these publications' studies is difficult for several reasons. First, the risk estimation methods vary among the published studies: this includes using either direct (e.g. TLD for OD estimation) or indirect measurements (e.g. mathematical modelling) of the radiation dose and different types of radiation detectors, phantoms, representative ages and imaging machines. Within this study, to ensure fair dosimetric comparisons among the imaging systems and increase the validity of the measurements, the same method and materials were used to quantify radiation dose from SPR, DR and EOS.

In addition to the dosimetry phantom and TLDs, the scoliosis shawl made from 0.5-mm lead-equivalent materials was assessed during the dose measurements to establish its effectiveness

in reducing the risk of developing radiation-induced cancer when using SPR and DR for assessing AIS. This study is, to the best of the author's knowledge, the first to use the scoliosis shawl in the dose measurements and report its effect on radiation dose. In the dosimetry experiment, the shawl was used when measuring radiation dose for AP projections only for SPR and DR. It was not used when using the EOS, and this was so for two reasons: 1) the EOS can acquire two projection simulations (i.e. AP and lateral projection), whereas the shawl is not designed to protect the breast while acquiring lateral images; and 2) because further reduction in the dose delivered to patients can be achieved using specialised imaging protocols (e.g. the micro dose imaging protocol) (Hui et al., 2016; Newton et al., 2016).

5.2.1 OD for SPR exposure

5.2.1.1 *Analysis of the OD: without using the scoliosis shawl*

The radiation dose delivered by the SPR mode in a CT scan when used to image the spine has not been previously investigated. In general, studies that investigated the radiation dose from SPR are very limited. This is probably so because of the widespread assumption that the amount of delivered radiation is negligible (Nauer et al., 2009); for example, the ED of an abdominopelvic examination in SPR is 0.27 mSv (Schmidt et al., 2013) compared with 14.4 mSv of the standard (i.e. helical) CT examination of the same area (ICRP, 2007). Consequently, there is little information on the delivered dose when using SPR, and where this information exists, it describes the amount of radiation from using SPR for scanning other parts of the body, other than the spine (Daniel et al., 2005; Nauer et al., 2009; Schmidt et al., 2013; M.S. Kim et al., 2017). In the SPR mode, the radiation dose delivered to the [dosimetry] phantom used in this study was affected strongly by the acquisition parameters (i.e. kV and mA) and tube position. These findings are in agreement with the existing

literature on SPR of other body parts (i.e. head, thorax and abdominopelvic) (Daniel et al., 2005; Nauer et al., 2009; Schmidt et al., 2013; M.S. Kim et al., 2017).

When assessing AIS using SPR to acquire AP images without the scoliosis shawl, the thymus, breasts, heart, thyroid and stomach received the highest radiation dose. As the scanning range was set to include the entire spine, these organs were inside the primary beam. **Figure 4.1–Figure 4.5** on **pages 117–119** show the OD values for these organs in terms of the imaging parameters and projections. The figures show that the OD was affected by the projection of the imaging in SPR mode (i.e. AP or PA), in which organs in close proximity to the X-ray tube received a significantly ($p < 0.05$) higher radiation dose than the organs located further away. Overall, organs received a lower OD in PA when the phantom was in the PA position. The reduction was achieved due to the low-energy X-rays being absorbed by the superficial tissue and organs closest to the X-ray tube. The X-ray beam is attenuated as it progresses through the body, consequently reducing the number of X-rays available for absorption (Wong et al., 2011).

The above finding can be clarified by way of an example. The breast OD was reduced, on average, from 0.148 mGy (*SD* = 0.134, range 0.027 to 0.436 mGy) to 0.041 mGy (*SD* = 0.042, range 0.006 to 0.0135 mGy) when the imaging projection was changed from AP to PA. Because of the breast positions in PA projections in relation to the X-ray tube, the body attenuated the X-ray photons as they passed through it. Additionally, when the tube was positioned to acquire PA images, the CT table contributed to absorbing some of the X-ray photons before they reached the phantom (Daniel et al., 2005). A recent study investigated the effect of the CT table on patient dose and found that the table attenuates approximately 20% of breast OD (Nowik et al., 2017). It is worth mentioning that the study was performed using

simulation software, and the measurements were performed on an adult phantom with and without the presence of the table.

Figure 4.1– Figure 4.5 on **pages 117–119** also show that the OD values are affected by changes in the tube kV and mA. Lowering the kV and mA decreased the OD values. This is because, as the kV decreases, X-ray photons become less penetrative (i.e. lower energy), meaning they are more likely to be absorbed by the superficial tissue (Ofori et al., 2016). The OD decreases exponentially as the kV decreases (Mayo-Smith et al., 2014; Kaza et al., 2014; Hoye et al., 2019); a study by Kaza *et al.* (2014) demonstrated that reducing the kV from 120 to 80 (~33% reduction) resulted in a 65% reduction in the dose. Similarly, lowering the mA decreases the quantity of the generated X-ray photons; hence, fewer X-ray photons interact with the phantom (Elojeimy et al., 2010; Chang et al., 2013). However, the relationship between the dose and the mA is linear; meaning a 50% decrease in the mA results in a 50% decrease in the dose (Raman et al., 2013; Zacharias et al., 2013)

When acquiring lateral images where the right side of the phantom faces the CT image receptors (Whitley et al., 2005), the spleen received the highest dose (0.135 mGy) because it is on the left side of the body and was, therefore, close to the tube. In clinical practice, the side of lateral projection is selected based on the direction of the curve in the AP or PA images, in which the bent part of the spine is positioned near the imaging receptor for better image visualisation; despite that, the right lateral projection is preferred because the radiation risk is slightly lower (Ben-Shlomo et al., 2016). Nonetheless, no significant difference between the overall dose received at right and left lateral projections has been reported (Chaparian et al., 2014).

5.2.1.2 *Analysis of the OD: with using the scoliosis shawl*

When using the scoliosis shawl on the phantom and when irradiated using the SPR mode in AP projections, the dose to the breasts was reduced by more than 80%; on average, the dose was reduced from 0.148 mGy (*SD* = 0.134, range 0.027 to 0.436 mGy) to 0.021 mGy (*SD* = 0.022, range 0.002 to 0.073 mGy) (**Figure 4.10** on **page 123**). The shawl significantly ($p < 0.05$) reduced the dose to the breasts by absorbing most of the X-ray photons from the primary beam, but the breasts still received a few higher-energy photons that passed through the shawl and some of the scatter radiation inside the phantom. **Figure 4.11** on **page 124** shows the effect of using the shawl on the lungs OD. Similar to the breasts OD, the lungs OD was reduced significantly ($p < 0.05$) by more than 70%; on average, the dose was reduced from 0.102 (*SD* = 0.089, range 0.020 to 0.297 mGy) mGy to 0.029 mGy (*SD* = 0.0313, range 0.004 to 0.015 mGy). Overall, the shawl reduced the dose to a similarly low level achieved when the phantom was irradiated in the PA projection with no significant difference ($p > 0.05$). However, for the radiosensitive organs, the breasts and lungs, the shawl reduced the dose significantly in the AP projection compared with the PA without using the shawl ($p < 0.05$). This suggests that, for SPR images, AP with scoliosis shawl is better than PA in terms of breast dose reduction. The shawl could potentially have greater implications on the reduction of the risk associated with the repeated use of X-rays when assessing AIS using SPR because of the substantial dose reduction.

5.2.2 Comparison of SPR OD with that of DR and EOS

Only a few studies have investigated the risk associated with using X-ray for assessing AIS (**Table 2.6** on **page 55**). As shown in **Table 5.1**, the breast OD values were lower for DR and EOS than those published by Damet *et al.* (2014), Branchini *et al.* (2018) and Hwang *et al.*

(2018). For DR, this dose difference could have been due to the use of different dose measurement/estimation methods. Hwang *et al.* (2018) used PCXMC to calculate the OD from DR when used for assessing AIS. PCXMC has been shown to significantly overestimate OD values, especially for paediatric patients because of how the [stylised] phantoms used in PCXMC oversimplify the human body (Siiskonen et al., 2007; Borrego et al., 2018). Moreover, the difference between the OD values could have been due to differences in the acquisition methods and parameters used in the imaging experiments. In the case of the EOS, Damet *et al.* (2014) and Branchini *et al.* (2018) used the standard EOS protocol, the dose of which is higher than the microdose used in this study (Ilharreborde et al., 2016). Additionally, they used phantoms representing adults; therefore, they used higher kV and mA values during imaging. They used 90 kV and 200–250 mA for AP images and 105 kV and 250–320 mA for lateral images, whereas for the work in this study used 75 kV and 200 mA for AP images and 95 kV and 200 mA for lateral images. As discussed previously, lowering the acquisition parameters reduces the dose delivered to patients.

Table 5.1: Breast OD when using DR and EOS compared with breast OD reported in the literature.

Study	Imaging machines	Human age that the phantom represents	Type of measurements	Imaging projection	Breast OD (mGy)
Damet *et al.* (2014)	EOS	Adult	Direct (TLD)	AP+Lateral	~ 0.34
Branchini *et al.* (2018)	EOS	Adult	Direct (TLD)†	AP+Lateral	0.34
This study	EOS	Child (10-year-old)	Direct (TLD)	AP+Lateral	0.04
Hwang *et al.* (2018)	DR	Child (10-year-old)	Indirect	AP	0.38–0.85
This study	DR	Child (10-year-old)	Direct (TLD)	AP	0.12

† Breast OD was not measured directly; instead, the liver and stomach OD values were averaged to obtain the breast OD.

For DR and EOS OD values, a similar trend for the SPR OD values was observed, in which organs in close proximity to the X-ray tube had higher OD values (**Table 4.2** on **page 126**). Moreover, the breast was among the organs that received a high radiation dose. The effect of changing the imaging parameters on the OD for DR and EOS was not tested because the irradiation of the phantom was carried out once in each projection (i.e. AP, PA and lateral for DR and AP+Lateral, AP and lateral for EOS). As mentioned in **Section 3.2.2** on **page 82**, the imaging parameters used to irradiate the phantom were based on the local guidelines for imaging an average 10-year-old child.

When comparing the average OD values of the SPR imaging protocols with those of DR and EOS and as shown in **Table 4.3** on **page 132** and **Table 4.5** on **page 133**, some of the SPR imaging protocols used to irradiate the phantom delivered lower radiation dose than those of DR. These SPR imaging protocols are were: CT1 (AP, 120 kV, 10 mA), CT7 (AP, 100 kV, 10 mA), CT8 (AP, 100 kV, 20 mA), CT13 (AP, 80 kV, 10 mA) and CT14 (AP, 120 kV, 10 mA), and they delivered significantly ($p < 0.05$) lower radiation dose than DR1 (AP, 85 kV, [5.9 and 9.5 mA]) when acquiring AP images. On the other hand, when acquiring PA images, CT4 (PA, 120 kV, 10 mA), CT5 (PA, 120 kV, 20 mA), CT10 (PA, 100 kV, 10 mA), CT11 (PA, 100 kV, 20 mA), CT16 (PA, 80 kV, 10 mA), CT17 (PA, 80 kV, 20 mA) and CT18 (PA, 80 kV, 30 mA) delivered significantly ($p < 0.05$) lower radiation dose than DR2 (PA, 85 kV, [4.3 and 12.2 mA]). The single projection EOS imaging (i.e. EOS2) delivered the lowest radiation dose compared with the AP imaging projections of SPR and DR.

The reason behind lower radiation dose in SPR imaging protocols compared with DR, even with higher values of kV and mA used with SPR, could be the auto-stitching feature in DR. This feature was introduced to enable DR to capture the entire spine in one image. To do so, DR irradiation is overlapped at the area where the images will be stitched together; the

overlap enables the software used in DR to identify the end of one image and the start of the other (Yang et al., 2016; Hwang et al., 2018). An overlapping regain might occupy 16–32% of the image (Yang et al., 2016). This occurred as some of the TLDs inside the phantom were exposed twice, resulting in recording in high radiation dose when using DR compared with SPR.

Using the scoliosis shawl contributed to dose reduction when using DR and SPR. Several SPR imaging protocols with the scoliosis shawl: CT1, CT7, CT8, CT13, CT14 and CT15 delivered significantly lower radiation dose than DR with the scoliosis shawl. However, the dose measurement results confirmed that three SPR AP imaging protocols without the shawl were capable of delivering significantly ($p < 0.05$) lower radiation dose than DR with the shawl. The benefit of this is that SPR could be used instead of DR, especially in AIS with severe cases, in which using the shawl could interrupt the appearance of the spine. More interesting is that SPR imaging protocol CT13 with the shawl delivered a similar level of radiation dose to the dosimetry phantom to that of the EOS when it was used to acquire an AP image with no significant difference ($p > 0.05$). This could be promising for patients in terms of reduction where EOS is not available.

Acquiring lateral images using SPR, DR and EOS, in general, delivered lower radiation dose to the phantom compared with acquiring AP and PA images. As discussed earlier, this is because most of the organs are not in close proximity to the X-ray beam as in the AP and PA projections. Compared with DR3 (lateral), eight out of nine SPR lateral imaging protocols delivered significantly lower radiation dose. EOS delivered the lowest dose when acquiring lateral images. The DR delivered the highest for lateral images, which could be because of the auto-stitching feature, as previously mentioned. These findings illustrate the advantages of the EOS over SPR and DR in terms of dose reduction to the phantom; however, SPR has the

potential of reducing the dose to AIS patients compared with DR when optimised to acquire lateral images.

The results from the SPR OD values indicated that, from a dose level perspective, SPR can be used instead of DR with significant does reduction to AIS patients compared with DR. Further reduction in the SPR dose can be achieved by using the scoliosis shawl. However, the OD values only show the amount of radiation delivered to the dosimetry phantom without providing information about the radiation-related risk. As discussed in **Section 2.2.1.1** on **page 19**, the OD does not take into account the radiation type and the sensitivity of the organ to be radiated. The following section discusses the ED, which has a better description of the risk associated with radiation than the OD.

5.2.3 ED

Though ED has been criticised recently (NAS, 2006; Brenner, 2008; Brenner, 2012; Andersson et al., 2017), it is worth including it in this study as many publications have reported on this concept in recent years. Unlike the OD, the ED provides a better description of the risk of health damage from radiation. The ED accounts for the type of radiation and the sensitivity of the organ to radiation (Costa et al., 2016). Despite the controversy regarding how organ sensitivity to radiation is calculated and its periodical review, the ED is a useful tool for comparing the potential risk delivered by different imaging systems and their imaging protocols (Mettler et al., 2008; IAEA, 2013; Harrison and Lopez, 2015). As discussed earlier (**Section 2.2.1.2** on **page 20**), the calculation of the ED is dependent on the basic dosimetry quantities and cannot be directly measured by a dosimeter (Bor et al., 2004; ICRP, 2007).

The ED of the SPR imaging protocols (**Table 4.8** on **page 137**) varied with the imaging projection, acquisition parameters and the usage of the scoliosis shawl. As the ED is

calculated based on the OD, a trend for changes similar to that of the OD was observed when these factors were altered. The ED of SPR, when used for assessing AIS, has not been reported in the literature; consequently, the data in this study are novel. However, the ED from the conventional radiography machines (SF, CR, DR) and the EOS have been widely investigated (Chamberlain *et al.*, 2000; Hensen *et al.*, 2003; Lee, McLean and Robinson, 2005; Abul-Kasim *et al.*, 2008, 2010; Gialousis *et al.*, 2008; Abul-Kasim, Strömbeck, *et al.*, 2009; Deschênes *et al.*, 2010; Mogaadi, Ben Omrane and Hammou, 2012; Ben-Shlomo *et al.*, 2013; Ilharreborde *et al.*, 2013; Kalra *et al.*, 2013; Damet *et al.*, 2014; Luo *et al.*, 2015; Hui *et al.*, 2016; Law *et al.*, 2016, 2018; Branchini *et al.*, 2018; Hwang *et al.*, 2018) (**Table 2.6** on **page 55**).

From the OD data in this study, the calculated ED of AP projections for SPR without using the scoliosis shawl was 0.02–0.25 mSv depending on the acquisition parameters compared with 0.08 mSv (AP using DR), 0.03 mSv (AP+Lateral using EOS1) and 0.01 mSv (AP using EOS2) (**Table 4.8** on **page 137**). The ED of five SPR imaging protocols for AP projections, CT1, CT7, CT8, CT13 and CT14, were lower than the ED of the DR imaging protocol DR1 that was used for irradiating the phantom in the AP projection. As discussed previously, the OD values of those SPR imaging protocols were significantly lower than those of DR1 ($p < 0.05$). The ED of SPR AP imaging protocols and DR AP imaging protocol were higher than those of the EOS2 (AP).

For SPR, the calculated ED of the PA imaging protocols (**Table 4.8** on **page 137)** ranged from >0.01 mSv to 0.10 mSv, depending on the acquisition parameters, whereas the calculated ED for the PA projection when using DR was 0.03 mSv. The EDs of five SPR imaging protocols, CT 4, CT10, CT11, CT16 and CT17, were lower than the ED of DR2 (PA). The OD values of these SPR imaging protocols were significantly ($p < 0.05$) lower than

the OD values of DR2. As previously noted in **Section 4.2.1.1** on **page 125**, the OD values of CT18 were found to be significantly lower than DR2; however, the ED of CT18 and DR2 are equal (0.03 mSv), which confirms the limitation of the OD in describing the risk of radiation. Lastly, the ED of PA imaging projections in SPR were all lower than the ED of the AP imaging projections of the same acquisition parameters because organs receive a lower radiation dose in the PA projections than in the AP projection, as discussed earlier.

Table 5.2 shows the ED of DR and EOS in this study compared with the reported ED in the literature. The calculated ED of DR1 (AP) and DR2 (PA) were lower than the findings of Hwang et al. (2018) and Hui et al. (2016), respectively, because, as mentioned previously, they used PCXMC to calculate the ED, which overestimates the risk for paediatrics. Additionally, Hwang et al. (2018) scanned a larger area (from the supraorbital margin to ~2.5 cm below the symphysis pubis) compared with this study (from the C3 to the upper part of the pelvis), which could have contributed to the increase in the dose (Hwang et al. 2018). In Hui's work, the authors had to calculate the ED in 'three sections', using auto-stitching, to simulate the imaging conditions of DR when used for assessing AIS, which could have led to overlap in their simulation; in turn, this could have increased the ED.

For EOS, the ED of the AP projection with the EOS2 was much lower than the ED reported by Luo *et al.* because they used the standard EOS imaging protocol, indirect measurements to estimate the dose and a different age-representing phantom, and they scanned a larger area. For the EOS when used to acquire two images simultaneously (i.e. AP and lateral images), the ED of EOS1 (0.03 mSv) was higher than the findings of Pedersen *et al.* (2018) when they used a phantom representing a 5-year old child (0.02 mSv), but lower than their findings with the phantom representing an adult (0.04 mSv). This slight difference in the measurements could be because of size difference in the scanning area in this study and that of Pedersen *et*

al. (2018). However, the ED of EOS1 (0.03 mSv) was much lower than Damet *et al.*'s (2014) (0.20 mSv) findings mainly because they used the standard EOS imaging protocol.

Table 5.2: ED from DR and the EOS when used for assessing AIS.

Imaging machine	Study	Imaging projection	Type of dose measurement	ED (mSv)
DR	Hui et al. (2016)	PA	Indirect	0.07
	Hwang et al. (2018)	AP	Indirect	0.2–0.3
	This study	AP	Direct	0.08
		PA	Direct	0.03
EOS	Damet *et al.* (2014)	AP+Lateral	Indirect	0.2
	Pedersen *et al.* (2018)		Direct	0.04[A]
			Direct	0.02[B]
	This study		Direct	0.03
	Luo *et al.* (2015)	AP	Indirect	0.12
	This study		Direct	0.01

[A] A phantom representing an adult.
[B] A phantom representing a 5-year-old child.

Using the scoliosis shawl significantly ($p < 0.05$) reduced the ED of all AP positions in SPR and DR, giving an overall 2–3 fold reduction in ED compared with using the same imaging parameters without the scoliosis shawl as shown in **Table 4.8** on **page 137**. In SPR, the ED of the AP positions when using the scoliosis shawl was almost equal to that of the PA position (Table 5.3). Furthermore, three SPR AP imaging protocols without the shawl (namely CT7, CT13 and CT14) had a lower ED than DR with the shawl. The average OD values of these imaging protocol were significantly ($p < 0.05$) lower than DR1 with the shawl. The ED of DR in all positions, even with the scoliosis shawl, were higher than those of the EOS; however, several SPR AP imaging protocols: CT 7, CT13 and CT14 with the shawl had similar EDs to that of the EOS2 (AP).

For the AP and PA positions, these results suggest that a substantial reduction in ED for AIS patients can be achieved by using SPR in two ways: 1) using PA positions instead of AP positions or 2) using the AP position with the scoliosis shawl. For DR, using the shawl not

only reduced the dose but also improved the appearance of the spine, as the spine is closer to the image receptors in AP images, which means it appears less magnified and distorted (Ben-Shlomo et al., 2016), and the shawl could also reduce scatter and thus reduce noise in the image. **Figure 4.24** on **page 139** illustrates an overall comparison of the ED for SPR, DR and EOS; the results indicate that ED levels comparable to that of EOS can be achieved using SPR and the scoliosis shawl.

Table 5.3: The ED of PA in SPR compared to AP when using the scoliosis shawl when using the same kV and mA values*.

Imaging protocol	PA ED (mSv)	Imaging protocol	AP with scoliosis shawl ED (mSv)
CT4	0.02	CT1	0.02
CT5	0.04	CT2	0.04
CT6	0.10	CT3	0.11
CT10	0.01	CT7	0.01
CT11	0.02	CT8	0.02
CT12	0.06	CT9	0.07
CT16	> 0.01	CT13	0.01
CT17	0.01	CT14	0.01
CT18	0.03	CT15	0.03

* For example, the kV and mA values used with CT4 and CT1 are 120 and 10, respectively (list of the imaging protocols is shown in **Table 3.3** on **page 84**).

For lateral projections, the ED of EOS3 (lateral) was the lowest compared with SPR and DR lateral imaging protocols. The ED of all SPR lateral imaging protocols, except CT21, were lower than that of DR3 (lateral). Overall, the ED of lateral projections was lower than that of AP and PA projections across SPR, DR and EOS, as radiosensitive organs such as the breasts do not face towards the X-ray tube in lateral projections. The DR3 (lateral) ED of this study (0.05 mSv) was lower than that of Mogaadi, Ben Omrane and Hammou (2012) (0.59 mSv). However, Mogaadi *et al.*'s values cannot be compared easily to the data in this study because their measurements were performed on CR using PCXMC; additionally, they did not use up

to date tissue weighting factors when they calculated the ED. Moreover, the lateral ED values for DR have not been reported in the literature.

The findings from calculating the ED for SPR, DR and EOS suggest the risk from radiation dose to AIS patients can be lowered by using SPR. From the radiation dose level, SPR can be used as an alternative to DR for AIS assessment in order to lower the risk from radiation to the patients. The risk could be lowered further to the levels of the EOS by using the scoliosis shawl. However, the ED does not describe the risk of radiation in terms of age and gender (Brenner, 2008), so a better description of the radiation risk can be obtained by calculating the ER, which is the main topic of the following section.

5.2.4 ER

The ER describes the risk of X-ray examinations as a function of gender and age. Like ED, the ER in this study was calculated based on the OD. This means that the ER changes with the imaging projections and parameters in a similar trend to that of the OD. The results showed that, when female and male patients with AIS are exposed to the same number of X-ray examinations, female patients are at higher risk of developing cancer than male patients. This is probably due to the higher sensitivity of breast tissue in female patients (Ronckers et al., 2005; Ronckers et al., 2008; Brenner et al., 2018).

As shown in **Table 4.12** on **page 141**, when the projection was changed for SPR from AP to PA, female patients' risk of developing radiation-induced cancer was reduced, on average, by 66% (*SD* = 3.9, range 61% to 74%); the risk was, on average, reduced from 2.76 cases/10^6 (*SD* = 2.40, range 0.53 to 7.9 cases/10^6) to 0.98 cases/10^6 (*SD* = 0.95, range 0.14 to 3.1 cases/10^6). The main contributor to this risk reduction was, again, the breasts receiving a lower radiation dose in PA projections. The breasts received a dose that was on average 73%

(*SD* = 3.06, range 68% to 77%) higher in the AP projection compared with the PA projection, which makes PA projections preferred for imaging female patients because the breasts are further away from the beam point, and consequently the risk of developing radiation-induced cancer is reduced (Levy et al., 1996; Ron, 2003; Ronckers et al., 2010; Shuryak et al., 2010; Simony et al., 2016).

For the AP and PA projections, the risk of developing radiation-induced cancer is lower, on average, by 56% (*SD* = 2.88, range 52 to 62 %) for male patients than for female patients. In general, this agrees with the literature (Boice, 1996; German Commission on Radiological Protection, 2009; Lin, 2010; Frush, 2013; Andersson et al., 2017) and several studies that investigated the radiation risk from AIS imaging (Knott *et al.*, 2014; Law *et al.*, 2017; Yamato and Matsuyama, 2018). The higher risk for female patients with AIS is, compared with males, more likely because of the radio sensitivity of the breast tissue. The incidence of breast cancer in male patients is negligible compared with that in female patients (**Table 2.3** on **page 24**) (NAS, 2006; Feng et al., 2010; Brenner et al., 2018). Another factor that contributes to the higher risk of cancer in female patients is the lungs. The lungs have a large volume which cannot be avoided during irradiation due their location; the incidence of lung cancer due to its radio sensitivity is double in females compared with males.

Using the scoliosis shawl during SPR and DR imaging for the AP projections reduced the amount of radiation received by some radiosensitive organs, such as the breasts, lungs and kidneys, and the reduction was significant for those organs ($p < 0.05$). The female patients' risk of developing radiation-induced cancer dropped on average by approximately 64% (*SD* = 3.82, range 58% to 69%); on average, the risk dropped from 2.76 cases/10^6 (*SD* = 2.39, range 0.53 to 7.9 cases/10^6) to 1.02 cases/10^6 (*SD* 0.97, range 0.16 to 3.22 cases/10^6) (**Table 4.12** on **page 141)**. When using SPR, the breasts received, on average, an 87% (*SD* = 3.29, range 83%

to 94%) lower radiation dose in the AP projection when using the shawl compared with not using the shawl. Compared with the risk from the imaging in the PA, the risk from imaging the spine in the AP and using the scoliosis shawl was slightly increased, on average, by 7% (*SD* = 5); in PA projections, the risk was, on average, 0.98 cases/10^6, while in AP projections when using the shawl, it was 1.02 cases/10^6 .

In conclusion, the findings of this section have shown that EOS, when it was used to irradiate the dosimetry phantom in the AP position, had the lowest ED and ER compared with SPR and DR when irradiating the phantom at the same position. However, further reduction in the potential risk from using SPR for female patients can be achieved by using the scoliosis shawl and using the following parameters: 80 kV and 10 mA, or changing the position in SPR to the PA and using 80kV and 10 mA. Compared with DR, multiple SPR imaging across all evaluated kV and mA values was capable of reducing radiation risk for AIS patients significantly. From the radiation dose perspective, the results suggest that SPR can be an alternative to DR and EOS for AIS assessment.

5.3 Construction and validation of a phantom with a scoliotic spine

5.3.1 Phantom construction and validation

A phantom was built to test the accuracy of Cobb angle measurements and for optimising AIS imaging. In previously published studies, the IQ of AIS radiographic images was evaluated using patient images and optimised AIS imaging techniques using phantoms with a normal spine or an IQ phantom (e.g. the CDRAD) (Deschênes et al., 2010; Yvert et al., 2015; Ernst et al., 2018). Such studies evaluated IQ as a surrogate rather than considering the accuracy of the measurements per se. For this study, the accuracy of the Cobb angle method was considered to be a more valid approach, rather than using the surrogate measure of IQ from which an

inference might be made about accuracy. Moreover, SPR has not been used for AIS assessment; therefore, it was necessary to test the accuracy of its Cobb angle measurements. Consequently, a novel anthropomorphic phantom with AIS was constructed of a 10-year-old child. The phantom used in this study was made of inexpensive and widely available materials, and its manufacturing process was not complicated, though the time to produce it was not insignificant.

The physical characteristics of the phantom were validated using HU and SNR values. The HU of the PoP was compared with that of the endplates of a human vertebra (10-year-old girl) and a sheep vertebra, the latter being within the phantom. For validation purposes, the whole vertebra of the human or sheep was not included in the comparative evaluation because the Cobb method only uses the endplates. The vertebral body of human and sheep comprises trabecular tissue, whereas the endplates are a denser cortical bone (Bogduk, 2014; Palepu et al., 2019). The PoP vertebra was made of a mixture that simulated the endplates only to simplify the process of the phantom manufacturing. **Table 4.16** on page **146** shows that the HU values of the human, sheep and PoP vertebrae are comparable. The cortical tissue of the human vertebra showed an average HU value of 598 (*SD* = 79), which was 4.78% lower than the average HU value of the PoP vertebra (HU = 628, *SD* = 56). The cortical tissue of the sheep vertebra was, on average, 605 HU (*SD* = 83), which was 2.87% lower than the average HU value of the PoP vertebra. The *SD* of HU values can be used to show the homogeneity of the material from the CT images (Homolka et al., 2002), which means that the PoP had the same level of homogeneity as the cortical bone of the human and sheep vertebrae. Overall, the HU measurements showed that PoP is radiographically suitable to substitute for the spine of a 10-year-old child in the phantom; this is in agreement with previous studies and is within the acceptable 5% margin of error (Watanabe and Constantinou, 2006; Mohammed Ali et al.,

2018). **Table 4.17** on **page 146** shows the HU values of PMMA, which was used as a soft tissue substitute when constructing the phantom, and the HU values of soft tissue of the 10-year-old girl. The HU value of the PMMA had a small variation due to the its homogeneity; however, when the HU values of soft tissue of the girl were calculated, a huge variation was observed due to heterogeneity of the human body. Nevertheless, PMMA has been identified as an adequate soft tissue substitute in radiation dosimetry and measurement (Report 44) (ICRU, 1989) and is widely used as such, especially for non-dosimetry phantoms (Lofthag-Hansen, 2010; Chung et al., 2010; Garcia et al., 2010; Barnes and Temperton, 2011; McCullagh et al., 2011; Koivisto et al., 2013; Chambers, 2014; Yvert et al., 2015; Sossin et al., 2017).

The other measure used to validate the phantom was SNR. The PoP phantom and the anthropomorphic chest phantom (Lungman) were irradiated using different kV and mAs values (**Table 3.8** on page **106**) to determine the correlation between the PoP phantom and the Lungman phantom when irradiated under the same conditions. The correlation coefficient between the PoP and Lungman phantoms was positive and very strong ($p < 0.05$), indicating high validity for the PoP phantom when compared with the Lungman phantom. **Table 4.18** and **Table** 4.19 on **page 146** demonstrate the correlation between the SNR values of the two phantoms over the range of kV and mA; a strong or very strong correlation was observed for each kV and mA value. This high level of correlation between the PoP and Lungman phantoms illustrates the high level of physical properties (i.e. radiological properties) replication of the PoP phantom.

5.3.2 Initial visual evaluation of the PoP phantom images to determine suitability for inclusion in Cobb angle analysis

After validating the PoP phantom, the SPR images of the phantom were acquired to test the accuracy of the Cobb angle measurements. However, prior to assessing Cobb angle accuracy from the images, the images were visually evaluated to check their suitability for the Cobb angle measurement in order to eliminate images that were not fit for the purpose. Images deemed fit for the purpose had to have clearly demonstrated vertebral endplates. Using a scale, observers evaluated the endplates of the PoP spine and, based on their clarity, decided whether an image was suitable for Cobb angle measurement. Only when all observers ($N = 4$) agreed that the endplate clarity was of an acceptable standard were the endplates considered for performing Cobb angle measurements.

The scale used for selecting the images was a hybrid scale that combined the European criteria for IQ (CEC, 1996b) that was suitable for the phantom, and a scale previously used by AlQaroot (2012). This ensured that only images with a clear endplate appearance would be chosen for the measurements. In previous studies, AIS IQ was evaluated using the European criteria for IQ (CEC, 1996b), and Cobb angle measurements were evaluated by the mean inter- and intra-observer agreement (Hui et al., 2016; Ernst et al., 2018). However, these studies were performed to optimise an existing technology (i.e. DR and EOS), whereas this was not possible at this stage in the present study because this imaging mode and the PoP phantom had not been used for IQ assessment. The aim of the visual assessment in this study was to identify SPR images that were suitable for Cobb angle measurement, which is discussed in the following section. Accordingly, 10 images were selected to be of suitable quality for Cobb angle assessment.

Ultimately, the PoP phantom was constructed from low-cost materials. The cost of building this phantom was less than £200, excluding labour; in comparison, phantoms designed for radiological studies cost, on average, £10,000 or more, and normally these have a normal

straight spine. An alternative method for constructing the phantom could be 3D printing. Although this approach is still under development, the technology is promising for phantom production. The technology has enabled researchers to produce phantoms for specific purposes, such as the inclusion of pathologies (Mitsouras et al., 2015; Hazelaar et al., 2018). However, the process of constructing a phantom using 3D printers is complex and expensive (M.-J. Kim et al., 2017; Filippou and Tsoumpas, 2018; Squelch, 2018). The technology is capable of mimicking the geometry of the human body accurately; however, the materials used to produce the phantoms are still not tissue equivalent materials (M.-J. Kim et al., 2017; Solc et al., 2018; Hazelaar et al., 2018). Besides testing the accuracy of Cobb angle measurements in SPR images, as was done in this study, the phantom has the potential of becoming a tool for optimising imaging machines for AIS assessments.

5.4 Cobb angle accuracy analysis

The observers (n = 13) were trained to perform the Cobb angle measurements on two images of patients with AIS. Overall, the observers' measurements of the training images were consistent and within the clinically acceptable margin of error; consequently, all observers were processed for inclusion in the study. The *SD* of the measurements for both images were small, meaning there was not much variation in the data, suggesting that the difference between and within observers was small, as shown in **Table 4.21** on **page 148**.

For the Cobb angle measurements of the SPR images, the results from the observers suggest that SPR images can be used for evaluating AIS using Cobb's method. The Cobb angle measurements of the 10 images were within an acceptable variation of 5° among the observers, which is clinically acceptable (**Figure 4.27** on **page 149**) (Carman et al., 1990; Shea et al., 1998; Cracknell et al., 2015; Lechner et al., 2017). The average difference from

the true angle of the phantom was –2.75° (*SD* = 1.46°). Averages of 6.34°, 3.62°, 2.1° and 3.75° of variation in Cobb angle measurements have been reported in recent studies (Gstoettner *et al.*, 2007; Chan *et al.*, 2014; Lechner *et al.*, 2017; Chung *et al.*, 2018, respectively). The finding of this study is in agreement with the published variations. It is worth mentioning that the measurements were compared with a known angle of the curved spine, unlike in the previously published studies where the comparison was made within the measurements of the observers. The inter-observer agreement of the Cobb angle measurements in this study (ICC = 0.86) showed very reliable measurements and was comparable to the ICC of the conventional methods (CR and DR) with an ICC range of 0.83–0.99 (Allen et al., 2008; Srinivasalu et al., 2008; Tanure et al., 2010; Zhang, Lou, Hill, et al., 2010; Qiao et al., 2012; Langensiepen et al., 2013). The measurements were also comparable to those of EOS imaging systems with an ICC range of 0.73–0.99 (Somoskeöy et al., 2012; Ilharreborde et al., 2016; Newton et al., 2016; Goodbody et al., 2017; Bagheri et al., 2018; Morel et al., 2018).

However, when comparing the Cobb angle measurements with the known angle of the phantom spine (i.e. 14°), it appears that the angle was underestimated in 9 out of 10 images (**Figure 4.27** on **page 149**). Given the number of images used for the measurement (*N* = 10), this underestimation could not be linked to a specific reason.

The finding of this section suggests that SPR can be used in the assessment of AIS in 10-year-old children. The outcomes are promising for patients and health providers. Out of the 10 images used to test the accuracy of the Cobb angle on SPR images, the images of CT4, 8 and 11 for both genders and CT5 for male patients only were capable of providing Cobb angle measurements with the clinically acceptable margin of error at lower risk from the radiation compared with the widely used DR. Health providers will benefit from saving the cost of

installing specialised imaging machines, such as the EOS, and staff training by utilising the CT scanners which are widely available for AIS assessment.

5.5 The implications of using SPR for assessing AIS

The SPR mode in CT scanning is currently used to plan the actual CT examinations and control the acquisition parameters (i.e. mA) based on the attenuation recorded in the SPR mode. Despite being named differently by various CT manufacturers, the main principle of the SPR is similar for all such machines, in that the X-ray tube and detectors are stationary while acquiring the images. The findings of this study suggest that SPR has the potential to be used in the assessment of AIS in 10-year-old children, especially when the number of X-rays acquired during the disorder management is estimated to be between 22 and 27 as indicated in **Section 1.2** on **page 7**. Prior to using a CT scanner for this purpose in the SPR mode, optimisation needs to occur in order to reduce the dose whilst providing images of acceptable quality for Cobb angle evaluation. In many cases, such optimisation should produce dose reductions compared with DR imaging as an alternative, and the use of a radiation shield can reduce the dose for the AP position. Compared with DR, SPR has the additional advantage of not requiring image stitching. Compared with technology dedicated to AIS imaging, such as EOS, optimised SPR imaging can offer a similar or, in some circumstances, reduced dose along with the advantage of still offering images for acceptably accurate Cobb angle assessments.

CT scanners are widely available as they have many applications and are cited in various guidelines for diagnosis and treatment planning. In 2015, the Clinical Imaging Board, representing the RCRs, Society and College of Radiographers (SCoR) and Institute of Physics and Engineering in Medicine (IPEM), reported that there are 298 CT scanners in the UK.

These CT scanners are in 117 National Health Services (NHS) organisations representing 64% of NHS organisations in the UK (Clinical Imaging Board, 2015). The remaining organisations did not provide information about their CT scanners in this report. This figure shows the availability of CT scanners in the UK, which suggests performing SPR is possible in wider regions compared with the EOS, of which, as of October 2018, only three imaging machines were operating in the UK (**Table 5.4**).

Table 5.4: The availability of EOS imaging systems in the UK (Chris Davis, 2018, personal communication, 1 October).

Hospital	Status
Alder Hospital Liverpool	Installed
Sheffield Children's Hospital	Installed
Great Ormond Street Hospital London	Installed
St George's Hospital London	Awaiting final installation

CT scanners are an essential part of radiography departments. *The Diagnostic Imaging Data Set* published by NHS England showed that, from March 2017 to March 2018, 5.15 million CT scans were performed (NHS, 2018) and 0.5 million scans were performed in March 2019 (NHS, 2019). On average, the number of patients per day is 32 (Clinical Imaging Board, 2015) (Table 5.5); this means that an average of four patients are scanned in one hour per 8-hour work day. However, using SPR to assess AIS might add pressure to the current appointment system and staff working time. Patients would require the same amount of time for preparation and positioning for the SPR examination as would for CT scan; however, the duration for acquiring SPR images is much shorter than the actual CT examination. In the actual CT examination, an CT operator acquires SPR images first to visualise the patient's anatomy and set the scanning range, and then the actual examination is performed (Goldman,

2007; Hsieh, 2009). The potential of dose reduction for AIS patients when using SPR might slightly affect the current work flow, but at the same time, it could reduce the cost of installing specialised AIS imaging systems and addressing the associated staff training needed.

Table 5.5: Number of patients scanned per day by CT scanners in the UK (Clinical Imaging Board, 2015)

Daily throughput (patients/day)	Number of scanners
<10	12
10–19	31
20–29	85
30–39	95
40–49	43
>50	26
Unknown	6
Total	298

The current CT systems allow for changing the acquisition parameters and tube position when acquiring SPR images. **Table 5.6** shows all CT systems that are in the NHS Supply Chain (NHS Supply Chain, 2019) and their different manufacturers. These CT scanners share the same feature, where an operator has a limited selection of kV and wide range of mA in the SPR mode. The X-ray tube in these imaging machines can be positioned as required, which allows for acquiring images from different positions. Manipulating the acquisition parameters and imaging projection in SPR provide an opportunity for dose optimisation (Schmidt et al., 2013; Saltybaeva et al., 2019). Recent studies have shown that the SPR dose can be significantly reduced while maintaining the quality of its images (Bohrer et al., 2017; Schmidt et al., 2017); that means the SPR mode in CT scanning can be optimised to be used for AIS assessment.

Table 5.6: Specifications of all CT scanners in the NHS Supply Chain†.				
Manufacturer	Model	kV selection	mA range	SPR acquiring time
Toshiba (used in this study)	Aquilion CT 16	80, 100, 120, 135	10–1050	Images appear as soon as the scan finishes.
Canon*	Aquilion Lightning	80, 100, 120, 135	10–420	
	Aquilion Prime SP (80 and 160 slice)	80, 100, 120, 135	10–600	
	Aquilion One Genesis	80, 100, 120, 135	10–900	
GE	Revolution CT	70, 80, 100, 120, 140	10–740	
	Revolution Frontier	80, 100, 120, 140	10–835	
	Revolution EVO	80, 100, 120, 140	10–560	
	Optima 520 and 540	80, 100, 120, 140	10–440	
	Cardiographe	80–140	50–600	
	Optima 660 SE	80,100, 120, 140	10–560	
	Revolution SE	70, 80, 100, 120, 140	10–740	
	Revolution GSi and HD	80, 100, 120, 140	10–835	
Neurologica	Body Tom	80–140	0–300	
	Cere Tom	80, 100, 120, 140	1–7	
	NeuViz 16	90, 120, 140	30–420	
	NeuViz 64	80, 100, 120, 140	30–420	
	NeuViz 128	80, 100, 120, 140	30–667	
Philips	MX 16 EVO	90, 120, 140	30–420	
	Brilliance iCT SP	80, 100, 120, 140	10–1000	
	Ingenuity Flex, Core and Elite	80, 100, 120, 140	20–665	
	Iqon Spectral CT	80, 100, 120, 140	10–1000	
	Incisive	70, 80, 100, 120, 140	10-420	
Siemens	Somatom Scope Power	80, 110, 130	25–345	
	Somatom Force	70–150	20–1300	
	Somatom Drive	70–140	650 and 750	
	Somatom Definition AS+	70, 80, 100, 120, 140	20–666	
	Somatom Definition Stellar Edge	70, 80, 100, 120, 140	20–800	

	Somatom Edge Plus	70–140	20-800	
	SOMATOM Definition Flash	70, 80, 90, 100, 120, 140	28–800	
	SOMATOM Go.Up and Go Now	80, 110, Sn110, 130, Sn130	13–400	
	SOMATOM Go.Top and Go All	70, 80, 90, 100, 110, 120, 130, 140	13–825	
	Somatom Perspective 64 and 128	80, 110, 130	20–345	
	Somatom Perspective 64 and 128	80, 110, 130	20–345	
* In 2016, Canon acquired Toshiba Medical System and changed their CT to the Canon CT scanner. † The data in this table were gathered from the following sources: (Philips Healthcare, 2010a; Philips Healthcare, 2010b; GE Healthcare, 2010; Siemens Healthcare, 2012; Siemens Healthineers, 2017; Siemens Healthcare, 2018; Siemens Healthineers, 2018; NHS Supply Chain, 2019; Imaging Technology News, 2019; Philips Healthcare, 2019).				

A major drawback of using SPR to assess scoliosis is that the scanning is performed in a non-weight bearing position. This means the scoliosis measurements are slightly underestimated when using the Cobb angle (Torell *et al.*, 1985; Lee, Solomito and Patel, 2013; Keenan *et al.*, 2014; Brink *et al.*, 2017). However, previous studies have shown that these measurements are reliable and strongly correlated to measurements performed on standing images, meaning a mathematical correction to a weight-bearing measurements is achievable (Wessberg, Danielson and Willen, 2006; Brink *et al.*, 2017). The difference between Cobb angle measurements of SPR images and those of upright images might be minimal when patients are wearing spinal orthoses, such as a Boston brace that helps to straighten the spine and prevent spinal deformity. Therefore, as spinal movement is limited (Lee, 2018; Rolin and Carter, 2019), accurate measurements can be achieved from images acquired in a non-weight bearing position while patients are wearing a brace. In addition, the difference between standing and supine measurements is reduced as the AIS patients ages due to bone stiffening, as indicated in **Section 2.5.1.2** on **page 47**. In these occasions, the difference between standing and supine measurements is minimum, which suggests that Cobb angle

measurements comparable to the DR can be achieved using SPR. Recommending the use SPR in the initial assessment was not the intention for this study. Instead, the SPR mode can be used for follow-up imaging where the progression of AIS is monitored. By doing so, the dose to patients can be lower than with DR, and further reduction can be achieved by using the scoliosis shawl.

5.6 Limitations

Every possible effort was made to ensure the accuracy and validity of the findings. Nevertheless, the study was carried out under ideal conditions and using phantoms. In doing so, some factors that usually influence AIS examinations were not considered, such as patient movement during the scan. The following sections detail the limitations of each section of this study.

5.6.1 Limitations of radiation dose measurements

The study findings provide an indication of the risk associated with the X-ray imaging system used to irradiate the phantom; however, due to the stochastic nature of X-rays and the differing output of the various imaging systems, radiation dose measurements might be different when using other CT scanners. The dosimetry phantom should be used to estimate the dose for the SPR mode in the other CT scanners. Using other measures such as CTDI ($CTDI_{vol}$ for SPR, in particular) for estimating patients' dose is not recommended. Despite being used by several CT manufacturers for measuring patients' dose in the SPR mode, the American Association of Physicists in Medicine (AAPM) recommend against using CTDI for this purpose because it was adopted by the manufacturers without scientific support (Andersson et al., 2019). AAPM claims that CDTI is designed for estimating dose in a CT scanner with a rotating X-ray tube, contrary to SPR, where the tube is fixed during the

irradiation. If $CTDI_{vol}$ for SPR validity is eventually approved, this could speed the process for estimating with different types of CT scanners.

The phantom used for the dose measurements represented an average 10-year-old child; however, children at that age develop at different paces and have different shapes. With the current valid approaches for dose measurement, this can be overcome by using another phantom representing the patients from 15 and 18 years of age to estimate the dose from SPR when used for AIS assessment. This would provide a range of dosimetry data that could be used as indications of radiation risk for AIS patients who are 10 to 18 years of age. Another limitation in the dose measurements is that the dosimetry phantom represents a child with a normal spine, and the phantom does not account for the organ dislocation associated with AIS. Additionally, since the locations of organs inside the human body are not fixed, as in a dosimetry phantom, moving from a standing position to supine may affect the radiation dosimetry estimations. Further, the effect that the mass of the scoliosis shawl used in this study has on the spine and Cobb angle measurements is unknown. A further limitation concerning the shawl is that, in this study, the optimum location for placing the shawl was identified by irradiating the phantom several times. This is not possible when the shawl is used for humans for ethical reasons.

5.6.2 Limitations of the PoP phantom and selection of SPR images

Although the PoP phantom represented the spine of a patient with AIS very well, it was not, however, without limitations. The PoP phantom did not permit for lateral images, as the configuration of the PMMA slabs produced considerable artefacts. Second, the PMMA and PoP had a uniform representation of soft tissue and bone, respectively, which did not reflect the nature of the human body. The geometry of the phantom may not be similar to the

geometry of a human in reality, which is complex and cannot be replicated using the inexpensive materials used in this study. For instance, an approximate shape was used for the lungs to ensure the presence of air inside the phantom. In general, phantoms suffer from this problem in experimental research as they only intend to approximate a clinical situation. In addition, the phantom did not include the pelvis region, which could have had an impact on scatter within the image. The inclusion of the pelvis in the phantom is suggested for future work. Lastly, the spine inside the phantom was fixed, so it did not allow the testing of weight-bearing position changes. It is expected that, as 3D printing becomes more available in the future, tissue substitute materials for 3D printing might be introduced. Thus, 3D printing technology could offer better presentations of human body geometry compared with the PoP phantom.

5.6.3 Limitations of Cobb angle measurements

A relationship between the dose and the accuracy of the Cobb angle could not be established. The reasons behind this are: 1) large variation in the Cobb angle measurements is expected and 2) variation also existed in the selected most tilted vertebrae. Establishing this would require the acquisition of several SPR images with different acquisition parameters and the recruitment of a large number of observers to perform the measurement, which could not be performed in the present study due to time and resource restrictions. Further, the phantom used for the measurements represents one type of AIS (i.e. mild case), using phantoms that represent the other types (i.e. moderate and severe) would have increased the validity of the study.

5.7 Chapter summary

This chapter has discussed the results of quantifying radiation dose measurement from SPR, DR and the EOS for assessing AIS. Due to the different methods used for quantifying the radiation dose, it was difficult to compare the present findings with those of published studies. Comparison in the present study found that the EOS has the lowest dose, and SPR delivered a lower radiation dose than DR. The construction and validation of a phantom with a scoliotic spine was also discussed; the phantom has been proven valid for testing the accuracy of Cobb angle measurements or for optimising an imaging system for assessing AIS. Further, the phantom was used to test the accuracy of Cobb angle measurements on SPR images; it was shown that the SPR mode can yield measurements with an acceptable margin of error.

Chapter 6: Conclusion

This study aimed to test the suitability of using the SPR mode in CT scanning to assess AIS from the perspective of radiation dose and the accuracy of the Cobb angle measurement. All imaging machines that are currently used clinically or that are being developed for assessing AIS were examined. The advantages and disadvantages of each imaging system were evaluated. Reviewing the literature indicated that the SPR mode is not widely used for diagnostic purposes and, in particular, not for assessing AIS, despite the possibility of providing valuable information. Therefore, to test this scanning mode for assessing AIS, its radiation dose levels were quantified and compared with those of DR and the EOS using the same method and materials to ensure a fair comparison. SPR delivered lower radiation and had less risk compared with DR at certain acquisition parameters. Additionally, using the scoliosis shawl reduced the radiation dose by >80%.

To evaluate the accuracy of Cobb angle measurements on SPR images, a phantom with a scoliotic spine was built and validated. The phantom was scanned using SPR, and the findings suggested that SPR imaging can be used for assessing AIS. Accurate measurements were achieved with radiation dose lower than those of DR; however, prior to implementing the recommendations into practice, it is essential that optimisation be conducted to identify the SPR imaging parameters that lead to the most accurate Cobb angle measurements along with low dose.

Overall, the outcome of the present study is promising for patients and healthcare providers because it offers an opportunity to reduce patient dose and achieve clinically acceptable Cobb angle measurements while using existing CT technology that is available in most hospital settings. The latter, of course, could be important in a cost-challenged healthcare

environment. Patients will benefit from the reduction of the risk associated with using X-ray for scoliosis assessments while health providers will benefit from cost reduction by using an existing imaging technology instead of installing specialised imaging machines such as EOS. Patients are in the supine position when performing the scan using SPR, which is not ideal due to the absence of the gravitational load leading to an underestimation of Cobb angle, therefore this study recommends using SPR only for monitoring the progression of the curve. The measurements from SPR can then be correlated to the measurements from the initial assessment images acquired while patients are standing. In addition, SPR should not be used for AIS assessments where the EOS and other specialised non-ionising imaging machines such as the ST are already available.

6.1 The novelty of the study

This study is the first to measure the OD using TLD for all organs recommended in the ICRP 103 to estimate the risks associated with using X-rays to assess AIS. It is the first to quantify and analyse the radiation dose from the SPR mode in CT scanning for a phantom representing 10-year-old child. It is also the first to quantify the radiation dose from a DR imaging system with auto-stitching features using direct measurement and to measure the OD for all organs recommended in the ICRP 103. This study also used a scoliosis shawl in the dose measurements to evaluate its effectiveness in reducing patients' dose and, consequently, the risk associated with using radiation. The SPR data provide a comprehensive overview of the radiation dose levels to which a patient can safely be exposed. This study is also the first to test the accuracy of Cobb angle measurements on SPR images using a novel phantom with a scoliotic spine.

6.2 Future work

This study has shown that the SPR mode in CT scanning can be used to assess AIS by describing its radiation dose level and its Cobb angle measurements. Further work, however, can be carried out in the following areas:

1. Optimising SPR in CT scanners from different manufacturers to identify SPR image parameters could result in the most accurate Cobb angle measurements with the lowest dose for AIS measurements.
2. Acquiring more SPR images of the PoP phantom for Cobb angle measurements using similar acquisition parameters, recruiting observers to perform the measurements and repeating the measurements at specific intervals, such as one week, could establish, if any, a relationship between the accuracy of Cobb angle measurements and the dose.

3. Conducting clinical trials on patients positioning on the CT table to determine the optimum patient's position that provide Cobb angle measurements in supine position with the least difference to a weight-bearing position. However, this type of trails should not be conducted on adolescent for ethical reasons, and to the best of the author's knowledge, phantoms with flexible spine do not exist. An alternative to adolescents and phantoms can be adolescent cadaver; nevertheless, obtaining such a cadaver with scoliotic spine might be difficult.

Appendices

Appendix I. OD values for SPR, DR and EOS

Table I: OD values (mGy) when using different mA values and imaging projections in SPR at 120 kVp						
Imaging projection	AP			PA		
mA	10	20	30	10	20	30
Imaging protocol	CT1	CT2	CT3	CT4	CT5	CT6
Brain	0.001	0.001	0.001	0.001	0.001	0.002
Active Bone Marrow	0.022	0.045	0.105	0.013	0.028	0.082
Eyes	0.000	0.001	0.003	0.001	0.001	0.001
Thyroid	0.068	0.129	0.359	0.009	0.019	0.064
Oesophagus	0.041	0.084	0.256	0.025	0.054	0.153
Lungs	0.062	0.110	0.297	0.035	0.071	0.200
Breasts	0.075	0.158	0.436	0.019	0.040	0.135
Liver	0.073	0.131	0.311	0.018	0.038	0.107
Stomach	0.080	0.149	0.344	0.015	0.032	0.094
Urinary bladder	0.071	0.139	0.257	0.006	0.012	0.033
Colon	0.068	0.119	0.230	0.016	0.034	0.086
Ovaries	0.047	0.088	0.156	0.008	0.019	0.046
Salivary Glands	0.001	0.002	0.008	0.000	0.000	0.003
Thymus	0.111	0.183	0.480	0.009	0.021	0.072
Spleen	0.045	0.087	0.190	0.030	0.058	0.155
Kidneys	0.027	0.048	0.101	0.046	0.088	0.256
Adrenals	0.025	0.044	0.118	0.049	0.102	0.298
Heart	0.081	0.128	0.369	0.017	0.042	0.106
Pancreas	0.070	0.115	0.275	0.024	0.048	0.131
Gall Bladder	0.031	0.056	0.134	0.003	0.007	0.021
Uterus	0.016	0.032	0.054	0.002	0.007	0.018
Oral mucosa	0.001	0.003	0.011	0.000	0.001	0.005
Small Intestine	0.082	0.140	0.294	0.015	0.030	0.093
Extrathoracic region	0.032	0.055	0.178	0.017	0.036	0.113
Prostate	0.006	0.010	0.017	0.001	0.005	0.041
Testes	0.001	0.004	0.004	0.001	0.001	0.001

Table II : OD values (mGy) when using different mA values and imaging projections in SPR at 100 kVp						
Imaging projection	AP			PA		
mA	10	20	30	10	20	30
Imaging protocol	CT7	CT8	CT9	CT10	CT11	CT12
Brain	0.001	0.001	0.001	0.001	0.001	0.001
Active Bone Marrow	0.013	0.032	0.065	0.008	0.016	0.048
Eyes	0.001	0.001	0.001	0.001	0.001	0.001
Thyroid	0.042	0.081	0.237	0.005	0.010	0.035
Oesophagus	0.036	0.050	0.158	0.013	0.027	0.085
Lungs	0.035	0.069	0.185	0.020	0.040	0.127
Breasts	0.048	0.084	0.284	0.014	0.023	0.084
Liver	0.039	0.076	0.200	0.010	0.021	0.063
Stomach	0.047	0.089	0.225	0.008	0.017	0.053
Urinary bladder	0.037	0.084	0.162	0.002	0.006	0.020
Colon	0.032	0.069	0.152	0.008	0.017	0.050
Ovaries	0.028	0.056	0.081	0.004	0.008	0.025
Salivary Glands	0.001	0.001	0.002	0.001	0.001	0.001
Thymus	0.064	0.135	0.373	0.006	0.012	0.041
Spleen	0.024	0.045	0.113	0.016	0.032	0.096
Kidneys	0.011	0.026	0.065	0.028	0.051	0.170
Adrenals	0.012	0.025	0.067	0.030	0.062	0.189
Heart	0.039	0.080	0.233	0.012	0.025	0.063
Pancreas	0.036	0.078	0.180	0.012	0.027	0.079
Gall Bladder	0.016	0.033	0.088	0.002	0.004	0.012
Uterus	0.008	0.015	0.039	0.001	0.000	0.010
Oral mucosa	0.000	0.001	0.004	0.000	0.000	0.001
Small Intestine	0.039	0.087	0.192	0.008	0.017	0.051
Extrathoracic region	0.021	0.032	0.111	0.010	0.019	0.063
Prostate	0.001	0.006	0.007	0.001	0.001	0.008
Testes	0.001	0.001	0.001	0.001	0.001	0.001

Table III: OD values (mGy) when using different mA values and imaging projections in SPR at 80 kVp						
Imaging projection	AP			PA		
mA	10	20	30	10	20	30
Imaging protocol	CT13	CT14	CT15	CT16	CT17	CT18
Brain	0.001	0.001	0.001	0.001	0.001	0.002
Active Bone Marrow	0.022	0.045	0.105	0.013	0.028	0.082
Eyes	0.000	0.001	0.003	0.001	0.001	0.001
Thyroid	0.068	0.129	0.359	0.009	0.019	0.064
Oesophagus	0.041	0.084	0.256	0.025	0.054	0.153
Lungs	0.062	0.110	0.297	0.035	0.071	0.200
Breasts	0.075	0.158	0.436	0.019	0.040	0.135
Liver	0.073	0.131	0.311	0.018	0.038	0.107
Stomach	0.080	0.149	0.344	0.015	0.032	0.094
Urinary bladder	0.071	0.139	0.257	0.006	0.012	0.033
Colon	0.068	0.119	0.230	0.016	0.034	0.086
Ovaries	0.047	0.088	0.156	0.008	0.019	0.046
Salivary Glands	0.001	0.002	0.008	0.000	0.000	0.003
Thymus	0.111	0.183	0.480	0.009	0.021	0.072
Spleen	0.045	0.087	0.190	0.030	0.058	0.155
Kidneys	0.027	0.048	0.101	0.046	0.088	0.256
Adrenals	0.025	0.044	0.118	0.049	0.102	0.298
Heart	0.081	0.128	0.369	0.017	0.042	0.106
Pancreas	0.070	0.115	0.275	0.024	0.048	0.131
Gall Bladder	0.031	0.056	0.134	0.003	0.007	0.021
Uterus	0.016	0.032	0.054	0.002	0.007	0.018
Oral mucosa	0.001	0.003	0.011	0.000	0.001	0.005
Small Intestine	0.082	0.140	0.294	0.015	0.030	0.093
Extrathoracic region	0.032	0.055	0.178	0.017	0.036	0.113
Prostate	0.006	0.010	0.017	0.001	0.005	0.041
Testes	0.001	0.004	0.004	0.001	0.001	0.001

Table IV: OD values (mGy) when using the scoliosis shawl and different kVp and mA values and in SPR									
Imaging projection	AP								
kVp	120			100			80		
mA	10	20	30	10	20	30	10	20	30
Imaging protocol	CT1	CT2	CT3	CT7	CT8	CT9	CT13	CT14	CT15
Brain	0.000	0.000	0.000	0.000	0.000	0.000	0.000	0.000	0.000
Active Bone Marrow	0.011	0.019	0.060	0.007	0.012	0.035	0.004	0.007	0.019
Eyes	0.000	0.000	0.001	0.000	0.000	0.000	0.000	0.000	0.000
Thyroid	0.048	0.089	0.279	0.031	0.059	0.183	0.018	0.035	0.113
Oesophagus	0.031	0.063	0.178	0.018	0.032	0.106	0.008	0.018	0.056
Lungs	0.016	0.030	0.105	0.009	0.018	0.050	0.004	0.009	0.024
Breasts	0.010	0.025	0.073	0.006	0.012	0.038	0.002	0.006	0.017
Liver	0.030	0.059	0.156	0.017	0.034	0.099	0.009	0.018	0.049
Stomach	0.026	0.045	0.119	0.013	0.029	0.078	0.007	0.016	0.032
Urinary bladder	0.042	0.056	0.198	0.020	0.043	0.131	0.014	0.030	0.046
Colon	0.033	0.052	0.153	0.016	0.035	0.096	0.010	0.020	0.031
Ovaries	0.007	0.013	0.032	0.003	0.008	0.019	0.001	0.003	0.006
Salivary Glands	0.000	0.000	0.003	0.000	0.000	0.001	0.000	0.000	0.000
Thymus	0.070	0.141	0.430	0.048	0.092	0.294	0.027	0.054	0.177
Spleen	0.011	0.019	0.057	0.005	0.011	0.032	0.002	0.005	0.012
Kidneys	0.008	0.015	0.042	0.003	0.008	0.024	0.001	0.003	0.007
Adrenals	0.011	0.021	0.071	0.005	0.011	0.035	0.002	0.005	0.015
Heart	0.046	0.091	0.257	0.029	0.055	0.161	0.015	0.029	0.085
Pancreas	0.034	0.058	0.178	0.014	0.034	0.110	0.009	0.023	0.052
Gall Bladder	0.016	0.030	0.075	0.009	0.017	0.049	0.005	0.011	0.022
Uterus	0.006	0.011	0.036	0.003	0.007	0.020	0.001	0.003	0.007
Oral mucosa	0.000	0.001	0.005	0.000	0.000	0.002	0.000	0.000	0.000
Small Intestine	0.046	0.062	0.199	0.023	0.047	0.120	0.013	0.026	0.050
Extrathoracic region	0.020	0.035	0.120	0.010	0.020	0.078	0.005	0.012	0.038
Prostate	0.001	0.001	0.012	0.001	0.001	0.006	0.001	0.001	0.003
Testes	0.001	0.001	0.003	0.001	0.001	0.001	0.001	0.001	0.001

Table V: OD values (mGy) when using different kVp and mA values and in SPR									
Imaging projection	Lateral								
kVp	120			100			80		
mA	10	20	30	10	20	30	10	20	30
Imaging protocol	CT19	CT20	CT21	CT22	CT23	CT24	CT25	CT26	CT27
Brain	0.001	0.001	0.001	0.001	0.001	0.001	0.001	0.001	0.001
Active Bone Marrow	0.011	0.020	0.029	0.006	0.011	0.018	0.003	0.005	0.008
Eyes	0.000	0.000	0.000	0.000	0.000	0.000	0.000	0.000	0.000
Thyroid	0.020	0.034	0.048	0.011	0.021	0.032	0.005	0.011	0.018
Oesophagus	0.033	0.064	0.090	0.019	0.041	0.056	0.010	0.021	0.031
Lungs	0.028	0.052	0.075	0.017	0.033	0.046	0.008	0.017	0.026
Breasts	0.028	0.044	0.061	0.014	0.025	0.036	0.006	0.013	0.021
Liver	0.018	0.032	0.046	0.009	0.018	0.027	0.004	0.009	0.013
Stomach	0.039	0.070	0.095	0.020	0.039	0.061	0.011	0.022	0.029
Urinary bladder	0.009	0.019	0.023	0.004	0.005	0.014	0.001	0.003	0.004
Colon	0.018	0.034	0.048	0.009	0.015	0.028	0.004	0.008	0.011
Ovaries	0.019	0.034	0.049	0.011	0.017	0.031	0.005	0.010	0.014
Salivary Glands	0.000	0.000	0.001	0.000	0.000	0.000	0.000	0.000	0.000
Thymus	0.019	0.032	0.050	0.009	0.018	0.027	0.004	0.009	0.014
Spleen	0.051	0.093	0.135	0.029	0.058	0.085	0.017	0.031	0.046
Kidneys	0.021	0.040	0.058	0.011	0.021	0.033	0.005	0.009	0.015
Adrenals	0.021	0.046	0.069	0.014	0.029	0.042	0.008	0.015	0.023
Heart	0.039	0.070	0.092	0.019	0.038	0.053	0.009	0.020	0.030
Pancreas	0.020	0.035	0.050	0.008	0.019	0.024	0.004	0.008	0.014
Gall Bladder	0.003	0.007	0.008	0.001	0.004	0.005	0.001	0.001	0.002
Uterus	0.003	0.007	0.009	0.001	0.002	0.005	0.000	0.000	0.001
Oral mucosa	0.000	0.001	0.001	0.000	0.000	0.000	0.000	0.000	0.000
Small Intestine	0.019	0.037	0.046	0.010	0.018	0.031	0.005	0.008	0.012
Extrathoracic region	0.017	0.030	0.041	0.008	0.019	0.025	0.004	0.010	0.015
Prostate	0.001	0.003	0.004	0.001	0.001	0.001	0.001	0.001	0.001
Testes	0.001	0.001	0.001	0.001	0.001	0.001	0.001	0.001	0.001

Table VI: OD values (mGy) when using different imaging machines and imaging projections in DR and EOS.							
Imaging machine	DR				EOS		
Imaging protocol	DR1	DR1	DR2	DR3	EOS1	EOS2	EOS3
Imaging projection	AP	AP	PA	Lateral	AP + Lateral	AP	Lateral
Scoliosis shawl	No	Yes	No	No	No	No	No
Brain	0.000	0.000	0.001	0.003	0.003	0.001	0.001
Active Bone Marrow	0.028	0.010	0.026	0.028	0.015	0.003	0.001
Eyes	0.002	0.003	0.001	0.001	0.001	0.001	0.001
Thyroid	0.108	0.067	0.012	0.042	0.049	0.016	0.004
Oesophagus	0.035	0.026	0.023	0.052	0.033	0.006	0.004
Lungs	0.055	0.017	0.056	0.063	0.033	0.009	0.003
Breasts	0.119	0.009	0.028	0.033	0.039	0.015	0.003
Liver	0.120	0.070	0.047	0.119	0.027	0.008	0.002
Stomach	0.167	0.058	0.037	0.033	0.045	0.010	0.004
Urinary bladder	0.121	0.089	0.014	0.041	0.028	0.006	0.001
Colon	0.087	0.067	0.039	0.053	0.028	0.006	0.002
Ovaries	0.084	0.012	0.019	0.049	0.028	0.005	0.002
Salivary Glands	0.001	0.041	0.004	0.017	0.031	0.011	0.003
Thymus	0.071	0.047	0.008	0.026	0.034	0.014	0.002
Spleen	0.080	0.020	0.091	0.027	0.044	0.005	0.005
Kidneys	0.039	0.014	0.147	0.078	0.021	0.002	0.002
Adrenals	0.033	0.021	0.143	0.065	0.024	0.002	0.004
Heart	0.053	0.090	0.032	0.062	0.037	0.009	0.004
Pancreas	0.092	0.070	0.053	0.092	0.025	0.006	0.002
Gall Bladder	0.055	0.024	0.009	0.037	0.008	0.003	0.000
Uterus	0.081	0.013	0.014	0.023	0.021	0.005	0.001
Oral mucosa	0.002	0.036	0.006	0.025	0.026	0.009	0.002
Small Intestine	0.118	0.096	0.035	0.068	0.030	0.006	0.002
Extrathoracic region	0.028	0.009	0.025	0.025	0.026	0.005	0.003
Prostate	0.051	0.003	0.006	0.009	0.016	0.007	0.001
Testes	0.017	0.000	0.001	0.001	0.002	0.001	0.001

Appendix II. Ethical approval for the research

University of Salford MANCHESTER

Research, Enterprise and Engagement
Ethical Approval Panel

Doctoral & Research Support
Research and Knowledge Exchange,
Room 827, Maxwell Building,
University of Salford,
Manchester
M5 4WT

T +44(0)161 295 2280

www.salford.ac.uk

17 August 2018

Dear Faisal,

RE: ETHICS APPLICATION–HSR1718-104 – 'Using Scan Projection Radiographic (SPR) Images in Computed Tomography (CT) to Assess Scoliosis: Radiation Dose Estimation and Image Quality Assessment.'

Based on the information you provided, I am pleased to inform you that application HSR1718-104 has been approved.

If there are any changes to the project and/or its methodology, then please inform the Panel as soon as possible by contacting Health-ResearchEthics@salford.ac.uk

Yours sincerely,

Dr. Stephen Pearson
Deputy Chair of the Research Ethics Panel

Appendix III. CT performance and safety report

The Christie
NHS Foundation Trust

Christie Medical Physics & Engineering

The Christie NHS Foundation Trust

Withington, Manchester

M20 4BX, UK

Diagnostic X-Ray Equipment Performance and Radiation Safety Report

Report No: 0940/SUSFU/17	Report Date: 22 November, 2017

Visit	
Establishment:	Salford University
Equipment location:	CT Suite, Mary Seacole Building
Equipment summary:	Toshiba TSX-101A/GC Aquillion S16
Date of tests:	9/11/17
Performed by:	J Czajka, D Carrington
Reason:	Routine equipment performance measurements
Report	
Sent to:	Andrew Tootell, Radiation Protection Supervisor Chris Beaumont Radiation Protection Supervisor Christie Theodorakou, CMPE
Previous relevant reports:	743/susfu/16
Areas needing attention	**Urgency**
None	
Additional notes:	
Follow-up	

Please report any action taken and outcome to the contact below

Contact: Damian Carrington on (0161) 446 3551
or e-mail damian.carrington@christie.nhs.uk

Diagnostic Radiology and Radiation Protection Group

BSI registered - certificate number: FS 37543

1. List of Measurements Performed

Measurement	Tolerance	Outcome		
		Pass	**Fail**	**Ref**
General Radiation Safety				
Operation of controls and warning devices	Functioning as expected	Pass		
CT System				
Dosimetry CTDI	Baseline ±15%	Pass		**2.1.1**
Variation of output with mA, scan time, helical pitch	Mean ±20%	Pass		
Scan plane location indication	Within ±5mm (±2mm RT) laser lights; Within ±2mm SPR	Pass		
Image noise analysis	Inter slice mean ±10% Baseline ±10%	Pass		
CT number values	Baseline ±5HU(water) or ±10HU	Pass		
CT number uniformity	Difference between centre/periphery Body: Small ±10HU, Large ±20HU	Pass		
Image slice width	Within ± 1mm for slices >2mm	Pass		
Artefacts	No visible artefacts	Pass		
Automatic Exposure Control/Dose Modulation	Functioning as expected	Pass		

2. Summary of Results and Recommendations

The results below are included for information or because there are recommendations concerning performance or safety. The results of all other measurements were satisfactory.

2.1.1 Computed Tomography Dose Index (CTDI)

The measured $CTDI_{100}$ at the isocentre in air were:

kV	Beam/detector collimation (mm)	Mode/SFOV	$CTDI_{100}$ (mGy/100 mAs)
120	12 (4x3)	Head/Small	30.4
	2 (4x0.5)		77.8
	4(1x4)		50.7
	8 (4x2)		36.1
	16 (4x4)		30.5
	24 (4x6)		29.0
	32 (4x8)		29.3
80	12 (4x3)		12.7
100			20.6
135			38.3
120	12 (4x3)	Body/Large	45.4
	2 (4x0.5)		104.1
	4(1x4)		67.0
	8 (4x2)		47.8
	16 (4x4)		41.4
	24 (4x6)		41.7
	32 (4x8)		39.5
80	12 (4x3)		22.3
100			33.6
135			55.8

These results are consistent with our previous measurements

3. Conclusions

The results of our measurements were satisfactory and there are no recommendations to report.

References

Aaro, S., Dahlborn, M. and Svensson, L. 1978. Estimation of vertebral rotation in structural scoliosis by computer tomography. *Acta radiologica: diagnosis*. **19**(6), pp.990–992.

Abdelgawad, A. and Naga, O. 2014. *Pediatric Orthopedics*. New York: Springer.

Ben Abdennebi, A., Aubry, S., Ounalli, L., Fayache, M.S., Delabrousse, E. and Petegnief, Y. 2017. Comparative dose levels between CT-scanner and slot-scanning device (EOS system) in pregnant women pelvimetry. *Physica Medica*. **33**(2017), pp.77–86.

Abul-Kasim, K. 2010. Low-dose spine CT: Optimisation and clinical implementation. *Radiation Protection Dosimetry*. **139**(1–3), pp.169–172.

Abul-Kasim, K., Gunnarsson, M., Maly, P., Ohlin, A. and Sundgren, P. 2008. Radiation dose optimization in CT planning of corrective scoliosis surgery. A phantom study. *Neuroradiology Journal*. **21**(3), pp.374–382.

Abul-Kasim, K., Karlsson, M.K., Hasserius, R. and Ohlin, A. 2010. Measurement of vertebral rotation in adolescent idiopathic scoliosis with low-dose CT in prone position - method description and reliability analysis. *Scoliosis*. **5**(1), pp.1–8.

Abul-Kasim, K., Overgaard, A., Maly, P., Ohlin, A., Gunnarsson, M. and Sundgren, P.C. 2009. Low-dose helical computed tomography (CT) in the perioperative workup of adolescent idiopathic scoliosis. *European Radiology*. **19**(3), pp.610–618.

Abul-Kasim, K., Strömbeck, A., Ohlin, A., Maly, P. and Sundgren, P.C. 2009. Reliability of low-radiation dose CT in the assessment of screw placement after posterior scoliosis surgery, evaluated with a new grading system. *Spine*. **34**(9), pp.941–948.

Adam, C., Izatt, M. and Askin, G. 2010. Design and evaluation of an MRI compatible axial compression device for 3D assessment of spinal deformity and flexibility in AIS. *Studies in Health Technology and Informatics*. **158**, pp.38–43.

Adam, C.J., Izatt, M.T., Harvey, J.R. and Askin, G.N. 2005. Variability in Cobb angle measurements using reformatted computerized tomography scans. *Spine*. **30**(14), pp.1664–1669.

Adobor, R.D., Riise, R.B., Sørensen, R., Kibsgård, T.J., Steen, H. and Brox, J.I. 2012. Scoliosis detection, patient characteristics, referral patterns and treatment in the absence of a screening program in Norway. *Scoliosis*. **7**(1), p.18.

Adobor, R.D., Rimeslatten, S., Steen, H. and Brox, J.I. 2011. School screening and point prevalence of adolescent idiopathic scoliosis in 4000 norwegian children aged 12 years. *Scoliosis and Spinal Disorders Journal*. **6**(1), p.23.

Aichinger, H., Dierker, J., Joite-Barfuß, S. and Säbel, M. 2012. *Radiation Exposure and Image Quality in X-Ray Diagnostic Radiology Physical Principles and Clinical Applications* 2nd ed. Berlin: Springer.

Al-Aubaidi, Z., Lebel, D., Oudjhane, K. and Zeller, R. 2013. Three-dimensional imaging of the spine using the EOS system: is it reliable? A comparative study using computed tomography imaging. *Journal of pediatric orthopedics. Part B*. **22**(5), pp.409–412.

Al-Senan, R.M. and Hatab, M.R. 2011. Characteristics of an OSLD in the diagnostic energy range. *Medical Physics*. **38**(7), pp.4396–4405.

Ali, R. 2016. *Risk of Radiation-Induced Cancer from Screening Mammography*. University of Salford.

Ali, R.M., England, A., McEntee, M.F. and Hogg, P. 2015. A method for calculating effective lifetime risk of radiation-induced cancer from screening mammography. *Radiography*. **21**(4), pp.298–303.

Allam, Y., El-Fiky, T., Farghally, M.Y., Al-Sabagh, S. and Siam, A.E. 2016. Comparison between Oxford Cobbmeter and digital Cobbmeter for measurement of Cobb angle in adolescent idiopathic scoliosis. *European Spine Journal*. **25**(2), pp.444–449.

Allen, S., Parent, E., Khorasani, M., Hill, D.L., Lou, E. and Raso, J. V. 2008. Validity and reliability of active shape models for the estimation of Cobb angle in patients with adolescent idiopathic scoliosis. *Journal of Digital Imaging*. **21**(2), pp.208–218.

Allisy-Roberts, P. and Williams, J. 2008. *Farr's Physics for Medical Imaging* 2nd ed. Edinburgh: Saunders.

AlQaroot, B. 2012. *The effects of body fat percentage on inter-vertebral spinal mobility control from hyperextension spinal orthoses*. University of Salford, Salford, UK.

Alsleem, H. and Davidson, R. 2013. Quality parameters and assessment methods of digital radiography images. *Radiographer*. **59**(2), pp.46–55.

Alvarez, P., Kry, S.F., Stingo, F. and Followill, D. 2017. TLD and OSLD dosimetry systems for remote audits of radiotherapy external beam calibration. *Radiation measurements*. **106**, pp.412–415.

Andersson, J., Pavlicek, W., Al-Senan, R., Bolch, W., Bosmans, H., Cody, D., Dixon, R., Colombo, P., Dong, F., Edyvean, S. and Jansen, J. 2019. *Estimating patient organ dose with computed tomography: A review of present methodology and required DICOM information: Report 246*. Alexandria, VA: American Association of Physicists in Medicine.

Andersson, M., Eckerman, K. and Mattsson, S. 2017. Lifetime attributable risk as an alternative to effective dose to describe the risk of cancer for patients in diagnostic and therapeutic nuclear medicine. *Physics in Medicine and Biology*. **62**(24), pp.9177–9188.

Bacher, K., Smeets, P., Vereecken, L., De Hauwere, A., Duyck, P., De Man, R., Verstraete, K. and Thierens, H. 2006. Image quality and radiation dose on digital chest imaging: Comparison of amorphous silicon and amorphous selenium flat-panel systems. *American Journal of Roentgenology*. **187**(3), pp.630–637.

Bagheri, A., Liu, X.C., Tassone, C., Thometz, J. and Tarima, S. 2018. Reliability of three-dimensional spinal modeling of patients with idiopathic scoliosis using EOS system.

Spine Deformity. **6**(3), pp.207–212.

Barnes, P.J. and Temperton, D. 2011. *Compliance of full field digital mammography systems with the european protocol for image quality and dose* [Online]. International Atomic Energy Agency (IAEA): IAEA. Available from: http://www-pub.iaea.org/MTCD/Publications/PDF/P1514_web/p1514_vol2_web.pdf.

Bath, M. 2010. Evaluating Imaging Systems : Practical Applications. *Radiation Protection Dosimetry*. **139**(1–3), pp.26–36.

Båth, M. and Månsson, L.G. 2007. Visual grading characteristics (VGC) analysis: A non-parametric rank-invariant statistical method for image quality evaluation. *British Journal of Radiology*. **80**(951), pp.169–176.

Ben-Shlomo, A., Bartal, G., Mosseri, M., Avraham, B., Leitner, Y. and Shabat, S. 2016. Effective dose reduction in spine radiographic imaging by choosing the less radiation-sensitive side of the body. *Spine Journal*. **16**(4), pp.558–563.

Ben-Shlomo, A., Bartal, G., Shabat, S. and Mosseri, M. 2013. Effective dose and breast dose reduction in paediatric scoliosis x-ray radiography by an optimal positioning. *Radiation Protection Dosimetry*. **156**(1), pp.30–36.

Blevins, K., Battenberg, A. and Beck, A. 2018. The management of scoliosis. *Advances in Pediatrics*. **65**(1), pp.249–266.

Bochud, F.O., Toroi, P., Tapiovaara, M.J., Schegerer, A., Veldkamp, W.J.H., Edyvean, S., Marshall, N.W., Giron, I.H., Racine, D., Bouwman, R.W., Ott, J.G. and Verdun, F.R. 2015. Image quality in CT: From physical measurements to model observers. *Physica Medica*. **31**(8), pp.823–843.

Bogduk, N. 2014. *Clinical and Radiological Anatomy of the Lumbar Spine* [Online]. London, UNITED KINGDOM: Elsevier. Available from: http://ebookcentral.proquest.com/lib/salford/detail.action?docID=1724077.

Bohrer, E., Schäfer, S., Mäder, U., Noël, P.B., Krombach, G.A. and Fiebich, M. 2017. Optimizing radiation exposure for CT localizer radiographs. *Zeitschrift fur Medizinische Physik*. **27**(2), pp.145–158.

Boice, J.D. 1996. Cancer following irradiation in childhood and adolescence. *Medical and Pediatric Oncology*. **27**(1), pp.29–34.

Boice, J.D. 2017. The linear nonthreshold (LNT) model as used in radiation protection: An NCRP update. *International Journal of Radiation Biology*. **93**(10), pp.1079–1092.

Bonanni, P.G. 2017. Contour and Angle-Function Based Scoliosis Monitoring: Relaxing the Requirement on Image Quality in the Measurement of Spinal Curvature. *International Journal of Spine Surgery*. **11**(3), pp.173–182.

Bor, D., Sancak, T., Olgar, T., Elcim, Y., Adanali, A., Sanlidilek, U. and Akyar, S. 2004. Comparison of effective doses obtained from dose-area product and air kerma measurements in interventional radiology. *British Journal of Radiology*. **77**(916), pp.315–322.

Borrego, D., Lowe, E.M., Kitahara, C.M. and Lee, C. 2018. Assessment of PCXMC for patients with different body size in chest and abdominal x ray examinations: A Monte Carlo simulation study. *Physics in Medicine and Biology*. **63**(6), pp.321–338.

Branchini, M., del Vecchio, A., Gigliotti, C.R., Loria, A., Zerbi, A. and Calandrino, R. 2018. Organ doses and lifetime attributable risk evaluations for scoliosis examinations of adolescent patients with the EOS imaging system. *Radiologia Medica*. **123**(4), pp.305–313.

Brenner, A. V., Preston, D.L., Sakata, R., Sugiyama, H., de Gonzalez, A.B., French, B., Utada, M., Cahoon, E.K., Sadakane, A., Ozasa, K., Grant, E.J. and Mabuchi, K. 2018. Incidence of Breast Cancer in the Life Span Study of Atomic Bomb Survivors: 1958–2009. *Radiation Research*. **190**(4), pp.433–444.

Brenner, D.J. 2008. Effective dose - A flawed concept that could and should be replaced. *The British Journal of Radiology*. **81**, pp.521–523.

Brenner, D.J. 2011. Icrp 2011 *In*: *ICRP Sympsium* [Online]. New York, NY. Available from: http://dx.doi.org/10.1016/j.icrp.2012.07.001.

Brenner, D.J. 2012. We can do better than effective dose for estimating or comparing low-dose radiation risks. *Annals of the ICRP*. **41**(3–4), pp.124–128.

Brenner, D.J. and Hall, E.J. 2007. Computed Tomography — An Increasing Source of Radiation Exposure. *The New England Journal of Medicine*., pp.2277–2284.

Brink, R.C., Colo, D., Schlösser, T.P.C., Vincken, K.L., Van Stralen, M., Hui, S.C.N., Shi, L., Chu, W.C.W., Cheng, J.C.Y. and Castelein, R.M. 2017. Upright, prone, and supine spinal morphology and alignment in adolescent idiopathic scoliosis. *Scoliosis and Spinal Disorders*. **12**(1), pp.1–8.

Brink, R.C., Schlösser, T.P.C., Colo, D., Vincken, K.L., van Stralen, M., Hui, S.C.N., Chu, W.C.W., Cheng, J.C.Y. and Castelein, R.M. 2017. Asymmetry of the vertebral Body and pedicles in the true transverse plane in adolescent adiopathic scoliosis: A CT-based study. *Spine Deformity*. **5**(1), pp.37–45.

Brink, R.C., Wijdicks, S., Tromp, I.N., Schlösser, T.P.C., Kruyt, M.C., Beek, F.J. and Castelein, R.M. 2018. A reliability and validity study for different coronal angles using ultrasound imaging in adolescent idiopathic scoliosis. *The Spine Journal*. **18**(6), pp.979–985.

Brook, O.R., Guralnik, L. and Engel, A. 2007. CT scout view as an essential part of CT reading. *Australasian Radiology*. **51**(3), pp.211–217.

Busch, H.P. and Faulkner, K. 2006. Image quality and dose management in digital radiography: a new paradigm for optimisation. *Radiation Protection Dosimetry*. **117**(1–3), pp.143–147.

Bushberg, J.T., Seibert, J.A., Leidholdt JR, E.M. and Boone, J.M. 2012. *The Essential Physics of Medical Imaging* 3rd. Philadelphia, PA: Lippincott Williams & Wilkins.

Cakmak, E.D., Tuncel, N. and Sindir, B. 2015. Assessment of organ dose by direct and

indirect Measurements for a wide bore X-ray computed tomography unit that used in radiotherapy. *International Journal of Medical Physics, Cinical Engineering and Radiation Oncology*. **04**(02), pp.132–142.

Caldas, M. de P., Ramos-Perez, F.M. de M., Almeida, S.M. de and Haiter-Neto, F. 2011. Comparative evaluation among different materials to replace soft tissue in oral radiology studies. *Journal of Applied Oral Science*. **18**(3), pp.264–267.

Cardarelli, J.J. and Ulsh, B.A. 2018. It is time to move beyond the linear no-threshold theory for low-dose radiation protection. *Dose-Response*. **16**(3), pp.1–24.

Carlson, B.B., Burton, D.C. and Asher, M.A. 2013. Comparison of trunk and spine deformity in adolescent idiopathic scoliosis. *Scoliosis*. **8**(1), pp.2–5.

Carman, D.L., Browne, R.H. and Birch, J.G. 1990. Measurement of scoliosis and kyphosis radiographs. Intraobserver and interobserver variation. *The Journal of bone and joint surgery. American volume*. **72**(3), pp.328–333.

Carpenter, D.O. and Bushkin-Bedient, S. 2013. Exposure to chemicals and radiation during childhood and risk for cancer later in life. *Journal of Adolescent Health*. **52**(5), pp.S21–S29.

CEC 1996a. *European guidelines on quality criteria for computed tomography. Report EUR 16262 EN*. Luxembourg: Office for Official Publications of the European Communities.

CEC 1996b. *European guidelines on quality criteria for diagnostic radiographic images: report EUR 16260 EN*. Luxembourg: Office for Official Publications of the European Communities.

CEC 1996c. *European guidelines on quality criteria for diagnostic radiographic images in paediatrics. Report EUR 16261 EN*. Luxembourg: Office for official publications of the European Communities.

Chamberlain, C.C., Huda, W., Hojnowski, L.S., Perkins, A. and Scaramuzzino, A. 2000. Radiation doses to patients undergoing scoliosis radiography. *The British Journal of Radiology*. **73**(872), pp.847–853.

Chambers, D. 2014. *The effective dose of different scanning protocols using the Sirona Galileos comfort CBCT scanner*. The University of Western Ontario.

Chan, A.C.Y., Morrison, D.G., Nguyen, D. V., Hill, D.L., Parent, E. and Lou, E.H.M. 2014. Intra- and interobserver reliability of the cobb angle-vertebral rotation angle-spinous process angle for adolescent idiopathic scoliosis. *Spine Deformity*. **2**(3), pp.168–175.

Chan, C.T.P. and Fung, K.K.L. 2015. Dose optimization in pelvic radiography by air gap method on CR and DR systems – A phantom study. *Radiography*. **21**(3), pp.214–223.

Chang, K., Caovan, D., Grand, D., Huda, W. and Mayo-Smith, W. 2013. Reducing radiation dose at CT colonography: decreasing kVp to 100 Kilovolts. *Radiology*. **266**(3), pp.801–811.

Chaparian, A., Kanani, A. and Baghbanian, M. 2014. Reduction of radiation risks in patients undergoing some X-ray examinations by using optimal projections: A Monte Carlo

program-based mathematical calculation. *Journal of medical physics*. **39**(1), pp.32–39.

Chen, W., Lou, E.H.M., Zhang, P.Q., Le, L.H. and Hill, D. 2013. Reliability of assessing the coronal curvature of children with scoliosis by using ultrasound images. *Journal of Children's Orthopaedics*. **7**(6), pp.521–529.

Cheung, C.W.J., Zhou, G.Q., Law, S.Y., Mak, T.M., Lai, K.L. and Zheng, Y.P. 2015. Ultrasound volume projection imaging for assessment of scoliosis. *IEEE Transactions on Medical Imaging*. **34**(8), pp.1760–1768.

Cheung, J., Wever, D.J., Veldhuizen, A.G., Klein, J.P., Verdonck, B., Nijlunsing, R., Cool, J.C. and Van Horn, J.R. 2002. The reliability of quantitative analysis on digital images of the scoliotic spine. *European Spine Journal*. **11**(6), pp.535–542.

Ching, W., Robinson, J. and Mcentee, M. 2014. Patient-based radiographic exposure factor selection: A systematic review. *Journal of Medical Radiation Sciences*. **61**(3), pp.176–190.

Chodick, G., Ronckers, C.M., Shalev, V. and Ron, E. 2007. Excess lifetime cancer mortality risk attributable to radiation exposure from computed tomography examinations in children. *Israel Medical Association Journal*. **9**(8), pp.584–587.

Chow, L.S. and Paramesran, R. 2016. Review of medical image quality assessment. *Biomedical Signal Processing and Control*. **27**, pp.145–154.

Christner, J.A., Kofler, J.M. and Mccollough, C.H. 2010a. Estimating effective dose for CT using dose–length product compared with using organ doses: consequences of adopting international commission on radiological protection publication 103 or Dual-Energy Scanning. *Medical Physics and Informatics*. **194**(April), pp.881–889.

Christner, J.A., Kofler, J.M. and Mccollough, C.H. 2010b. Estimating effective dose for CT using dose–length product compared with using organ doses: consequences of adopting international commission on radiological protection publication 103 or Dual-Energy Scanning. *Medical Physics and Informatics*. **194**(April), pp.881–889.

Chung, E., Seuntjens, J., Soisson, E. and Bouchard, H. 2010. *Advanced dosimetry techniques for accurate verification of non-standard beams* [Online]. International Atomic Energy Agency (IAEA). Available from: http://inis.iaea.org/search/search.aspx?orig_q=RN:42026442.

Chung, N., Cheng, Y.H., Po, H.L., Ng, W.K., Cheung, K.C., Yung, H.Y. and Lai, Y.M. 2018. Spinal phantom comparability study of Cobb angle measurement of scoliosis using digital radiographic imaging. *Journal of Orthopaedic Translation*. **15**, pp.81–90.

Cilli, K., Tezeren, G., Tas, T., Bulut, O., Ozturk, H., Oztemur, Z. and Unsaldi, T. 2009. School screening for scoliosis in Sivas, Turkey Kansu. *Acta Orthopaedica et Traumatologica Turcica*. **43**(5), pp.426–430.

CIRS 2016. *Atom Dosimetry Phantoms: Models 701 - 706*. Norfolk, Verginia.

CIRS 2013. *Tissue Simulations & Phantom Technology*. Norfolk, Verginia: Computerized Imaging Reference Systems, Inc.

Clavel, A.H., Thevenard-Berger, P., Verdun, F.R., Létang, J.M. and Darbon, A. 2016. Organ radiation exposure with EOS: GATE simulations versus TLD measurements. *Medical Imaging 2016: Physics of Medical Imaging*. **9783**, p.978352.

Clinical Imaging Board 2015. *CT Equipment, Operations, Capacity and Planning in the NHS*.

Cobb, J. 1948. Outline for the study of scoliosis. *The American Academy of Orthopaedics Surgeons*. **5**, pp.261–275.

Costa, P.R., Yoshimura, E.M., Nersissian, D.Y. and Melo, C.S. 2016. Correlation between effective dose and radiological risk: general concepts. *Radiologia brasileira*. **49**(3), pp.176–181.

Courvoisier, A., Ilharreborde, B., Constantinou, B., Aubert, B., Vialle, R. and Skalli, W. 2013. Evaluation of a three-dimensional reconstruction method of the rib cage of mild scoliotic patients. *Spine Deformity*. **1**(5), pp.321–327.

Cracknell, J., Lawson, D.M. and Taylor, J.A. 2015. Intra- and inter-observer reliability of the Cobb measurement by chiropractic interns using digital evaluation methods. *The Journal of the Canadian Chiropractic Association*. **59**(3), pp.261–268.

Cristy, M. 1981. Active bone marrow distribution as a function of age in humans. *Physics in Medicine and Biology*. **26**(3), pp.389–400.

Cropp, R.J., Seslija, P., Tso, D. and Thakur, Y. 2013. Scanner and kVp dependence of measured CT numbers in the ACR CT phantom. *Journal of Applied Clinical Medical Physics*. **14**(6), pp.338–349.

Cunningham, C., Scheuer, L. and Black, S. 2016. *Developmental Juvenile Osteology: Second Edition* [Online]. Available from: https://www.scopus.com/inward/record.uri?eid=2-s2.0-85016823451&partnerID=40&md5=218d33d492935baa0999134ab1e6fb2e.

Cynthia, H.M., Leng, S., Yu, L., Cody, D.D., Boone, J.M. and McNitt-Gray, M.F. 2011. CT dose index and patient dose: they are not the same thing. *Radiology*. **259**(2), pp.311–316.

D'Souza, W.D., Madsen, E.L., Unal, O., Vigen, K.K., Frank, G.R. and Thomadsen, B.R. 2001. Tissue mimicking materials for a multi-imaging modality prostate phantom. *Medical Physics*. **28**(4), pp.688–700.

Damet, J., Fournier, P., Monnin, P., Sans-Merce, M., Ceroni, D., Zand, T., Verdun, F.R. and Baechler, S. 2014. Occupational and patient exposure as well as image quality for full spine examinations with the EOS imaging system. *Medical Physics*. **41**(6), p.063901.

Daniel, J.C.O., Stevens, D.M. and Cody, D.D. 2005. Reducing radiation exposure from survey CT scans. *Pediatric Imaging*. **185**(2), pp.509–515.

Deak, P., Smal, Y. and Kalender, W. 2010. Multisection CT protocols : Sex- and age-specific conversion factors used to determine dose from dose-length product. *Radiology*. **257**(1), pp.158–166.

Deogaonkar, K., Ghandour, A., Jones, A., Ahuja, S. and Lyons, K. 2008. Chronic recurrent multifocal osteomyelitis presenting as acute scoliosis: A case report and review of literature. *European Spine Journal*. **17**(SUPPL.2), pp.248–252.

Deschênes, S., Charron, G., Beaudoin, G., Labelle, H., Dubois, J., Miron, M.-C. and Parent, S. 2010. Diagnostic imaging of spinal deformities: reducing patients radiation dose with a new slot-scanning X-ray imager. *Spine*. **35**(9), pp.989–994.

Dewerd, L.A. and Kissick, M. 2014. *The phantoms of medical and health physics*. New York, NY: Springer.

Dimar, J.R., Carreon, L.Y., Labelle, H., Djurasovic, M., Weidenbaum, M., Brown, C. and Roussouly, P. 2008. Intra- and inter-observer reliability of determining radiographic sagittal parameters of the spine and pelvis using a manual and a computer-assisted methods. *European Spine Journal*. **17**(10), pp.1373–1379.

Dong, S.L., Chu, T.C., Lan, G.Y., Wu, T.H., Lin, Y.C. and Lee, J.S. 2002. Characterization of high-sensitivity metal oxide semiconductor field effect transistor dosimeters system and LiF:Mg,Cu,P thermoluminescence dosimeters for use in diagnostic radiology. *Applied Radiation and Isotopes*. **57**(6), pp.883–891.

Doody, M.M., Lonstein, J.E., Stovall, M., Hacker, D.G., Luckyanov, N. and Land, C.E. 2000. Breast cancer mortality after diagnostic radiography: findings from the U.S. Scoliosis Cohort Study. *Spine*. **25**(16), pp.2052–2063.

Dowsett, D.J., Kenny, P.A. and Johnson, R.E. 2006. *The physics of diagnostic imaging* 2nd ed. London: Hodder Arnold.

Elojeimy, S., Tipnis, S. and Huda, W. 2010. Relationship between radiographic techniques. *Radiation Protection Dosimetry*. **141**(1), pp.43–49.

Engen, R. Van, Young, K.C. and Bosmans, H. 2005. *The European protocol for the quality control of the physical and technical aspects of mammography screening.* [Online]. Available from: http://scholar.google.com/scholar?hl=en&btnG=Search&q=intitle:The+European+protocol+for+the+quality+control+of+the+physical+and+technical+aspects+of+mammography+screening.#0.

England, A., Evans, P., Harding, L., Taylor, E.M., Charnock, P. and Williams, G. 2015. Increasing source-to-image distance to reduce radiation dose from digital radiography pelvic examinations. *Radiologic technology*. **86**(3), pp.246–56.

EOS imaging 2019. EOS Solutions. [Accessed 7 April 2019]. Available from: https://www.eos-imaging.us/us/professionals/eos.

Ernst, C., Buls, N., Laumen, A., Van Gompel, G., Verhelle, F. and de Mey, J. 2018. Lowered dose full-spine radiography in pediatric patients with idiopathic scoliosis. *European Spine Journal*. **27**(5), pp.1089–1095.

European Commission 2009. *Technical Recommendations for Monitoring Individuals Occupationally Exposed to External Radiation: Report 160*. Luxembourg.

Evans, J.D. 1996. *Straightforward statistics for the behavioral sciences.* Belmont, CA: Thomson Brooks/Cole Publishing Co.

Faria, R., McKenna, C., Wade, R., Yang, H., Woolacott, N. and Sculpher, M. 2013. The EOS

2D/3D X-ray imaging system: A cost-effectiveness analysis quantifying the health benefits from reduced radiation exposure. *European Journal of Radiology*. **82**(8), pp.e342–e349.

Farrer, A.I., Odéen, H., de Bever, J., Coats, B., Parker, D.L., Payne, A. and Christensen, D.A. 2015. Characterization and evaluation of tissue-mimicking gelatin phantoms for use with MRgFUS. *Journal of Therapeutic Ultrasound*. **3**(1), pp.1–11.

Faul, F., Erdfelder, E. and Buchner, A. 2007. G*Power 3: A flexible statistical power analysis program for the social, behavioral, and biomedical sciences. *Behavior Research Methods*. **39**(2), pp.175–191.

Feng, S.T., Law, M.W.M., Huang, B., Ng, S., Li, Z.P., Meng, Q.F. and Khong, P.L. 2010. Radiation dose and cancer risk from pediatric CT examinations on 64-slice CT: A phantom study. *European Journal of Radiology*. **76**(2), pp.e19–e23.

Filippou, V. and Tsoumpas, C. 2018. Recent advances on the development of phantoms using 3D printing for imaging with CT, MRI, PET, SPECT, and ultrasound. *Medical Physics*. **45**(9), pp.e740–e760.

Fisher, D.R. and Fahey, F.H. 2017. Appropriate use of effective dose in radiation protection and risk assessment. *Health physics*. **113**(2), pp.102–109.

Fletcher, J.G. 2010. Adjusting kV to reduce dose or improve image quality - How to do it Right *In*: *Technology Assessment Institute: Summit on CT Dose*.

Florkowski, C.M. 2008. Sensitivity, specificity, receiver-operating characteristic (ROC) curves and likelihood ratios: communicating the performance of diagnostic tests. *The Clinical biochemist. Reviews*. **29**(August), pp.S83–S87.

Frerich, J., Hertzler, K., Knott, P. and Mardjetko, S. 2012. Comparison of radiographic and surface topography measurements in adolescents with idiopathic scoliosis. *The Open Orthopaedics Journal*. **6**(1), pp.261–265.

Frush, D.P. 2013. Radiation risks to children from medical imaging. *Revista Médica Clínica Las Condes*. **24**(1), pp.15–20.

Garcia, T., Perichon, N., Lourenco, V., Bordy, J.M. and Francois, P. 2010. *Calibration of helical tomotherapy using ESR/alanine dosimetry* [Online]. International Atomic Energy Agency (IAEA). Available from: http://inis.iaea.org/search/search.aspx?orig_q=RN:42026513.

GE Healthcare 2010. *Optima CT660: Product description*. Chicago, IL.

George, J., Eatough, J.P., Mountford, P.J., Koller, C.J., Oxtoby, J. and Frain, G. 2004. Patient dose optimization in plain radiography based on standard exposure factors. *British Journal of Radiology*. **77**(922), pp.858–863.

German Commission on Radiological Protection 2009. *Sex-specific differences in radiation sensitivity – epidemiological, clinical and biological studies*. Bonn, Germany.

Gialousis, G., Yiakoumakis, E.N., Makri, T.K., Papadoupoulou, D., Karlatira, M., Karaiskos, P., Papaodysseas, S., Evlogias, N., Dimitriou, P.A. and Georgiou, E.K. 2008.

Comparison of dose from radiological examination for scoliosis in children among two pediatric hospitals by Monte Carlo simulation. *Health Physics*. **94**(5), pp.471–478.

Glaser, D.A., Doan, J. and Newton, P.O. 2012. Comparison of 3-dimensional spinal reconstruction accuracy. *Spine*. **37**(16), pp.1391–1397.

Goldberg, M.S., Poitras, B., Mayo, N.E., Labelle, H., Bourassa, R. and Cloutier, R. 1988. Observer variation in assessing spinal curvature and skeletal development in adolescent idiopathic scoliosis. *Spine*. **13**(12), pp.1371–1377.

Goldman, L.W. 2007. Principles of CT: Radiation dose and image quality. *Journal of Nuclear Medicine Technology*. **35**(4), pp.213–225.

Goodbody, C., Kedem, P., Thompson, M., Do, H.T., Mintz, D.N., Widmann, R.F. and Dodwell, E.R. 2017. Reliability and Reproducibility of Subject Positioning with EOS Low-Dose Biplanar X-ray. *HSS Journal*. **13**(3), pp.263–266.

Greiner, K. 2002. Adolescent idiopathic scoliosis: Radiologic decision-making. *American Family Physician*. **65**(9), pp.1817–1822.

Grivas, T.B., Vasiliadis, E., Mouzakis, V., Mihas, C. and Koufopoulos, G. 2006. Association between adolescent idiopathic scoliosis prevalence and age at menarche in different geographic latitudes. *Scoliosis*. **1**(1), pp.1–12.

Grossman, D.C., Curry, S.J., Owens, D.K., Barry, M.J., Davidson, K.W., Doubeni, C.A., Epling, J.W., Kemper, A.R., Krist, A.H., Kurth, A.E., Landefeld, C.S., Mangione, C.M., Phipps, M.G., Silverstein, M., Simon, M.A. and Tseng, C.W. 2018. Screening for adolescent idiopathic scoliosis US preventive services task force recommendation statement. *JAMA - Journal of the American Medical Association*. **319**(2), pp.165–172.

Gstoettner, M., Sekyra, K., Walochnik, N., Winter, P., Wachter, R. and Bach, C.M. 2007. Inter- and intraobserver reliability assessment of the Cobb angle: Manual versus digital measurement tools. *European Spine Journal*. **16**(10), pp.1587–1592.

Gücük, A. and Uyetürk, U. 2014. Usefulness of hounsfield unit and density in the assessment and treatment of urinary stones. *World journal of nephrology*. **3**(4), pp.282–286.

Gur, D., Bandos, A.I., Fuhrman, C.R., Klym, A.H., King, J.L. and Rockette, H.E. 2007. The prevalence effect in a laboratory environment: Changing the confidence ratings. *Academic radiology*. **14**(1), pp.49–53.

Hamada, N. and Fujimichi, Y. 2014. Classification of radiation effects for dose limitation purposes: History, current situation and future prospects. *Journal of Radiation Research*. **55**(4), pp.629–640.

Hardesty, C.K., Aronson, J., Aronson, E.A., Ranade, A.S., McCracken, C.W., Nick, T.G. and Cordell, C.L. 2013. Interobserver variability using a commercially available system of archived digital radiography with integrated computer-assisted measurements for scoliosis Cobb angles. *Journal of pediatric orthopedics*. **33**(2), pp.163–169.

Harmer, H., Radford, S. and Smail, M. 2018. Feasibility study of using PCXMC 2.0 to estimate patient dose arising from DEXA scans. *Radiation Protection Dosimetry*. **181**(4),

pp.418–422.

Harrison, J. and Lopez, P.O. 2015. Use of effective dose in medicine. *Annals of the ICRP*. **44**(1 Suppl), pp.221–228.

Harrison, K.M., Ebert, M.A., Kron, T., Howlett, S.J., Cornes, D., Hamilton, C.S. and Denham, J.W. 2011. Design, manufacture, and evaluation of an anthropomorphic pelvic phantom purpose-built for radiotherapy dosimetric intercomparison. *Medical Physics*. **38**(10), pp.5330–5337.

Hart, D., Hillier, M. and Shrimpton, P. 2010. *Doses to patients from radiographic and fluoroscopic X-ray imaging procedures in the UK—2010 Review* [Online]. Didcot: Health Protection Agency. Available from: http://scholar.google.com/scholar?hl=en&btnG=Search&q=intitle:Doses+to+Patients+from+Radiographic+and+Fluoroscopic+X-ray+Imaging+Procedures+in+the+UK+–+2010+Review#5%5Cnhttp://scholar.google.com/scholar?hl=en&btnG=Search&q=intitle:HPA-RPD-029—doses+to+pat.

Hayashi, H., Mihara, Y., Kanazawa, Y., Tomita, E., Goto, S., Takegami, K., Okazaki, T., Hashizume, T. and Cruz, V.L.E. 2017. Necessity of Direct Dose Measurement during Current X-ray Diagnosis. *Medical Research Archives*. **5**(2).

Hazelaar, C., van Eijnatten, M., Dahele, M., Wolff, J., Forouzanfar, T., Slotman, B. and Verbakel, W.F.A.R. 2018. Using 3D printing techniques to create an anthropomorphic thorax phantom for medical imaging purposes. *Medical physics*. **45**(1), pp.92–100.

Heary, R.F. and Albert, T.J. 2014. *Spinal deformities: The essentials* 2 nd. New York: Thieme.

Hensen, J., Jurik, A.G., Fiirgaard, B. and Egund, N. 2003. Optimisation of scoliosis examinations in children. *Pediatric Radiology*. **33**(11), pp.752–765.

Hiles, P. 2014. *Recommended Standards for the Routine Performance Testing of Diagnostic X-Ray Imaging Systems*. York: Institute of Physics and Engineering in Medicine.

Hiles, P.A., Mackenzie, A., Scally, A. and Wall, B. 2005. IPEM Report 91 Recommended Standards for the Routine Performance Testing of Diagnostic X-Ray Imaging Systems. *York, UK: Institute of Physics and Engineering in Medicine*.

Ho, E.K., Upadhyay, S.S., Chan, F.L., Hsu, L.C. and Leong, J.C. 1993. New methods of measuring vertebral rotation from computed tomographic scans. An intraobserver and interobserver study on girls with scoliosis. *Spine*. **18**(9), pp.1173–1177.

Hoffman, D.A., Lonstein, J.E., Morin, M.M., Visscher, W., Harris, B.S. 3rd and Boice, J.D.J. 1989. Breast cancer in women with scoliosis exposed to multiple diagnostic x rays. *Journal of the National Cancer Institute*. **81**(17), pp.1307–1312.

Homolka, P., Gahleitner, A., Prokop, M. and Nowotny, R. 2002. Optimization of the composition of phantom materials for computed tomography. *Physics in Medicine and Biology*. **47**(16), pp.2907–2916.

Homolka, P. and Nowotny, R. 2002. Production of phantom materials using polymer powder

sintering under vacuum. *Physics in medicine and biology*. **47**(3), pp.N47-52.

Hoye, J., Sharma, S., Zhang, Y., Fu, W., Ria, F., Kapadia, A., Segars, W.P., Wilson, J. and Samei, E. 2019. Organ doses from CT localizer radiographs: Development, validation, and application of a Monte Carlo estimation technique. *Medical Physics*. **46**, pp.5262–5272.

Hsieh, J. 2009. *Computed Tomography: Principles, design, artifacts, and recent advances* 2nd ed. Bellingham, WA: SPIE.

Hubbell, J.H. and Seltzer, S.M. 2004. *Tables of X-ray mass attenuation coefficients and mass energy-absorption coefficients (version 1.4)*.

Huda, W. and Abrahams, R.B. 2015. Radiographic techniques, contrast, and noise in x-ray imaging. *AJR. American journal of roentgenology*. **204**(2), pp.W126–W131.

Huda, W. and Brad Abrahams, R. 2015. X-ray-based medical imaging and resolution. *American Journal of Roentgenology*. **204**(4), pp.W393–W397.

Huda, W., Magill, D. and He, W. 2011. CT effective dose per dose length product using ICRP 103 weighting factors. *Medical physics*. **38**(3), pp.1261–1265.

Hui, S.C.N., Pialasse, J.-P., Wong, J.Y.H., Lam, T., Ng, B.K.W., Cheng, J.C.Y. and Chu, W.C.W. 2016. Radiation dose of digital radiography (DR) versus micro-dose x-ray (EOS) on patients with adolescent idiopathic scoliosis: 2016 SOSORT- IRSSD "John Sevastic Award" Winner in Imaging Research. *Scoliosis and Spinal Disorders*. **11**(1), p.46.

Huo, X., Tan, J.Q., Qian, J., Cheng, L., Jing, J.H., Shao, K. and Li, B.N. 2017. An integrative framework for 3D cobb angle measurement on CT images. *Computers in Biology and Medicine*. **82**(January), pp.111–118.

Hwang, J.-H., Modi, H.N., Suh, S.-W., Hong, J.-Y., Park, Y.-H., Park, J.-H. and Yang, J.-H. 2010. Reliability of lumbar lordosis measurement in patients with spondylolisthesis: a case-control study comparing the Cobb, centroid, and posterior tangent methods. *Spine*. **35**(18), pp.1691–1700.

Hwang, Y.S., Lai, P.L., Tsai, H.Y., Kung, Y.C., Lin, Y.Y., He, R.J. and Wu, C. Te 2018. Radiation dose for pediatric scoliosis patients undergoing whole spine radiography: Effect of the radiographic length in an auto-stitching digital radiography system. *European Journal of Radiology*. **108**(April), pp.99–106.

IAEA 2014. *Diagnostic Radiology Physics* (D. R. Dance, S. Christofides, A. D. A. Maidment, I. D. McLean, & K. H. NG, eds.). Vienna: International Atomic Energy Agency.

IAEA 2007. *Dosimetry in Diagnostic Radiology: an Internacional Code of Practice*. Vienna: International Atomic Energy Agency.

IAEA 2013. *Dosimetry in diagnostic radiology for paediatric patients* [Online]. Vienna: International Atomic Energy Agency. Available from: http://www-pub.iaea.org/MTCD/publications/PDF/Pub1609_web.pdf%5Cnhttp://www.vomfi.univ.kiev.ua/assets/files/IAEA/Pub1462_web.pdf.

ICRP 1991. *1990 Recommendations of the International Commission on Radiological Protection*. Oxford, UK: Pergamon Press.

ICRP 2002. *Basic Anatomical and Physiological Data for Use in Radiological Protection Reference Values [report 89]* [Online]. Oxford, UK: Pergamon Press. Available from: http://www.sciencedirect.com/science/article/pii/S0146645303000022.

ICRP 2007. *ICRP 103: The 2007 Recommendations of the International Commission on Radiological Protection* [Online]. Oxford, UK: Pergamon Press. Available from: http://ani.sagepub.com/lookup/doi/10.1016/j.icrp.2007.10.001.

ICRP 2004. *Managing patient dose in digital radiology* [Online]. Available from: https://journals.sagepub.com/doi/abs/10.1016/j.icrp.2004.02.001.

ICRU 1992. *Phantoms and Computational Models in Therapy, Diagnosis and Protection (Report 48)* [Online]. Bethesda, Maryland: International Commission on Radiation Units and Measurements. Available from: https://doi.org/10.1093/jicru/os25.1.Report48.

ICRU 1989. *Tissue substitutes in radiation dosimetry and measurments*. Bethesda, MD: International Commission on Radiation Units and Measurments.

IEC 2012. *Medical electrical equipment —dosimeters with ionization chambers and/or semi-conductor detectors as used in X ray diagnostic imaging*. Geneva, Switzerland.

Ilharreborde, B., Ferrero, E., Alison, M. and Mazda, K. 2016. EOS microdose protocol for the radiological follow-up of adolescent idiopathic scoliosis. *European Spine Journal*. **25**(2), pp.526–531.

Ilharreborde, B., Sebag, G., Skalli, W. and Mazda, K. 2013. Adolescent idiopathic scoliosis treated with posteromedial translation: Radiologic evaluation with a 3D low-dose system. *European Spine Journal*. **22**(11), pp.2382–2391.

Ilharreborde, B., Steffen, J.S., Nectoux, E., Vital, J.M., Mazda, K., Skalli, W. and Obeid, I. 2011. Angle measurement reproducibility using EOS three-dimensional reconstructions in adolescent idiopathic scoliosis treated by posterior instrumentation. *Spine*. **36**(20), pp.1306–1313.

Illés, T., Tunyogi-Csapó, M. and Somoskeöy, S. 2011. Breakthrough in three-dimensional scoliosis diagnosis: Significance of horizontal plane view and vertebra vectors. *European Spine Journal*. **20**(1), pp.135–143.

Imaging Technology News 2019. CT systems: Comparsion chart. [Accessed 5 October 2019]. Available from: www.ITNonline.com.

ImPACT 2002. *ImPACT CT Dosimetry Calculator, imaging performance assessment of CT scanners* [Online]. London: St. George's hospital. Available from: www.impactscan.org.

John, E.M., Phipps, A.I., Knight, J.A., Milne, R.L., Dite, G.S., Hopper, J.L., Andrulis, I.L., Southey, M., Giles, G.G., West, D.W. and Whittemore, A.S. 2007. Medical radiation exposure and breast cancer risk : Findings from the breast cancer family registry. *international Journal of Cancer*. **394**, pp.386–394.

Johnson, J.N., Hornik, C.P., Li, J.S., Benjamin Jr, D.K., Yoshizumi, T.T., Reiman, R.E.,

Frush, D.P. and Hill, K.D. 2014. Cumulative radiation exposure and cancer risk estimation in children with heart disease. *Circulation*. **130**(2), pp.161–167.

Jones, A.K. 2006. *Dose versus image quality in pediatric radiology: Studies using a tomographic newborn physical phantom with an incorporated dosimetry system*. University of Florida.

Jones, A.K., Hintenlang, D.E. and Bolch, W.E. 2003. Tissue-equivalent materials for construction of tomographic dosimetry phantoms in pediatric radiology. *Medical Physics*. **30**(8), pp.2072–2081.

Jones, A.K., Pazik, F.D., Hintenlang, D.E. and Bolch, W.E. 2005. MOSFET dosimeter depth-dose measurements in heterogeneous tissue-equivalent phantoms at diagnostic x-ray energies. *Medical Physics*. **32**(10), pp.3209–3213.

Jones, J.K., Krow, A., Hariharan, S. and Weekes, L. 2008. Measuring angles on digitalized radiographic images using Microsoft PowerPoint. *The West Indian medical journal*. **57**(1), pp.14–19.

Jumriah, Dewang, S., Abdullah, B. and Tahir, D. 2018. Study of image quality, radiation dose and low contrast resolution from MSCT head by using low tube voltage. *Journal of Physics*. **979**(1).

Kalra, M.K., Quick, P., Singh, S., Sandborg, M. and Persson, A. 2013. Whole spine CT for evaluation of scoliosis in children: Feasibility of sub-milliSievert scanning protocol. *Acta Radiologica*. **54**(2), pp.226–230.

Kamtsiuris, P., Atzpodien, K., Ellert, U., Schlack, R. and Schlaud, M. 2007. Prevalence of somatic diseases in German children and adolescents. Results of the German Health Interview and Examination Survey for children and adolescents (KiGGS). *Bundesgesundheitsblatt - Gesundheitsforschung - Gesundheitsschutz*. **50**(5–6), pp.686–700.

Kaza, R.K., Platt, J.F., Goodsitt, M.M., Al-Hawary, M.M., Maturen, K.E., Wasnik, A.P. and Pandya, A. 2014. Emerging techniques for dose optimization in abdominal CT. *RadioGraphics*. **34**(1), pp.4–17.

Keenan, B.E., Izatt, M.T., Askin, G.N., Labrom, R.D., Pearcy, M.J. and Adam, C.J. 2014. Supine to standing Cobb angle change in idiopathic scoliosis: the effect of endplate pre-selection. *Scoliosis*. **9**(16), pp.1–9.

Kei Ma, W., Hogg, P. and Norton, S. 2014. Effects of kilovoltage, milliampere seconds, and focal spot size on image quality. *Radiol Technol*. **85**(5), pp.479–485.

Kiljunen, T., Tietavainen, A., Parviainen, T., Viitala, A. and Kortesniemi, M. 2009. Organ doses and effective doses in pediatric radiography: Patient-dose survey in Finland. *Acta Radiologica*. **50**(1), pp.114–124.

Kim, D., Jo, B., Lee, Y., Park, S.-J., Lee, D.-H. and Kim, H.-J. 2015. Evaluation of effective dose with chest digital tomosynthesis system using Monte Carlo simulation *In*: *Medical Imaging* [Online]. San Diego, CA: SPIE. Available from: http://proceedings.spiedigitallibrary.org/proceeding.aspx?doi=10.1117/12.2081778.

Kim, H., Kim, H.S., Moon, E.S., Yoon, C., Chung, T.-S., Song, H.-T., Suh, F.-S., Lee, Y.H. and Kim, S. 2010. Scoliosis Imaging : What radiologists should know. *RadioGraphics*. **30**(2006), pp.1823–42.

Kim, K., Jargalsuren, S., Khuyagbaatar, B., Park, W.M., Lee, S.K. and Kim, Y.H. 2018. Robustness of whole spine reconstruction using anterior-posterior and lateral planar X-ray images. *International Journal of Precision Engineering and Manufacturing*. **19**(2), pp.281–285.

Kim, M.-J., Lee, S.-R., Lee, M.-Y., Sohn, J.W., Yun, H.G., Choi, J.Y., Jeon, S.W. and Suh, T.S. 2017. Characterization of 3D printing techniques: Toward patient specific quality assurance spine-shaped phantom for stereotactic body radiation therapy. *PloS one*. **12**(5), p.e0176227.

Kim, M.S., Lee, J.W., Kim, S.G. and Kweon, D.C. 2017. Comparison of radiation dose and image quality with various computed-tomography scout views: The angular modulation technique based on information calculated from scout views. *Iranian Journal of Radiology*. **14**(1).

Kim, W., Porrino, J.A., Hood, K.A., Chadaz, T.S., Klauser, A.S. and Taljanovic, M.S. 2018. Clinical evaluation, imaging, and management of adolescent idiopathic and adult degenerative scoliosis. *Current Problems in Diagnostic Radiology*. **48**(4), pp.402–414.

Knott, P., Mardjetko, S., Rollet, M., Baute, S., Riemenschneider, M. and Muncie, L. 2010. Evaluation of the reproducibility of the formetric 4D measurements for scoliosis. *Scoliosis*. **5**(Suppl 1), p.O10.

Knott, P., Pappo, E., Cameron, M., Demauroy, J., Rivard, C., Kotwicki, T., Zaina, F., Wynne, J., Stikeleather, L., Bettany-Saltikov, J., Grivas, T.B., Durmala, J., Maruyama, T., Negrini, S., O'Brien, J.P. and Rigo, M. 2014. SOSORT 2012 consensus paper: reducing x-ray exposure in pediatric patients with scoliosis. *Scoliosis*. **9**(1), p.4.

Knott, P., Sturm, P., Lonner, B., Cahill, P., Betsch, M., McCarthy, R., Kelly, M., Lenke, L. and Betz, R. 2016. Multicenter comparison of 3D spinal measurements using surface topography with those from conventional radiography. *Spine Deformity*. **4**(2), pp.98–103.

Koivisto, J., Kiljunen, T., Wolff, J. and Kortesniemi, M. 2013. Characterization of MOSFET dosimeter angular dependence in three rotational axes measured free-In-Air and in soft-Tissue equivalent material. *Journal of Radiation Research*. **54**(5), pp.943–949.

Koivisto, J., Schulze, D., Wolff, J. and Rottke, D. 2014. Effective dose assessment in the maxillofacial region using thermoluminescent (TLD) and metal oxide semiconductor field-effect transistor (MOSFET) dosemeters: A comparative study. *Dentomaxillofacial Radiology*. **43**(8), pp.1–6.

Koivisto, J.H., Wolff, J.E., Kiljunen, T., Schulze, D. and Kortesniemi, M. 2015. Characterization of MOSFET dosimeters for low-dose measurements in maxillofacial anthropomorphic phantoms. *Journal of applied clinical medical physics / American College of Medical Physics*. **16**(4), p.5433.

Konieczny, M.R., Senyurt, H. and Krauspe, R. 2013. Epidemiology of adolescent idiopathic

scoliosis. *Journal of Children's Orthopaedics*. **7**(1), pp.3–9.

Konstantinidis, A. 2014. Physical parameters of image quality *In*: A. Brahme, ed. *Comprehensive Biomedical Physics*. Amsterdam: Elsevier, pp.49–63.

Koo, T.K. and Li, M.Y. 2016. A guideline of selecting and reporting intraclass correlation coefficients for reliability research. *Journal of Chiropractic Medicine*. **15**(2), pp.155–163.

Korner, M., Weber, C., Wirth, S., Pfeifer, K., Reiser, M. and Treitl, M. 2007. Advances in digital radiography: Physical principles and system overview. *RadioGraphics*. **27**(3), pp.675–686.

Kotwicki, T. 2008. Improved accuracy in Risser sign grading with lateral spinal radiography. *European Spine Journal*. **17**(12), pp.1676–1685.

Kramer, H., Moores, B. and Stieve, F. 2012. Dosimetry and diagnostic radiology and radiotherapy *In*: *Medical Radiological Physics*. Heidelberg: Springer.

Kuba, V.M., Leone, C. and Damiani, D. 2013. Is waist-to-height ratio a useful indicator of cardio-metabolic risk in 6-10-year-old children? *BMC pediatrics*. **13**, p.91.

Lam, G.C., Hill, D.L., Le, L.H., Raso, J. V. and Lou, E.H. 2008. Vertebral rotation measurement: A summary and comparison of common radiographic and CT methods. *Scoliosis*. **3**(1), pp.1–10.

Langensiepen, S., Semler, O., Sobottke, R., Fricke, O., Franklin, J., Schönau, E. and Eysel, P. 2013. Measuring procedures to determine the Cobb angle in idiopathic scoliosis: A systematic review. *European Spine Journal*. **22**(11), pp.2360–2371.

Latalski, M., Danielewicz-Bromberek, A., Fatyga, M., Latalska, M., Kröber, M. and Zwolak, P. 2017. Current insights into the aetiology of adolescent idiopathic scoliosis. *Archives of Orthopaedic and Trauma Surgery*. **137**(10), pp.1327–1333.

Law, M., Ma, W.K., Chan, E., Lau, D., Mui, C., Cheung, K., Yip, L. and Lam, W. 2017. Evaluation of cumulative effective dose and cancer risk from repetitive full spine imaging using EOS system: Impact to adolescent patients of different populations. *European Journal of Radiology*. **96**(July), pp.1–5.

Law, M., Ma, W.K., Chan, E., Mui, C., Ma, V., Ho, W.Y., Yip, L. and Lam, W. 2017. Cumulative Effective Dose and Cancer Risk of Pediatric Population in Repetitive Whole-Body Scan Using Dual-Energy X-Ray Absorptiometry. *Journal of Clinical Densitometry*., pp.1–7.

Law, M., Ma, W.K., Lau, D., Chan, E., Yip, L. and Lam, W. 2016. Cumulative radiation exposure and associated cancer risk estimates for scoliosis patients: Impact of repetitive full spine radiography. *European Journal of Radiology*. **85**(3), pp.625–628.

Law, M., Ma, W.K., Lau, D., Cheung, K., Ip, J., Yip, L. and Lam, W. 2018. Cumulative effective dose and cancer risk for pediatric population in repetitive full spine follow-up imaging: How micro dose is the EOS microdose protocol? *European Journal of Radiology*. **101**(February), pp.87–91.

Lechner, R., Putzer, D., Dammerer, D., Liebensteiner, M., Bach, C. and Thaler, M. 2017. Comparison of two- and three-dimensional measurement of the Cobb angle in scoliosis. *International Orthopaedics*. **41**(5), pp.957–962.

Lee, B., Lee, S., Yang, I. and Yoon, M. 2014. Evaluation of the stepwise collimation method for the reduction of the patient dose in full spine radiography. *Journal of the Korean Physical Society*. **64**(9), pp.1380–1384.

Lee, C.I., McLean, D. and Robinson, J. 2005. Measurement of effective dose for paediatric scoliotic patients. *Radiography*. **11**(2), pp.89–97.

Lee, M.C., Solomito, M. and Patel, A. 2013. Supine magnetic resonance imaging cobb measurements for idiopathic scoliosis are linearly related to measurements from standing plain radiographs. *Spine*. **38**(11).

Lee, W. 2018. Spinal Orthoses *In*: *Braddoms Rehabilitation Care: A Clinical Handbook* [Online]. Elsevier Inc., pp.85-91.e2. Available from: http://dx.doi.org/10.1016/B978-0-323-47904-2.00013-1.

Lemoigne, Y. and Caner, A. 2010. *Radiation Protection in Medical Physics*. Dordrecht: Springer.

Levy, A.R., Goldberg, M.S., Mayo, N.E., Hanley, J.A. and Poitras, B. 1996. Reducing the lifetime risk of cancer from spinal radiographs among people with adolescent idiopathic scoliosis. *Spine*. **21**(13), pp.1540–1547.

Lin, E.C. 2010. Radiation risk from medical imaging. *Mayo Clinic Proceedings*. **85**(12), pp.1142–1146.

Little, M.P., Wakeford, R., Tawn, E.J., Bouffler, S.D. and Berrington de Gonzalez, A. 2009. Risks associated with low doses and low dose rates of ionizing radiation: Why linearity may be (almost) the best we can Do. *Radiology*. **251**(1), pp.6–12.

Liu, J., Ma, L., He, J., Zhang, Q., Chen, H. and Pan, L. 2012. A comparative study of assessment methods for medical image quality. *2012 5th International Conference on Biomedical Engineering and Informatics, BMEI 2012*. (Bmei), pp.131–134.

Lofthag-Hansen, S. 2010. Cone beam computed tomography radiation dose and image quality assessments. *Swedish dental journal. Supplement*. (209), pp.4–55.

Louis, G.B., Damstra, T., Díaz-Barriga, F., Faustman, E., Hass, U., Kavlock, R., Kimmel, C., Kimmel, G., Krishnan, K., Luderer, U. and Sheldon, L. 2006. Environmental health criteria 237: Principles for evaluating health risks in children associated with exposure to chemicals. , pp.1–327.

Ludewig, E., Richter, A. and Frame, M. 2010. Diagnostic imaging - Evaluating image quality using visual grading characteristic (VGC) analysis. *Veterinary Research Communications*. **34**(5), pp.473–479.

Luo, T.D., Stans, A.A., Schueler, B.A. and Larson, A.N. 2015. Cumulative radiation exposure with EOS imaging compared with standard spine radiographs. *Spine Deformity*. **3**(2), pp.144–150.

Machida, M., Weinstein, S.L. and Dubousset, J. 2018. *Pathogenesis of idiopathic scoliosis*. Yokohama, Kanagawa, Japan: Springer.

Macmillan Cancer 2019. CT scan (computerised tomography). [Accessed 7 April 2019]. Available from: https://www.macmillan.org.uk/information-and-support/diagnosing/how-cancers-are-diagnosed/tests-and-scans/ct-scan.html.

Madu, M.J., Ndaliman and Oche, B. 2016. Evaluation of water-to-plaster ratio on products of nafada plaster of Paris (PoP). *International Journal of Emerging Engineering Research and Technology*. **4**(10), pp.23–27.

Mahboub-Ahari, A., Hajebrahimi, S., Yusefi, M. and Velayati, A. 2016. EOS imaging versus current radiography: A health technology assessment study. *Medical Journal of the Islamic Republic of Iran*. **30**(1).

Mahmoud Hamdy Abaza, A. 2017. New trend in radiation dosimeters. *American Journal of Modern Physics*. **7**(1), pp.21–30.

Maillot, C., Ferrero, E., Fort, D., Heyberger, C. and Le Huec, J.C. 2015. Reproducibility and repeatability of a new computerized software for sagittal spinopelvic and scoliosis curvature radiologic measurements: Keops®. *European Spine Journal*. **24**(7), pp.1574–1581.

Mangone, M., Raimondi, P., Paoloni, M., Pellanera, S., Di Michele, A., Di Renzo, S., Vanadia, M., Dimaggio, M., Murgia, M. and Santilli, V. 2013. Vertebral rotation in adolescent idiopathic scoliosis calculated by radiograph and back surface analysis-based methods: Correlation between the Raimondi method and rasterstereography. *European Spine Journal*. **22**(2), pp.367–371.

Mann, K.S., Kurudirek, M. and Sidhu, G.S. 2012. Verification of dosimetric materials to be used as tissue-substitutes in radiological diagnosis. *Applied Radiation and Isotopes*. **70**(4), pp.681–691.

Mansson, L.G. 2000. Methods for the evaluation of image quality: A review. *Radiation Protection Dosimetry*. **90**(1), pp.89–99.

Marieb, E.N., Wilhelm, P.B. and Mallatt, J. 2012. *Human Anatomy* 6th ed. London, UK: Benjamin Cummings.

Marshall, N.W., Mackenzie, A. and Honey, I.D. 2011. Quality control measurements for digital x-ray detectors. *Physics in Medicine and Biology*. **56**(4), pp.979–999.

Marshall, W.A. and Tanner, J.M. 1969. Variations in pattern of pubertal changes in girls. *Archives of Disease in Childhood*. **44**(235), pp.291–303.

Martin, C.J. 2007. An evaluation of semiconductor and ionization chamber detectors for diagnostic x-ray dosimetry measurements. *Physics in Medicine and Biology*. **52**(15), pp.4465–4480.

Mattsson, S. and Thomas, B.J. 2006. Development of methods for body composition studies. *Physics in medicine and biology*. **51**(13), pp.R203–R228.

Mayo-Smith, W.W., Hara, A.K., Mahesh, M., Sahani, D. V. and Pavlicek, W. 2014. How I do

it: Managing radiation dose in CT. *Radiology*. **273**(3), pp.657–672.

McCollough, C.H., Christner, J.A. and Kofler, J.M. 2010. How effective is effective dose as a predictor of radiation risk? *American Journal of Roentgenology*. **194**(4), pp.890–896.

Mccollough, C.H. and Schueler, B.A. 2000. Calculation of effective dose. *Medical Physics*. **27**(5), pp.828–837.

McCullagh, J.B., Baldelli, P. and Phelan, N. 2011. Clinical dose performance of full field digital mammography in a breast screening programme. *The British journal of radiology*. **84**(1007), pp.1027–1033.

McKenna, C., Wade, R., Faria, R., Yang, H., Stirk, L., Gummerson, N., Sculpher, M. and Woolacott, N. 2012. EOS 2D/3D X-ray imaging system: A systematic review and economic evaluation. *Health Technology Assessment*. **16**(14).

Meghzifene, A., Dance, D.R., McLean, D. and Kramer, H.M. 2010. Dosimetry in diagnostic radiology. *European Journal of Radiology*. **76**(1), pp.11–14.

Melhem, E., Assi, A., El Rachkidi, R. and Ghanem, I. 2016. EOS®biplanar X-ray imaging: concept, developments, benefits, and limitations. *Journal of Children's Orthopaedics*. **10**(1), pp.1–14.

Mertz, H.J., Jarrett, K., Moss, S., Salloum, M. and Zhao, Y. 2001. The hybrid III 10-year-Old Dummy. *Stapp car crash journal*. **45**, pp.319–328.

Mettler, F.A.J., Huda, W., Yoshizumi, T.T. and Mahesh, M. 2008. Effective doses in radiology and diagnostic nuclear medicine: a catalog. *Radiology*. **248**(1), pp.254–263.

Mitsouras, D., Liacouras, P., Imanzadeh, A., Giannopoulos, A.A., Cai, T., Kumamaru, K.K., George, E., Wake, N., Caterson, E.J., Pomahac, B., Ho, V.B., Grant, G.T. and Rybicki, F.J. 2015. Medical 3D printing for the radiologist. *Radiographics : a review publication of the Radiological Society of North America, Inc*. **35**(7), pp.1965–1988.

Mogaadi, M., Ben Omrane, L. and Hammou, A. 2012. Effective dose for scoliosispatients undergoing full spine radiography. *Radiation Protection Dosimetry*. **149**(3), pp.297–303.

Mohammed Ali, A. 2019. *An Investigation into Methods for Dose Optimisation for Paediatric AP Pelvis Projections When Considering Size Variations*. University of Salford.

Mohammed Ali, A., Hogg, P., Johansen, S. and England, A. 2018. Construction and validation of a low cost paediatric pelvis phantom. *European Journal of Radiology*. **108**(September), pp.84–91.

Morel, B., Moueddeb, S., Blondiaux, E., Richard, S., Bachy, M., Vialle, R. and Ducou Le Pointe, H. 2018. Dose, image quality and spine modeling assessment of biplanar EOS micro-dose radiographs for the follow-up of in-brace adolescent idiopathic scoliosis patients. *European Spine Journal*. (0123456789), pp.1–7.

Mori, M., Imai, K., Ikeda, M., Iida, Y., Ito, F., Yoneda, K. and Enchi, Y. 2013. Method of measuring contrast-to-noise ratio (CNR) in nonuniform image area in digital radiography. *Electronics and Communications in Japan*. **96**(7), pp.32–41.

Morrissy, R.T., Goldsmith, G.S., Hall, E.C., Kehl, D. and Cowie, G.H. 1990. Measurement of the Cobb angle on radiographs of patients who have scoliosis. Evaluation of intrinsic error. *The Journal of bone and joint surgery. American volume*. **72**(3), pp.320–327.

Mraity, H. 2015. *Optimisation of radiation dose and image quality for AP pelvis radiographic examination*. University of Salford.

Mraity, H., England, A. and Hogg, P. 2014. Developing and validating a psychometric scale for image quality assessment. *Radiography*. **20**(4), pp.306–311.

NAS 2006. *Health risks from exposure to low levels of ionizing radiation: Phase 2, BEIR. VII.* Washington, D.C: National Academy of Sciences.

Nash, C.L.J., Gregg, E.C., Brown, R.H. and Pillai, K. 1979. Risks of exposure to X-rays in patients undergoing long-term treatment for scoliosis. *Journal of Bone & Joint Surgery*. **61**(3), pp.371–374.

Nash, C.L.J.R. and Moe, J.H. 1969. A Study of vertebral rotation. *The Journal of Bone & Joint Surgery*. **51**(2), pp.223–229.

National Research Council 2012. *Analysis of cancer risks in populations near nuclear facilities: Phase 1* [Online]. Washington, DC: The National Academies Press. Available from: https://www.nap.edu/catalog/13388/analysis-of-cancer-risks-in-populations-near-nuclear-facilities-phase.

Nauer, C.B., Kellner-Weldon, F., Von Allmen, G., Schaller, D. and Gralla, J. 2009. Effective doses from scan projection radiographs of the head: Impact of different scanning practices and comparison with conventional radiography. *American Journal of Neuroradiology*. **30**(1), pp.155–159.

Nault, M.L., Parent, S., Phan, P., Roy-Beaudry, M., Labelle, H. and Rivard, M. 2010. A modified risser grading system predicts the curve acceleration phase of female adolescent idiopathic scoliosis. *Journal of Bone and Joint Surgery - Series A*. **92**(5), pp.1073–1081.

Nery, L.S., Halpern, R., Nery, P.C., Nehme, K.P. and Stein, A.T. 2010. Prevalence of scoliosis among school students in a town in southern Brazil. *Sao Paulo medical journal*. **128**(2), pp.69–73.

Newton, P.O., Khandwala, Y., Bartley, C.E., Reighard, F.G., Bastrom, T.P. and Yaszay, B. 2016. New EOS imaging protocol allows a substantial reduction in radiation exposure for scoliosis patients. *Spine Deformity*. **4**(2), pp.138–144.

Ng, J. and Shuryak, I. 2015. Minimizing second cancer risk following radiotherapy: current perspectives. *Cancer management and research*. **7**, pp.1–11.

Ng, S.-Y. and Bettany-Saltikov, J. 2017. Imaging in the diagnosis and monitoring of children with idiopathic scoliosis. *The Open Orthopaedics Journal*. **11**(Suppl-9, M5), pp.1500–1520.

NHS 2019. *Diagnostic Imaging Dataset Annual Statistical Release* [Online]. Leeds. Available from: https://www.england.nhs.uk/statistics/wp-content/uploads/sites/2/2014/06/Annual-

Statistical-Release-2013-14-DID-pdf-1118KB.pdf.

NHS 2018. *Diagnostic Imaging Dataset Statistical Release* [Online]. Leeds. Available from: https://www.england.nhs.uk/statistics/wp-content/uploads/sites/2/2015/08/Provisional-Monthly-Diagnostic-Imaging-Dataset-Statistics-2016-03-17.pdf.

NHS Supply Chain 2019. CT Scanners and Associated Options and Related Services. [Accessed 3 October 2019]. Available from: https://www.supplychain.nhs.uk/product-information/contract-launch-brief/ct-scanners-and-associated-options-and-related-services/?utm_source=ct-scanners-and-associated-options-and-related-services&utm_medium=Web&utm_campaign=Search.

NICE 2016. *Aquilion PRIME CT scanner for imaging coronary artery disease in adults in whom imaging is difficult* [Online]. Available from: https://www.nice.org.uk/terms-and-.

NICE 2011. *The EOS 2D/3D imaging system*.

Nowik, P., Bujila, R., Kull, L., Andersson, J. and Poludniowski, G. 2017. The dosimetric impact of including the patient table in CT dose estimates. *Physics in Medicine & Biology*. **62**(23), pp.N538–N547.

Nuri Sener, R., Ripeckyj, G.T., Otto, P.M., Rauch, R.A. and Jinkins, J.R. 1993. Recognition of abnormalities on computed scout images in CT examinations of the head and spine. *Neuroradiology*. **35**(3), pp.229–231.

O'Connor, M.K. 2017. Risk of low-dose radiation and the BEIR VII report: A critical review of what it does and doesn't say. *Physica Medica*. **43**, pp.153–158.

Obuchowski, N.A. 2003. Receiver operating characteristic curves and their use in radiology. *Radiology*. **229**(1), pp.3–8.

Ofori, E.K., Ofori-Manteaw, B.B., Gawugah, J.N.K. and Nathan, J.A. 2016. Relationship between patient anatomical thickness and radiographic exposure factors for selected radiologic examinations. *Journal of Health, Medicine and Nursing*. **23**, pp.150–162.

Oliveira, M.L. de, Maia, A.F., Nascimento, N.C. do E.S., Fragoso, M. da C. de F., Galindo, R.S. and Hazin, C.A. 2010. Influence of thermoluminescent dosimeters energy dependence on the measurement of entrance skin dose in radiographic procedures*. *Radiologia Brasileira*. **43**(2), pp.113–118.

Ozturk, C., Karadereler, S., Ornek, I., Enercan, M., Ganiyusufoglu, K. and Hamzaoglu, A. 2010. The role of routine magnetic resonance imaging in the preoperative evaluation of adolescent idiopathic scoliosis. *International Orthopaedics*. **34**(4), pp.543–546.

Pace, N., Ricci, L. and Negrini, S. 2013. A comparison approach to explain risks related to X-ray imaging for scoliosis, 2012 SOSORT award winner. *Scoliosis*. **8**(1), p.11.

Palepu, V., Rayaprolu, S.D. and Nagaraja, S. 2019. Differences in trabecular bone, cortical shell, and endplate microstructure across the lumbar spine. *International journal of spine surgery*. **13**(4), pp.361–370.

Paquet, F., Bailey, M.R., Leggett, R.W. and Harrison, J.D. 2016. Assessment and interpretation of internal doses: uncertainty and variability. *Annals of the ICRP*. **45**(1

Suppl), pp.202–214.

Pedersen, P.H., Petersen, A.G., Estgaard, S.E., Tvedebrink, T. and Eiskjær, S.P. 2018. EOS micro-dose protocol: First full-spine radiation dose measurements in anthropomorphic phantoms and comparisons with EOS standard-dose and conventional digital radiology. *Spine*. **43**(22), pp.E1313–E1321.

Perdriolle, R. and Vidal, J. 1985. Thoracic idiopathic scoliosis curve evolution and prognosis. *Spine*. **10**(9), pp.785–791.

Philips Healthcare 2010a. *Brilliant Performance: Philips Brilliance CT 64-channel with Essence technology*. Best, Netherlands.

Philips Healthcare 2010b. *Clinical confidence in action Philips Ingenuity CT specifications*. Best, Netherlands.

Philips Healthcare 2019. *Intellect at every step Philips Incisive CT*. Best, Netherlands.

Pina, D.R., Duarte, S.B., Ghilardi Netto, T. and Morceli, J. 2009. Phantom development for radiographic image optimization of chest, skull and pelvis examination for nonstandard patient. *Applied Radiation and Isotopes*. **67**(1), pp.61–69.

Pinto, T.C.N.O., Antonio, P.L., Gronchi, C.C. and Caldas, L.V.E. 2014. Light induced fading associated with the application of OSL to personal dosimetry. *Radiation Measurements*. **71**, pp.425–429.

Podnieks, E.C. and Negus, I.S. 2012. Practical patient dosimetry for partial rotation cone beam CT. *British Journal of Radiology*. **85**(1010), pp.161–167.

Pomero, V., Mitton, D., Laporte, S., De Guise, J.A. and Skalli, W. 2004. Fast accurate stereoradiographic 3D-reconstruction of the spine using a combined geometric and statistic model. *Clinical Biomechanics*. **19**(3), pp.240–247.

Portney, L. and Watkins, M. 2000. *Foundations of clinical research: applications to practice*. new Jersey: Prentice Hall.

Presciutti, S.M., Karukanda, T. and Lee, M. 2014. Management decisions for adolescent idiopathic scoliosis significantly affect patient radiation exposure. *Spine Journal*. **14**(9), pp.1984–1990.

Pruijs, J.E.H., Hageman, M.A.P.E., Keessen, W., van der Meer, R. and van Wieringen, J.C. 1994. Variation in Cobb angle measurements in scoliosis. *Skeletal Radiology*. **23**(7), pp.517–520.

Qiao, J., Liu, Z., Xu, L., Wu, T., Zheng, X., Zhu, Z., Zhu, F., Qian, B. and Qiu, Y. 2012. Reliability Analysis of a Smartphone-aided Measurement Method for the Cobb Angle of Scoliosis. *Clinical Spine Surgery*. **25**(4).

Raman, S.P., Mahesh, M., Blasko, R. V. and Fishman, E.K. 2013. CT scan parameters and radiation dose: Practical advice for radiologists. *Journal of the American College of Radiology*. **10**(11), pp.840–846.

Ramanaidu, S., Sta Maria, R.B., Ng, K.H., George, J. and Kumar, G. 2006. Evaluation of

radiation dose and image quality following changes to tube potential (kVp) in conventional paediatric chest radiography. *Biomedical Imaging and Intervention Journal*. **2**(3).

RCR 2019. *Picture archiving and communication systems (PACS) and guidelines on diagnostic display devices* [Online] (3rd, ed.). London, UK. Available from: https://www.rcr.ac.uk/system/files/publication/field_publication_files/bfcr192_pacs-diagnostic-display.pdf.

Regulla, D.F., Hieber, L.B. and Seidenbusch, M. 1998. Physical and biological interface dose effects in tissue due to X-ray-induced release of secondary radiation from metallic gold surfaces. *Radiation Research*. **150**(1), pp.92–100.

Rehm, J., Germann, T., Akbar, M., Pepke, W., Kauczor, H.U., Weber, M.A. and Spira, D. 2017. 3D-modeling of the spine using EOS imaging system: Inter-reader reproducibility and reliability. *PLoS ONE*. **12**(2), pp.1–13.

Ritter, R., Nagasse, Y., Ribeiro, I., Yamazato, C., Oliveira, F.M. de and Kusabara, R. 2016. Comparison of cobb angle measurement in scoliosis by residents and spine experts. *Coluna/Columna*. **15**, pp.13–16.

Robinson, J.B.B., Ali, R.M.M., Tootell, A.K.K. and Hogg, P. 2017. Does collimation affect patient dose in antero-posterior thoraco-lumbar spine? *Radiography*. **23**(3), pp.211–215.

Rolin, O.Y. and Carter, W.E. 2019. Biomechanics of the Spine *In*: J. B. Webster and D. P. B. T.-A. of O. and A. D. (Fifth E. Murphy, eds. *Atlas of Orthoses and Assistive Devices* [Online]. Philadelphia: Content Repository Only!, pp.64-68.e1. Available from: https://doi.org/10.1016/B978-0-323-48323-0.00005-6.

Ron, E. 2003. Cancer risks from medical radiation. *Health Phys*. **85**(1), pp.47–59.

Ronckers, C.M., Doody, M.M., Lonstein, J.E., Stovall, M. and Land, C.E. 2008. Multiple diagnostic X-rays for spine deformities and risk of breast cancer. *Cancer Epidemiology Biomarkers and Prevention*. **17**(3), pp.605–613.

Ronckers, C.M., Erdmann, C.A. and Land, C.E. 2005. Radiation and breast cancer: a review of current evidence. *Breast cancer research : BCR*. **7**(1), pp.21–32.

Ronckers, C.M., Land, C.E., Miller, J.S., Stovall, M., Lonstein, J.E.J.E. and Doody, M.M. 2010. Cancer Mortality among Women Frequently Exposed to Radiographic Examinations for Spinal Disorders. *Radiation Research*. **174**(1), pp.83–90.

Rosner, B. 2016. *Fundamentals of Biostatistics* 8th ed. Boston, MA: Cengage Learning.

Rousseau, M.-A., Laporte, S., Chavary-Bernier, E., Lazennec, J.-Y. and Skalli, W. 2007. Reproducibility of measuring the shape and three-dimensional position of cervical vertebrae in upright position using the EOS stereoradiography system. *Spine*. **32**(23).

Rueden, C.T., Schindelin, J., Hiner, M.C., DeZonia, B.E., Walter, A.E., Arena, E.T. and Eliceiri, K.W. 2017. ImageJ2: ImageJ for the next generation of scientific image data. *BMC Bioinformatics*. **18**(1), pp.1–26.

Rühm, W., Azizova, T. V., Bouffler, S.D., Little, M.P., Shore, R.E., Walsh, L. and

Woloschak, G.E. 2015. Dose-rate effects in radiation biology and radiation protection. *Annals of the ICRP*. **45**, pp.262–279.

Russell, M.T., Fink, J.R., Rebeles, F., Kanal, K., Ramos, M. and Anzai, Y. 2008. Balancing radiation dose and image quality: Clinical applications of neck volume CT. *American Journal of Neuroradiology*. **29**(4), pp.727–731.

Russo, P. 2014. Physical basic of X-ray imaging *In*: *Comprehensive Biomedical Physics*. Elsevier.

Ryan, P.M., Puttler, E.G., Stotler, W.M. and Ferguson, R.L. 2007. Role of the triradiate cartilage in predicting curve progression in adolescent idiopathic scoliosis. *Journal of Pediatric Orthopaedics*. **27**(6), pp.671–676.

Saltybaeva, N., Krauss, A. and Alkadhi, H. 2019. Technical Note: Radiation dose reduction from computed tomography localizer radiographs using a tin spectral shaping filter. *Medical Physics*. **46**(2), pp.544–549.

Samei, E., Badano, A., Chakraborty, D., Compton, K., Cornelius, C., Corrigan, K., Flynn, M.J., Hemminger, B., Hangiandreou, N., Johnson, J., Moxley-Stevens, D.M., Pavlicek, W., Roehrig, H., Rutz, L., Shepard, J., Uzenoff, R.A., Wang, J. and Willis, C.E. 2005. Assessment of display performance for medical imaging systems: executive summary of AAPM TG18 report. *Medical physics*. **32**(4), pp.1205–1225.

Sanada, S., Kawahara, K., Yamamoto, T. and Takashima, T. 1999. New tissue substitutes representing cortical bone and adipose tissue in quantitative radiology. *Physics in Medicine and Biology*. **44**(6), pp.N107–N112.

Sanders, J.O., Browne, R.H., McConnell, S.J., Margraf, S.A., Cooney, T.E. and Finegold, D.N. 2007. Maturity assessment and curve progression in girls with idiopathic scoliosis. *Journal of Bone and Joint Surgery - Series A*. **89**(1), pp.64–73.

Schmid, S.L., Buck, F.M., Böni, T. and Farshad, M. 2016. Radiographic measurement error of the scoliotic curve angle depending on positioning of the patient and the side of scoliotic curve. *European Spine Journal*. **25**(2).

Schmidt, B., Saltybaeva, N., Kolditz, D. and Kalender, W.A. 2013. Assessment of patient dose from CT localizer radiographs. *Medical Physics*. **40**(8), pp.1–8.

Schmidt, B.T., Hupfer, M., Saltybaeva, N., Kolditz, D. and Kalender, W.A. 2017. Dose optimization for computed tomography localizer radiographs for low-dose lung computed tomography examinations. *Investigative Radiology*. **52**(2), pp.81–86.

Schropp, L., Alyass, N.S., Wenzel, A. and Stavropoulos, A. 2012. Validity of wax and acrylic as soft-tissue simulation materials used in in vitro radiographic studies. *Dentomaxillofacial Radiology*. **41**(8), pp.686–690.

Science Photo Library Limited 2018. Scince photo library. [Accessed 3 October 2018]. Available from: https://www.sciencephoto.com/media/946253/view/scoliosis-x-ray.

Segundo, S. de T. de S.P., Valesin Filho, E.S., Lenza, M., Santos, D. do C.B., Rosemberg, L.A. and Ferretti, M. 2016. Interobserver reproducibility of radiographic evaluation of

lumbar spine instability. *Einstein (São Paulo)*. **14**(3), pp.378–383.

Seibert, J.A. 2008. Digital radiography: Image quality and radiation dose. *Health Physics*. **95**(5), pp.586–598.

Seidenbusch, M.C., Harder, D., Regulla, D.F. and Schneider, K. 2014. Conversion factors for determining organ doses received by paediatric patients in high-resolution single slice computed tomography with narrow collimation. *Zeitschrift fur Medizinische Physik*. **24**(2), pp.123–137.

Sensakovic, W.F., Warden IV, D.R. and Bancroft, L.W. 2017. The Link Between Radiation Optimization and Quality. *Journal of the American College of Radiology*. **14**(6), pp.850–851.

De Sèze, M., Randriaminahisoa, T., Gaunelle, A., de Korvin, G. and Mazaux, J.M. 2013. Inter-observer reproducibility of back surface topography parameters allowing assessment of scoliotic thoracic gibbosity and comparison with two standard postures. *Annals of Physical and Rehabilitation Medicine*. **56**(9–10), pp.599–612.

Shah, D.J., Sachs, R.K. and Wilson, D.J. 2012. Radiation-induced cancer: A modern view. *British Journal of Radiology*. **85**(1020), pp.1166–1173.

Sharma, H. and Prabu, D. 2013. Plaster of Paris: Past, present and future. *Journal of Clinical Orthopaedics and Trauma*. **4**(3), pp.107–109.

Shaw, M., Adam, C.J., Izatt, M.T., Licina, P. and Askin, G.N. 2012. Use of the iPhone for Cobb angle measurement in scoliosis. *European Spine Journal*. **21**(6), pp.1062–1068.

Shea, K.G., Stevens, P.M., Nelson, M., Smith, J.T., Masters, K.S. and Yandow, S. 1998. A comparison of manual versus computer-assisted radiographic measurement. Intraobserver measurement variability for Cobb angles. *Spine*. **23**(5), pp.551–555.

Sheng, S.-R., Wang, X.-Y., Xu, H.-Z., Zhu, G.-Q. and Zhou, Y.-F. 2010. Anatomy of large animal spines and its comparison to the human spine: a systematic review. *European spine journal*. **19**(1), pp.46–56.

Shet, N., Chen, J. and Siegel, E.L. 2011. Continuing challenges in defining image quality. *Pediatric Radiology*. **41**(5), pp.582–587.

Shi, B., Mao, S., Wang, Z., Lam, T.P., Yu, F.W.P., Ng, B.K.W., Chu, W.C.W., Zhu, Z., Qiu, Y. and Cheng, J.C.Y. 2015. How does the supine MRI correlate with standing radiographs of different curve severity in adolescent idiopathic scoliosis? *Spine*. **40**(15), pp.1206–1212.

Shimadzu Europa GmbH 2017. RADspeed Pro EDGE High-performance digital radiographic system with extended functionality. [Accessed 15 February 2019]. Available from: https://www.shimadzu-medical.eu/radspeed-pro-edge.

Shirazi, A., Mahdavi, S.R., Khodadadee, A., Ghaffory, M. and Mesbahi, A. 2008. Monte Carlo simulation of TLD response function: Scattered radiation field application. *Reports of Practical Oncology & Radiotherapy*. **13**(1), pp.23–28.

Shrimpton, P.., M.C., H., Meeson, S. and Golding, S.J. 2014. *Public Health England - Doses*

from Computed Tomography (CT) Examinations in the UK – 2011 Review DRLS HPA-CRCE-013 [Online]. Available from: https://www.gov.uk/government/uploads/system/uploads/attachment_data/file/349188/PHE_CRCE_013.pdf.

Shuryak, I., Hahnfeldt, P., Hlatky, L., Sachs, R.K. and Brenner, D.J. 2009. A new view of radiation-induced cancer: Integrating short- and long-term processes. Part II: Second cancer risk estimation. *Radiation and Environmental Biophysics*. **48**(3), pp.275–286.

Shuryak, I., Sachs, R.K. and Brenner, D.J. 2010. Cancer risks after radiation exposure in middle age. *Journal of the National Cancer Institute*. **102**(21), pp.1628–1636.

Siemens Healthcare 2018. *Drive precision for all Somaton Drive*. Erlangen, Germany.

Siemens Healthcare 2012. *Somatom Definition AS Open 20 / 64 – RT Pro edition*. Muenchen, Germany.

Siemens Healthineers 2017. *Blaze a new trail in RT SOMATOM Confidence RT Pro*. Erlangen Germany.

Siemens Healthineers 2018. *Changing views in CT somatom Edge Plus*. Erlangen, Germany.

Siiskonen, T., Tapiovaara, M., Kosunen, A., Lehtinen, M. and Vartiainen, E. 2007. Monte Carlo simulations of occupational radiation doses in interventional radiology. *The British Journal of Radiology*. **80**(954), pp.460–468.

Simony, A., Hansen, E.J., Christensen, S.B., Carreon, L.Y. and Andersen, M.O. 2016. Incidence of cancer in adolescent idiopathic scoliosis patients treated 25 years previously. *European Spine Journal*. **25**(10), pp.3366–3370.

Sinclair, L., Griglock, T.M., Cormack, B., Bidari, S., Arreola, M., Rill, L. and Mench, A. 2015. Determining organ doses from CT with Direct measurements in postmortem subjects: part 1—methodology and validation. *Radiology*. **277**(2), pp.463–470.

Singh, R. 2016. Radiography *In*: *Applied Welding Engineering* [Online]. Amsterdam: Elsevier, pp.305–326. Available from: http://www.sciencedirect.com/science/article/pii/B9780128041765000232.

Singh, V.H. and Pradhan, H. 2015. Neonatal chest radiography - Comparing image quality and dose for contact-techniques vs. under-tray techniques. *Radiography Open*. **2**(1), p.65.

Singh, V.P., Badiger, N.M. and Kucuk, N. 2014. Determination of Effective Atomic Numbers Using Different Methods for Some Low- Z Materials . *Journal of Nuclear Chemistry*. **2014**, pp.1–7.

Smans, K., Struelens, L., Smet, M., Bosmans, H. and Vanhavere, F. 2010. Cu filtration for dose reduction in neonatal chest imaging. *Radiation Protection Dosimetry*. **139**(1–3), pp.281–286.

Solc, J., Vrba, T. and Burianova, L. 2018. Tissue-equivalence of 3D-printed plastics for medical phantoms in radiology. *Journal of Instrumentation*. **13**(9).

Somoskeöy, S., Tunyogi-Csapó, M., Bogyó, C. and Illés, T. 2012. Accuracy and reliability of coronal and sagittal spinal curvature data based on patient-specific three-dimensional models created by the EOS 2D/3D imaging system. *Spine Journal*. **12**(11), pp.1052–1059.

Sossin, A., Rebuffel, V., Tabary, J., Létang, J.M., Freud, N. and Verger, L. 2017. Characterizing the behavior of scattered radiation in multi-energy x-ray imaging.

Soucacos, P., Zacharis, K., Beris, A., Xenakis, A. and Greece, J. 1997. School-Screening for Scoliosis. *The Journal of Bone and Joint Surgery*., pp.1498–1503.

Sprawls, P. 1995. *Physical principles of principles medical imaging* 2nd. Madison, Wisconsin: Medical Physics Publishing.

Squelch, A. 2018. 3D printing and medical imaging. *Journal of medical radiation sciences*. **65**(3), pp.171–172.

Srinivasalu, S., Modi, H.N., SMehta, S., Suh, S.-W., Chen, T. and Murun, T. 2008. Cobb Angle Measurement of Scoliosis Using Computer Measurement of Digitally Acquired Radiographs-Intraobserver and Interobserver Variability. *Asian Spine Journal*. **2**(2), p.90.

SRS 2000. Revised glossary of terms. [Accessed 12 March 2018]. Available from: https://www.srs.org/professionals/online-education-and-resources/glossary/revised-glossary-of-terms.

Stokes, I.A., Bigalow, L.C. and Moreland, M.S. 1986. Measurement of axial rotation of vertebrae in scoliosis. *Spine*. **11**(3), pp.213–218.

Streffer, C. 2007. *The ICRP 2007 recommendations* [Online]. Oxford, UK: Pergamon Press. Available from: https://dx.doi.org/10.1093/rpd/ncm246.

Suh, S.W., Modi, H.N., Yang, J.H. and Hong, J.Y. 2011. Idiopathic scoliosis in Korean schoolchildren: A prospective screening study of over 1 million children. *European Spine Journal*. **20**(7), pp.1087–1094.

Tanure, M.C., Pinheiro, A.P. and Oliveira, A.S. 2010. Reliability assessment of Cobb angle measurements using manual and digital methods. *Spine Journal*. **10**(9), pp.769–774.

Tapiovaara, M. 2012. *PCXMC 2.0 Supplementary programs user's guide*. Helsinki, Finland: STUK - Radiation and Nuclear Safety Authority.

Tapiovaara, M. and Siiskonen, T. 2008. *A Monte Carlo program for calculating patient doses in medical x-ray examinations* 2nd ed. Helsinki, FINLAND.

Tasi, D.-Y. and Matsuyama, E. 2015. Recent Advances of Quality Assessment for Medical Imaging Systems and Medical Images *In*: *Visual Signal Quality Assessment*. London, UK: Springer.

Tauchi, R., Tsuji, T., Cahill, P.J., Flynn, J.M., Flynn, J.M., Glotzbecker, M., El-Hawary, R., Heflin, J.A., Imagama, S., Joshi, A.P., Nohara, A., Ramirez, N., Roye, D.P., Saito, T., Sawyer, J.R., Smith, J.T. and Kawakami, N. 2016. Reliability analysis of Cobb angle measurements of congenital scoliosis using X-ray and 3D-CT images. *European Journal*

of Orthopaedic Surgery and Traumatology. **26**(1), pp.53–57.

Tavares, A., Lança, L. and Machado, N. 2015. Effect of technical parameters on dose and image quality in a computed radiography system *In*: *European Congress of Radiology*. Vienna.

Telefield Medical Imaging Ltd. 2019. Scolioscan. [Accessed 15 March 2019]. Available from: http://www.telefield-imaging.com.hk/.

The Christie 2018. *Patient Dosimetry and Diagnostic Reference Level Report*. Manchester.

Thermo Fisher Scientific Inc. 2016. *Thermo Scientific Harshaw TLD Materials and Dosimeters*.

Tootell, A. 2018. *Radiation Dose Assessment: Measurement, Estimation and Interpretation*. University of Salford.

Tootell, A., Lundie, M., Szczepura, K. and Hogg, P. 2012. Reducing error in TLD dose radiation measurements. *In*: *United Kingdom Radiological Congress*. Manchester 25-27 June.

Tootell, A., Szczepura, K. and Hogg, P. 2014. An overview of measuring and modelling dose and risk from ionising radiation for medical exposures. *Radiography*. **20**(4), pp.323–332.

Torell, G., Nachemson, A., Haderspeck-Grib, K. and Schultz, A. 1985. Standing and supine Cobb measures in girls with idiopathic scoliosis.pdf. *Spine*. (10), pp.425–427.

Tran, L. and Seeram, E. 2017. Current perspectives on the use of the linear non-threshold (LNT) model in radiation protection. *International Journal of Radiology & Medical Imaging*. **3**(123).

Tubiana, M., Feinendegen, L.E., Yang, C. and Kaminski, J.M. 2009. The linear no-threshold relationship is inconsistent with radiation biologic and experimental data. *Radiology*. **251**(1), pp.13–22.

Ueno, M., Takaso, M., Nakazawa, T., Imura, T., Saito, W., Shintani, R., Uchida, K., Fukuda, M., Takahashi, K., Ohtori, S., Kotani, T. and Minami, S. 2011. A 5-year epidemiological study on the prevalence rate of idiopathic scoliosis in Tokyo: School screening of more than 250,000 children. *Journal of Orthopaedic Science*. **16**(1), pp.1–6.

Uffmann, M. and Schaefer-Prokop, C. 2009. Digital radiography: The balance between image quality and required radiation dose. *European Journal of Radiology*. **72**(2), pp.202–208.

UK National Screening Committee 2015. *Screening for Adolescent Idiopatic Scoliosis*.

Ulsh, B.A. 2018. A critical evaluation of the NCRP Commentary 27 endorsement of the linear no-threshold model of radiation effects. *Environmental Research*. **167**(August), pp.472–487.

Vassileva, J. 2002. A phantom for dose-image quality optimization in chest radiography. *The British journal of radiology*. **75**(898), pp.837–842.

Vavruch, L. and Tropp, H. 2016. A Comparison of Cobb Angle: Standing Versus Supine

Images of Late-onset Idiopathic Scoliosis. *Polish Journal of Radiology*. **81**, pp.270–276.

Visvikis, D., Bardies, M., Chiavassa, S., Danford, C., Kirov, A., Lamare, F., Maigne, L., Staelens, S. and Taschereau, R. 2006. Use of the GATE Monte Carlo package for dosimetry applications. *Nuclear Instruments and Methods in Physics Research Section A: Accelerators, Spectrometers, Detectors and Associated Equipment*. **569**(2), pp.335–340.

Vodovatov, A. V, Kamishanskaya, I.G., Drozdov, A.A. and Bernhardsson, C. 2017. Quality assessment of digital X-ray chest images using an anthropomorphic chest phantom. *Journal of Physics: Conference Series*. **808**(1), p.011001.

Vrtovec, T., Janssen, M.M.A., Likar, B., Castelein, R.M., Viergever, M.A. and Pernuš, F. 2013. Evaluation of pelvic morphology in the sagittal plane. *The Spine Journal*. **13**(11), pp.1500–1509.

Vrtovec, T., Pernuš, F. and Likar, B. 2009. A review of methods for quantitative evaluation of axial vertebral rotation. *European Spine Journal*. **18**(8), pp.1079–1090.

Wade, R., Yang, H., McKenna, C., Faria, R., Gummerson, N. and Woolacott, N. 2013. A systematic review of the clinical effectiveness of EOS 2D/3D X-ray imaging system. *European Spine Journal*. **22**(2), pp.296–304.

Wall, B.F., Haylock, R., Jansen, J.T.M., Hillier, M.C., Hart, D. and Shrimpton, P.C. 2011. *Radiation Risks from Medical X-ray Examinations as a Function of the Age and Sex of the Patient* [Online]. Chilton, Didcot: Health Protection Agency Centre. Available from: https://pdfs.semanticscholar.org/d90f/22c2c119c618c6822eb094087464e5ca3c4b.pdf.

Wang, B., Kim, C.-H. and Xu, X.G. 2004. Monte Carlo modeling of a high-Sensitivity MOSFET dosimeter for low- and medium-energy photon sources. *Medical Physics*. **31**(5), p.1003.

Watanabe, Y. and Constantinou, C. 2006. Phantom material for radiology *In*: *Encyclopedia of Medical Devices and Instrumentation*. John Wiley&Sons.

Weinstein, S.L., Dolan, L.A., Cheng, J.C.Y., Danielsson, A. and Morcuende, J.A. 2008. Adolescent idiopathic scoliosis. *Lancet (London, England)*. **371**(9623), pp.1527–1537.

Wells, R.G. 2018. Dose reduction is good but it is image quality that matters. *Journal of Nuclear Cardiology*., pp.1–3.

Wessberg, P., Danielson, B.I. and Willen, J. 2006. Comparison of Cobb angles in idiopathic scoliosis on standing radiographs and supine axially loaded MRI. *Spine*. **31**(26), pp.3039–3044.

White, D.R. and Constantinou, C. 1982. Anthropomorphic phantom materials: Progress in medical radiation physics *In*: C. G. Orton, ed. Boston, MA: Springer US, pp.133–193. Available from: https://doi.org/10.1007/978-1-4615-7691-4_3.

Whitley, A.S., Sloane, C., Hoadley, G., Moore, A.D. and Alsop, C.W. 2005. *Clark's positioning in radiography* 12th ed. London: Hodder Arnold.

Williams, M.B., Krupinski, E.A., Strauss, K.J., Breeden, W.K., Rzeszotarski, M.S.,

Applegate, K., Wyatt, M., Bjork, S. and Seibert, J.A. 2007. Digital radiography image quality: Image acquisition. *Journal of the American College of Radiology*. **4**(6), pp.371–388.

Winslow, J.F., Hyer, D.E., Fisher, R.F., Tien, C.J. and Hintenlang, D.E. 2009. Construction of anthropomorphic phantoms for use in dosimetry studies. *Journal of Applied Clinical Medical Physics*. **10**(3), pp.195–204.

Wong, H.-K., Hui, J.H.P., Rajan, U. and Chia, H.-P. 2005. Idiopathic scoliosis in Singapore schoolchildren: a prevalence study 15 years into the screening program. *Spine*. **30**(10), pp.1188–1196.

Wong, M.D., Wu, X. and Liu, H. 2011. The effects of x-ray beam hardening on detective quantum efficiency and radiation dose. *Journal of X-Ray Science and Technology*. **19**(4), pp.509–519.

World Health Organization 2016. *Communicating radiation risks in paediatric imaging*. Geneva, Switzerland: World Health Organization.

Yamato, Y. and Matsuyama, Y. 2018. Will a low-dose biplanar radiograph become "gold standard" for three-dimensional assessment of spinal deformity in patients with adolescent idiopathic scoliosis? *Journal of Spine Surgery*. **4**(2), pp.465–466.

Yan, H., Cervino, L., Jia, X. and Jiang, S. 2012. A comprehensive study on the relationship between image quality and imaging dose in low-dose cone beam CT. *Medical Physics*. **39**(6), p.3912.

Yang, F., He, Y., Deng, Z.S. and Yan, A. 2016. Improvement of automated image stitching system for DR X-ray images. *Computers in Biology and Medicine*. **71**, pp.108–114.

Yazici, M., Acaroglu, E.R., Alanay, A., Deviren, V., Cila, A. and Surat, A. 2001. Measurement of vertebral rotation in standing versus supine position in adolescent idiopathic scoliosis. *Journal of Pediatric Orthopaedics*. **21**(2), pp.252–256.

Yifrah, T., Abraham, A., Weinstein, M., Pelled, O., German, U. and Mintz, M. 2014. About Background Correction for LiF:Mg,Ti readout. *Dosimetry*. **16**(30), pp.120–124.

Yoshiura, K. 2012. Image quality assessment of digital intraoral radiography - perception to caries diagnosis. *Japanese Dental Science Review*. **48**(1), pp.42–47.

Young, M., Hill, D.L., Zheng, R. and Lou, E. 2015. Reliability and accuracy of ultrasound measurements with and without the aid of previous radiographs in adolescent idiopathic scoliosis (AIS). *European Spine Journal*. **24**(7), pp.1427–1433.

Yu, C. and Luxton, G. 1999. TLD dose measurement: A simplified accurate technique for the dose range from 0.5 cGy to 1000 cGy. *Medical Physics*. **26**(6), pp.1010–1016.

Yvert, M., Diallo, A., Bessou, P., Rehel, J.L., Lhomme, E. and Chateil, J.F. 2015. Radiography of scoliosis: Comparative dose levels and image quality between a dynamic flat-panel detector and a slot-scanning device (EOS system). *Diagnostic and interventional imaging*. **96**(11), pp.1177–1188.

Zacharias, C., Alessio, A.M., Otto, R.K., Iyer, R.S., Philips, G.S., Swanson, J.O. and Thapa,

M.M. 2013. Pediatric CT: strategies to lower radiation dose. *AJR. American journal of roentgenology*. **200**(5), pp.950–956.

Zarb, F. and Rainford, L. 2014. Psychophysical evaluation of Catphan®600 CT image quality findings using human observers and software analysis. *Radiography*. **20**(4), pp.318–322.

Zarb, F., Rainford, L. and McEntee, M.F. 2010. Image quality assessment tools for optimization of CT images. *Radiography*. **16**(2), pp.147–153.

Zhang, G., Shao, Y., Kim, Y. and Guo, W. 2016. Vertebrae detection algorithm in CT scout images. *Communications in Computer and Information Science*. **634**(July 2016), pp.230–237.

Zhang, J., Lou, E., Hill, D.L., Raso, J. V., Wang, Y., Le, L.H. and Shi, X. 2010. Computer-aided assessment of scoliosis on posteroanterior radiographs. *Medical and Biological Engineering and Computing*. **48**(2), pp.185–195.

Zhang, J., Lou, E., Shi, X., Wang, Y., Hill, D.L., Raso, J. V, Le, L.H., Lv, L. and Mm, J. 2010. A Computer-aided Cobb Angle Measurement Method. *J Spinal Disord Tech*. **23**(6), pp.383–387.

Zheng, R., Chan, A.C.Y., Chen, W., Hill, D.L., Le, L.H., Hedden, D., Moreau, M., Mahood, J., Southon, S. and Lou, E. 2015. Intra- and inter-rater reliability of coronal curvature measurement for adolescent idiopathic scoliosis using ultrasonic imaging method - A pilot study. *Spine Deformity*. **3**(2), pp.151–158.

Zheng, R., Hill, V., Hedden, D., Mahood, J., Moreau, V., Southon, S. and Lou, E. 2018. Factors influencing spinal curvature measurements on ultrasound images for children with adolescent idiopathic scoliosis (AIS). *PLoS ONE*. **13**(6), pp.1–16.

Zheng, R., Young, M., Hill, D., Le, L.H., Hedden, D., Moreau, M., Mahood, J., Southon, S. and Lou, E. 2016. Improvement on the accuracy and reliability of ultrasound coronal curvature measurement on adolescent idiopathic scoliosis with the aid of previous radiographs. *Spine*. **41**(5), pp.404–411.

Zheng, Y., Lee, T., Lai, K., Yip, B., Zhou, G., Jiang, W., Cheung, J., Wong, M., Ng, B., Cheng, J.C.Y. and Lam, T.P. 2016. A reliability and validity study for Scolioscan: A radiation-free scoliosis assessment system using 3D ultrasound imaging. *Scoliosis and Spinal Disorders*. **11**(1), pp.1–15.

Zurl, B., Tiefling, R., Winkler, P., Kindl, P. and Kapp, K.S. 2014. Hounsfield units variations. *Strahlentherapie und Onkologie*. **190**(1), pp.88–93.